AFRL-IF-RS-TR-2002-157
Final Technical Report
July 2002

100 GB/s TIME DIVISION MULTIPLEX (TDM) ACCESS NODES AND REGENERATORS BASED ON NOVEL LOOP MIRRORS WITH HIGH NONLINEARITY FIBERS

University of Michigan

Sponsored by
Defense Advanced Research Projects Agency
DARPA Order No. C512

APPROVED FOR PUBLIC RELEASE; DISTRIBUTION UNLIMITED.

AIR FORCE RESEARCH LABORATORY
INFORMATION DIRECTORATE
ROME RESEARCH SITE
ROME, NEW YORK

This report has been reviewed by the Air Force Research Laboratory, Information Directorate, Public Affairs Office (IFOIPA) and is releasable to the National Technical Information Service (NTIS). At NTIS it will be releasable to the general public, including foreign nations.

AFRL-IF-RS-TR-2002-157 has been reviewed and is approved for publication.

APPROVED: 

PAUL SIERAK
Project Engineer

FOR THE DIRECTOR:

WARREN H. DEBANY, Technical Advisor
Information Grid Division
Information Directorate

REPORT DOCUMENTATION PAGE

Form Approved
OMB No. 074-0188

1. AGENCY USE ONLY (Leave blank)	2. REPORT DATE	3. REPORT TYPE AND DATES COVERED
	JULY 2002	Final May 97 – May 01

4. TITLE AND SUBTITLE
100 GB/s TIME DIVISION MULTIPLEX (TDM) ACCESS NODES AND REGENERATORS BASED ON NOVEL LOOP MIRRORS WITH HIGH NONLINEARITY FIBERS

5. FUNDING NUMBERS
C - F30602-97-1-0202
PE - 61101E
PR - C512
TA - 00
WU - 01

6. AUTHOR(S)
Mohammed N. Islam

7. PERFORMING ORGANIZATION NAME(S) AND ADDRESS(ES)
University of Michigan
1301 Beal Avenue
Ann Arbor Michigan 48109-2122

8. PERFORMING ORGANIZATION REPORT NUMBER
N/A

9. SPONSORING / MONITORING AGENCY NAME(S) AND ADDRESS(ES)
Defense Advanced Research Projects Agency AFRL/IFGA
3701 North Fairfax Drive 525 Brooks Road
Arlington Virginia 22203-1714 Rome New York 13441-4505

10. SPONSORING / MONITORING AGENCY REPORT NUMBER
AFRL-IF-RS-TR-2002-157

11. SUPPLEMENTARY NOTES
AFRL Project Engineer: Paul Sierak/IFGA/(315) 330-7346/ Paul.Sierak@rl.af.mil

12a. DISTRIBUTION / AVAILABILITY STATEMENT
APPROVED FOR PUBLIC RELEASE; DISTRIBUTION UNLIMITED.

12b. DISTRIBUTION CODE

13. ABSTRACT ***(Maximum 200 Words)***
This report covers work on the development of twisted and spun optical fiber for use in a polarization insensitive nonlinear optical loop mirror. Work is also described in the area of optical wavelength conversion based on parametric amplification in highly nonlinear fiber. In addition an optical time domain demultiplexer was demonstrated at 80 Gbps using the nonlinear optical loop mirror as part of its structure.

14. SUBJECT TERMS
TDM, Regenerators, Fiber Optics, Nonlinear Optical Loop Mirrors

15. NUMBER OF PAGES
193

16. PRICE CODE

17. SECURITY CLASSIFICATION OF REPORT	18. SECURITY CLASSIFICATION OF THIS PAGE	19. SECURITY CLASSIFICATION OF ABSTRACT	20. LIMITATION OF ABSTRACT
UNCLASSIFIED	UNCLASSIFIED	UNCLASSIFIED	UL

Table of Contents

Integrating overview

When originally proposed, there were four main thrusts in the joint University of Michigan (UM) and Corning project. The first two thrusts related to nonlinear optical loop mirrors (NOLMs) using high-nonlinearity (HiNL) fiber. The first thrust was in using one-wavelength NOLMs (1W-NOLM) for operations such as logic gates, while the second thrust was on two-wavelength NOLMs (2W-NOLM) for applications such as demultiplexing. The final two thrusts related to sub-systems that employed the NOLMs developed in the first part. In particular, the third thrust was an all-optical regenerator (AOR), which was envisioned to use the 1W-NOLM plus a synchronized laser and short pulse source. Finally, the fourth thrust was an opto-electronic access node (OEAN), which would use the 2W-NOLM as a demultiplexer at high speeds.

Our actual work on the project touched on all four of the thrust areas, although our approach evolved as we learned more about each of the thrusts. For the first two thrusts, we developed a new measurement technique to quantify the nonlinearity of the fibers being used. This technique used solitons to measure the path average nonlinearity of optical fibers (paper [3], patent [1]). Then, for the first thrust we demonstrated a new twisted fiber for polarization insensitive operation of the NOLM (paper [5], patent [3]). For the second thrust of the 2W-NOLM, we demonstrated polarization insensitive demultiplexing of 100Gb/s words using a twisted fiber NOLM (paper [6], patent [2]). Finally, a detailed experimental measurement and simulation of the circularly polarized spun fiber in the 2W-NOLM was conducted (paper [10]).

A considerable amount of work was done on the last two sub-system thrusts. We realized that both thrusts needed novel, broadband, high-repetition-rate sources that could be synchronized very accurately. Therefore, we first invented a novel self-synchronization scheme for high speed packet networks (paper [2], patent [4]). Second, we invented a broadband supercontinuum source that was very stable because the broadband signal was generated in a short length of dispersion-shifted fiber (paper [7], patent [5]). Third, we refined this supercontinuum source to operate at 10Gb/s with low noise performance (paper [12]). On the fourth OEAN thrust, we first demonstrated and did a performance analysis of the off-ramp portion of the OEAN (paper [4]). Then, we used a 100Gb/s and the full OEAN and demonstrated the cascadability of the node by looping it back on itself (paper [8]). Finally, demultiplexing at high repetition rates was conducted by sending a graduate student to Corning to work with their high-speed testbed. In particular, 80Gb/s to 10Gb/s polarization-insensitive demultiplexing with circularly polarized spun fiber was demonstrated (paper [9]). On the third thrust, we decided that the AOR could best be implemented using a wavelength conversion scheme based on parametric amplification. Therefore, we first demonstrated a low-power, high-efficiency wavelength converter based on modulational instability in high nonlinearity fiber (paper [1], patent [6]). This work was further refined to achieve gain enhancement in cascaded fiber parametric amplifiers by splicing together different fiber types to re-adjust the phase matching (paper [11]).

Throughout the project, there was close collaboration between UM and Corning. There were at least quarterly visits between the two sites in addition to numerous phone, fax and email communications. Corning made several generations of HiNL fiber for the project, and we interacted very closely on each iteration. In the last year of the project, graduate student Janet Lou went to Corning and worked on their high-speed testbed to experimentally demonstrate the 80Gb/s to 10Gb/s demultiplexing. Beyond this close collaboration, there were also six patents

filed, many of them jointly with Corning. This will give some advantage and protection if Corning chooses to commercialize the devices or sub-systems.

In summary, the main accomplishment in the first two thrusts was the development of twisted and spun fiber for implementing a polarization insensitive NOLM. We identified the primary problem as being the polarization sensitivity of the NOLM, and we fixed the fundamental problem that lead to the polarization behavior. For the AON thrust, we changed our approach to focus on wavelength conversion based on parametric amplification in HiNL fiber. Our biggest accomplishment was the OEAN thrust, were we demonstrated a full OEAN node and also worked with the Corning testbed to demonstrate operation at 80Gb/s for the demultiplexer.

In the following, a detailed description of the various technical accomplishments will be given. Also, one section details the collaboration with Corning. Finally, the patents and publications will be listed, and the papers will be attached in the Appendix.

Technical Details

Path Average Measurements of Optical Fiber Nonlinearity Using Solitons

We experimentally demonstrate a new method to determine the optical nonlinearity of single mode optical fiber. The technique takes advantage of the well-known nonlinear response of optical fibers and well-developed models for soliton pulse propagation to extract information about the fiber characteristics. Fiber nonlinearity can degrade the performance of communication systems by, for example, causing crosstalk and signal distortions. Measuring the fiber nonlinearity would greatly aid system designers in building and upgrading communication systems. The method is utilized to determine values for n_2/A_{eff}, where n_2 is the nonlinearity of the glass and A_{eff} is effective area of the core, on various lengths of Corning SMF-28 fiber and Corning SMF-DS fiber. Experimentally measured propagation results for short (≈2 ps) optical pulses are compared to computer simulated models to determine the fiber nonlinearity. The method finds $n_2/A_{eff} = 3.0\text{x}10^{-10}$ W^{-1} values for short lengths (≈400 m) of Corning SMF-28 fiber and values of $2.7\text{x}10^{-10}$ W^{-1} for longer lengths (≈6.5 km and ≈20 km). The difference is expected due to the 8/9 polarization scrambling factor, and the values are in agreement with reported literature. The method also determines $n_2/A_{eff} = 5.6\text{x}10^{-10}$ W^{-1} for a ≈12 km Corning dispersion shifted fiber. The method has two major regimes of operation based on the soliton period, a characteristic length for solitons. For few soliton periods ($Z/Z_o < \sim 4$) the output phase is measured as a function of launched power; for many soliton periods ($Z/Z_o > \sim 4$) the output pulsewidth is measured as a function of launched power. The method's major advantage is its capability to measure long lengths of standard fiber, where it uses only standard diagnostic tools such as autocorrelation and optical power measurements. However, the method is only applicable in the soliton regime of fibers.

Polarization Insensitive NOLM Demultiplexer using Twisted Fiber

We experimentally demonstrate the reduction of the polarization sensitivity of a NOLM from 5dB to 0.5dB by using 550m of twisted dispersion-shifted fiber with a twist rate of 8 turns/m (24 turns/beat length). The twisting of fiber induces circular birefringence and equates the parallel- and orthogonal-polarization nonlinear phase shift terms. Experimental results show that the polarization sensitivity monotonically decreases from 5dB for non-twisted fiber to 0.5dB for 8 turns/m, and the twist rate should be above 4 turns/m (>10 turns/beat length) to emulate circularly polarized fiber. The minimum polarization sensitivity occurs when control pulse polarization is aligned on one of the eigenmodes of the twisted fiber. With the twisted fiber at 8 turns/m in the NOLM, the nonlinear transmission is 23% at switching energy of 4pJ/pulse. Simulations confirm the observed behavior and indicate that the remaining polarization sensitivity results from energy transfer between orthogonal modes of the signal pulse.

Polarization Insensitive Demultiplexing of 100Gb/s Words in a Twisted Fiber NOLM

We demultiplex 100Gb/s words using a 2W-NOLM with polarization sensitivity <0.5dB obtained by using fiber twisted at 8 turns/m. This polarization insensitive demultiplexer is more suitable than conventional non-twisted fiber NOLMs for use in high-speed all-optical networks where the input states of polarization are arbitrary. The demultiplexer consists of synchronized erbium-doped fiber lasers (λ_1=1535nm, τ_1=1.3ps; λ_2=1543nm, τ_2=2.2ps), a 100Gb/s fixed word encoder, and a NOLM using 450m of twisted fiber with λ_0=1518nm. For inputs of arbitrary polarization, we measure a ~5.5ps timing window and contrast ratio >15dB. To understand the improvement in performance of the system due to the polarization insensitivity, we apply a statistical method of measuring the Q-parameter for the twisted and non-twisted fiber demultiplexers. The Q-parameter of ~15 for the twisted fiber NOLM is improved over that of the NOLM with non-twisted fiber (Q~10), and is consistent with an increased minimum nonlinear transmission.

Novel Self-Synchronization Scheme for High-Speed Networks

We demonstrate a novel self-synchronization scheme for high speed packet TDM networks using an easily saturated but slowly recovered gain or loss combined with intensity discrimination. This self-synchronization scheme does not use marker pulses in packets. In particular, we use a semiconductor optical amplifier (SOA) as the slow recovery gain element, and an unbalanced nonlinear optical loop mirror (NOLM) or a dispersion-shifted (DS) fiber/optical filter as the intensity discriminator. The contrast ratio of the first pulse to the remaining pulses of a 100Gb/s eight-bit packet is >3dB at the output of the SOA and >20dB at the outputs of both intensity discriminators.

Stable Supercontinuum Generation in Short Length of Dispersion-Shifted Fiber

By propagating 500fs pulses through 2.5m of standard fiber followed by 2m of dispersion-shifted fiber, we generate >200nm of spectral continuum between 1430 and 1630 nm, which is flat to less than +/- 0.5dB over more than 60nm. Pulses obtained by filtering the continuum show no increase in timing jitter over the source laser and are pedestal-free to > 28dB, indicating excellent stability and coherence. We show that the 2nd and 3rd order dispersions of the continuum fiber and self-phase modulation are primarily responsible for the continuum generation and spectral shaping and find close agreement between simulations and experiments.

Multi-wavelength Source based on Longitudinal Mode Carving of SC

We demonstrate a high power, multi-wavelength short pulse source at 10 Gb/s by spectral slicing of supercontinuum generated in short fibers. We show that short fiber SC can be used for DWDM applications because of its >7.9 dBm/nm power spectral density, 140 nm spectral bandwidth and ±0.5 dB spectral uniformity over 40 nm. Pulse carving up to 60 nm away from the pump wavelength indicates that the coherence of the SC is maintained. By using high nonlinearity fibers the spectral bandwidth is increased to 250 nm, which can accommodate >300 wavelength channels with 0.8 nm wavelength spacing and >3 Tb/s data rate. Mechanisms contributing to the SC generation and its coherence degradation are also investigated.

Off-Ramp Portion of an OEAN

Ultrafast processing of packets is demonstrated and the performance analyzed for the off-ramp portion of an OEAN. The off-ramp consists of synchronized fiber lasers driving an all-optical header processor that includes nonlinear optical loop mirrors (NOLM), electro-optic router, and demultiplexer in the form of a two-wavelength NOLM. We achieve switching contrasts of 10:1 for the header processor and demultiplexer with switching energies of 10 pJ and 1 pJ, respectively. Also, a proposed measurement technique to obtain eye diagrams is used to analyze the all-optical header processor using the synchronized lasers. Using this technique, we obtain an eye diagram with a Q value of 7.1±0.36, which corresponds to a worst case BER value of 8.8×10^{-12} for a 95% confidence level. Finally, simulation models are used to verify and compare the experimental results, and we find good agreement. We also use the model to study the various causes for the degradation of the Q value through our system.

100Gb/s-Word OEAN in a Looped-back Configuration

We experimentally demonstrate the adding, dropping, and passing-through of 100Gb/s-word packets in a looped-back all-optical time-division-multiplexed (TDM) access node. Packets are routed with 17dB contrast ratio and demultiplexed with 20dB contrast ratio. This node uses short 100Gb/s words in order to demonstrate its potential to process data packets from multiple sources and to perform packet-switching in a multi-node ring network configuration. The add function involves generating a new packet that is switched onto the network when an incoming packet is removed. The drop function requires a local source synchronized to each individual packet to perform address checking in the header processor, demultiplexing of the packet payload, and routing of the incoming packet either to the local node or to the network. The ability to tolerate timing jitter as well as varying input signal characteristics is essential to an all-optical access node in a multi-node network. For 2ps input pulses, the header processor has a timing window of ~5ps and the demultiplexer has a timing window of ~5.5ps. This allows tolerance to bit-to-bit timing jitters or to an increase in the pulse width of up to 3ps. Packet-to-packet timing jitter is detected and compensated by the technique used to synchronize the local source to each packet.

The key enabling technologies of an all-optical TDM packet add/drop multiplexer are discussed, including a passively mode-locked erbium-doped fiber laser (λ~1535-1550nm, $\Delta\tau$~1-5ps), a low-birefringence nonlinear optical loop mirror logic gate, self-synchronization to incoming packets using a fast-saturation/slow-recovery gain element followed by an intensity discriminator, a two-wavelength nonlinear optical loop mirror demultiplexer, and synchronization of new packets to the network packet rate using a phase-locked-loop. The logic gate has a contrast ratio of at least 10dB, and the demultiplexer has an extinction ratio of at least 20dB. The local source is automatically synchronized to the incoming packet because it uses an extracted pulse from the packet, which has a contrast ratio of >20dB to the rest of the packet.

Finally, new packets are added using a local laser and a synchronization method, which gives a timing jitter of ~1ps. Using a statistical method of measuring Q-value with picosecond resolution, we show that a header processor with two cascaded logic gates has a Q-value of 7.1 with a 95% confidence level. The Q-value is limited by the extinction ratio of the logic gates.

80Gb/s to 10Gb/s Polarization-Insensitive Demultiplexing with 2W-NOLM

We demonstrate and simulate a polarization insensitive two-wavelength nonlinear optical loop mirror demultiplexer with circularly polarized spun fiber. Demultiplexing of 10Gb/s channels from 80Gb/s pseudo-random bit streams shows the polarization sensitivity of the device is reduced to <1dB for >90% transmission and is confirmed by simulations based on the nonlinear Schrödinger equation. Bit-error-rate measurements show that the remaining polarization sensitivity leads to a power penalty difference of 1.5dB. The power penalty is due to a combination of timing window induced amplitude fluctuations and cross-talk between the control and the unwanted channels of the counter-propagating signal. The nonlinear transmission is 91% for a switching energy of 3.4pJ/pulse and the full-width-half-maximum timing window is 9.6ps. Simulations show that for the perfectly circularly-polarized fiber NOLM, the range of switching energy where polarization sensitivity is <1dB is at least 7.3dB. This demultiplexer is measured to have a polarization sensitivity <1.3dB for control and signal up to 20nm, which is in good agreement with simulation results showing <1dB polarization sensitivity. In contrast, simulation of a linear fiber nonlinear optical loop mirror shows that it has polarization sensitivity >5dB.

A short pulse laser at 1554nm is used to generate the 10Gb/s bit stream input to a LiNbO3 modulator. A pseudo-random pattern generator is used to drive the modulator to encode the bit stream, and the 80Gb/s bit stream is created by optically multiplexing the encoded bit stream. The local source is generated by modulating the output of a continuous-wave source (λ=1550nm) with an electro-absorption modulator. The modulated output is propagated through 12.2km of dispersion-decreasing fiber to compress the pulses. The resulting pulse stream has a pulse width of 7.7ps and an extinction ratio of 13dB. The circularly-polarized spun fiber has a length of ~1km, and ~4.1 times higher nonlinearity than that of conventional dispersion-shifted fiber. The linear birefringence before spinning is n=1×10-6, and the spin rate is 16 turns/m, corresponding to 25 turns/beat length.

Low-Power High-Efficiency Wavelength Conversion

Bandwidth and peak efficiency are enhanced for wavelength conversion based on induced modulation instability by using dispersion-shifted fiber in which the nonlinearity (n_2/A_{eff}) is enhanced by a factor of ~4.5 over conventional dispersion-shifted fiber. We experimentally obtain a peak conversion efficiency as high as 28 dB over a 40nm bandwidth with 600mW peak pump power. Considerations for further enhancement of fiber-based wavelength conversion are also studied.

Gain Enhancement in Cascaded Fiber Parametric Amplifiers

We show a novel gain enhancement scheme for fiber-optic parametric amplifiers utilizing quasi-phase matching (QPM) and cascaded amplification. The conditions for maximizing parametric gain using QPM are rigorously derived based on degenerate four-wave mixing theory. By implementing the rules, we experimentally achieve > 12 dB gain improvement in a 3-stage dispersion-shifted fiber parametric amplifier. 16 dB overall gain is obtained with 11 nm separation between zero-dispersion wavelength and pump wavelength. The experimental results

show good agreement with theory and simulations. The influence of quasi-phase matching on spectral characteristics of parametric gain is investigated with numerical simulations.

Corning Collaboration

The DARPA funded Corning Incorporated – University of Michigan joint project was primarily aimed at understanding and improving the environmental and polarization instabilities of fiber based NOLMs. NOLMs are well known for their ultra-fast switching and optical processing capabilities. However, they are also known for their environmental and polarization instabilities. Jointly, we proposed that the primary source of this environmental instability was that the switching of the signal pulse was very sensitive to the relationship of the polarization states of the switching pulse and signal pulse. We proposed that since these polarization states can wander with temperature and other environmental perturbations, by addressing the polarization concerns we will have addressed the environmental concerns as well.

We had many joint meetings both at Corning and at the University of Michigan. During these meetings, we proposed and outlined the experiments and modeling projects to be conducted. The switching and optical processing experiments were for the most part conducted at the university, although a good amount of it was done at Corning during Janet Lou's internship. The fiber fabrication and characterization was for the most part done at Corning. The switching and optical processing experiments were for the most part done at the University of Michigan, although a good amount of it was done at Corning during Janet Lou's internship.

The key accomplishment of the joint project was the concept, simulation and eventual demonstration that the use of quasi-circularly polarized fiber in the loop enables nearly polarization independent switching in a NOLM. A circularly polarized pump signal is required, but the incoming signal can be of an arbitrary polarization state. This concept was first demonstrated with numerical simulations, then experimentally using twisted fiber in a NOLM and finally using a specially fabricated circularly polarized fiber by spinning the fiber during the fabrication process.

The polarization dependence of the NOLM was reduced from 5 dB to nearly 0.5 dB when using a twisted highly nonlinear fiber. The fiber was twisted 8 times per meter or approximately 24 times per beat length in order to achieve the nearly circularly polarized fiber.

We were able to fabricate a nearly - circularly polarized - spun fiber while simultaneously maintaining the highly nonlinear properties and all the required dispersion properties of the non-polarization maintaining fiber. This includes the wavelength position of the dispersion zero as well as the dispersion slope. This was achieved by spinning the fiber preform using a specially designed spinning apparatus.

Using this fiber, less than 1 dB polarization dependence was achieved when the fiber had a spin rate of 16 times per meter. A joint patent was filed.

List of Papers and Patents

Patents resulting from Research:

1. Patent pending on "Soliton Pulse Transmission over Long Waveguide Fiber Lengths," M.N. Islam, G.A. Nowak and T.J. Xia.
2. Patent pending on "Polarization independent switching in two-wavelength devices using circularly polarized fiber," M.N. Islam and D.A. Nolan.
3. Patent pending on "Circularly Polarized Fiber for Multiple-Wavelength Transmission Systems and Enhanced all-Optical Switching," M.N. Islam and D.A. Nolan.
4. Patent pending on "novel Self-Synchronization Scheme for High Speed Packet TDM Networks," M.N. Islam and T.J. Xia.
5. Patent pending on "Method and system for generating a broadband spectral continuum and continuous wave generating system utilizing same," M.N. Islam, J. Kim and O. Boyraz.
6. Patent pending on "Wavelength Band Transmitters using Modulation Instability Based Wavelength Converters," M.N. Islam, O. Boyraz, and C. DeWilde.

Publications resulting from Research (attached documents):

1. G.A. Nowak, Y.-H. Kao, T.J. Xia, M.N. Islam and D. Nolan, "Low-power high-efficiency wavelength conversion based on modulational instability in high nonlinearity fiber," Opt Lett. **23**, 936-938 (1998)
2. T.J. Xia, Y.-H. Kao, Y. Liang, J.W. Lou, K.H. Ahn, O. Boyraz, A.A. Said and M.N. Islam, "Novel Self-Synchronization Scheme for High Speed Packet TDM Networks," IEEE Phot. Tech. Lett. **11**, 269-271 (1999).
3. Y. Liang, J.W. Lou, J.C. Stocker, O. Boyraz, J.K. Anderson, M.N. Islam and D.A. Nolan, "Polarization insensitive nonlinear optical loop mirror demultiplexer using twisted fiber," Opt. Lett. **24**, 726-728 (1999).
4. J.W. Lou, J.K. Anderson, J.C. Stocker, M.N. Islam, and D.A. Nolan, "Polarization Insensitive Demultiplexing of 100-Gb/s Words Using a Twisted Fiber Nonlinear Optical Loop Mirror," IEEE Photonics Technology Letters. Vol. 11, No. 2, pp. 1602-1604, Dec. 1999.
5. G.A. Nowak, J. Kim, and M.N. Islam, "Stable Supercontinuum Generation in Short Length of Conventional Dispersion-Shifted Fiber," Applied Optics, Vol. 38, No. 36, pp. 7364-7369, Dec. 1999.
6. J.W. Lou, Y. Liang, O. Boyraz, and M.N. Islam, "All-optical 100Gb/s-word Packet-Time-Division-Multiplexed Access node in a Looped-back Configuration: Enabling Technologies for Sequential Add/Drop Functionality," Applied Optics 2000, Vol. 39, Iss 29, pp. 5280-5294.

7. J.W. Lou, K.S. Jepsen, D.a. Nolan, S.H. Tarcza, W.J. Bouton, A.F. evans, M.N. Islam, "80Gb/s to 10Gb/s Polarization-Insensitive Demultiplexing With Circularly Polarized Spun Fiber in a Two-Wavelength Nonlinear Optical Loop Mirror," IEEE Photonics Technology Letters 2000, Vol. 12, Iss 12, pp. 1701-1703.
8. J.W. Lou, K.S. Jepsen, D.A. Nolan, S.H. Tarcza, W.J. Bouton, A.F. Evans, and M.N. Islam, "Experimental Measurement and Simulation of Circularly Polarized Spun Fiber in a Two-Wavelength Nonlinear Optical Loop Mirror Polarization Insensitive Demultiplexer," (submitted to Journal of Lightwave Technology).
9. J.Kim, J.H. Lim, O. Boyraz, and M.N. Islam, "Gain Enhancement in cascaded Fiber parametric Amplifier with Quasi-Phase Matching: Theory and Experiment," IEEE Journal of Lightwave Technology 2001, vol. 19, Iss 2, pp. 247-251).
10. O. Boyraz, J. Kim and M.N. Islam, "A Mult-wavelength CW Source Based on Longitudinal Mode Carving of Supercontinuum Generated in Fibers and Noise Performance," (submitted to Journal of Lightwave Technology).
11. O. Boyraz, J. Kim, M.N. Islam, F. Coppinger, and B. Jalali, "10 Gb/s Multiple Wavelength, Coherent Short Pulse Source Based on Spectral Carving of Supercontinuum Generated in Fibers," Journal of Lightwave Technology, Vol. 18, No. 12, December 2000.
12. J.K. Anderson, G.A. Nowak, J.W. Lou, M.N. Islam, R.M. Fortenberry and S.A. Newton, "Path Average Measurements of Optical Fiber Nonlinearity Using Solitons," J. Lightwave Tech. **16**, 2328-2335 (1998).
13. O. Boyraz, J.W. Lou, K.H. Ahn, Y. Liang, T.J. Xia, Y.-H. Kao, and M.N. Islam, "Demonstration and Performance Analysis for the Off-Ramp Portion of an All-Optical Access Node," J. Lightwave Tech. **17**, 998-1010 (1999).
14. J.W. Lou, "All-Optical Network Access and Demultiplexing Using Nonlinear Optical Loop Mirrors with Novel Fibers," University of Michigan dissertation, 2000.

Appendix A

Low power, high-efficiency wavelength conversion based on modulational instability in high nonlinearity fiber

G.A. Nowak, Y.-H. Kao, T.J. Xia, and M.N. Islam
Department of Electrical Engineering and Computer Science, University of Michigan
1301 Beal Avenue, Ann Arbor, Michigan 48109-2122
D. Nolan
Research, Development and Engineering Division, Corning, Inc.,Corning, New York 14831

ABSTRACT

Bandwidth and peak efficiency are enhanced for wavelength conversion based on induced modulation instability by using dispersion-shifted fiber in which the nonlinearity (n_2/A_{eff}) is enhanced by a factor of ~4.5 over conventional dispersion-shifted fiber. We experimentally obtain a peak conversion efficiency as high as 28 dB over a 40nm bandwidth with 600mW peak pump power. Considerations for further enhancement of fiber-based wavelength conversion are also discussed.

We demonstrate high-efficiency wavelength conversion at low pump powers based on induced modulational instability (MI) in low dispersion, high nonlinearity (Hi-NL) optical fiber. We achieve conversion with a peak efficiency of +28dB over a bandwidth of 40nm using a pulsed pump with a peak power of approximately 600mW. By using 720m of dispersion-shifted (DS) fiber in which the effective nonlinearity has been increased by a factor of ~4.5X, we obtain higher peak conversion efficiencies and broader conversion bandwidths at lower pump power-fiber length products than have been previously reported for conventional DS fibers[1,8].

Wavelength conversion enhances the capacity and flexibility of routing protocols in wavelength-division multiplexed networks by enabling wavelength reuse and dynamic switching and routing. It is also an underlying technology for gateways between time-division multiplexed and wavelength-division multiplexed network interfaces. Key performance parameters for wavelength conversion schemes include conversion efficiency, which we define as the ratio of the converted power to input signal power, as well as bit-rate and modulation format transparency[2,3]. Wavelength converters based on semiconductor optical amplifiers (SOAs) exhibit many attractive performance features, but are generally limited to signal rates of ~ 40 Gb/s due to carrier recombination lifetimes or intraband dynamics[9]. Also, only cross-gain modulation based SOA wavelength converters can provide gain with conversion, typically < 10dB.[2]

Converters based on parametric processes such as MI and four-wave mixing (4WM) in fibers can support almost unlimited bit rates and are transparent to signal modulation format because of the nearly instantaneous response of the third order nonlinearity in fused silica. MI-based converters provide the additional benefit of high gain with conversion compared with 4WM or SOA-based converters, thereby reducing requirements for additional amplification and associated noise increase at the converted wavelength. Fiber wavelength converters, however, require relatively high pump powers (~watts) and long fiber lengths (~kilometers) to achieve significant parametric photon mixing because of the typically weak nonlinearity of fused silica fiber. By increasing the effective nonlinearity, the power-dependent functions of the fiber can be enhanced for a given power or, conversely, the power requirements or lengths can be reduced. We demonstrate the enhancement of the conversion bandwidth, which is to the wavelength range over which the MI process can be phase matched, and the peak gain by using DS fiber in which the effective nonlinearity has been increased by a factor of ~4.5 over typical DS fibers (i.e. Corning SMF-DS).

The bandwidth and efficiency of MI-based wavelength conversion depend on the nonlinearity-assisted phase matching of the propagation vectors and the nonlinearity induced parametric gain. If the propagation constants of the copropagating signal, converted wavelength and pump are k_S, k_a, and k_p, respectively, then the linear phase mismatch is $\Delta k = k_S + k_a - 2k_p$. The phase mismatch with induced nonlinearity is, then

$$\kappa = \Delta k + 2\gamma P \qquad (1)$$

where $\gamma = \frac{2\pi}{\lambda_p}\frac{n_2}{A_{eff}}$ is the nonlinearity coefficient of the fiber, λ_p is the pump wavelength, n_2 is the nonlinear refractive index, A_{eff} is the effective mode-field area, and P is the pump power. The parametric gain[4] is given by,

$$g = \sqrt{(\gamma P)^2 - \left[\frac{\kappa}{2}\right]^2} \tag{2}$$

and represents real gain over a conversion bandwidth corresponding to $-4\gamma P < \Delta k < 0$. If Δk is expanded to 3rd order about the pump wavelength and the pump wavelength lies in the vicinity of the zero-dispersion wavelength (λ_o), it can be expressed as

$$\Delta k \approx -\frac{2\pi c}{\lambda_p^2}\left[\frac{dD}{d\lambda}\bigg|_{\lambda_o}\left(\lambda_p - \lambda_o\right)\right](\Delta\lambda)^2 \tag{3}$$

where $\left.\frac{dD}{d\lambda}\right|_{\lambda_o}$ is the third order dispersion of the fiber and $\Delta\lambda = (\lambda_p - \lambda_a) = (\lambda_s - \lambda_p)$ describes the wavelength separation between the pump and signal or converted wavelengths and is half of the conversion bandwidth. Equations (2) and (3), subject to the requirement that g be real, indicate the explicit nonlinearity dependence of the conversion bandwidth experiencing parametric gain is $\Delta\lambda \propto 2(\gamma P)^{1/2}$.

The MI conversion efficiency, assuming single mode propagation and same polarization for pump, signal, and converted wavelengths is

$$\eta = \frac{P_a(L)}{P_s(0)} = \left(\frac{\gamma P}{g}\right)^2 \sinh^2(gL) \tag{4}$$

where L is the fiber length. The degradation of conversion efficiency with polarization mismatch between the pump and signal is the same as for all 4WM processes in silica fiber ($\sim \cos^2\theta$, where θ is the mismatch in polarization states)[7]. The derivation of equation (4) ignores pump depletion, fiber loss, competing nonlinear processes such as self- and cross-phase modulation, and walk-off between the pump and signal in pulsed systems. Since these effects would lower the parametric gain by lowering the pump power or reduce the interaction length between the pump and signal, the conversion efficiency in (4) is effectively maximum. When the pump and signal are pulsed, dispersion-induced walk-off between them also restricts the maximum bit rates that can be converted, regardless of the response speed of the medium[8]. This is not a restriction, however, with a CW pump. Under a fixed phase-matching condition (i.e. for $\Delta k = -2\gamma P$), the explicit conversion efficiency dependence on nonlinearity is $\eta \propto \sinh^2(\gamma PL)$. Figure 1 illustrates the calculated conversion bandwidth and conversion efficiency dependence on fiber nonlinearity for fixed fiber dispersion characteristics and length at a fixed pump power (600mW). The 4.5-fold increase in parametric gain due to nonlinearity enhancement provides a 24nm increase in conversion bandwidth and 30dB improvement in peak conversion efficiency.

We prove experimentally the enhancements in bandwidth and conversion efficiency provided by Hi-NL fiber in MI-based wavelength conversion. The experimental set-up is shown in Fig. 2. The CW signal is generated by a color center laser and amplitude modulated at 150MHz to suppress Brillouin scattering. Input signal power is ~1mW. In the pump arm, a tunable-wavelength, passively modelocked erbium-doped fiber laser generates a 13.3 MHz train of 2.5 psec pulses at λ= 1534.6nm. The pulses are broadened to approximately 100 psec to increase the interaction length with the input and converted signals and amplified to an average

power of 4mW. A 2nm optical bandpass filter is used to remove excess amplified spontaneous emission from the pump. A variable attenuator is used to set the pump intensity, and a polarization controller optimizes the interaction between the pump and signal. The output of the Hi-NL fiber is monitored by an optical spectrum analyzer and a fast photodiode connected to an oscilloscope. The signal and converted wavelengths are selected with a 2nm optical bandpass filter, and pulse amplitudes are measured on the oscilloscope to determine power gain and conversion efficiency. Since only pulse amplitudes at the laser repetition rate are measured, ASE power does not corrupt the measurement.

The Hi-NL fiber (λ_o = 1534nm) is 720m long with an effective nonlinearity of 9.9 $W^{-1}km^{-1}$ and ~0.6 dB/km loss. The effective nonlinearity is enhanced by decreasing the mode field area (A_{eff}) to approximately 16.5 μm^2 and increasing the n_2 by a factor of ~1.35 times that of typical DS fiber by increasing the concentration of GeO_2 in the core. The range for adjusting each of these parameters is restricted by fiber attenuation and uniformity considerations[5].

Figure 3 illustrates conversion efficiency versus wavelength separation of the signal from the pump. The experimentally measured conversion efficiencies are shown as dots. Approximately 40nm of bandwidth that experiences parametric gain is converted. Peak efficiencies of ~28dB are 16dB greater than those achievable by four-wave mixing in the absence of modulational instability. Since the pump was a relatively narrow pulse (~2.5psec, before chirping), the spectra of the parametrically amplified signal and converted wavelength broadened to the pump linewidth under the MI conversion process. The solid theoretical curve assumes the stated values of Hi-NL fiber parameters, a measured dispersion slope of .05 ps/nm^2-km at 1534 nm and 560mW of path-averaged pump power. The pump linewidth broadens slightly due to self-phase modulation (SPM) at this pump power and indications of pump depletion are minimal. Higher order sideband generation and gain asymmetry due to Raman effects are insignificant.

The conversion efficiency as a function of pump power at a fixed signal wavelength ($\lambda_p - \lambda_S$ = 10.4nm) is shown in Fig. 4. The conversion efficiency saturates for pump powers greater than ~600mW, as indicated by the divergence of the experimentally measured efficiencies from the theoretically predicted values. The theoretical curve corresponds to a linear phase mismatch $\Delta k = -4 \times 10^{-3}\ m^{-1}$, which is calculated from the measured dispersion for the given pump and signal wavelengths. The onset of saturation coincides with increased broadening of the pump and signal spectra due to SPM and the emergence of higher orders of converted wavelengths with further increase of pump power.

The experiment confirms the predicted enhancements to conversion efficiency and bandwidth provided by increased effective nonlinearity. Discrepancies between experimental results and theoretical predictions, particularly in Fig. 4, can be explained on the basis of the assumed simplifications to the theory. The appearance of higher orders of converted wavelengths indicates that the pump power is adequate to phase match a greater bandwidth than predicted by equation (3), which accounts for dispersion only up to the third order. Also, equation (4) results from a simple set of two coupled-mode equations, which exclude the possibility of coupling into higher orders and ignore pump depletion and spectral broadening. All of these effects would contribute to the observed saturation of conversion efficiency with increasing pump power.

A key issue is the engineering of fiber parameters that will enhance fiber-based wavelength conversion by reducing pump power and fiber length requirements. As demonstrated, increasing the effective nonlinearity of the fiber improves both the conversion bandwidth and peak efficiency achievable for a fixed pump power and fiber length. Further increasing fiber nonlinearity, however, must be balanced with considerations of the fiber's dispersion profile, dispersion uniformity with length, and attenuation. The dispersion profile, particularly its "flatness" due to third and fourth order dispersion values[1], dictates the parametric gain required to phase-match a certain conversion bandwidth. The dispersion profile, as well as the dispersion uniformity with length, also dictate the allowable displacement of the pump wavelength from the fiber's zero dispersion wavelength. From Eq. (3), a small displacement is desired for optimizing conversion bandwidth for a given pump power, while uniformity along the fiber length of the zero dispersion wavelength sets a lower limit on the displacement to insure that the pump remains in the anomolous dispersion regime. Finally, the attenuation dictates the fiber length limits at which propagation loss will negate parametric gain through signal loss and/or pump depletion[6].

In conclusion, we have demonstrated wavelength conversion over 40nm with a peak efficiency of 28dB at P_{pump} = 600mW by employing induced modulation instability in dispersion-shifted fiber with a 4.5X enhancement of effective nonlinearity. The nonlinearity enhancement reduces pump power requirements by a factor of 4.5 and improves the peak efficiency by ~26dB over corresponding lengths of conventional DS fiber for similar conversion bandwidths.

This work was supported by DARPA and NSF.

References

1. M.E. Marhic, N. Kagi, T.-K. Chiang, and L.G. Kazovsky, Opt. Lett., **21**, 573 (1996).

2. S.J.B. Yoo, J. of Light. Tech., **14**, 955 (1996).

3. R. Sabella and E. Iannone, IEEE J. Sel. Areas of Comm., **14**, 968 (1996).

4. R.H. Stolen and J.E.Bjorkholm, IEEE J. Quantum Electron., QE- **18**, 1062 (1982).

5. M.J. Holmes, D.L. Williams, and R.J.Manning, IEEE Photon. Technol. Lett., **7**, 1045 (1995).

6. W.Wu, P.Yeh, and S.Chi, IEEE Photon. Technol. Lett., **6**, 1448 (1994).

7. K. Inoue, IEEE J. Quantum Electron., QE-**28**, 883 (1992).

8. P.O. Hedekvist, M.Karlsson, and P.A.Andrekson, J. of Light. Tech., **15**, 2051 (1997).

9. A.E.Kelly, D.D. Marcenac, and D. Neset, Electron. Lett., **33**, 2123 (1997).

Figure captions

Figure 1. Calculated conversion bandwidth and conversion efficiency versus parametric gain for $dD/d\lambda \cong .05$ ps/(nm^2-km), L = 720m, and P_{pump} = 600mW. Vertical dashed lines correspond to parametric gains for normal DS fiber ($\gamma \cong 2.2$ W^{-1}km^{-1}) and Hi-NL DS fiber ($\gamma \cong 9.9$ W^{-1}km^{-1}) at the same pump powers.

Figure 2. Experimental Setup. The signal is generated by a color center laser; the pump is provided by a passively modelocked ring EDFL. MOD: modulator; EDFL(A): Erbium-doped fiber laser (amplifier); OBF: optical bandpass filter; OSA: optical spectrum analyzer; PC: polarization controller; PD: photodetector.

Figure 3. Conversion efficiency vs. wavelength separation between pump and signal wavelengths. Symbols indicate experimental data; the solid curve is the theoretically predicted conversion efficiency for path averaged power, P_{pump} = 560 mW.

Figure 4. Conversion efficiency vs. pump power at $\lambda_p - \lambda_S$ = -10.4nm. Symbols indicate experimental data; the curve corresponds to theoretically predicted conversion efficiency for $\Delta k = -4 \times 10^{-3}$ m^{-1} assuming only MI-conversion.

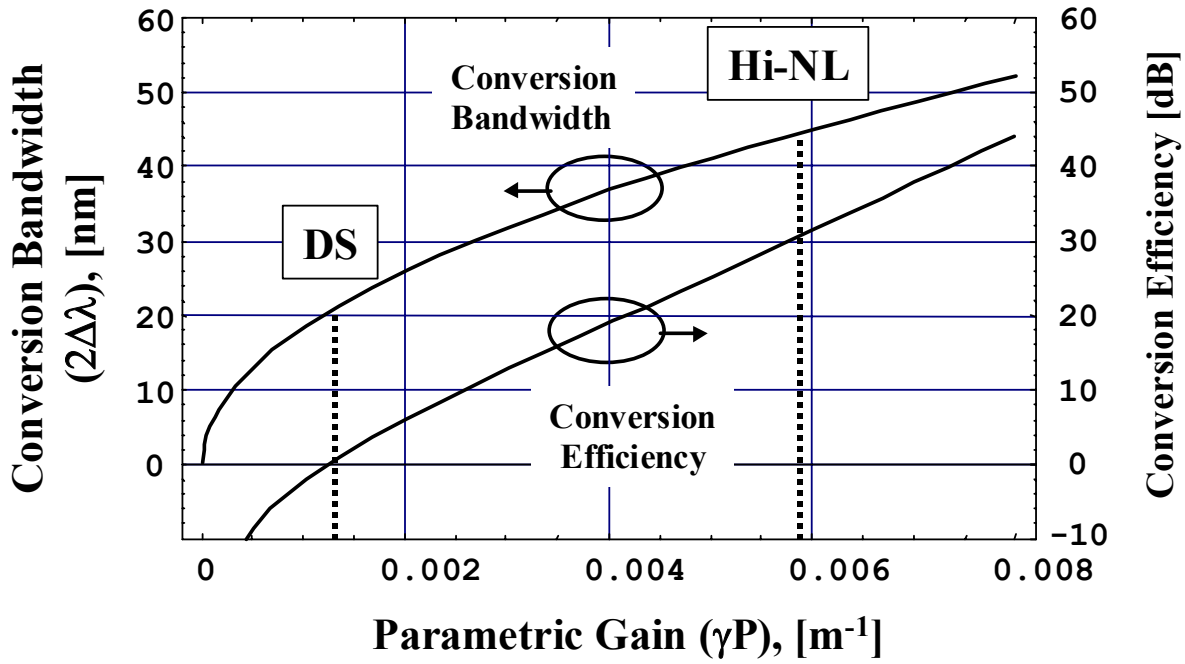

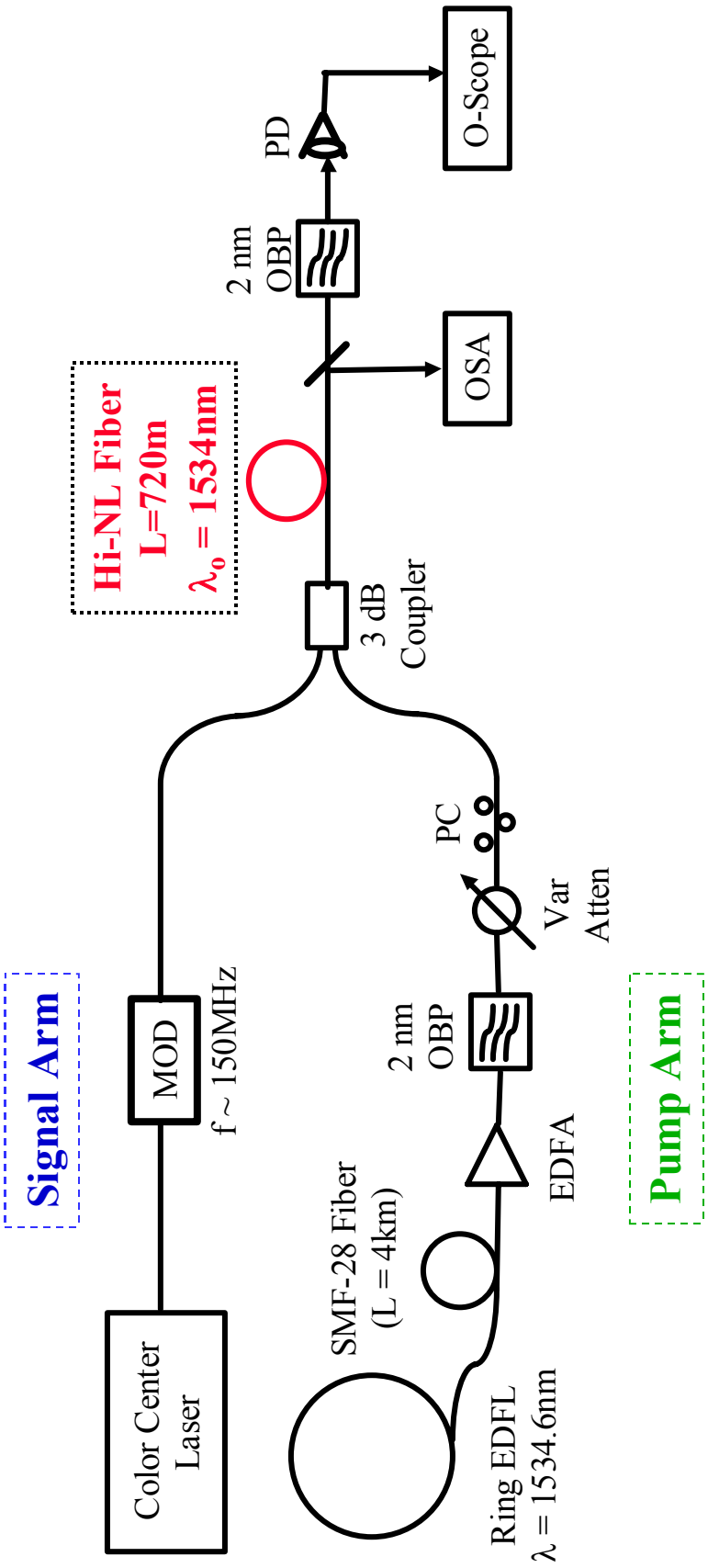
Signal Arm
Pump Arm
Color Center Laser
MOD
f ~ 150MHz
Ring EDFL
λ = 1534.6nm
SMF-28 Fiber
(L = 4km)
2 nm
OBP
EDFA
PC
Var
Atten
3 dB
Coupler
Hi-NL Fiber
L=720m
λo = 1534nm
2 nm
OBP
PD
O-Scope
OSA

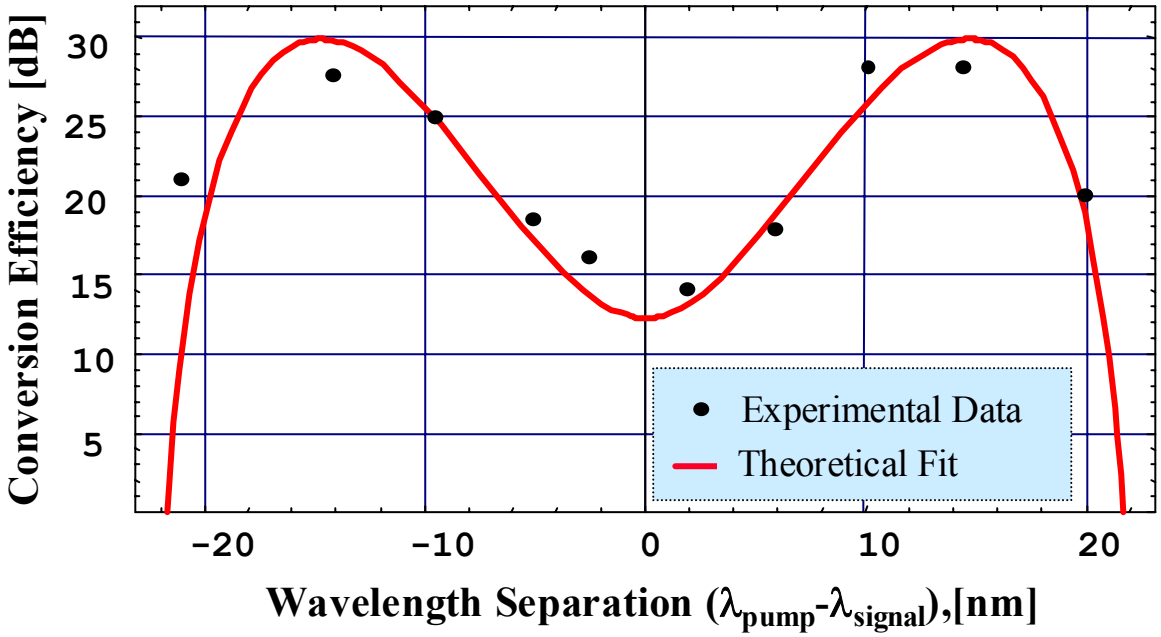
Conversion Efficiency [dB]
30
25
20
15
10
5
-20
-10
0
10
20
Wavelength Separation (λpump-λsignal),[nm]
Experimental Data
Theoretical Fit

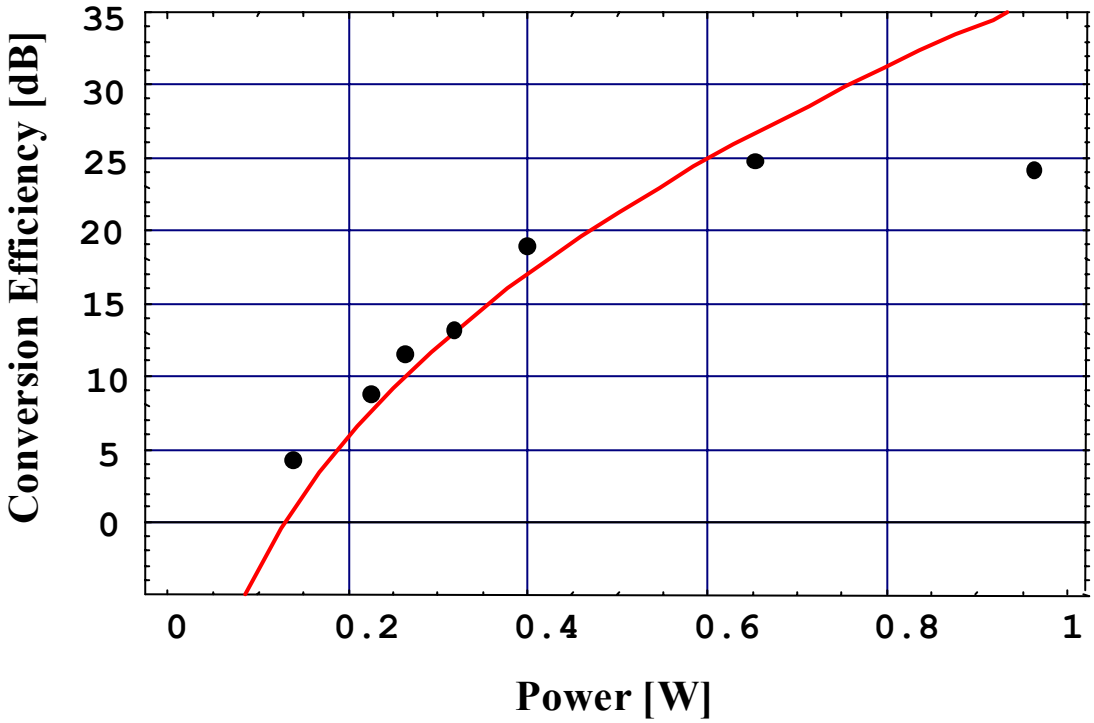
Conversion Efficiency [dB]
35
30
25
20
15
10
5
0
0
0.2
0.4
0.6
0.8
1
Power [W]

Appendix B

Novel Self-Synchronization Scheme for High Speed Packet TDM Networks

T. J. Xia*, Y. -H. Kao, Y. Liang, J. W. Lou, K. H. Ahn, O. Boyraz, G. A. Nowak, A. A. Said, and M. N. Islam

Department of Electrical Engineering and Computer Science
The University of Michigan
1301 Beal Avenue
Ann Arbor, Michigan 48109, USA

Abstract

We demonstrate a novel self-synchronization scheme for high speed packet TDM networks using a fast saturated but slowly recovered gain (or loss) combined with intensity discrimination. The marker pulse used in this self-synchronization scheme is the same as other pulses in the packets. In particular, we use a semiconductor optical amplifier (SOA) as the fast saturated but slowly recovered gain element, and an unbalanced nonlinear optical loop mirror or a dispersion-shifted fiber/optical filter combination as an intensity discriminator. The contrast ratio of the first pulse to the remaining pulses of a 100Gb/s packet, '10111000' is >3dB at the output of the SOA and >20dB at the outputs of both intensity discriminators.

Index Terms - Synchronization, optical saturation, optical fiber communication, packet switching, optical signal processing, ultrafast optics.

* Present address: MCI, 2400 N Glenville Dr, Richardson, TX 75082

Novel Self-Synchronization Scheme for High Speed Packet TDM Networks

T. J. Xia, Y. -H. Kao, Y. Liang, J. W. Lou, K. H. Ahn, O. Boyraz, G.A. Nowak, A. A. Said, and M. N. Islam

Department of Electrical Engineering and Computer Science
The University of Michigan
1301 Beal Avenue
Ann Arbor, Michigan 48109, USA

Self-synchronization is an important issue in high-speed packet networks [1-4]. With self-synchronization, instead of performing clock recovery, a local access node on the network selects a single pulse from an incoming data packet. This single pulse can be used as a seed pulse to generate various local bit patterns, such as local clocks or local addresses. Because the extracted seed pulse is automatically synchronized to the incoming packet, these local bit patterns can be aligned with the incoming packet with high accuracy. This seed pulse is only used for the packet that contains it, therefore, this synchronization scheme is tolerant to timing jitter between packets. We demonstrate a novel self-synchronization scheme that uses a semiconductor optical amplifier (SOA) and one of two intensity discriminators for packets with a generic pulse frame, i.e. the marker pulse is identical to the other pulses in the packet. In this scheme, the first pulse of a packet is transmitted through the SOA with a >3dB intensity contrast ratio over the other pulses in the packet due to fast gain saturation. The intensity ratio is further enhanced to >20dB when the packet passes through intensity discriminators.

Previous demonstrations of self-synchronization schemes have involved using marker pulses which are different from other pulses in the packets. Shimazu and Tsukada use marker pulses of different wavelength, which can be separated by a wavelength filter at a receiver [1]. Glesk *et al.* use a marker pulse whose polarization is orthogonal to that of the remaining pulses in the packet and can be selected with a polarizer [2]. The marker pulse used by Cotter *et al.* is placed ahead of the packet with a separation of one and a half bit-period. This pulse is extracted by an AND gate with one and a half bit period shift between the control and signal pulse trains [3]. In addition, Deng *et al.* demonstrated a self-synchronization scheme by using a marker pulse five times stronger than other pulses in the packet. The marker pulse is distinguished by a terahertz optical asymmetric demultiplexer [4]. Using these markers requires that the data packet have a special pulse, which complicates the generation and transmission of the packets. Marker pulses of different wavelength may lose their timing relation with other pulses in the packet due to the dispersion in fibers. Marker pulses with different polarization or different intensity may lose their uniqueness after propagating a long distance. For marker pulses with different bit-period, packet generation becomes complicated and any jitter between pulses could cause trouble in extraction of the marker pulse.

We design a new approach to extract a single pulse, i.e., the first pulse, from packets. Here we can consider the first pulse as a marker. Figure 1 shows a schematic diagram for the design. First, a transmission function with a fast saturated/slowly recovered gain medium is imposed across the packet to create higher intensity for the first pulse in the packet. Then, the remaining pulses of the packet are removed with an intensity discriminator. This design does not require the marker pulse to be different from the other pulses. The only requirement is that the

guard time between packets be longer than the recovery time of the gain element. A fast saturated / slowly recovered loss medium can be used for the same purpose.

We choose an SOA to perform the fast saturated/slowly recovered transmission function. SOAs have very fast gain saturation when excited with short optical pulses and the saturation can occur during one pulse width for pulses of several picoseconds[5]. The saturated gain of the SOA, however, has a relatively long recovery time, which ranges from 0.2 to 1 nsec depending on different SOAs [6]. By properly setting the input power of the optical pulses and bias current of the SOA, only the first pulse in the packet experiences an unsaturated gain, while the remaining pulses experience a gain saturated by the first pulse. The gain difference causes the first pulse of a transmitted packet to have a greater intensity than the remaining pulses. An intensity discriminator then selects the first pulse and suppresses the rest, resulting in a single pulse being extracted from the packet.

We design two types of intensity discriminators. One is an unbalanced nonlinear optical loop mirror (NOLM) with a polarizer, and the other employs spectral broadening due to self-phase modulation (SPM) in fiber combined with an optical filter. For the intensity discriminator using the unbalanced NOLM, the coupler in the loop has an uneven beam splitting ratio, and the clockwise and counterclockwise beams in the loop experience different nonlinear phase shifts. This phase shift difference is a function of input intensity of the pulses. The NOLM can be adjusted so that it has a higher transmission for the high intensity pulse than that for low intensity pulses. Additionally, since nonlinear polarization rotation induced in the fiber of the loop mirror is also intensity dependent, a polarizer at the output of the loop mirror increases the contrast ratio. For the SPM/filter intensity discriminator, a fiber with a zero dispersion wavelength λ_0 very close to the working wavelength is used to obtain sufficient spectral broadening. The width of the broadened spectrum of a pulse has a nonlinear dependence on input intensity. We set a band pass filter at a wavelength slightly away from the input wavelength, so that only the pulse with enough intensity can pass this filter, and all others will be eliminated.

Figure 2 shows the experimental setup of our self-synchronization design. A data packet (the shortest duration between pulses is 10psec, i.e. 100Gb/s) is generated by a passively mode-locked fiber laser (λ = 1535nm, τ = 1.5psec) followed by a fiber encoder comprised of couplers and delay lines. The data packet is sent to an SOA to obtain a pulse train with a strong first pulse. The output from the SOA is sent to one of the intensity discriminators via an erbium-doped fiber amplifier (EDFA) to compensate for the 1dB net insertion loss of the SOA and to enhance the energy in the pulses. The energy of the first pulse is 15pJ at the output of the EDFA. For the unbalanced NOLM intensity discriminator, we use a 40/60 coupler, and a dispersion-shifted fiber (L = 400m with λ_0 = 1493nm). For the SPM/filter intensity discriminator, we use a 250m dispersion-shifted fiber (λ_0 = 1539nm), and tunable band-pass filter (central wavelength is tuned to 1542.5nm with 2.3nm bandwidth). The pulses in the packet are analyzed with a cross-correlator, an auto-correlator, and a spectrum analyzer at the outputs of the SOA and intensity discriminators.

Figure 3 shows the cross-correlation at different stages of the self-synchronization unit. Using an input energy of 2pJ/pulse to saturate the SOA at a current of 50mA, we obtain an intensity contrast ratio of more than 3dB between the first pulse and the remaining ones in the packet for a uniform input pulse train (Fig 3b). The resultant 3dB contrast ratio is not sensitive to input pulse energy. This intensity contrast is further enhanced to >20dB after the unbalanced NOLM (Fig 3c) or the SPM/filter (Fig 3d) intensity discriminator. The net insertion loss of the

SOA is 1dB for the first pulse. With the EDFA between the SOA and the intensity discriminators, the overall insertion gain for the first pulse of the packet is 6.5dB using the NOLM discriminator and 3.5dB using the SPM/filter discriminator.

The auto-correlation and optical spectra of these extracted single pulses at the output of the self-synchronization setup are illustrated in Fig. 4 and compared to those of the input pulses. It is important to maintain the pulse quality with insertion of the self-synchronization unit as the extracted pulse will be used as a seed pulse to generate local bit patterns. A slight frequency shift can be seen for the case using the unbalanced loop mirror as the intensity discriminator. It is a typical phenomena related to gain saturation in a SOA device [5]. The time-bandwidth-product of the extracted pulse is 0.34 using the unbalanced NOLM intensity discriminator (Fig. 4a-b) and 0.48 using the SPM/filter intensity discriminator (Fig. 4c-d).

The two types of intensity discriminators fit different applications. The extracted pulse emerging from the unbalanced NOLM intensity discriminator has nearly the same wavelength as that of the input packet. This pulse is a suitable source for generating bit patterns for devices requiring inputs of similar wavelengths, such as in cascaded logic operations [7]. The extracted pulse emerging from the SPM/filter intensity discriminator has a shifted wavelength from that of the output packet. A device requiring inputs with two wavelengths, such as the all-optical demultiplexer [8], can use the extracted pulse as a source.

This self-synchronization does place some restrictions on the packet frames. It requires a time guard band between packets to be longer than the SOA recovery time. A long series of zeros followed by ones in the packet may also be misinterpreted as the beginning of a new packet because of the SOA gain recovery. Adding an extra gate that is turned off after receiving the first extracted pulse and turned on after the fixed packet duration is a possible solution. Such a gate would also prevent most of the pulses in the packet from going to the self-synchronization unit, thereby guaranteeing that the first pulse of the subsequent packet obtains maximum gain.

In summary, we demonstrate a self-synchronization technique that extracts the first pulse of a 100Gb/s packet, ‘10111000’, with contrast ratio of >20dB by using the fast saturated/slowly recovered gain in an SOA and two types of intensity discriminators. The extracted pulse experiences a net gain of 6.5dB at the original wavelength using the NOLM discriminator and a net gain of 3.5dB at a different wavelength using the SPM/filter discriminator. This synchronization scheme can be used for high-speed packet networks or ultrafast optical sampling.

This work is sponsored by DARPA.

References

1. Y. Shimazu and M. Tsukada, "Ultrafast photonic ATM switch with optical output buffers," *J. Lightwave Technology*, vol. 10, no. 2, pp. 265-272, 1992.
2. I. Glesk, J. P. Solokoff and P. R. Prucnal, "All-optical address recognition and self-routing in a 250Gbit/s packet-switched network," *Electr. Lett.*, vol. 30, no. 16, pp. 1322-1333, 1994.
3. D. Cotter, J. K. Lucek, M. Shabeer, K. Smith, D. C. Rogers, D. Nesset and P. Gunning, "Self-routing of 100Gbit/s packets using 6 bit 'keyword' address recognition," *Electron. Lett.*, vol. 31, no. 25, pp. 2201-2202, 1995.
4. K. -L. Deng, I. Glesk, K. I. Kang, and P. R. Prucnal, "Unbalanced TOAD for optical data and clock separation in self-clocked transparent OTDM networks," *IEEE Photo. Tech. Lett.*, vol. 9, pp. 830-832, 1997.
5. G. P. Agrawal and N. A. Olsson, "Self-phase modulation and spectral broadening of optical pulses in semiconductor laser amplifiers," *IEEE J. Quantum Electron.*, vol. 25, pp. 2297-2303, 1989.
6. K. T. Hall, G. Lenz, A. M. Darwish, and E. P. Ippen, "Subpicosecond gain and index nonlinearities in InGaAsP diode lasers," *Optics Communications*, vol. 111, pp. 589-612, 1994.
7. K. H. Ahn, M. Vaziri, B. C. Barnett, G. R. Williams, X. D. Cao, M. N. Islam, B. Malo, K. O. Hill, and D. Q. Chowdhury, "Experimental demonstration of a low-latency fiber soliton logic gate," *J. Lightwave Technology*, vol. 14, no. 8, pp. 1768-1775, 1996.
8. X. D. Cao, M. Jiang, P. Dasika, M. N. Islam, A. F. Evans, R. M. Hawk, D. A. Nolan, D. A. Pastel, D. L. Weidman, and D. G. Moodie, "All-optical 40 GHz demultiplexing in a NOLM with sub-pJ switching energy," *Conference on Lasers and Electro-Optics*, vol. 11, pp. 446-447, 1997.

Figure captions

Figure 1: Schematic diagram of the self-synchronization scheme. It contains two elements: Fast saturated/slowly recovered gain medium and intensity discriminator. G_0 - unsaturated gain.

Figure 2: Experimental set-up for self-synchronization. A semiconductor optical amplifier (SOA) is used as the fast saturated/slowly recovered gain element. Two types of intensity discriminators, unbalanced fiber loop mirror and SPM/filter, are used. PC - polarization controller, P - polarizer, DSF - dispersion-shifted fiber, SPM - self-phase modulation, BP – bandpass, EDFA – erbium-doped fiber amplifier.

Figure 3: Cross-correlation results of the self-synchronization scheme. (a) Input data packet. (b) Output data packet from the SOA. (c) Extracted single pulse from the unbalanced loop mirror intensity discriminator. (d) Extracted single pulse from the SPM/filter intensity discriminator.

Figure 4: Auto-correlation and spectra of the extracted pulse from (a-b) the unbalanced loop mirror intensity discriminator, and (c-d) the SPM/filter intensity discriminator.

Appendix C

Polarization Insensitive Nonlinear Optical Loop Mirror Demultiplexer Using Twisted Fiber

Y. Liang, J. W. Lou, J. K. Andersen, J. C. Stocker, O. Boyraz, and M. N. Islam
Department of Electrical Engineering & Computer Science
The University of Michigan
1301 Beal Avenue, Ann Arbor, MI 48109-2122

D. A. Nolan
Corning, Inc.
Corning, NY 14831

Abstract

We experimentally demonstrate the reduction of the polarization sensitivity of a nonlinear optical loop mirror (NOLM) from 5dB to 0.5dB by using 550m of twisted dispersion-shifted fiber with a twist rate of 8 turns/m (24 turns/beat length). The twisting of fiber induces circular birefringence and equates the parallel- and orthogonal-polarization nonlinear phase shift terms. Experimental results show that the polarization sensitivity monotonically decreases from 5dB for non-twisted fiber to 0.5dB for 8 turns/m, and the twist rate should be above 4 turns/m (>10 turns/beat length) to emulate circularly polarized fiber. The minimum polarization sensitivity occurs when control pulse polarization is aligned with one of the eigenmodes of the twisted fiber. With the twisted fiber at 8 turns/m in the NOLM, the nonlinear transmission is 23% at switching energy of 4 pJ/pulse. Simulations confirm the observed behavior and show that the remaining polarization sensitivity results from energy transfer between orthogonal modes of the signal pulse.

The nonlinear optical loop mirror (NOLM) is an attractive candidate for all-optical demultiplexing of 40 Gb/s and higher rate data streams [1]. However, the 5dB sensitivity to the signal input polarization state in a typical NOLM is an obstacle to its applications in a real system where the signal polarization varies with environmental conditions. We experimentally demonstrate the reduction of the polarization sensitivity of the NOLM from 5dB to as low as 0.5dB by twisting 550m dispersion shifted (DS) fiber at 8 turns/m (24 turns/beat length). The twisting of the fiber creates circularly polarized fiber (CPF) and equates the parallel and orthogonal polarization nonlinear phase shift terms. The difference in these nonlinear terms is the fundamental cause for polarization sensitivity in a NOLM. We find that the polarization sensitivity of the NOLM can be reduced significantly when the twist rate is greater than ~4 turns/meter (>10 turns/beat length), making the fiber close to CPF. We also find that the minimum polarization sensitivity occurs when the polarization of the control pulse polarization is aligned with one of the eigenmodes of the twisted fiber. Numerical simulations agree with the experimentally observed behavior and predict that the polarization sensitivity should approach 0.3dB by using CPF. The remaining polarization sensitivity arises from energy transfer between orthogonal polarization modes of the fiber.

Previous methods of reducing polarization sensitivity of the NOLM rely on either changing the switch architecture or using long fiber lengths. One method by Uchiyama, *et al.*, is to switch the orthogonal polarization modes independently by cross-splicing two pieces of polarization maintaining (PM) DS fibers with the same length and launching the control pulse at 45^0 to the axis of the PM fiber [2]. All the components must be made with PM fiber, which complicates the device, in order to build this PM NOLM. Rather than splitting the control pulse, two diodes can be used so that each diode is launch onto a different control axis [3]. Olsson and Andrekson have demonstrated two different methods. The first method randomizes the polarizations of the pulses by using long lengths (13km) of DS fiber with moderate polarization mode dispersion and a specific zero dispersion λ_0 to increase walk-off length [4]. The second method uses a birefringent crystal as a full-wave plate for the signal wavelength and a half-wave plate for the control wavelength in the loop [5]. Long fiber lengths increase the environmental sensitivity and the walk-off restrictions limit the wavelength range of operation. The birefringent crystal can also limit the operating wavelength range. Whitaker, *et al.*, use a fix signal polarization by splitting the two orthogonal modes of the signal pulse and using a polarization rotator to make the two modes parallel [6]. Splitting one signal pulse into two separate signals lowers the operating signal data rate.

Rather than compensating for the difference in nonlinearities with the architecture, we attempt to solve the fundamental cause of polarization sensitivity by using CPF. Polarization sensitivity of the NOLM comes from the difference in cross-phase-modulation (XPM) for parallel-polarized and cross-polarized pulses. In linearly polarized fiber, the parallel and cross-polarized nonlinear phase shift coefficients induce by XPM from the control pulse are 2 and 2/3 respectively, while in CPF the coefficients are both 4/3 [7]. Therefore, using CPF can fundamentally eliminate the source of polarization sensitivity. CPF can be emulated by twisting the fiber at a much higher rate (>10×) than its linear birefringence, or with the twist length L_T (the length for one turn) shorter than 1/10 of the beat length L_B [8]. Note that because the birefringence varies for different fibers, the necessary number of turns per meter is dependent on the fiber type.

The NOLM is tested in the configuration of Fig. 1, where the source is an erbium-doped fiber laser (λ_1=1542nm, $\Delta\lambda$~2.9nm, $\Delta\tau$~0.5ps). Ten percent of the laser output is amplified and filtered as the control input. The signal input is frequency shifted 7nm (λ_2=1535nm) from laser wavelength by filtering the broadened spectrum due to self-phase-modulation in a 12m high nonlinearity fiber (λ_0=1534nm, n_2 ~ 4.5x that of normal DS fiber) with 90% of the laser output. The bandwidth of both filters is 2nm and the filtered pulse widths are 1.8ps. A polarization controller and two zero-order waveplates are used to sweep through all possible polarization states at the signal and control inputs. The tested fiber in the loop is 550m DS fiber with λ_0=1518nm and a measured linear birefringence $\Delta n \sim 5x10^{-7}$ (beat length L_B~3 m) at wavelength of 1550nm.

Figure 2a compares the polarization sensitivity of non-twisted fiber (twist rate = 0) and twisted fiber at different twist rates. To test polarization sensitivity of the NOLM, we vary a half-wave plate from 0^0 to 90^0 and a quarter-wave plate from 0^0 to 180^0 to adjust polarizations for the control input. For each fixed control polarization, the polarization controller at the signal input is swept through all the possible polarizations to check the polarization sensitivity of the NOLM. We find that the minimum polarization sensitivity occurs when control pulse polarization is aligned with one of the polarization eigenmodes of the twisted fiber. To show the change from linear to circular polarization, we vary the twist rate from non-twisted to 8 turns/m (24 turns/L_B). The switching sensitivity based upon the polarization of the input signal approaches 5dB in non-twisted fiber, while twisting the same fiber at a rate of 8 turns/m (24 turns/L_B) results in a switching variation as low as 0.5dB. As expected, we find that at a twist rate of 4 turns/m (12 turns/L_B), the slope of the polarization sensitivity curve levels off because the fiber becomes approximately circularly polarized.

To illustrate the polarization dependence, Fig. 2b shows the nonlinear transmission of non-twisted (square data) and twisted fiber (triangle data) at a switching energy of 4 pJ/pulse. To obtain the data, a polarizer followed by a half-wave plate and a quarter-wave plate are used in the signal arm to replace the polarization controller and to vary the input polarization states. The polarization sensitivity and nonlinear transmission results are summarized in Table 1.

The nonlinear transmission is a squared sinusoidal function of nonlinear phase shift caused by nonlinear index change. The peak nonlinear index change induced by the control wavelength has a factor of 2 for linearly polarized fiber and 4/3 for circularly polarized fiber. Thus, if the peak transmission for the NOLM using non-twisted fiber is $\sin^2(\phi_L)$=47%, the peak transmission of the NOLM using CPF is expected to be $\sin^2(2\phi_L/3)$=23% with the same fiber length and switching energy. Our experimental result matches well with this theoretical value.

To understand the lower limits on polarization sensitivity for the twisted fiber, we numerically solve the coupled nonlinear Schrödinger equation in linearly and circularly polarized fiber. The cross-coupling coefficient of the orthogonal axis equals 2/3 for linearly polarized fiber and 2 for CPF [5]. The simulation curves in Fig. 3a verify the observed behavior in Fig. 2b. Here, the x-axis is the signal launch polarization. The signal is parallel to the control polarization at 0^0 and 180^0 but orthogonal to the control polarization at 90^0. The discrepancy in peak transmissions between simulation and experimental results comes from assumption errors of fiber connection loss and stress-induced circular birefringence in twisted fiber, which is different from perfect CPF. It may also explain why the experimental limit on the polarization sensitivity is 0.5dB instead of 0.3dB, as predicted by the simulation for the CPF NOLM.

Additionally, simulations show that the limit on polarization sensitivity arises from the generation of shadow energy on the opposite state of polarization of the signal pulse [9]. The signal pulse's state of polarization is altered as the control pulse walks through the signal pulse. For example, the calculated shadow energy (λ=1535nm) as a percentage of the signal energy corresponding to the simulation of Fig. 3a is shown in Fig. 3b. The change in the state of polarization effects the absolute phase of the signal pulse, resulting in a change in the transmission of the NOLM. The amount of energy transfer depends on the relative states of polarization between the control and signal. When the control and signal states of polarization are entirely parallel or orthogonal, the state of polarization of the signal is not changed. However, when the control polarization has a component that is parallel as well as a component orthogonal to the signal, the signal polarization is rotated. That is to say, a portion of the signal energy is moved from its original axis to the orthogonal axis. The exact quantity of this energy transfer is dependent on the walk-off time and the pulse power.

In summary, we demonstrate a polarization insensitive NOLM demultiplexer by twisting 550m dispersion shifted fiber to create circular birefringence and eliminate the fundamental cause of polarization sensitivity of the NOLM. By varying the twist rate, we reduce the polarization sensitivity from 5dB for linearly birefringent fiber (non-twisted fiber) down to 0.5dB for twisted fiber at 8 turns/m (~24 turns/beat length). It is necessary to align the control pulse polarization with one of the eigenmodes of the twisted fiber and to twist the fiber at over 10 turns/beat length. This makes the fiber approximately CPF and has the minimum polarization sensitivity for the NOLM. Simulations verify the experimental behavior and predict that the polarization sensitivity would be at least 0.3dB due to the nonlinear energy transfer between the orthogonal modes of the signal pulse. The nonlinear transmission of the NOLM using twisted fiber at 8 turns/m is 23% at switching energy of 4 pJ/ pulse. The difference in peak transmission between the non-twisted and twisted fibers agrees with the expected nonlinear coefficient.

This work is supported by DARPA.

References

1. K.J. Blow, N.J. Doran, B.P. Nelson, Electron. Lett., 26, 962, (1990).
2. K. Uchiyama, H. Takara, K. Kawanishi, T. Morioka and M. Saruwatari, Electron. Lett., 28,1864, (1992).
3. H. Bülow, G. Veith, Electron. Lett., 29, 589 (1993).
4. Bengt-Erik Olsson, Peter A. Andrekson, Technical Dig. of Conf. Optical Fiber Commun., FA7, (1998).
5. Bengt-Erik Olsson, Peter A. Andrekson, IEEE Photonics Technol. Lett., 9, 764, (1997).
6. N.A. Whitaker, Jr., P.M.W. French, M.C. Gabriel, H. Avramopoulos, IEEE Photonics Technol. Lett., 4, 260, (1992).
7. C.-J. Chen, P.K.A. Wai, C.R. Menyuk, Opt. Lett., 15, 477, (1990).
8. R. Ulrich, A. Simon, Appl. Opt., 18, 2241, (1979).
9. L.F. Mollenauer, J.P. Gordon, F. Heismann, Opt. Lett., 20, 2060, (1995).

Table 1: Comparison of experimental results of non-twisted fiber NOLM versustwisted fiber (8 turns/m) fiber NOLM.

	Twisted Fiber (8 turns/m)	**Non-twisted Fiber**
Polarization Sensitivity	10%	65%
Peak Nonlinear Transmission	23%	47%
Minimum Nonlinear Transmission	21%	14%

Figure Captions

Figure 1: Experimental setup for testing polarization insensitive NOLM. EDFL: erbium-doped-fiber-laser; EDFA: erbium-doped-fiber-amplifier; BPF: band-pass-filter; SPM: self-phase-modulation.

Figure 2: (a) Polarization sensitivity versus fiber twist rate. Zero twist rate corresponds to non-twisted fiber. (b) Nonlinear transmission versus signal input polarization for non-twisted fiber (square) and twisted fiber at 8 turns/m (triangle). The upper scale is for non-twisted fiber and the bottom scale is for twisted fiber.

Figure 3: (a) Simulated nonlinear transmission for linearly birefringent fiber and circularly birefringent fibers. Squares are for linearly birefringent fiber. Circles are for circularly birefringent fiber. (b) Shadow energy corresponding to the simulation in Fig. 3a. The x-axes in both figures are signal launch polarizations. The signal polarization is parallel to control polarization at 0^0 and 180^0, but orthogonal to control polarization at 90^0.

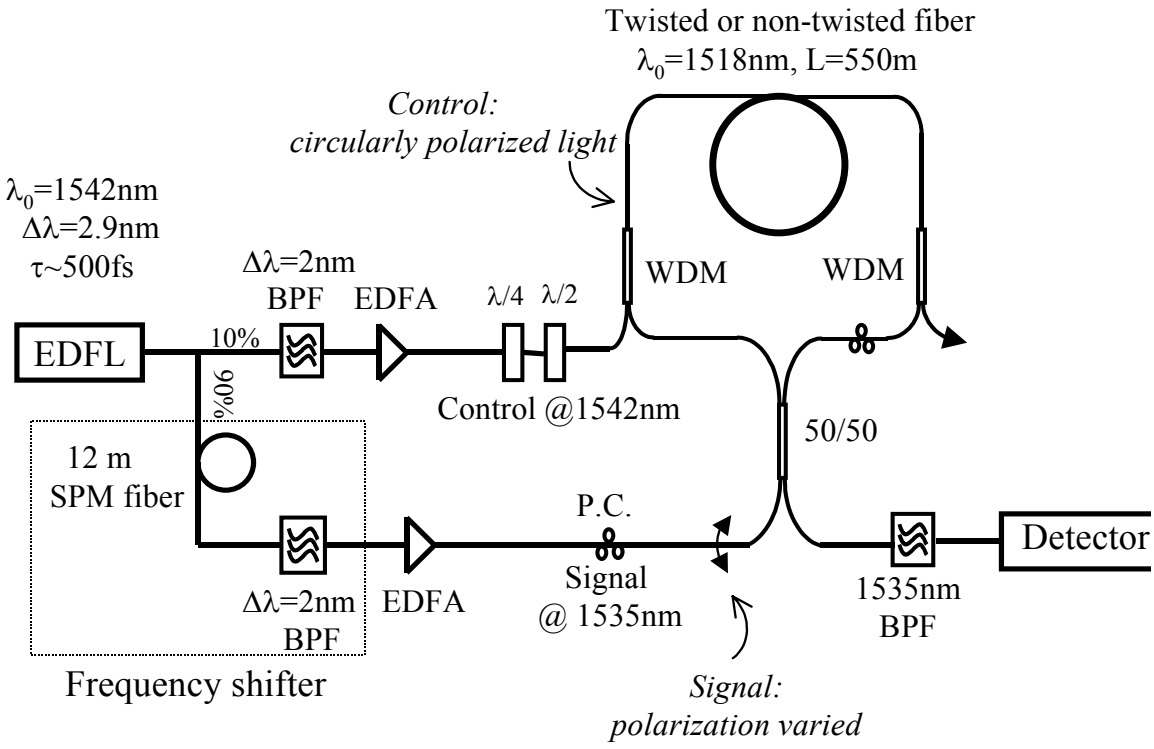
Twisted or non-twisted fiber
λ_0=1518nm, L=550m
Control:
circularly polarized light
λ_0=1542nm
Δλ=2.9nm
τ~500fs
Δλ=2nm
BPF
EDFA
λ/4
λ/2
WDM
WDM
EDFL
10%
90%
Control @1542nm
50/50
12 m
SPM fiber
P.C.
Detector
Δλ=2nm
BPF
EDFA
Signal
@ 1535nm
1535nm
BPF
Frequency shifter
Signal:
polarization varied

Figure 1

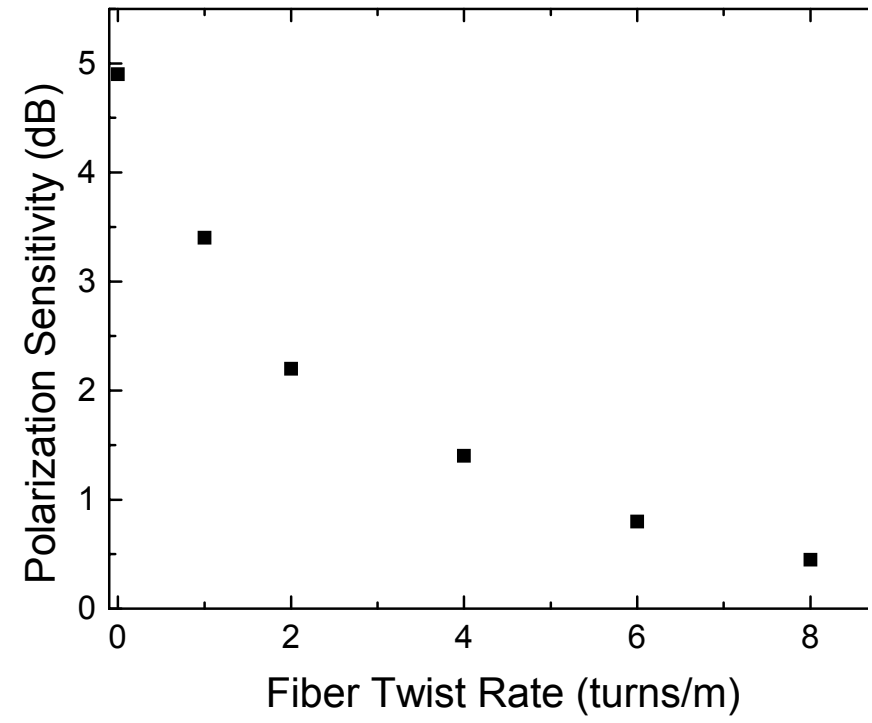
Polarization Sensitivity (dB)
0
1
2
3
4
5
0
2
4
6
8
Fiber Twist Rate (turns/m)

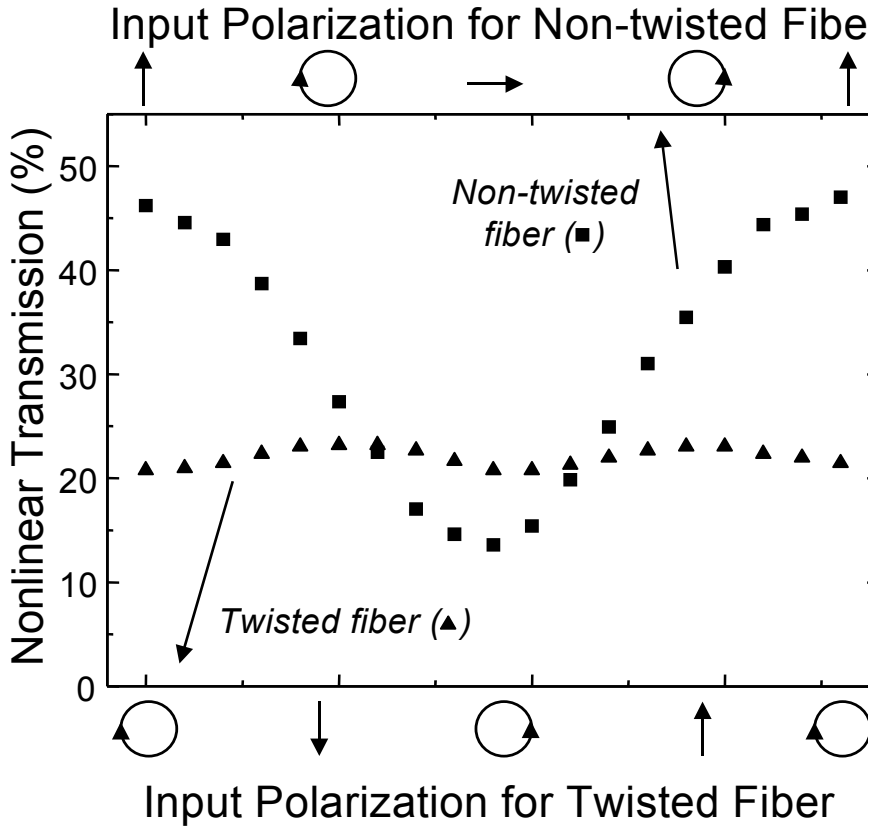
Input Polarization for Non-twisted Fibe
Nonlinear Transmission (%)
0
10
20
30
40
50
Non-twisted
fiber (■)
Twisted fiber (▲)
Input Polarization for Twisted Fiber

(a)
(b)

Figure 2

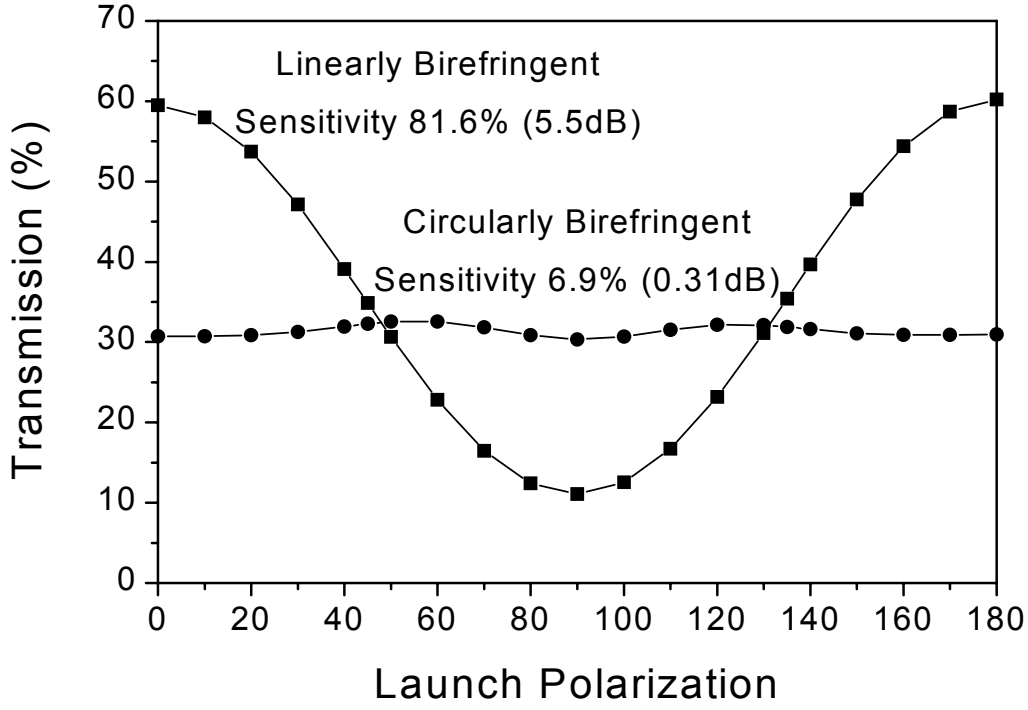
Linearly Birefringent
Sensitivity 81.6% (5.5dB)
Circularly Birefringent
Sensitivity 6.9% (0.31dB)
Transmission (%)
Launch Polarization
0
10
20
30
40
50
60
70
0
20
40
60
80
100
120
140
160
180

(a)

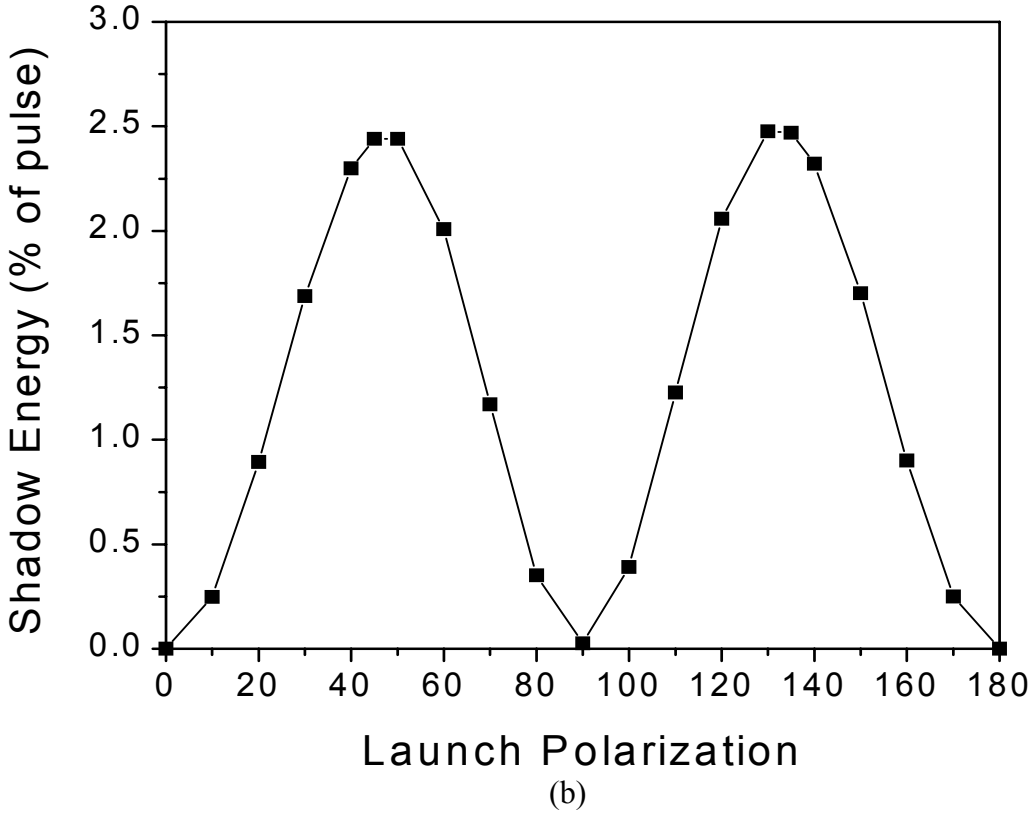
Shadow Energy (% of pulse)
Launch Polarization
0.0
0.5
1.0
1.5
2.0
2.5
3.0
0
20
40
60
80
100
120
140
160
180

(b)

Figure 3

Appendix D

Polarization insensitive demultiplexing of 100Gb/s words using a twisted fiber nonlinear optical loop mirror

J. W. Lou, *Student Member*, **J. K. Andersen**, *Student Member*, **J. C. Stocker**, *Student Member* **and M. N. Islam,** *Senior Member*

The University of Michigan

1301 Beal Avenue, Ann Arbor, MI 48109-2122

D. A. Nolan, *Member*

Corning, Inc.

Corning, NY 14831

Abstract

We demultiplex 100Gb/s words using a two-wavelength nonlinear optical loop mirror (2λ NOLM) with polarization sensitivity <0.5dB obtained by using fiber twisted at 8 turns/m. This polarization insensitive demultiplexer is more suitable than conventional non-twisted fiber NOLMs for use in high-speed all-optical networks where the input states of polarization are arbitrary. The demultiplexer consists of synchronized erbium-doped fiber lasers (λ_1=1535nm, τ_1=1.3ps; λ_2=1543nm, τ_2=2.2ps), a 100Gb/s fixed word encoder, and a NOLM using 450m of twisted fiber with λ_0=1518nm. For inputs of arbitrary polarization, we measure a ~5.5ps timing window and contrast ratio >15dB. To understand the improvement in performance of the system due to the polarization insensitivity, we apply a statistical method of measuring the Q-parameter for the twisted and non-twisted fiber demultiplexers. The Q-parameter of ~15 for the twisted fiber NOLM is improved over that of the NOLM with non-twisted fiber (Q~10), and is consistent with an increased minimum nonlinear transmission.

Index Terms—demultiplexing, optical fiber communication, nonlinear optics, optical switches, and optical fiber applications

All-optical demultiplexing may be used to increase the speed of future communication networks. We demonstrate a 100Gb/s-word demultiplexer for data with arbitrary input states of polarization using a polarization insensitive, two-wavelength, nonlinear optical loop mirror (2λ NOLM). Two-wavelength NOLMs have an inherent sensitivity to the input polarization because the parallel and orthogonal nonlinear phase shift coefficients of the fiber are different. We reduce this difference in the nonlinear coefficient terms by twisting the fiber to induce circular birefringence [1]. The polarization insensitivity removes a fundamental limitation to the implementation of 2λ NOLMs in all-optical networks. In this paper, we demonstrate an improved Q-parameter for the twisted-fiber demultiplexer using 100Gb/s words as input data signals and a synchronized laser with a phase-locked-loop synchronization scheme as the local control pulse source. The device uses 450m of twisted fiber at 8 turns/m to achieve polarization sensitivity <0.5dB, timing window ~5.5ps, contrast ratio >15dB, and Q-parameter >15. The improved Q-parameter is consistent with the increased minimum nonlinear transmission of the twisted fiber NOLM (20%) as compared to that of the non-twisted fiber NOLM (13%).

Demultiplexing of arbitrarily polarized 100Gb/s words is accomplished by combining the polarization insensitive 2λ NOLM with a local laser and synchronization circuit based on a phase-locked-loop and an acousto-optic modulator and grating in the laser [2]. Several other groups have demonstrated demultiplexing or rate down-conversion using optical fiber as well as semiconductor materials. Patel, *et al.*, demonstrate 80Gb/s rate conversion by using a dispersion-shifted fiber NOLM to optically sample and time dilate the data packets [3]. This method has the same polarization sensitivity as the non-twisted fiber NOLM described in this paper. Polarization-independent four-wave-mixing (FWM) in polarization-maintaining fiber [4] and in semiconductor laser amplifiers [5] for demultiplexing of 100^{+}Gb/s channels has been studied by Morioka, *et al.* Dispersion-shifted fiber in combination with a faraday rotator mirror is used to perform polarization independent demultiplexing through FWM, as described by Calvani, *et al.* [6]. Because FWM inherently requires phase-matching between the pump and the signal, the process is highly dependent on the exact wavelengths. The 2λ NOLM has a wider wavelength range of operation. Using a semiconductor optical amplifier (SOA) in a Sagnac loop, the terahertz optical asymmetric demultiplexer is demonstrated by Sokoloff, *et al.* [7]. Recently, the use of SOA-based monolithically integrated Mach-Zehnder interferometers to simultaneously add and drop 40Gb/s optical time-domain multiplexed (OTDM) channels has been reported [8]. The SOA material limits the polarization insensitivity of these devices. Add/drop multiplexing from 100Gb/s OTDM channels, based on photonic downconversion and FWM using electro-absorption modulators, is reported by Kamatani, *et al.* [9]. Electro-absorption modulators have also been reported by Phillips, *et al.* [10] but the extinction ratio is still dependent on the input signal polarization. Previously, twisted fiber NOLMs driven by a single laser source are used to demonstrate that by twisting the fiber to induce circular birefringence, the parallel and orthogonal nonlinear phase shift contributions in the nonlinear element (fiber) can be equated and thus, the polarization sensitivity reduced [1].

We demultiplex individual bits from a 100Gb/s word using the experimental setup shown in Fig. 1. An erbium-doped fiber laser (EDFL #1: τ~1.3ps, Δλ~1.8nm, λ=1535nm, 21MHz repetition rate) followed by a 100Gb/s-fixed-word encoder ('101110…') are used to emulate the remote signal. The amplifier used after the encoder is measured to have a noise figure of ~4.9dB. The local control source, EDFL #2 (τ~2.2ps, Δλ~1nm, λ=1543nm), is synchronized to the incoming packet repetition rate through a phase-locked-loop with timing jitter of ~2ps. For long packets, a technique using a fast-saturation and slow-recovery element such as described by

Xia, *et al.* [11], may be used to select the first pulse for synchronization at the packet rate. The amplifier used for the local control pulse is measured to have a noise figure of ~4dB. Each individual bit in the packet can be demultiplexed by adjusting the variable delay stage, and changing the relative timing between the control and signal inputs. The NOLM uses 450m of fiber with zero dispersion at 1518nm, twisted at a rate of 8 turns/m (~24 turns/beat length). The local source (control) is coupled into the NOLM through WDM #1, and the polarization is fixed at one of the eigenmodes of the twisted fiber. The control is removed using WDM #2. The two Mach-Zehnder WDM fiber couplers have a periodic spacing of 8nm. The input polarization of the remote signal can be varied with a polarization controller and/or a set of half-wave and quarter-wave plates. The NOLM output is filtered at the signal wavelength to further attenuate the control leakage, and then amplified (amplifier noise figure ~4.6dB) and detected.

Figure 2 shows the operation of the polarization insensitive NOLM as a 100Gb/s-word demultiplexer. Cross-correlations of the incoming packet (trace 1) and the demultiplexed bits (traces 2-6) are shown in Fig. 2a. The contrast ratio is greater than 15dB, and the residue pulse in the '0' bit position (trace 3) is due to control leakage. The output pulses are broadened in comparison with the input pulses because the 1nm output filter spectrally limits the pulses. Figure 2b shows the timing windows of the NOLM for the input polarizations corresponding to the maximum '1' and the minimum '1' transmissions. Note that the variation in the peak value at the center of the timing window corresponds to the 0.5dB polarization sensitivity of the NOLM. The full-width-half-maximum of the timing window is ~5.5ps in both cases.

Figure 3 illustrates a statistical study of the NOLM demultiplexer performance. By measuring the output signal with a detector (5ns rise time), the voltage peaks of 1200 output pulses each for the input polarizations corresponding to the maximum '1' and the minimum '1' NOLM transmissions are sampled. We also measure 1200 samples of the output without the local control (i.e., leakage of '1's). For long sequences of pulses, a high-speed detector with a fixed sampling period may be used to limit the number of '1's detected as leakage. The measured values are shown in Fig. 3a, and illustrate the variances in the signals due to noise from the amplifiers and timing jitter between the local and remote sources. Figure 3b shows the calculated Q-parameter as a function of the input states of polarization for both twisted and non-twisted fibers. The input state of polarization of the linearly polarized signal is varied by rotating a quarter-wave plate. The Q-parameter is calculated assuming Gaussian statistics, where $Q = (I_1-I_0)/(\sigma_1+\sigma_0)$, I_1 and I_0 are the means of the '1' and '0' bits, and σ_1 and σ_0 are the standard deviations of the '1' and '0' bits. We determine that the worst case Q-parameter for twisted fiber is ~15 and for the non-twisted fiber is ~10. Because the Q-parameter calculation is statistical, we must also consider the confidence interval. For 1200 samples each of '1's and '0's, the confidence interval is 95%. Thus, the worst case Q-parameter is actually between 14.25 and 15.75 for the twisted fiber NOLM and between 9.5 and 10.5 for the non-twisted fiber NOLM.

The Q-parameter of the twisted fiber NOLM with polarization sensitivity <0.5dB is improved by 50% compared with that of the conventional non-twisted fiber NOLM. This is consistent with the 20% minimum nonlinear transmission for the twisted fiber case and the 13% minimum transmission for the non-twisted fiber case. For the same noise levels, the Q-parameter is dominated by the I_1 and I_0 signal levels. The 0.5dB polarization sensitivity of the twisted-fiber NOLM leads to a lower variation in the Q-parameter for arbitrary input states of polarization, since the polarization dependence of I_1 in the Q-parameter definition is minimized for the twisted fiber. However, the Q-parameters do not follow exactly the periodicity of the

polarization dependence of I_1 because noise due to timing jitter and amplified spontaneous emission still affects the standard deviations of the received signals.

The minimum amount of nonlinear phase shift induced in linearly birefringent fiber has a nonlinear coefficient of 2/3, whereas in circularly birefringent fiber, the nonlinear coefficient is 4/3. The minimum transmission for the twisted fiber NOLM is $\sin^2(\phi)$~20%, implying a phase shift of ~27^o. For linearly polarized fiber, the amount of induced phase shift should be decreased by a factor of 2 from that of perfectly circularly birefringent fiber. In the non-twisted fiber NOLM, if the phase shift is decreased by a factor of 2, the minimum transmission should be 5% instead of 13%. There are several possibilities for this inconsistency. The first is that leakage (i.e., background transmission) dominates the detected signal for low nonlinear transmission levels. The second possibility is that for a twist rate of 8 turns/m, the fiber is still not perfectly circularly polarized and in fact, the difference in the induced phase shift is not a factor of 2 but closer to 4/3. In either case, we expect that the twisted fiber NOLM will give a higher minimum transmission level than the non-twisted fiber NOLM and thus, an improved Q-parameter.

The statistical Q-parameter is related to the bit-error-rate (BER) by the following equation: $BER=0.5\times\mathrm{erfc}(Q/\sqrt{2})$. Considering that traditional digital systems require a Q>6 (i.e., BER<10^{-9}), and current high-speed telecommunications systems require Q>8 (i.e., BER<10^{-15}), it would seem that even the non-twisted fiber NOLM with a Q of ~10 is more than adequate. However, there are two important considerations. The first is that this device is only a part of a system consisting of transmitters, amplifiers, regenerators, fiber propagation, and others. In a real deployed system, any one of these components may degrade the Q of the incoming signal and thus, degrade the output of the demultiplexer. Therefore, it is desirable to have a demultiplexer unit with the highest Q-parameter possible so that it has the least degradation on the Q of the entire system. The second consideration is that as the single channels speeds of telecommunication systems continue to increase, the required Q-parameters will increase accordingly to obtain lower and lower BERs.

Another figure of merit is the energy contrast ratio, which is defined as I_1/I_0. The contrast ratio of the demultiplexed output is directly related to the shape of the timing window. The number of walk-off lengths in the NOLM fiber determines the width of the timing window. The shape of the control pulse determines the slopes at the edges of the timing window. Thus, the contrast ratio can be improved by sharpening the edges or narrowing the width of the timing window, so that there is less leakage due to the adjacent pulse being switched out.

In conclusion, we demonstrate a 2λ NOLM demultiplexer for arbitrarily polarized 100Gb/s words using twisted fiber with a Q-parameter of ~15 and a polarization sensitivity of <0.5dB. In comparison, non-twisted fiber has a polarization sensitivity of ~5dB and a Q-parameter dropping to 10. This shows that the polarization insensitive NOLM has an improved system performance, which makes it more viable for high-speed all-optical communications networks. The demultiplexer uses a locally generated control pulse (λ=1543nm), which is synchronized to the incoming signal packet (λ=1535nm) through a phase-locked-loop, to switch out individual bits from the packet. Erbium-doped fiber lasers are used to generate the pulses and fixed-word encoders are used to generate the packets. The NOLM consists of 450m of 8 turns/m twisted fiber with λ_0 = 1518nm. The timing window is ~5.5ps and the contrast ratio of this NOLM is >15dB.

This work is supported by DARPA.

References

(1) Y. Liang, J. W. Lou, J. K. Andersen, J. C. Stocker, O. Boyraz, M. N. Islam, D. A. Nolan, "Polarization Insensitive Nonlinear Optical Loop Mirror Demultiplexer Using Twisted Fiber", *Opt. Lett.*, vol. 24, no. 11, pp.726-728, 1999.

(2) M. Jiang, K. H. Ahn, X.-D. Cao, P. Dasika, Y. Liang, M. N. Islam, A. F. Evans, R. M. Hawk, D. A. Nolan, D. L. Weidman, "Synchronization of Passively Mode-locked Erbium-doped Fiber Lasers and Its Application to Optical Communication Networks", *J. Lightwave Technol.*, vol. 15, no. 11, pp. 2020-2028, 1997.

(3) N. S. Patel, K. L. Hall, K. A. Rauschenbach, "Optical Rate Conversion for High-Speed TDM Networks", *IEEE Photon. Technol. Lett.*, vol. 9, no. 9, pp.1277-1279, 1997.

(4) T. Morioka, S. Kawanishi, K. Uchiyama, H. Takara, M. Saruwatari, "Polarisation-independent 100Gbit/s All-optical Demultiplexer Using Four-wave-mixing in a Polarisation-maintaining Fibre Loop", *Electron. Lett.*, vol. 30, no. 7, pp.591-592, 1994.

(5) T. Morioka, H. Takara, S. Kawanishi, K. Uchiyama, M. Saruwatari, "Polarisation-independent all-optical demultiplexing up to 200Gbit/s using four-wave mixing in semiconductor laser amplifier", *Electron.. Lett.*, vol. 32, no. 9, pp.840-842, 1996.

(6) R. Calvani, F. Cisternino, R. Girardi, E. Riccardi, "Polarisation independent all-optical demultiplexing using four wave mixing in dispersion shifted fibre", *Electron. Lett.*, vol. 35, no. 1, pp.72-73, 1999.

(7) J. P. Sokoloff, P. R. Prucnal, I. Glesk, M. Kane, "A Terahertz Optical Asymmetric Demultiplexer (TOAD)", *IEEE Photon. Technol. Lett.*, vol. 5, no. 7, pp.787-790, 1993.

(8) K. S. Jepsen, B. Mikkelsen, M. Vaa, H. N. Poulsen, A. T. Clausen, K. E. Stubkjaer, R. Hess, M. Duelk, W. Vogt, E. Gamper, E. Gini, P. A. Besse, H. Melchior, S. Bouchoule, "Simultaneous All-optical Add and Drop Multiplexing of 40-Gbit/s OTDM Signals Using Monolithically Integrated Mach-Zehnder Interferometer", *Technical Dig. of Optical Fiber Commun. Conf.*, Paper ThN2, 1998.

(9) Osamu Kamatani, Yoshitada Katagiri, Satoki Kawanishi, "100-Gbit/s Optical TDM Add/drop Multiplexer Based on Photonic Downconversion and Four-wave-mixing", *Technical Dig. of Optical Fiber Commun. Conf.*, Paper WC2, 1998.

(10) I. D. Phillips, A. Gloag, D. G. Moodie, N. J. Doran, I. Bennion, A. D. Ellis, "Drop and Insert Multiplexing with Simultaneous Clock Recovery Using an Electro-absorption Modulator", *IEEE Photon. Technol. Lett.*, vol. 10, no. 2, pp.291-293, 1998.

(11) T. J. Xia, Y.-H. Kao, Y. Liang, J. W. Lou, K. H. Ahn, O. Boyraz, A. A. Said, M. N. Islam, "Novel Self-Synchronization Scheme for High Speed Packet TDM Networks", *IEEE Photon. Technol. Lett.*, vol. 11, no. 2, pp.269-272, 1999.

Figure Captions

Figure 1: Experimental setup of polarization insensitive NOLM. The input polarizations can be varied with polarization controllers. The bandpass filter at the output attenuates the control leakage. EDFL (erbium-doped fiber laser) #1: □~1.3ps, □□~1.8nm, □=1535nm; EDFL #2: □~2.2ps, □□~1nm, □=1543nm; Encoder: generates '101110…' packet; PLL=phase-locked-loop; Twisted fiber: 450m, □0=1518nm, twisted at 8 turns/m.

Figure 2: (a) Cross-correlation of incoming packet (trace 1) and demultiplexed bits (traces 2-6). Contrast ratio > 15dB. (b) Timing window for input polarizations corresponding to maximum and minimum transmissions. The 3dB width is ~5.5ps for both cases. The contrast ratio may be improved by properly designing the timing window.

Figure 3: (a) Detector signal levels of demultiplexed '1' (maximum and minimum transmission cases) and leakage for '1'. The Q-parameter is calculated for each '1', assuming Gaussian statistics, to be ~15 with a confidence level of 95%. (b) Calculated Q-parameter values vs. input states of polarization (quarter-wave plate angle) of the signal. The signal is linearly polarized before entering the quarter-wave plate and the control is at a fixed polarization. The worst case Q-parameter for twisted fiber is ~15, whereas for non-twisted fiber is ~10.

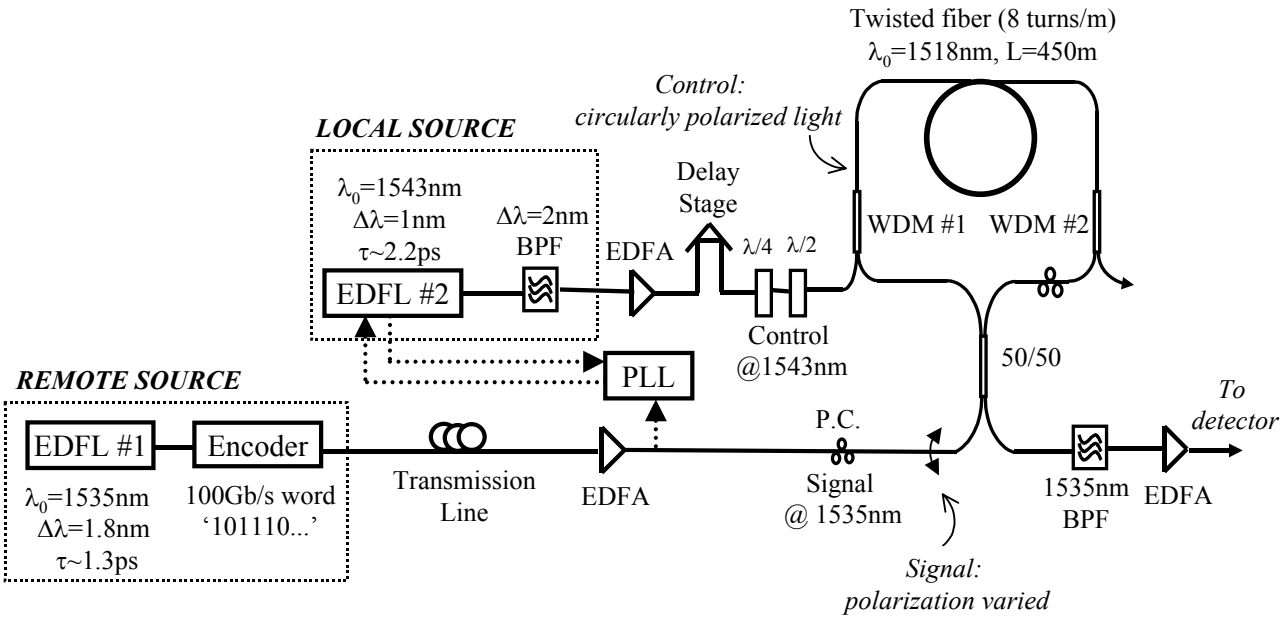
Twisted fiber (8 turns/m)
λ0=1518nm, L=450m
Control:
circularly polarized light
LOCAL SOURCE
λ0=1543nm
Δλ=1nm
τ~2.2ps
Δλ=2nm
BPF
EDFL #2
Delay
Stage
EDFA
λ/4
λ/2
WDM #1
WDM #2
Control
@1543nm
50/50
PLL
REMOTE SOURCE
EDFL #1
Encoder
λ0=1535nm
Δλ=1.8nm
τ~1.3ps
100Gb/s word
'101110...'
Transmission
Line
EDFA
P.C.
Signal
@ 1535nm
1535nm
BPF
EDFA
To
detector
Signal:
polarization varied

Figure 1

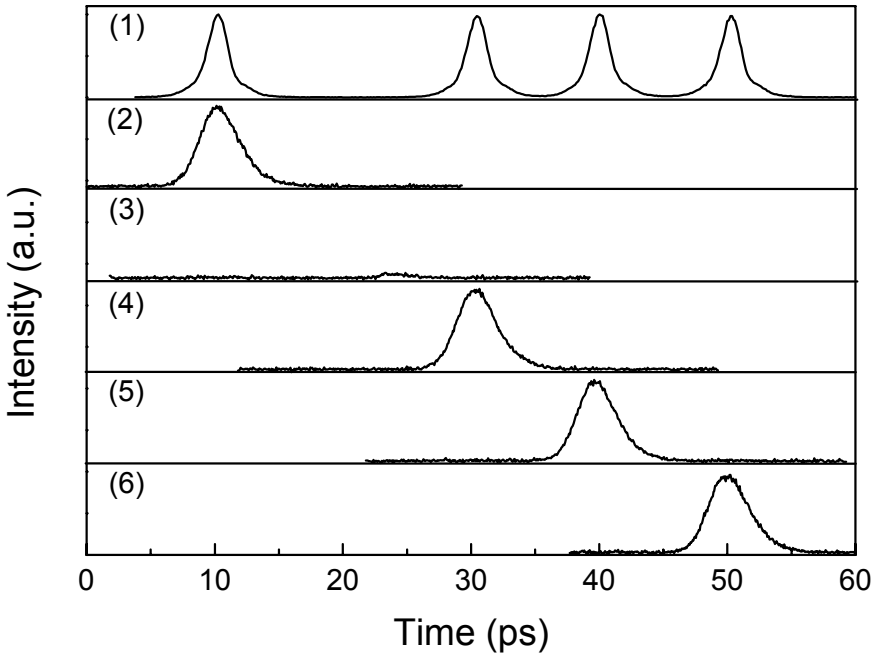
(1)
(2)
(3)
(4)
(5)
(6)
Intensity (a.u.)
0
10
20
30
40
50
60
Time (ps)

(a)

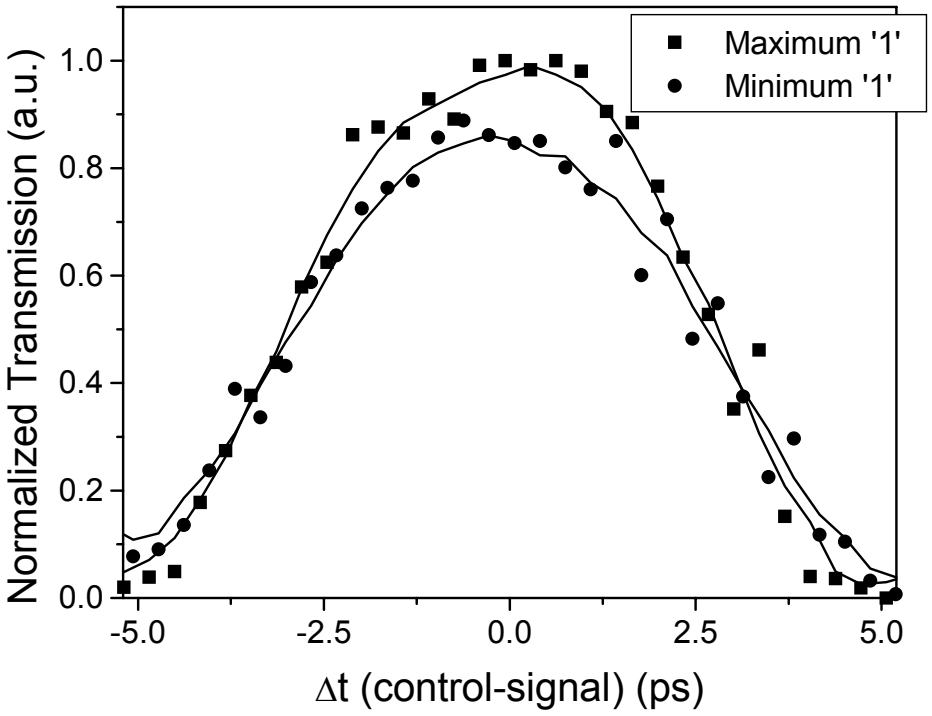
Maximum '1'
Minimum '1'
Normalized Transmission (a.u.)
0.0
0.2
0.4
0.6
0.8
1.0
-5.0
-2.5
0.0
2.5
5.0
Δt (control-signal) (ps)

(b)

Figure 2

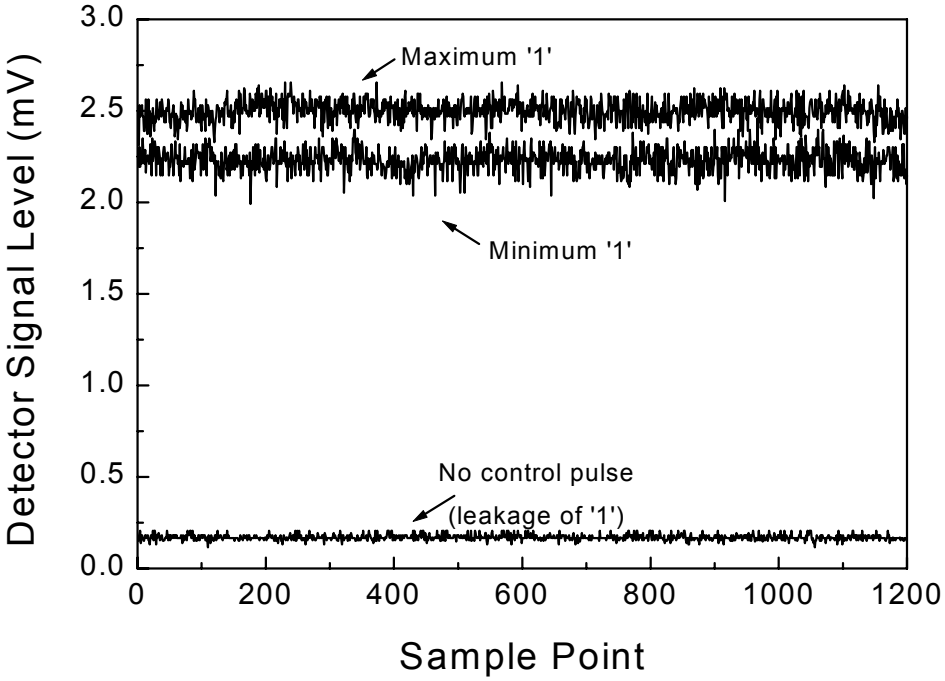
Detector Signal Level (mV)
Sample Point
Maximum '1'
Minimum '1'
No control pulse
(leakage of '1')
3.0
2.5
2.0
1.5
1.0
0.5
0.0
0
200
400
600
800
1000
1200

(a)

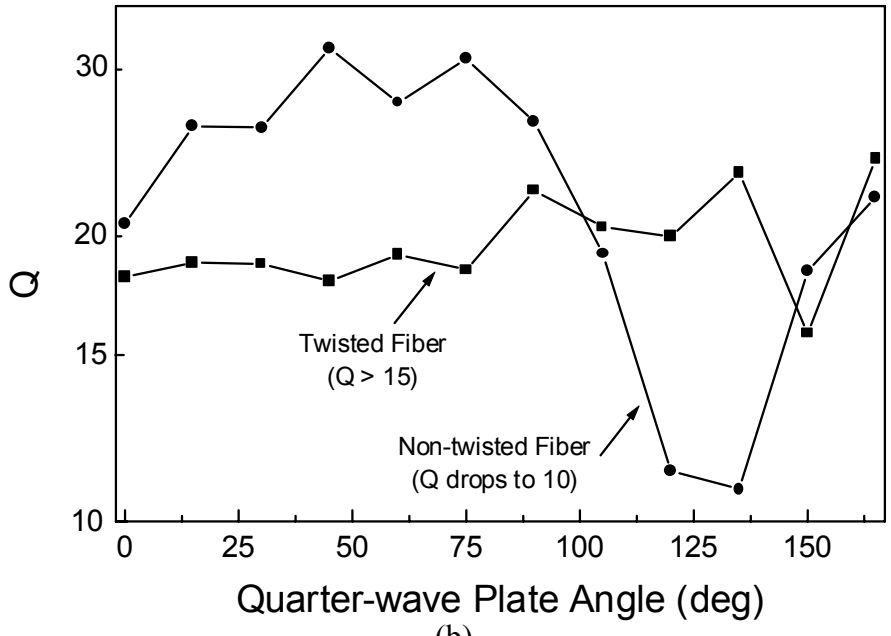
Q
Quarter-wave Plate Angle (deg)
Twisted Fiber
(Q > 15)
Non-twisted Fiber
(Q drops to 10)
30
20
15
10
0
25
50
75
100
125
150

(b)

Figure 3

Appendix E

Stable supercontinuum generation in short lengths of conventional dispersion-shifted fiber

G.A. Nowak, J. Kim and M.N. Islam

Department of Electrical Engineering and Computer Science
The University of Michigan
1301 Beal Avenue
Ann Arbor, Michigan 48109-2122
734-936-1879 (Office)
734-647-2718 (Fax)
ganowak@eecs.umich.edu

Abstract

By propagating 500fs pulses through 2.5m of standard fiber followed by 2m of dispersion-shifted fiber, we generate >200nm of spectral continuum between 1430 and 1630 nm, which is flat to less than +/- 0.5dB over more than 60nm. Pulses obtained by filtering the continuum show no increase in timing jitter over the source laser and are pedestal-free to > 28dB, indicating excellent stability and coherence. We show that the 2^{nd} and 3^{rd} order dispersions of the continuum fiber and self-phase modulation are primarily responsible for the continuum generation and spectral shaping and find close agreement between simulations and experiments.

Stable supercontinuum generation in short lengths of conventional dispersion-shifted fiber

G.A. Nowak, J. Kim and M.N. Islam

Department of Electrical Engineering and Computer Science
The University of Michigan
1301 Beal Avenue
Ann Arbor, Michigan 48109-2122

1. Introduction

Supercontinuum (SC) generation, in general, describes extreme, nearly continuous spectral broadening induced by high-intensity picosecond and sub-picosecond pulse propagation through a nonlinear medium [1]. Super-broadened spectra have been used for spectroscopy and dispersion measurements, and as multiple-wavelength channel pulse sources for high bandwidth TDM/WDM systems[1,2,3]. SC generated in optical fiber is a convenient source for such systems because it provides a very broad bandwidth (> 200nm) that can be sliced, as required, into short pulses at individual WDM channels. The pulse trains in each channel have the repetition rate of the source laser and, when the spectrum is flat and of uniform phase, pulse widths that are transforms of the spectral filter function. These features make the continuum source an attractive alternative to numerous discrete laser diodes, particularly for high bit-rate OTDM systems, since a single short pulse source provides chirp-free, ultra-short pulses simultaneously for multiple wavelength channels. Also, the SC source requires the relatively simpler stabilization of passive filters rather than of the operating wavelengths of multiple laser diodes [4]. Finally, since the SC has a continuous high power spectral density outside the erbium gain band compared with thermal sources or superluminescent LEDs [5], it is also useful for characterizing passive components and amplifiers in spectral regions of emerging interest.

Several groups have reported the generation of SC in fiber using various fiber dispersion profiles to obtain spectra that are suitable for spectrally-sliced pulse sources. Morioka, et.al. [6] and Okuno, et.al. [7] employ fiber in which the anomalous group velocity dispersion (GVD) decreases over the fiber length from D ~ 3 – 4 ps/nm-km, through the zero dispersion point, to a normal dispersion value, D ~ - 1.5 ps/nm-km. The 3rd order dispersion of the fiber is flattened to inhibit pulse break-up. The input soliton is adiabatically compressed in the anomalous dispersion segment of the dispersion-decreasing fiber, its spectrum super-broadens in the vicinity of the zero dispersion point, and the continuum is shaped with propagation over the normal dispersion region of the fiber. The spectral broadening is attributed to a combination of various $\chi^{(3)}$ processes, including self-phase modulation (SPM), cross-phase modulation (XPM), four-wave mixing (4WM), and stimulated Raman scattering (SRS) [6,7]. Sotobayashi, et.al. [8] obtain ~ 325nm continuum at –20dB using 4km of constant anomalous dispersion fiber (D~0.762 ps/nm-km) followed by 2km of dispersion flattened, normal dispersion fiber (D ~ - 0.197 ps/nm-km). Recently, Takushima, et.al. [9] reported SC generation using 10.2km of dispersion decreasing fiber to obtain adiabatic soliton compression, followed by 1.7km of normal GVD fiber of D ~ - 0.13 ps/nm-km, in which the 3rd order dispersion is flattened. All these demonstrations of continuum generation use specialty fibers of total lengths ranging from 1 to 12 km.

In this paper we report supercontinuum generation using a 2-stage soliton-effect compressor that consists of a total of 4.5m of fiber. The SC results from higher-order soliton compression in fibers of step-wise decreasing anomalous dispersion and spectral shaping by 3rd order dispersion effects. This allows for the use of conventional, commercially-available fibers that are 3 orders of magnitude shorter than those used in related experiments. The spectrum is more than 200nm wide at –20dB and is flat to less than +/- 0.5dB over 60nm. The continuum exhibits excellent piecewise coherence, as evidenced by obtaining <500 fs pulses that are pedestal-free to >28 dB, even when the spectrum is carved more than 70 nm from the pump wavelength. Also, the timing jitter of the carved pulses indicates no degradation compared to the source laser. Experiments match simulations well, and indicate that the continuum is generated almost exclusively by self-phase modulation and shaped primarily by 3rd order dispersion effects.

2. Theory

SC generation in fused-silica optical fiber depends on two constituent processes: pulse compression and spectral shaping. Pulse compression creates the high peak powers necessary to achieve significant nonlinear action in fibers. Spectral shaping results from the combined effects of pulse shape evolution with propagation and the generation of new spectral components by high intensity portions of the pulse through nonlinearities.

Although pulse compression and spectral shaping mechanisms are coupled in a real fiber, they can be sorted into dominant regimes with regard to continuum generation. The pulse compression regime, characterized by symmetrical spectral evolution, depends on the balance between dispersion and nonlinearity that is necessary for soliton existence in the fiber. The spectral shaping regime is defined by the increased impact of higher-order dispersion and / or a higher-order nonlinearity such as SRS or self-steepening on pulse shape evolution. The dominant higher-order effect inhibits further pulse compression and causes an asymmetry in the spectrum. In low second-order dispersion fibers ($D < 2$ ps/nm-km), for sufficiently narrow pulse widths, the third-order dispersion is the dominant higher-order mechanism that determines the profile of the SC.

The two principal techniques for all-fiber pulse compression are soliton-effect compression (SEC) and adiabatic soliton compression (ASC). SEC requires launching of higher-order ($N \geq 2$) solitons, which periodically compress and expand with propagation in the anomalous dispersion regime of a fiber. Depending on the soliton order, the pulse achieves a minimal width at some fraction of the soliton period (Z_0) [10]. When the fiber is cut at the length corresponding to a minimum width location, a broadened spectrum corresponding to the compressed pulse is obtained. To first order, only SPM contributes to the spectral broadening.

ASC derives from a fundamental (N=1) soliton's tendency to decrease its pulse width to maintain a constant area in response to gradually decreasing dispersion or increasing energy with propagation. When resulting from a dispersion-decreasing fiber, the amount of compression depends on the ratio of the initial to final dispersions, and compression ratios of ~16 have been reported [11].

Comparing the two mechanisms, SEC provides higher compression ratios than are possible with ASC and leads to optimal compression in a fraction of the soliton period. ASC requires a longer fiber because the dispersion must decrease gradually over the soliton period. Moreover, SEC is achievable in conventional, constant-dispersion DS fiber, allowing for simple implementation, whereas fibers for ASC are not available commercially. SEC, however, does

not compress the low-intensity portions of the pulse, causing some of the input pulse energy to remain in wings and not contribute to the continuum generation. For soliton orders up to N~4, the fraction of energy remaining in the wings at maximum compression is below 25% [10]. SEC, then, provides the narrow pulse width and high peak power necessary for continuum generation within a shorter length of fiber than ASC.

Once a pulse is compressed to a sufficiently narrow width, a higher-order dispersion or nonlinear mechanism affects the subsequent pulse and spectral shape evolution. Since our experiment relies on SEC in low GVD fiber, we simulate spectral broadening resulting from SEC in the presence of 3rd order dispersion to examine its effects on spectral shape evolution. We solve the nonlinear Schrödinger equation using the split-step Fourier method [12] for fiber parameters, D=0.786 ps/nm-km, $n_2 = 2.7x10^{-20}$ m^2/W, $A_{eff} = 50\mu m^2$ and an unchirped, N=3 soliton. Figure 1 shows the simulated broadened spectrum of a 180 fsec pulse that undergoes soliton-effect compression, with and without 3rd order dispersion. The spectrum broadens symmetrically in the absence of 3rd order dispersion and the maximum bandwidth is achieved at the point of optimal compression for this soliton order ($L = 0.25Z_0$). In the presence of 3rd order dispersion ($dD/d\lambda = 0.03$ ps/nm^2-km), the spectrum develops a broad (~100nm) and flat (+/- 1dB) region to the anti-Stokes side of the center seed wavelength. The flat region evolves at a slightly longer length of fiber ($L = 0.27Z_0$) than the point of optimal compression. Beyond this length, deep dips develop in the spectral profile, degrading its suitability for a spectrally-carved source. The simulation indicates the potential for achieving a super-broadened spectrum with a flat region of significant extent by taking advantage of SEC and 3rd order dispersion effects on pulse shape evolution in short lengths of conventional DS fiber.

3. Experimental Setup and Results

We investigate the continuum generation using the experimental set-up in Fig. 2. A passively mode-locked erbium-doped fiber laser generates a 15MHz train of 470 fsec, transform-limited, hyperbolic-secant pulses centered at 1560nm. The pulses broaden dispersively to ~980fs with propagation through 5.1m of SMF-28 fiber pigtails and a polarization controller. An erbium-doped fiber amplifier (EDFA) consisting of 1.5m of 2000ppm-doped Er gain fiber amplifies the signal to an average power of 5mW. Following the EDFA, the pulse is compressed to ~120 fsec through soliton compression effect in 2.5 m of standard fiber. The energy per pulse is approximately 90 pJ. The compressed pulse is launched into the 2m DS fiber with D = 0.76 ps/nm-km and a dispersion slope of ~ 0.056 ps/nm^2-km. A polarization controller sets the state of the signal polarization at the input to the EDFA, and a variable attenuator sets the signal power. To measure the coherence of the spectrum, a 25nm bandpass filter (flat passband, Gaussian roll-off) centered at 1490 nm is used to carve the continuum, and the filtered pulse propagates through 22m of λ_0 = 1560nm fiber to compensate for residual 2nd order dispersion accumulated in the filter pigtails. Diagnostics consist of an optical spectrum analyzer, autocorrelator, fast photodiode and RF spectrum analyzer.

A sample continuum generated by an average signal input power of 3.2mW is indicated in Fig. 3. The continuum has a 20dB bandwidth of 211 nm and a 61nm wide spectral region between 1475 to 1535 nm that is flat to within +/- 0.5dB (inset). The power spectral density across the flat region is approximately –18 dBm/nm. The peak in the vicinity of 1560nm includes low intensity energy that was not compressed in the soliton, ASE, and seed pulse energy that is polarized orthogonally to the continuum. The PC setting is critical to optimizing pulse compression in the first-stage standard fiber by aligning the seed pulse polarization with a

polarization eigenmode of the fiber. Polarization does not appear to play a role in the continuum generation process in the second-stage DS fiber compressor, however, since the SC spectrum changes negligibly when the DS fiber is manually manipulated.

The autocorrelation and spectrum of the pulse carved from the continuum at $\lambda = 1490$ nm are shown in Fig. 4a. The autocorrelation shows that the 400 fsec pulse is pedestal free to >28dB with an excellent Gaussian fit, indicating a high degree of coherence among the carved spectral components and negligible incoherent power. The time-bandwidth product of the compensated pulse is ~0.45, assuming Gaussian fit of the spectrum, indicating negligible chirp across the broadened spectrum in this region. Figure 4b shows the timing jitter of the seed laser pulses and the pulses carved from the continuum. The jitter was evaluated by measuring the sideband energy at the 430^{th} harmonic of the fundamental repetition rate over a 5KHz span with 30Hz resolution [13]. The carved pulses show no jitter increase, even over a 10 msec measurement time.

4. Discussion and Conclusion

The suitability of the SC as a source for multi-channel, high bit-rate applications depends on its stability, piecewise coherence, and flatness over a broad spectrum. These characteristics enable the carving of low-noise, low-jitter short pulses from the continuum and reduce requirements for pulse shaping and power equalization among channels. The SC stability is defined by the amplitude and timing jitter of the carved pulses. The timing jitter of carved pulses results from source laser jitter, the jitter that seed pulses develop with propagation, and jitter due to variations in the power spectral density within the bandwidth of the filters that carve pulses from the continuum. The jitter that develops with propagation typically results from random pulse center-frequency variations due to additive noise from amplifiers (Gordon-Haus effect) [14] or energy fluctuations in pulses experiencing Raman-induced self-frequency shift [15]. In both cases, the jitter scales linearly with the effective length of the fiber in which the continuum is generated. Variations in the power spectral density within filter bandwidths derive from changes in the nonlinear process(es) contributing to the continuum and changes in the polarization state of seed pulses due to environmental perturbations of fiber parameters. Minimizing the length of the continuum fiber minimizes these potential variations and constrains the degradation of the timing jitter of the carved pulses.

The coherence of the continuum is defined by the correlation of the spectrum over a fixed bandwidth. Loss of coherence delimits the shortest pulse widths that can be carved from the continuum as well as setting the noise floor due to incoherent energy present within a filter bandwidth. By using a short length of fiber, the coherence across the continuum is controlled by restricting the nonlinear mechanisms contributing to the continuum to self-phase modulation (SPM). A short interaction length between the seed (pump) pulse and incoherent energy due to ASE or dispersive energy shed by the seed also minimizes mapping of the incoherent energy across the broadened spectrum through four-wave mixing.

By comparing the experiment with simulations, we confirm that the principal mechanisms responsible for the continuum are self-phase modulation (SPM) and pulse-shaping by the 2^{nd} and 3^{rd} order dispersion. SPM is the dominant nonlinear mechanism that broadens the spectrum of the input signal. The 2^{nd} order dispersion of the DS fiber creates a high peak-power pulse through soliton compression of the output from the SMF-28 fiber. The 3^{rd} order dispersion sharpens the trailing (for $dD/d\lambda > 0$) or leading (for $dD/d\lambda < 0$) edge of the pulse, causing the

asymmetric broadening to the anti-Stokes or Stokes sides of the seed center wavelength, respectively. Also, for a typical background birefringence of 10^{-6}, the beat length is ~2m, which describes the length in which the input state's polarization evolves. In fiber lengths of that order, the state of polarization of the input pulse is not randomized, so the output spectral components remain co-polarized. We confirmed that this was the case by passing the continuum through a polarizing beam splitter. The continuum is transmitted uniformly, except for the spectral region in the immediate vicinity of the pump, which is attenuated by ~ 5 dB.

We simulate the spectral broadening using the nonlinear Schrödinger equation for the experimental parameter values described above, including only 2nd and 3rd order dispersion and SPM effects in the simulation model. Figure 5a shows the simulated and experimental spectra, and the good agreement between the two indicates that the continuum results largely from these well-defined processes. The peak power of the input to the DS fiber was used as the simulation fitting parameter, and was varied by < 10% from the experimentally measured value to obtain the indicated fit. The spectral structure in the vicinity of the pump of the experimental continuum is the residual input signal discussed previously. When Raman and self-steepening terms were included in the propagation equation, the continuum spectrum showed negligible changes for the given parameters, indicating that these mechanisms do not play a substantial role in the continuum generation in this regime.

Figure 5b shows a simulation for the same experimental parameters, except with $dD/d\lambda < 0$ for the DS fiber. By reversing the sign of the 3rd order dispersion, the leading edge of the pulse is steepened, causing the continuum on the Stokes side of the seed wavelength to be broadened and flattened. This indicates the potential for tailoring the continuum by choosing the appropriate dispersion values for the continuum fiber. To optimize the spectral broadening, the 2nd order dispersion should be anomalous to achieve higher-order soliton compression over the fiber span. The minimum value of D is set so that the optimal compression occurs over a short fiber length and the maximum value is constrained by the available pulse energies for the desired soliton order. To minimize pulse energy lost to low intensity wings, soliton orders should be below N=4 in all stages. The sign of $dD/d\lambda$ determines the direction of spectral broadening asymmetry while the absolute value determines the extent of spectral broadening versus its flatness. For D~1.0 ps/nm-km, low values of $dD/d\lambda$ (~ 0.001-0.02 ps/nm^2-km) provide a broader, but less flat spectrum than that generated in fibers with typical values of $dD/d\lambda$ (~ 0.3 – 0.6 ps/nm^2-km).

In summary, we generate a 210nm spectral continuum through 2-stage soliton-effect compression of 480fsec pulses using 2.5 meters of SMF-28 fiber followed by 2 meters of DS fiber. The continuum is stable and very flat from 1470 to 1530nm, and ~400 fsec pulses are carved as far as 70nm from the pump wavelength. The continuum results from SPM-induced spectral broadening and pulse shaping caused by the combined effects of the 2nd and 3rd order dispersions. Although the continuum is obtained at a low repetition rate (15MHz), the results indicate the potential for generation of SC with attractive features within very short lengths of conventional, off-the-shelf fiber. Based on required energies of ~ 90pJ/pulse, this method of continuum generation scales to 10Gb/s pulse rates, requiring an average power of ~ 1W. Such saturation output powers are achievable in commercially available amplifiers. By tailoring the dispersion properties of the fiber, the continuum characteristics can be optimized for the desired application.

This work is supported by DARPA.

References:

1. R.R. Alfano, Ed., "The Supercontinuum Laser Source," Springer-Verlag, New York, 1989.
2. K. Mori, T. Morioka, and M. Saruwatari, "Ultrawide spectral range group-velocity dispersion management using supercontinuum in an optical fiber pumped by a 1.5μm compact laser source," IEEE Transactions on Instrumentation and Measurement, **44**, 712-715 (1995).
3. T.Morioka, H.Takara, S.Kawanishi, O.Kamatani, K.Takiguchi, K.Uchiyama, M.Saruwatari, H.Takahashi, M.Yamada, T.Kanamori, and H.Ono, "1 Tbit/s (100 Gbit/s x 10 channel) OTDM/WDM transmission using a single supercontinuum WDM source," Electron. Lett., **32**, 906 (1996).
4. A.K. Srivastava, Y.Sun, J.W.Sulhoff, C.Wolf, M.Zirngibl, R.Monnard, A.R.Chraplyvy, A.A.Abramov, R.P.Espindola, T.A.Strasser, J.R.Pedrazzani, A.M.Vengsarkar, J.L.Zyskind, J.Zhou, D.A.Ferrand, P.F.Wysocki, J.B.Judkins, and Y.P.Li, "1Tb/s transmission of 100 WDM 10Gb/s channels over 400km of TrueWave fiber," Proc. OFC'98, PD-10 (1998).
5. Hewlett Packard Co., Lightwave Test and Measurement Catalog, 62 (1997).
6. T.Morioka, S.Kawanishi, K.Mori and M.Saruwatari, "Nearly penalty-free, <4ps supercontinuum Gbit/s pulse generation over 1535-1560 nm," Electron. Lett., **30**, 1166 (1994); K.Mori, H. Takara, S. Kawanishi, M..Saruwatari, and T. Morioka, "Flatly broadened supersontinuum spectrum generated in a dispersion decreasing fibre with convex dispersion profile," Electron. Lett., **33**, 1806 (1997)
7. T. Okuno, M. Onishi, and M. Nishimura, "Generation of ultra-broad-band supercontinuum by dispersion-flattened and decreasing fiber," IEEE Photonics Techno. Lett., **10**, 72 (1998).
8. H. Sotobayashi and K. Kitayama, "325nm bandwidth supercontinuum generation at 10Gb/s using dispersion-flattened and non-decreasing normal dispersion fiber with pulse compression technique," Electron. Lett., **34**, 1336 (1998).
9. Y. Takushima, F. Futami, and K. Kikuchi, "Generation of over 140-nm-wide super-continuum from a normal dispersion fiber by using a mode-locked semiconductor laser source," IEEE Photonics Techno. Lett., **10**, 1560 (1998).
10. L.F.Mollenauer, R.H.Stolen, J.P.Gordon, W.J.Tomlinson, "Extreme picosecond pulse narrowing by means of soliton effect in single-mode optical fibers," Opt. Lett. **8**, 289-291 (1986).
11. S.V.Chernikov, E.M.Dianov, D.S.Richardson, and D.N.Payne, "Soliton pulse compression in dispersion decreasing fiber," Opt. Lett. **18**, 476-478 (1993).
12. P.K.A.Wai, C.R.Menyuk, H.H.Chen and Y.C.Lee, "Soliton at the zero-group-dispersion wavelength of a single-mode fiber," Opt. Lett. **12**, 628-630 (1987).
13. D. von der Linde, "Characterization of the noise in continuously operating mode-locked lasers," Appl. Phys. B, **39**, 201-217 (1986).
14. D. Marcuse, "An alternative derivation of the Gordon-Haus effect," J. Lightwave Technol. **10**, 273-278 (1992).
15. D. Wood, "Constraints on the bit-rates in direct detection optical communication systems using linear or soliton pulses," IEEE Journal of Lightwave Techno., **8**, 1097-1106 (1990).

Figure Captions

Figure 1. Simulated spectral broadening due to soliton–effect compression for a τ_{FWHM} = 180 fsec, N=3 soliton in D = 0.786 fiber. Dashed line is the input spectrum. Dotted line is the output spectrum for $dD/d\lambda = 0$ at $L = 0.25Z_0 = 4.035$m. Solid line is the output spectrum for $dD/d\lambda = 0.03$ ps/nm^2-km at $L = 0.27Z_0 = 4.37$ m, which is the point of maximal spectral flatness.

Figure 2. Experimental Setup. EDFL/A=>Erbium-doped fiber laser/amplifier; PC => polarization controller; OBF=> optical bandpass filter; SC-DS=> supercontinuum DS fiber; CF=> compensation fiber. Diagnostics consist of an autocorrelator, optical spectrum analyzer, a fast photodetector, and an RF spectrum analyzer.

Figure 3. Spectral continuum generated in 2m of D = 1.3 ps/nm-km fiber with inset of 1474-1535nm spectral range.

Figure 4. (a) Autocorrelation and spectrum of pulse carved from supercontinuum at 1490nm. (b) Timing jitter of laser output and carved pulses at 1490nm.

Figure 5. (a) Experimental and simulated supercontinuum. (b) Simulated supercontinuum for the same parameters, except with $dD/d\lambda = -0.07$ ps/nm^2-km. The seed pulse center wavelength is 1560nm.

Appendix F

All-optical 100Gb/s-word Packet-TDM Access Node in a Looped-back Configuration: Enabling Technologies for Sequential Add/Drop Functionality

J. W. Lou, Y. Liang, O. Boyraz, and M. N. Islam, *Fellow, OSA*

1301 Beal Avenue
The University of Michigan
Ann Arbor, MI 48109-2122

Abstract

We experimentally demonstrate the adding, dropping, and passing-through of 100Gb/s-word packets in a looped-back all-optical time-division-multiplexed (TDM) access node. Packets are routed with 17dB contrast ratio and demultiplexed with 20dB contrast ratio. This node uses short 100Gb/s words in order to demonstrate its potential to process data packets from multiple sources and to perform packet-switching in a multi-node ring network configuration. The ability to tolerate timing jitter as well as varying input signal characteristics is essential to an all-optical access node in a multi-node network. For 2ps input pulses, the header processor has a timing window of ~5ps and the demultiplexer has a timing window of ~5.5ps. This allows tolerance to bit-to-bit timing jitters or to an increase in the pulse width of up to 3ps. Packet-to-packet timing jitter is detected and compensated by the technique used to synchronize the local source to each packet.

The key enabling technologies of an all-optical TDM packet add/drop multiplexer are discussed, including an erbium-doped fiber laser, a nonlinear optical loop mirror logic gate, self-synchronization to incoming packets using a fast-saturation/slow-recovery gain element followed by an intensity discriminator, a two-wavelength nonlinear optical loop mirror demultiplexer, and synchronization of new packets to the network packet rate using a phase-locked-loop. The local source is automatically synchronized to the incoming packet because it uses an extracted pulse from the packet, which has a contrast ratio of >20dB to the rest of the packet. Finally, new packets are added using a local laser and a synchronization method, which gives a timing jitter of ~1ps. Using a statistical method of measuring Q-value with picosecond resolution, we show that a header processor with two cascaded logic gates has a Q-value of 7.1 with a 95% confidence level.

I. All-Optical Packet Time-Division-Multiplexed Network Access

High-speed network access through all-optical time-division-multiplexed (TDM) add/drop multiplexers (ADMs) can help to increase single channel speeds and network flexibility. TDM network technologies can be advantageous for high-speed networks because they lead more naturally to packet switching. Also, the system architecture and protocol can be simplified since less control is required for one TDM channel than multiple WDM channels. Applications such as shared memory computing can be simplified because TDM packets on a single channel arrive in the order they were sent out. In addition, TDM technologies complement WDM research since each wavelength channel can be upgraded to higher speeds.

Several TDM network architectures have been proposed and tested. L.P. Barry, *et al.*, propose a star network design where a phase-locked-loop is used for clock recovery, and electro-absorption modulators are used for the channel drop and the demultiplexing functions [1]. The design for a packet-switched helical local area network (H-LAN) structure as well as several key all-optical components has also been developed [2]. All-optical devices for logic at 100Gb/s and rate conversion at 80Gb/s have been demonstrated using a single signal source [3,4]. Additionally, a TDM ShuffleNet design, using terahertz optical asymmetric devices for logic switching as well as demultiplexing has been developed [5]. The ShuffleNet design has been implemented as a packet switching network with a special header coding for routing and demultiplexing using fast tunable delay lines [6].

Subsystems involving adding and/or dropping have also been demonstrated. The simultaneous add and drop of 40Gb/s TDM channels using monolithically integrated Mach-Zehnder interferometers is demonstrated by Jepsen, *et al.* [7]. Also, electro-absorption modulators have been used in bit-interleaved TDM network ADMs at 40GHz [8]. The drop function of an access node has been demonstrated by Cotter, *et al.*, where packets are routed by extracting the marker pulse at a different bit period or different polarization [9]. The address recognition is performed by an AND-function logic gate using four-wave-mixing (FWM) in a semiconductor laser amplifier [10]. Kamatani, *et al.*, describe a method of extracting the clock timing using a phase-locked-loop based on FWM in a semiconductor laser amplifier, followed by demultiplexing using FWM in fiber [11]. Additionally, the interoperability of all-optical devices for the packet-drop functionality has been demonstrated using lasers synchronized through a phase-locked-loop [12]. Phase-locked-loop synchronization for header processing of individual packets is not tolerant to the inter-packet jitter that may occur as multiple nodes attempt to access the same network. A method of synchronizing to incoming packets with no special marker pulses has been proposed [13], although the output pulses have not been cascaded to other all-optical devices. The interoperability of all-optical nodes within a network, critical to the design and implementation of a network, has not yet been demonstrated.

In this paper, we present an ADM comprised of all-optical fiber devices. The instantaneous nonlinearities of optical fiber make it a potential candidate for high speed optical processing. Using 100Gb/s words, we demonstrate for the first time to our knowledge both the add and drop functions controlled by an all-optical header processor, by looping the ADM on itself to form a simple sequential network. The cascading of the ADM functions is a necessary step to demonstrating a multi-node all-optical network. That is to say, while dropping and demultiplexing of packets may be demonstrated with one ADM, it is necessary to have a second ADM to drop and demultiplex packets from the first ADM in order to determine if the first ADM has successfully added a packet. Among the key technologies that are necessary is the capability to route and demultiplex on a packet-by-packet basis with tolerance to inter-packet jitter, inter-

bit jitter, and varying input pulse characteristics. Such packet-switching technology has the potential to increase network flexibility. The adding, dropping, and passing-through of packets is determined by an all-optical header processor, and the reading of the payload bits is performed by an all-optical demultiplexer. Additionally, the current method of sending a long bit pattern through a telecommunication device and counting the number of errors that occur, in order to measure its performance, is currently limited to about 15Gb/s. For testing the reliability of all-optical devices operating at much higher speeds, we demonstrate a method of analysis by looking at the performance of the logic gates used in the header processor.

We use 100Gb/s words to show the compatibility of this all-optical packet-TDM demonstration-ADM for use in a multi-node ring configuration by looping the back-to-network port back to the input of the node. The key enabling technologies include transmitters, a header processor, synchronization circuits for individual packets as well as at the average packet rate, and a demultiplexer. The transmitters are passively mode-locked erbium-doped fiber lasers (λ~1535-1550nm, $\Delta\tau$~1-5ps) followed by fixed-word encoders. The header processor unit is an all-optical low-birefringence nonlinear optical loop mirror logic gate. Self-synchronization to extract a bit from the incoming packet allows the bit to be used as the local source for packet-by-packet synchronization. The self-synchronization unit uses a fast-saturation/slow-recovery gain element followed by an intensity discriminator. All-optical demultiplexing is accomplished using a two-wavelength nonlinear optical loop mirror with high-nonlinearity fiber. And finally, synchronization of new packets to the network packet rate is achieved using a phase-locked-loop between the incoming packets and the local transmitter. Packet routing is performed by a commercially available $LiNbO_3$ modulator. Each of these ADM components have been individually tested and characterized to confirm their functionality. The output of two cascaded logic gates, like the one used in the header processor, has a contrast ratio of 10dB and a statistically determined Q-value of 7.1, corresponding to a BER of $7x10^{-13}$. Extraction of the first pulse of incoming packets (for use as the local source) is achieved with a contrast ratio of >20dB, and synchronization of the local transmitter to the incoming packet gives an inter-laser timing jitter of ~1ps. For the ADM looped back on itself, we achieve contrast ratios of 17dB in the router and 20dB in the demultiplexer.

This demonstration provides insights into the compatibility issues of several all-optical components. We show that these all-optical components can be brought to function together to perform key ADM functions. For any cascaded function, the output pulse characteristics of the first device must be compatible for use as the input pulse of the second device. Conversely, the second device must have some tolerance to varying input pulse characteristics. We also demonstrate the ability to synchronize on a packet-by-packet basis using self-synchronization as well as at the packet repetition rate of the network using a phase-locked-loop. The main challenge to extending this demonstration to even higher bit rates and/or longer packets is in providing the necessary power levels without degrading the signal to noise ratio. High-powered amplifiers with short lengths of highly-doped erbium fibers are needed for short pulse amplification. Amplified spontaneous emission (ASE) and dispersive wave shedding by solitons are the leading causes of signal background and noise. Bandpass filtering is used to limit the ASE outside the signal wavelength as well as to spectrally reshape the pulses at various points to compensate for pulse distortions.

This paper describes the demonstration of packet add/drop functionality in an all-optical ADM. First, an overview of a potential network architecture is described in Section II. In Section III, we discuss the setup and configuration of the looped-back ADM. We show the

results of all-optical components integrated into an ADM looped back on itself in Section IV. A performance analysis of the header processor through a statistical method is discussed in Section V. In Section VI, the key enabling technologies for the ADM are described and the performance of each component is evaluated. Discussion of the challenges of this access node follows in Section VII. Finally, Section VIII summarizes the demonstration.

II. Ring Network Architecture

One possible network architecture that uses the ADMs discussed in this paper is a ring slotted-TDM metropolitan area network, shown schematically in Fig. 1. The ADMs allow access of data packets to the network. The focus of this paper will be on the demonstration of the ADM and the key enabling technologies necessary for high-speed all-optical TDM networking. A simplistic protocol for address checking is adopted where if the address of the incoming packet matches that of the local node, the packet is taken off the network (dropped) and a new packet is allowed onto the network. Otherwise, the incoming packet is allowed to continue on the network. By implementing the access node all-optically, we can overcome the bottlenecks of optical-electronic-optical conversions and increase the single channel speed of TDM networks.

For compatibility with high-speed all-optical processing, the packet ring architecture has a number of advantages over the bus and star topologies. First, access to the ring network is deterministic, not contention-based. By avoiding contention, we reduce the need for optical buffering. Second, the ring's inherent symmetry forms a natural basis for fairness guarantee mechanisms, which does not become less fair as the geometry is increased. Also, the ring has protective switching capabilities. Moreover, the absence of a central switch permits lower entry cost and ease of expansion. In contrast, a bus is vulnerable to physical damage and has an inherent headend asymmetry and unfairness. Architectures such as the H-LAN [2] attempt to overcome the limitations of buses, but the three fiber implementation may be considered an inefficient use of resources and still does not guard against physical damage. Star systems are unattractive because power is distributed among all the nodes, and power is a limited resource at high speeds.

However, the slotted ring does have some drawbacks. First, the average latency is half of the ring round-trip time for a unidirectional ring. Second, each node must operate at the aggregate traffic speed rather than the average speed available to the node. Finally, like a laser, the ring network permits recirculation of noise from previous passes, which requires the use of a management node as well as perhaps all-optical regenerators for system clean-up.

Focusing specifically on the ADMs in this ring network, there are several key functions that must be performed by the building blocks of each ADM in order for multiple ADMs to be able to operate with each other on the network scale. As discussed earlier, an important first step demonstration is that of an ADM looped back on itself, which demonstrates the interoperability of the building blocks and both the successful adding and dropping of packets from the network. Figure 2 shows a block diagram of the ADM looped back on itself. A remote transmitter generates an incoming packet. The synchronized local source generates the local clock and the local fixed address for the address recognition. The header processor compares the local address to the incoming packet address and the output triggers the packet router. The local transmitter is synchronized to the network packet rate and generates new packets to be added to the network. The demultiplexer bit-rate-downconverts from the packet bit rate to the packet repetition rate.

III. Setup of Sequential ADM Circuit Demonstration

A more detailed setup of the ADM is shown in Fig. 3. A remote transmitter sends a chopped sequence of packets (packet #1 = '100110...'). When the chopper is blocking packet #1, the packets looped back from the packet router (a chopped sequence from the back-to-network port) are transmitted. Although both packets are fixed and repetitive, the interleaving of the sequences of packets can be used to simulate instantaneous packet-to-packet changes in content and timing. The packet repetition rate is 21MHz and is limited by the repetition rate of the erbium-doped fiber lasers (EDFLs). The chopping frequency is 195Hz, which means that many of the same packets are transmitted for each sequence of packets. However, because the fiber has no memory, receiving the same packet many times should not affect the performance of the header processor or demultiplexer. The self-synchronization unit extracts from the incoming packets, a single bit that is used as the local source for the header processor and the demultiplexer. The address of the incoming packet is compared to the local address in the header processor. The output of the header processor is used to control the packet router. If the packet is determined to be for the local node (i.e., addresses match), the packet is routed to demultiplexer. Otherwise, it is sent back to the network, which in this case, loops back to the input of the node again. The demultiplexer is used to demonstrate down-conversion from the 100GHz bit rate to the packet rate by extracting individual bits in the payload of the packet. A new packet (pattern #2 = '100100...') may be added by using a local transmitter which is synchronized to the average packet rate of the network through a phase-locked-loop.

A. Devices outside the access node

The components that emulate the network outside the node are the remote transmitter and the back-to-the-network loop-back. The transmitter (discussed in detail in Section VI-D) consist of an EDFL (λ=1535nm, $\Delta\tau$=2ps) followed by a 100Gb/s fixed word encoder. The first three bits are considered the address header, and the rest are the data payload. Note that it is not necessary for the data packet to occupy such a small fraction of the data stream. The packet size and rate may both be increased to accommodate more data when implemented in a real network. The spacing between packets must simply be longer than the recovery time of the self-synchronization unit (~0.5ns). The back-to-network port is looped back to the input of the access node through an acousto-optic modulator (AOM) and a fiber coupler. The AOM is synchronized to the frequency of the chopper at the output of encoder #1. This means that the packets looped-back to the input are also a chopped sequence, and proper setting of the phase of the modulation signal ensures that the packets will not collide with the packets from encoder #1.

B. Devices comprising the access node

The four main components that make up the local access node are the self-synchronization unit, the header processor, the demultiplexer, and the local transmitter. Each component will be discussed in detail in Section VI. At the input to the node, part of the packet energy is tapped for synchronization, part for the header processor to check the address, and the remainder is sent to the modulator to be routed. For header processing, we generate a synchronized local clock ('111') and a local address ('011') for an all-optical logic gate [14]. The output of the header processor is sent to a threshold detector, which generates the control pulse for the packet router.

The self-synchronization unit selects the first pulse from an incoming packet, making it automatically synchronized with the incoming packet [12]. We can consider the first pulse as a marker pulse although it is optically the same as the other pulses in the packets. First, a transmission function with a fast-saturation/slow-recovery gain medium is imposed across the packet to create higher intensity for the first pulse in the packet. Then, the remaining pulses of the packet are removed with an intensity discriminator. Note that the guard time between packets must be longer than the recovery time of the gain element.

The all-optical logic gates used for header processing are realized by using low-birefringence nonlinear optical loop mirrors (low-bi NOLMs). The low birefringence is generated by wrapping fibers with very low background birefringence on aluminum mandrels. This low birefringence allows the co-propagating pulses along orthogonal polarizations in the loop to phase shift through cross-phase modulation, and insures that two pulses have a reasonably long interaction length. The timing window makes the NOLMs tolerant to possible timing jitter between the bits.

The demultiplexer is a two-wavelength (2λ) NOLM [15] using high-nonlinearity fiber. The device uses a control pulse at a different wavelength than the incoming signal. By adjusting the relative timing between the control pulse and the signal packet, the position within the packet that is to be demultiplexed can be selected. The timing window is determined by the group velocity walk-off between the two wavelengths.

The local transmitter is another EDFL, which is synchronized to the self-synchronization unit output through a phase-locked-loop and an AOM/grating pair in the laser [15], followed by a 100Gb/s fixed word encoder. The EDFL is a passively modelocked Er/Yb co-doped fiber laser in a linear cavity configuration. The fixed word encoder is constructed by fiber couplers and delay lines. A single laser pulse is split into four pulses, each pulse is time-delayed with respect to the others, and the pulses are recombined to form the word packet with 10ps bit-to-bit separation.

IV. Experimental Results of Looped-back ADM

In this section, we demonstrate the sequential adding and dropping of packets by the ADM. Subsection A focuses on the packet routing of packets from the remote as well as the local transmitters. When the packet is dropped from the network, it is sent to the demultiplexer, and the demultiplexing results are discussed in Subsection B.

A. Packet Routing

A commercial 2x2 $LiNbO_3$ modulator is used as the packet router. Figures 4a and 4b show the output of the control unit for the packet router when the address of packets from encoder #1 and #2 are different (i.e., one matches and the other does not match the local address). To switch the packet router, a 6V control signal is applied to the modulator. The figures indicate that the header processor correctly checks the addresses and triggers the modulator to route the packets appropriately in each case, and the packets are routed on a packet-by-packet basis. For example in Fig. 4a, the chopped sequence of packets from encoder #1 trigger the modulator to route each packet back to the network, whereas the interleaved sequence of packets from encoder #2 do not trigger the modulator.

We demonstrate sequential adding, dropping, and passing-through of packets from different sources in our access node. Figure 5 shows cross-correlations of the outgoing packets at the back-to-the-network port, immediately after the packet router. Figure 5a shows that the packet from encoder #1 ('100110...') can be passed-through (sent back to the network) and Fig. 5b shows when the packet is dropped with at least 17dB contrast ratio. As shown in Fig. 5c, a new packet ('100100...') can be added when the old packet has been dropped. The contrast ratio of the packet routing is limited by the extinction ratio of the $LiNbO_3$ modulator. The figures show that each incoming packet can be correctly routed using the information in the address header without conversion to electronics.

B. Demultiplexing of Bits

Figure 6 shows that when the address of the incoming packet matches the local address, the demultiplexer can read the bits in the packet. A simplified header ('100') is generated by both encoders so that both packets will be routed to the demultiplexer. We show the cross-correlation of the incoming packets to the node from encoders #1 and #2 in Figs. 6a and 6e, respectively. In the top figure, the payload ('110...') of encoder #1 is shown by cross-correlation to be demultiplexed (Figs. 6b-6d). Likewise, the bottom figure shows the demultiplexed payload of encoder #2 ('100...') in Figs. 6f-6h. The bits are individually demultiplexed by adjusting the relative timing between the control pulse and the incoming packet. In a real network, *N* demultiplexers will be necessary for *1/N* demultiplexing of the entire packet. The energy contrast ratio between the demultiplexed '1' and '0' is at least 20dB and the switching energy is less than 1pJ/pulse. Note that while the input pulse widths of encoder #1 and the demultiplexed bits are approximately the same, this is not the case for encoder #2. This is because the output pulse width is set by a narrow-band (0.9nm) spectral filter at the output of the demultiplexer. In a real network, the demultiplexed bits will be sent to energy detectors and converted to electronic signals and thus, the pulse width may not have much of an effect as long as it is shorter than the bit period. The residue that can be seen in the '0' bit positions is the leakage of the control pulse. This leakage is at a different wavelength than the switched out signal and can be further attenuated with another bandpass filter.

V. Q-value Analysis Technique and Its Application to the Header Processor

New measurement techniques for testing and monitoring the performance of all-optical devices are needed as all-optical telecommunication devices start to push the single channel speeds towards 100Gb/s and beyond. A sampling technique [16,17] using a cross-correlator and reference can be used to perform Q-value analysis of high-speed optical devices. This method allows us to measure eye diagrams with picosecond resolutions. However, the speed of the technique is limited to the sampling speed. This technique has possible applications as a statistical monitor of potential system performance in high-speed optical networks. Although it cannot be used to detect and/or correct specific errors in data packets, the technique gives a statistical Q-value from which a BER can be inferred.

To demonstrate this technique, we apply this technique to an all-optical header processor consisting of two synchronized lasers, 100Gb/s fixed word encoders, and two NOLM logic gates. The setup for the logic gates is shown in Fig. 7. This setup is more complex than that shown in Fig. 3 in that this setup consists of two levels of logic. The first gate, an inverter, checks to see if the address header is all '1's, indicating an empty packet. The second gate, an

exclusive-OR (XOR), checks to see if the address matches the local address or not. Thus, this setup allows for more complete header checking. Although the implementation of the measurement technique is not dependent on the number of levels of logic, the results show that the overall Q-value from a header processor with cascaded logic gates is still acceptable.

The output of the header processor is split and sent to the diagnostics for performance analysis. Cross-correlator 2 is used to control timing drifts caused by thermal fluctuations. By adjusting the relative timing between the master laser encoder and the slave laser encoder with a variable delay stage, we can obtain any one of eight possible 3-bit patterns. Cross-correlator 1 is slightly modified by using the fast response (~10ns rise and decay time) of the photomultiplier tube (PMT) to remove any averaging effects. By using a digital scope to take single-shot scans of the signal from the PMT, a single pulse response is taken per scan. We take a large number of scans while varying the timing between the reference pulse and the output of the header processor. Then, by overlaying the scans, we can map out the eye diagram with picosecond resolution for all the possible patterns.

The eye diagram for the header processor is shown in Fig. 8. The eye diagram is for return-to-zero, hyperbolic secant pulses, and it is an overlay of all possible outputs from the header processor. The input header is equally varied between all of the eight possible 3-bit combinations. The local address is '010' and thus, the local address bit may be a '1' or '0' depending on which bit is scanned. Because the NOLM has a finite polarization extinction ratio, there is pump leakage present. Consequently, in the XOR (^) gate, the '0' level is different for the case without any pump pulses (i.e. 0 ^ 0 = 0) and for the case with two-pump pulses (i.e. 1 ^ 1 = 0 + leakage). This leads to a spread of the '0' level in the eye diagram. However, there is no such spread for the '1' level because the nonlinear transmission from the NOLM dominates any pump leakage.

By fixing the reference pulse at the center of the bit period, we can measure the Q-value at the center of the eye opening from which we can statistically calculate the potential BER. The Q-value is defined by $Q = (I_1-I_0)/(\sigma_1+\sigma_0)$, with I_1 and I_0 being the sampled means of the 'on' and 'off', respectively and with σ_1 and σ_0 being the sampled standard deviations of the 'on' and 'off', respectively [19]. The measured Q-value is an optical Q where we have neglected the relatively small electronic noise in the PMT. The statistical BER is given by $BER = 0.5 \times erfc(Q/\sqrt{2})$, where the *erfc* is the complementary error function. Note that by sampling in the middle of the eye, we are measuring the instantaneous response of the header processor output cross-correlated with a reference pulse. The resolution of the sample is determined by the pulse width of the reference pulse. Thus, the cross-correlation technique takes only one sample point in the bit period but actually integrates the overlapped energy between the signal and the reference. For each 3-bit pattern, 150 data points are taken. Because there are eight different possible 3-bit patterns, the total number of data points is 1200. In addition, because the local bit can be '0' or '1', there are 1200 data points for the '1' level and the '0' level. With these points, we find a Q-value of 7.1, which corresponds to a BER of 7.0×10^{-13} for a 12pJ switching energy [18]. For one logic gate operation, the Q-value should be much higher since the cascading of logic gates tends to degrade the contrast ratio and therefore, degrade the Q-value.

Because this is a statistical method, we must look at the associated confidence interval to calculate possible errors in the measurement. The confidence interval is an interval of values that contains the true value of a parameter with a given confidence level. For a given system, the confidence interval for the mean [20] is given by:

$$P[I_n - t_{n-1,1-\alpha/2}\frac{\sigma_n}{\sqrt{n}} < \mu < I_n + t_{n-1,1-\alpha/2}\frac{\sigma_n}{\sqrt{n}}] = 1-\alpha\,, \quad (1)$$

and the confidence interval for the variance is given by:

$$P[\frac{(n-1)\sigma_n^2}{\chi^2_{n-1,1-\alpha/2}} < \sigma^2 < \frac{(n-1)\sigma_n^2}{\chi^2_{n-1,\alpha/2}}] = 1-\alpha\,, \quad (2)$$

where I_n is the sampled mean, μ is the (unknown) true mean, σ_n is the sampled standard deviation, σ is the (unknown) true standard deviation, n is the number of sampled points, and (1 - α) x 100% is the confidence interval level. The $t_{v,p}$ and the $\chi_{v,p}$ are the standard t-distribution and the chi-square distribution, respectively, with subscripts being appropriately substituted with the subscripts defined by the confidence intervals. By looking at the confidence interval and setting the confidence level to 95%, we can calculate the error range of the Q-value to be from 6.7 to 7.4 for the eye diagram of Fig. 8. This means a worst case BER of $8.8\text{x}10^{-12}$ and a best case BER of $4.8\text{x}10^{-14}$. Note that this error range is inversely related to the number of sample points for a given confidence level.

VI. Details of Key Enabling Technologies

In this section, we describe the four key enabling technologies of this ADM. Each component has been individually tested to demonstrate its functionality. The self-synchronization unit described in Subsection A allows packet-by-packet timing extraction. Subsection B discusses the header processor, and Subsection C discusses the demultiplexer. Finally, in Subsection D, the local transmitter and synchronization to the packet rate for the adding of new packets is described.

A. Self-synchronization Unit

In a ring network, an incoming packet may be from any of the nodes on the network. When originally added to the network or during propagation, different packets may experience different delays. This introduces an inter-packet jitter, which the ADM must be able to tolerate in order to correctly process the header bits and demultiplex the data payload of each individual packet. Figure 9 shows a schematic diagram for the functional design (i.e., extraction of the packet timing directly from the packet). Data packets begin with a '1' bit, which serves as the marker bit. Note that its temporal, spectral, and polarization characteristics are not distinguished from the rest of the packet. A differential intensity profile is imposed on the incoming packet so that the first bit has a higher intensity than the rest of the packet. Then, an intensity discriminator is used to extract the higher intensity pulse, which is the marker pulse in this case.

We have demonstrated the self-synchronization unit using the setup shown in Fig. 10. A 100Gb/s word packet is generated by a passively mode-locked fiber laser (λ = 1535nm, $\Delta\tau$ = 1.5psec) followed by a fixed word encoder. The data packet is sent to the fast-saturation/slow-recovery gain element to obtain a pulse train with a strong first pulse. Then, the output is sent to the intensity discriminator via an erbium-doped fiber amplifier (EDFA) to compensate for the 1dB net insertion loss of the gain element as well as to enhance the energy in the pulses. The energy of the first pulse is 15pJ at the output of the EDFA.

We choose a semiconductor optical amplifier (SOA) to perform the fast-saturation/slow-recovery transmission function. SOAs have very fast gain saturation when excited with short optical pulses and the saturation can occur during one pulse width for pulses of several picoseconds [21]. The saturated gain of the SOA, however, has a relatively long recovery time, which ranges from 0.2 to 1ns depending on different SOAs [22]. By properly setting the input power of the optical pulses and bias current of the SOA, only the first pulse in the packet experiences an unsaturated gain. The remaining pulses experience a gain saturated by the first pulse. This gain difference causes the first pulse of a transmitted packet to have a greater intensity than the remaining pulses.

An intensity discriminator then selects the first pulse and suppresses the rest, resulting in a single pulse being extracted from the packet. We use the combination of an unbalanced NOLM and a polarizer as the intensity discriminator. The coupler in the loop has an uneven power splitting ratio of 40:60, and the fiber is a 400m dispersion-shifted fiber with λ_0=1493nm. The clockwise and counterclockwise beams in the loop experience different nonlinear phase shifts because of the different input intensities of the pulses. The NOLM can be adjusted so that it has a higher transmission for the high intensity pulse than for low intensity pulses. Additionally, since nonlinear polarization rotation induced in the fiber of the loop mirror is also intensity dependent, a polarizer at the output of the loop mirror increases the contrast ratio.

Figure 11 shows the cross-correlation at different stages of the self-synchronization unit. Using an input energy of 2pJ/pulse to saturate the SOA at a current of 50mA, we obtain an intensity contrast ratio of more than 3dB between the first pulse and the remaining ones in the packet for a uniform input pulse train (Fig 11b). The resultant 3dB contrast ratio is not sensitive to input pulse energy. This intensity contrast is further enhanced to >20dB after the unbalanced NOLM (Fig 11c) intensity discriminator. With the EDFA between the SOA and the intensity discriminator, the overall insertion gain for the first pulse of the packet is 6.5dB.

The auto-correlation and optical spectra of these extracted single pulses at the output of the self-synchronization setup are illustrated in Fig. 12 and compared to those of the input pulses. It is important to maintain the pulse quality through the self-synchronization unit since the extracted pulse will be used as the local source for the header processor and the demultiplexer. A typical phenomenon related to gain saturation in an SOA device leads to a slight frequency shift [21]. The time-bandwidth-product of the extracted pulse is 0.34.

This self-synchronization does place some restrictions on the packet frames. It requires a time guard band between packets to be longer than the SOA recovery time. One-half the length of time between the end of the self-synchronization recovery time and the nominal start of the packet is the amount of inter-packet timing jitter that can be tolerated. Also, if the packets are very long, there could be two detrimental effects in the current configuration. The first is if there is a long series of ‘0’s, which will allow the SOA to recover, followed by a ‘1’, which may then be mistaken for the beginning of the next packet. The second is that long packets tend to have much higher average powers that may damage the SOA device. A possible solution is to add an electronic gate that is turned off after receiving the first extracted pulse and turned on after a fixed packet duration so as to block most of the bits in the packets. Such a gate would thereby guarantee that the first pulse of the subsequent packet obtains maximum gain.

B. Header Processor

Incoming packets may also have accumulated inter-bit jitter within the packet. In order for the packet header to be processed by logic gates, the gates must be designed to have a timing window of about half the bit period. In our case, the control clock pulses are split by a 50:50 coupler and counter-propagate in the NOLM along one axis of the wrapped low-bi fiber. The signals to be compared are coupled into each propagation direction through polarization beam splitters and aligned along the other axis of the fiber. Co-propagating control and signal pulses acquire a nonlinear phase shift through cross-phase modulation, and the counter-propagating clock pulses interfere when they recombine at the 50:50 coupler. The NOLM is biased so that when the two arms are balanced, the clock pulses are reflected. Otherwise, the pulses are transmitted. The walk-off length between orthogonal axes is ~115m (birefringence, $\Delta n \sim 3 \times 10^{-6}$), and the total length of the fiber is ~300m. Thus, rotating the polarization axis after each walk-off length gives measured timing windows of ~5ps for 2ps pulses. The high extinction ratio between the orthogonal polarizations (~40:1) helps to maintain a good output contrast ratio. The logic gates have switching energies of 10pJ/pulse for nonlinear transmissions of 50% [14].

To demonstrate the functionality of these logic gates, we implement an inverter gate followed by an XOR gate, as shown in Fig. 13. This is a more complex header processor than that used in the ADM demonstration, where we use only one gate (XOR) for comparing the incoming address with the local address. Note that the low-bi NOLM logic gates are cascadable and Boolean complete. The sources for the header processor are the master laser representing a transmitter and the slave laser acting as the local laser. They are synchronized using a phase-locked-loop. Both lasers produce 2ps pulses at 1535nm. A 2.3nm bandpass filter spectrally shapes the slave laser pulse used as the local address bit, making the pulse closer to transform-limited. The output from the master laser passes through a fixed-word encoder to produce the packet pattern ‘0001011100’. Similarly, the output from the slave laser passes through the clock generator to produce the 3-bit pattern ‘111’. The inverter determines whether the incoming packet address is all ‘1’s, corresponding to the special case for an empty packet, and the XOR gate determines if the addresses match. In the case when the packet is empty, the output of the first gate is ‘000’. Likewise, when the addresses match, the output of the second gate is ‘000’. We use a threshold detector to distinguish these two cases from the not-empty and unmatched cases, which have at least one ‘1’ in the output.

The header processor output is detailed in Fig. 14. The data packet including the header is given in Fig. 14a, while the inverted header output from the inverter, which is used as the input of the second logic gate (XOR), is given in Fig. 14b. The XOR gate output when the header matches (no match) the local header is given in Fig. 14c (14d). The on-off contrast ratio after the cascaded gates is 10dB. The contrast ratio is limited by pulse distortion from the EDFAs, which leads to incomplete switching through degradation of the polarization extinction ratio.

The length of the address can readily be scaled up since the logic gate performs a bit-by-bit comparison. Because the logic gate is Boolean complete and cascadable, even though one gate compares just one address at a time, several cascaded gates can create multiple levels of logic, which may be used to recognize more than one address.

C. Demultiplexer

The 2λ-NOLM used for demultiplexing uses a local control pulse at a different wavelength from the incoming packet. The incoming signal is split by a 50:50 coupler and counter-propagated through the NOLM. The second wavelength (control) is coupled in through a wavelength-division-multiplexer (WDM) and the control and signal propagate through each other due to the difference in group velocity dispersion. Through cross-phase modulation between different wavelengths, a nonlinear phase shift is imposed on the signal pulse that is to be demultiplexed. When the counter-propagating pulses recombine at the 50:50 coupler, the signal pulse with the induced phase shift is transmitted while the rest of the packet is reflected. Whereas the low-bi NOLMs are designed to work for a single wavelength, the 2λ-NOLM could be designed to work for any of a range of signal wavelengths because the walk-off is determined by the dispersion of the fiber. In our case, we also lower the required switching energy to less than 1pJ/pulse by using high-nonlinearity fiber. The fiber has a smaller core size (effective area $A_{eff} \sim 16.5\mu m^2$) for increased optical intensity as compared to normal dispersion-shifted fiber with an $A_{eff} \sim 50\mu m^2$. The germanium doping is also increased to increase the intrinsic nonlinear coefficient. The effective nonlinearity is 4.5 times that of a normal dispersion-shifted fiber.

The experimental setup for demonstration of the 2λ-NOLM is shown in Fig. 15. The device consists of a 50:50 fiber coupler for signal input/output, two WDM couplers for add/drop of the control pulses, and high-nonlinearity fiber. The WDM couplers are periodic with a spacing of ~7.5nm. One laser provides signal pulses at 1535nm ($\Delta\tau$=2ps) while a second synchronized laser provides control pulses at 1542nm ($\Delta\tau$=0.8ps). The timing tolerance of the 2λ-NOLM relies on the wavelength dependent group velocity dispersion, and the high-nonlinearity fiber is designed with a dispersion of 0.51ps/nm/km (λ_0~1530.5nm, L~1.65km) to yield a measured timing window of ~5.5ps for this setup.

To characterize this device, we measure the timing window, the switching energy, the nonlinear transmission, and the contrast ratio. The timing window is repeatedly measured at various switching energy levels. At a switching energy of 0.8pJ/pulse, the timing window is nearly square (Fig. 16a). Above this energy, the timing window remains squarely shaped with the width increasing to 7ps at 1.2pJ/pulse. Using the same data, we observe that the nonlinear transmission increases linearly with the switching energy below 0.8pJ/pulse, as expected (Fig. 16b). At a switching energy of 0.8pJ/pulse, the nonlinear transmission reaches about 90% implying a nearly π phase shift in the signal pulse. At higher pulse energies, self-phase modulation of the control pulse causes spectral broadening and leakage through the WDM. Because of this leakage, the intensity measured at the output port remains nearly constant instead of decreasing sinusoidally. The contrast ratio, measured at 0.8pJ/pulse switching energy, is 20dB for signal pulse energies less than 0.5pJ.

To ensure the pulse quality of the 2λ-NOLM output pulse, we measure the auto-correlation and optical spectra of the output pulse and compare them with the input. For switching energy below 1pJ/pulse and signal pulse energy below 0.5pJ, the auto-correlation shows that there is negligible pulse distortion (Fig.17). For switching energy above 1pJ/pulse, strong leakage from both signal and control pulses to the output port leads to severe degradation of the 2λ-NOLM.

To estimate how timing jitter affects the performance of the 2λ-NOLM, we compare the experimental data with computer simulations in which the timing jitter is not included. The simulation is based on the well-known nonlinear Schrödinger equation. For the timing window (Fig. 16a), the data also agrees well with the simulation except the small dip in the middle of the timing window. Notice that this dip is only about 2ps wide, implying that it is caused by the presence of timing jitter (see Section VI-D for a discussion on the synchronization method).

For the looped-back node demonstration, we use part of the extracted single bit from the self-synchronization unit to generate the second (control) wavelength. By propagating the pulse through 400m of high-nonlinearity fiber with λ_0=1534nm, we broaden the spectrum through self-phase modulation. Then, we use a 2nm bandpass filter to select the wavelength at 1542nm for use as the control pulse. This automatically synchronized control pulse should reduce the detrimental effects of timing jitter on the 2λ-NOLM.

D. Local Transmitter

The linear cavity Er/Yb co-doped fiber laser is passively modelocked by a semiconductor saturable absorber, as shown in Fig. 18. The 1.05μm pump beam from a diode-pumped Nd:YLF laser is introduced via a WDM coupler. The WDM coupler has one port spliced to a 1.2 meter Er/Yb co-doped gain fiber, whose cleaved end may serve as the laser output coupler. The beam from the other port of the WDM is collimated and focused on the semiconductor saturable absorber, which is mounted directly on the high reflector. The phase correction, is achieved by using an AOM/grating scheme [15] depicted in the dashed box of Fig. 18. The wavelength can be tuned from 1535nm to 1550nm and the pulse width can be varied from 1ps to 5ps depending on the wavelength, pump power, and cavity loss. In our case, we use λ~1535nm and Δτ~2.3ps.

To add new packets to the network, the local transmitter should be synchronized to the packet rate of the network. While self-synchronization is necessary to find the exact timing of each packet in order to process the packets from the network with inter-packet jitter, it is not necessary to replace packets with such precision. Thus, we use a phase-locked-loop scheme to synchronize a local laser to the average incoming packet rate.

The phase-locked-loop using AOM/grating for phase correction works as follows. The output from the gain fiber end (angle cleaved to prevent reflection) is separated into two parts by the AOM. The non-deflected zeroth order beam serves as the laser output. The deflected first order beam is reflected by a grating, which is set at an angle (α) to give good reflection as well as sufficient cavity tuning. The AOM deflection angle (θ), proportional to the carrier frequency, varies with the error signal sent to the AOM driver. The change in the AOM deflection angle induces two additive effects in the cavity length: first, a change of the first order beam angle modifies the wavelength selected by the grating according to $\Delta\lambda=(\lambda\times\Delta\theta)/\tan(\alpha)$; hence, the effective cavity length is adjusted through the fiber dispersion. More dominantly, the variation of the deflection direction gives a physical change in the optical path with $\Delta l_2=(l\times\Delta\theta)\tan(\alpha)$, where l is the distance between the AOM and the grating. The value of l and α are chosen to achieve sufficient cavity length tuning, limited wavelength fluctuation, and good coupling to the gain fiber. For example, with l=25cm and α=26.7 degrees, a change of 1MHz in AOM drive frequency results in Δl_2=80μm and Δλ=1.9nm. The physical change Δl_2 provides more than 85% of the 1kHz change in the repetition rate measured by a spectrum analyzer. Under normal

operation conditions of the phase-locked-loop, the AOM needs to be tuned only about a couple of tens of kHz, and the wavelength fluctuation in the slave laser is less than 0.005nm.

By measuring the radio-frequency power spectrum at the local laser fundamental frequency and at a sufficiently high harmonic (N), we can extract the timing jitter. The power spectra contains information about the amplitude as well as phase noise with the relative importance of the phase noise increasing as N^2 [15]. The timing jitter of the free running lasers is first studied to determine the tuning range and the bandwidth of the phase-locked-loop required to synchronize the lasers. We measure the power spectrum at the 1st and the 10th harmonic (a typical example is shown in Fig. 19a), and calculate the timing jitter according to the standard technique, which is discussed in detail in Ref. 14. For the free running laser ("PLL OFF" in Fig. 19b), the timing jitter is on the order of one picosecond for frequencies above 2kHz. However, the low frequency jitter can be orders of magnitude larger, mainly due to pump power fluctuations, mode beating noise, thermal fluctuations and mechanical vibrations. This noise characteristic is very typical in a passively mode-locked laser: the timing jitter between adjacent pulses is inconsequential, yet the jitter accumulated over a long period can be significantly large. Hence, an effective phase-locked-loop requires a high temporal resolution to detect the phase mismatch but relatively low bandwidth to track those fluctuations as long as the tuning range is sufficiently large to correct the timing jitter accumulated over the period. The AOM/grating scheme makes the synchronization of the two fiber lasers possible.

The phase mismatch between the two pulse series is obtained by direct detection. As shown in Fig. 20, each laser has a part of the beam (~2%) sent to a fast detector (response time ~ 100ps) whose output is amplified. The phase mismatch is detected by a radio-frequency mixer, passed through a low pass filter, and amplified. This error signal is then sent to control a signal generator, which drives the AOM placed inside the slave laser. With this simple direct detection method, we find that an EDFL can be well-locked to an electronic synthesizer with a timing jitter of approximately 2ps ("PLL ON" in Fig.19b). The result is achieved by locking the laser to its 4th harmonic, the highest possible from our synthesizer, in order to enhance the phase sensitivity of the phase-locked-loop. However, when the synthesizer is replaced by a free running EDFL, we synchronize using the 25th harmonic and achieve an inter-laser timing jitter of ~1ps. We use the cross-correlation of the lasers to determine the timing jitter [15]. For simplification, we assume that both lasers have Gaussian pulses and that the timing jitter experiences a Gaussian distribution. Then, the full width at half maximum (FWHM) of the cross-correlation profile can be approximated as $\Delta_x = \sqrt{(\Delta_1)^2 + (\Delta_2)^2 + J^2}$, where J is the mean square root of the timing jitter, and $\Delta_{1,2,}$ are the FWHM of the auto-correlation of the lasers.

By using a higher harmonic, we reduce the effect of amplitude fluctuations in the error signal. However, precautions must be taken since there are N locking points representing fixed yet different phases during a fundamental period of the laser. When the phase-locked-loop is turned on, the two lasers are locked to an arbitrary one of the N equivalent locking points. If the timing jitter of the laser (slow drift or sudden spur) is sufficiently large, the phase-locked-loop may jump between the different locking points. In this case, the two EDFLs are no longer locked to a determined phase even though the error signal stays near zero. For our EDFL with 2-3% amplitude fluctuation, we find that the phase-locked-loop works best for N=25 considering both the phase sensitivity and the long-term stability.

VII. Discussion

Among the challenges that need to be addressed in a high-speed TDM network is the ability of local nodes to process incoming data from various locations quickly and reliably. By processing data all-optically, we remove the bottlenecks associated with conversion from optics to electronics and back to optics again. However, this introduces new challenges in terms of synchronization (bit-to-bit as well as packet-to-packet). Additionally, whereas electronic detection systems are only concerned with total energy, there is now a strong dependence on pulse shape and intensity. These new challenges are accentuated as the number of nodes on the network increases. In Subsection A, we will discuss how this ADM demonstration overcomes some of the challenges of multiple user access to the network. Subsection B contains further discussion regarding the extension of this ADM to higher packet rates.

A. Multi-user Access to Network

The results of the looped-back ADM show the potential of this access node to overcome system degradations caused by timing jitter and varying pulse characteristics of incoming packets from a multi-node network. The self-synchronization unit is tolerant to inter-packet jitter, which may occur as different nodes at different locations attempt to access the same network. Uneven input levels require the bias of the SOA to be set low enough to accept the low signals. All the higher level signals should be clamped by the SOA gain. Because the packets are from different sources and propagate through different paths, the NOLM logic gate must be tolerant to the different pulse qualities. The header processor has been shown to operate on individual packets independent of the packet source. The timing windows of the header processor and demultiplexer compensate for bit-to-bit jitter within each packet.

After the header processor, it is also necessary to set the bias of the energy detector to distinguish between the matched and unmatched cases for all input packets. Additionally, the threshold level must be set to tolerate output signal fluctuations, which may be as high as ±15% due to interference between the logic gate control leakage and the output signal. This interference may be reduced by increasing the extinction ratio of the logic gate.

B. Extension to Higher Packet Rate

One major challenge to increasing this demonstration to longer and more closely spaced packets is in achieving the power levels within the node that are needed to switch the logic gates. The work with high-nonlinearity fiber in the demultiplexer implies that specialty fibers can be used to lower the switching energy and thus, the power requirements for the node. At a pulse energy of 1pJ/pulse and a bit rate of 100Gb/s, the average power necessary from an amplifier is on the order of 100mW, which is well within the range of commercially available amplifiers. This will help lower the levels of ASE and minimize pulse distortions through amplifiers.

Another source of degradation is from the amplifiers for the data packets. Both ASE and breakup of the pulse due to the necessarily high amplification levels cause degradation of the signal to noise ratio. Dispersive waves and ASE background accumulate after several amplifiers. We currently use short-length, high-gain, erbium-doped fiber amplifiers as well as spectral filters to minimize the ASE and reshape the spectrum of the pulses. For the future, there has been promising technological advances in the area of large-area-fiber amplifiers, which aim to minimize nonlinear pulse distortions by lowering the peak intensity within the fiber [23].

VIII. Conclusion

A. Integration Results

In conclusion, the main functions of an all-optical packet TDM access node in a looped-back configuration have been demonstrated. This emulates a ring network with at least one other node and is the simplest sequential circuit using the access nodes. The add function involves generating a new packet, which is switched onto the network when an incoming packet is removed. Erbium-doped fiber lasers followed by fixed word encoders are used to generate new packets. The drop function requires address checking in the header processor with a synchronized local source, routing of the incoming packet either to the local node or to the network, and demultiplexing of the packet payload. The contrast ratio for dropping a packet from the network with a $LiNbO_3$ modulator is 17dB. The payload of the dropped packet is demultiplexed by a 2λ-NOLM with a 20dB contrast ratio. The system is not severely degraded by inter-packet jitter, which is compensated for by the self-synchronization unit, or by inter-bit jitter, which is absorbed by the timing windows of the NOLMs. This demonstration shows that the ADM is capable of being cascaded to form a high-speed multi-node ring network because of its ability to process and route data packets all-optically.

We find that the necessary high power levels make the system difficult to set up and maintain. ASE and pulse distortions through high-powered amplifiers degrade the signal to noise ratio. The use of bandpass filters as well as high-powered, short-length, amplifiers help to eliminate some of the background noise. Energy detectors are carefully set to distinguish between different cases since background noise not only raises the '0' levels, but also gives fluctuations to the '1' levels through interference. For the future, the use of high-nonlinearity fibers and new amplifier technologies show great promise in lowering switching energies and providing undistorted amplification. By lowering the energy requirements and improving the amplification process, extension of the system to higher packet rates will be possible.

B. Statistical Performance Analysis

A method of statistically determining the Q-value of a 100Gb/s system has been presented. As an example, we look at the output of two cascaded low-bi NOLM logic gates. We determined the Q-value to be 7.1 with a confidence level of 95%. This corresponds to a bit error rate range from 4.8×10^{-14} to 8.8×10^{-12}. The main source of Q-value degradation is from the leakage of the signals, which raises the levels of the '0's. This method can also be applied to other high-speed optical devices as well as the entire node for monitoring of the system performance.

C. Key Enabling Components

The self-synchronization unit extracts the first pulse from the incoming packet to generate an automatically synchronized local source. An SOA acts as a fast-saturation/slow-recovery element, which imposes an intensity differential across an incoming packet. Then, a 40:60 unbalanced NOLM and polarizer act as an intensity discriminator to extract the highest intensity pulse (the first pulse) and reject the lower intensity pulses. The contrast ratio of the first pulse to the rest of the packet is >20dB. With input pulse energies of 2pJ and a current of

50mA for the SOA, the overall unit has an insertion gain of 6.5dB for the first pulse. The output pulses are nearly transform-limited ($\Delta\tau\Delta\nu$~0.34) with a slight shift in the center wavelength.

Packet-by-packet header processing is achieved with a low-bi NOLM logic gate (contrast ratio 10dB). A birefringence of $\Delta n \sim 3x10^{-6}$ is achieved by wrapping fiber with low background birefringence on aluminum mandrels. The walk-off between the control and signal polarizations is determined by the birefringence of the fiber. We demonstrate the header processing unit and the cascadability and Boolean completeness of the logic gates by testing an inverter gate and an XOR gate, cascaded together. The timing windows for the gates are ~5ps for 2ps pulses. The polarization extinction ratio is at least 40:1. Nonlinear transmission of 50% is achieved for a switching energy of 10pJ/pulse.

On the other hand, the switching energy is only 0.8 pJ/pulse for 90% nonlinear transmission due to the 1.65km of high-nonlinearity fiber in the 2λ-NOLM demultiplexer. The high-nonlinearity fiber has an effective nonlinearity of ~4.5 times that of normal dispersion-shifted fiber. The 2λ-NOLM has a switching window of ~5.5ps for 2ps pulses and a contrast ratio of 20dB. In this case, the walk-off between the control and signal wavelengths is due to the group velocity dispersion of the fiber.

The local transmitter is an Er/Yb co-doped linear cavity fiber laser, modified by an AOM and grating, followed by a 100Gb/s fixed word encoder. A phase-lock-loop provides the error signal between the local laser and the incoming packet rate. The error signal is used to drive the AOM, which deflects the first order beam accordingly. The first order beam is reflected by the grating and forms one end of the laser cavity. Thus, the deflection by the AOM changes the overall cavity length. The zeroth order beam is used as the output of the laser source. By using the 25^{th} harmonic of the fundamental packet repetition rate frequencies, we can extract the phase noise between the two lasers and synchronize to a timing jitter of ~1ps. The fixed word encoders are formed by splitting the laser pulse using a 1x4 coupler, time delaying each pulse with respect to the others by propagating through different lengths of fiber, and then recombining the pulses using a 4x1 coupler.

IX. Acknowledgements

This work is supported by DARPA and DOD.

References

1. L. P. Barry, P. Guignard, J. Debeau, R. Boittin, and M. Bernard, "A High-Speed Optical Star Network Using TDMA and All-Optical Demultiplexing Techniques," IEEE J. Select. Areas in Commun. 14, 1030-1038 (1996).
2. V. W. S. Chan, K. L. Hall, E. Modiano, and K. A. Rauschenbach, "Architectures and Technologies for High-Speed Optical Data Networks," J. Lightwave Technol. 16, 2146-2168 (1998); R. A. Barry, V. W. S. Chan, K. L. Hall, E. S. Kintzer, J. D. Moores, K. A. Rauschenbach, E. A. Swanson, L. E. Adams, C. R. Doerr, S. G. Finn, H. A. Haus, E. P. Ippen, W. S. Wong, and M. Haner, "All-Optical Network Consortium – Ultrafast TDM Networks," IEEE J. Select. Areas in Commun. 14, 999-1013 (1996).
3. K. L. Hall and K. A. Rauschenbach, "100-Gbit/s bitwise logic," Opt. Lett. 23, 1271-1273 (1998).
4. N. S. Patel, K. L. Hall, and K. A. Rauschenbach, "Optical Rate Conversion for High-Speed TDM Networks," IEEE Photon. Technol. Lett. 9, 1277-1279 (1997).
5. P. Toliver, I. Glesk, R. J. Runser, K.-L. Deng, B. Y. Yu, and P. R. Prucnal, "Routing of 100 Gb/s Words in a Packet-Switched Optical Networking Demonstration (POND) Node," J. Lightwave Technol. 16, 2169-2180 (1998); S.-W. Seo, K. Bergman, and P. R. Prucnal, "Transparent Optical Networks with Time-Division Multiplexing," IEEE J. Select. Areas in Commun. 14, 1039-1051 (1996).
6. B. Y. Yu, R. Runser, P. Toliver, K.-L. Deng, D. Zhou, T. Chang, S. W. Seo, K. I. Kang, I. Glesk, and P. R. Prucnal, "Network demonstration of 100 Gbit/s optical packet switching with self-routing," Electron. Lett. 33, 1401-1403 (1997).
7. K. S. Jepsen, B. Mikkelson, M. Vaa, H. N. Poulsen, A. T. Clausen, K. E. Stubkjaer, R. Hess, M. Daelk, W. Vogt, E. Gamper, E. Gini, P. A. Besse, H. Melchior, and S. Bouchoule, "Simultaneous all-optical add and drop multiplexing of 40-Gbit/s OTDM signals using monolithically integrated Mach-Zehnder interferometer," Techn. Dig. Opt. Fiber Commun. Conf. 2, 310-311 (1998).
8. I. D. Phillips, A. Gloag, D. G. Moodie, N. J. Doran, I. Bennion, and A. D. Ellis, "Drop and Insert Multiplexing with Simultaneous Clock Recovery Using an Electroabsorption Modulator," IEEE Photon. Technol. Lett. 10, 291-293 (1998).
9. D. Cotter, J. K. Lucek, M. Shabeer, K. Smith, D. C. Rogers, D. Nesset, and P. Gunning, "Self-routing of 100 Gbit/s packets using 6 bit 'keyword' address recognition," Electron. Lett. 31, 2201-2202 (1995).
10. D. Nesset, M. C. Tatham, L. D. Westbrook, and D. Cotter, "Degenerate wavelength operation of an ultrafast all-optical ADD gate using four wave mixing in a semiconductor laser amplifier," Electron. Lett. 30, 1938-1940 (1994).
11. O. Kamatani, Y. Katagiri, and S. Kawanishi, "100-Gbit/s optical TDM add/drop multiplexer based on photonic downconversion and four-wave mixing," Techn. Dig. Opt. Fiber Commun. Conf. 2, 112-113 (1998).
12. T. J. Xia, Y. Liang, K. H. Ahn, J. W. Lou, O. Boyraz, Y.-H. Kao, X. D. Cao, S. Chaikamnerd, J. K. Andersen, and M. N. Islam, "All-Optical Packet-Drop Demonstration Using 100-Gb/s Words by Integrating Fiber-Based Components," IEEE Photon. Technol. Lett. 10, 153-155 (1998).
13. T. J. Xia, Y.-H. Kao, Y. Liang, J. W. Lou, K. H. Ahn, O. Boyraz, A. A. Said, and M. N. Islam, "Novel Self-Synchronization Scheme for High-Speed Packet TDM Networks," IEEE Photon. Technol. Lett. 11, 269-271 (1999).

14. K. H. Ahn, X. D. Cao, Y. Liang, B. C. Barnett, S. Chaikamnerd, and M. N. Islam, "Cascadability and Functionality of All-Optical Low-Birefringent Nonlinear Optical Loop Mirror: Experimental Demonstration," J. Opt. Soc. Amer. B 14, 1228-1236 (1997).
15. M. Jiang, K. H. Ahn, X.-D. Cao, P. Dasika, Y. Liang, M. N. Islam, A. F. Evans, R. M. Hawk, D. A. Nolan, and D. L. Weidman, "Synchronization of Passively Mode-Locked Erbium-Doped Fiber Lasers and its Application to Optical Communication Networks," J. Lightwave Technol. 15, 2020-2028 (1997).
16. T. Kanada and D. L. Franzen, "Single-mode fiber dispersion measurements using a mode-locked laser diode," Opt. Lett. 11, 4-6 (1986).
17. H. Takara, S. Kawanishi, and M. Saruwatari, "Optical signal eye diagram measurement with subpicosecond resolution using optical sampling," Electron. Lett. 32, 1399-1400 (1996).
18. K. H. Ahn, J. W. Lou, Y. Liang, O. Boyraz, T. J. Xia, Y.-H. Kao, and M. N. Islam, "System Performance Measurements for an All-Optical Header Processor Using 100-Gb/s Packets," IEEE Photon. Technol. Lett. 11, 140-142 (1999).
19. G. P. Agrawal, *Fiber-Optic Communication Systems*, New York: Wiley, 1992.
20. R. M. Bethea, B. S. Duran, and T. L. Boullion, *Statistical Methods for Engineers and Scientists*, New York: Marcel Dekker, 1995.
21. G. P. Agrawal and N. A. Olsson, "Self-Phase Modulation and Spectral Broadening of Optical Pulses in Semiconductor Laser Amplifiers," IEEE J. Quantum Electron. 25, 2297-2306 (1989).
22. K. L. Hall, G. Lenz, A. M. Darwish, and E. P. Ippen, "Subpicosecond gain and index nonlinearities in InGaAsP diode lasers," Opt. Commun. 111, 589-612 (1994).
23. M. E. Fermann, A. Galvanauskas, D. Harter, J. D. Minelly, and J. E. Caplen, "High-power single-mode fiber amplifiers using multimode fibers," Techn. Dig. Optical Fiber Commun. Conf. 2, 39-40 (1998).

Figure Captions

Figure 1. Schematic of slotted-TDM metropolitan area ring network. ADM = add/drop multiplexer.

Figure 2. Schematic diagram of looped-back node. A self-synchronization unit generates the local clock sources used by the header processor, and the synchronized local pulse source used by the demultiplexer. The header processor checks the addresses of the incoming packets and determines the direction of the routing. The demultiplexer is used to read the data in the packet. A synchronizer at the packet repetition rate is used to synchronize the local transmitter (new packet generator) to the network. The back-to-the-network port is looped back to the input.

Figure 3. Experimental setup of access node. EDFL = erbium-doped fiber laser, NOLM = nonlinear optical loop mirror, SOA = semiconductor optical amplifier, PLL = phase-locked-loop, XOR = exclusive-OR, SPM = self-phase modulation, AOM = acousto-optic modulator. Fixed word encoders create 100Gb/s-word packets from EDFLs. The NOLM logic gate performs an XOR function to compare the addresses of the incoming packets and the output triggers the packet router. The 2-wavelength (2λ) NOLM demultiplexes the individual bits in the packet payload.

Figure 4. Digital scope traces of the control signal to the packet router for different address packets. In order to switch the packet router, a 6V control signal is needed to drive the modulator. (a) Control signal to modulator when encoder #2 has a matching address and encoder #1 does not have a matching address. (b) Control signal to modulator when encoder #1 has a matching address and encoder #2 does not have a matching address.

Figure 5. Cross correlation of packets at the back-to-the-network port immediately after the $LiNbO_3$ packet router. Depending on the output of the header processor, an incoming packet may be routed back to the network or dropped to the demultiplexer. A new packet may also be added when the incoming packet is dropped. (a) Packet is passed-through (back to the network). (b) Packet is dropped with 17dB contrast ratio. (c) New packet is added when incoming packet is dropped off the network.

Figure 6. Cross correlations of incoming packets and demultiplexed bits from the payload at the output of the demultiplexer. The pump leakage, which can be seen as residue in the '0' bit positions, may be attenuated with a bandpass filter. Contrast ratio is >20dB between the demultiplexed '1's and '0's. (a) Incoming packet from encoder #1. (b)-(d) Demultiplexed payload of encoder #1. (e) Incoming packet from encoder #2. (f)-(h) Demultiplexed payload from encoder #2.

Figure 7. Experimental setup of Q-analysis technique. The master laser passes through the encoder producing '0001011100', and the slave laser passes through clock producing '111'. The output of the header processor, consisting of two NOLMs, is sent to cross correlator 1 for measuring the eye diagram. Cross correlator 2 is used for environmental drift control. PLL = phase-locked-loop, NOLM = nonlinear optical loop mirror, AOM = acousto-optic modulator, EDFA = erbium-doped fiber amplifier, PBS = polarization beam splitter.

Figure 8. Eye diagram of header processor. This is the trace of the eye diagrams taken with the setup of Fig. 7 where the trace is taken by moving an optical delay stage in cross correlator 1. It is an overlay of all the different possible combinations of the 3-bit incoming header and the two possible values of '0' or '1' for the local bit.

Figure 9. Schematic diagram of the self-synchronization scheme. It contains two elements: Fast-saturation/slow-recovery gain element and intensity discriminator. G_0 = unsaturated gain.

Figure 10. Experimental setup for self-synchronization. A semiconductor optical amplifier (SOA) is used as the fast-saturation/slow-recovery gain element. The intensity discriminator is a 40:60 unbalanced nonlinear optical loop mirror (NOLM). EDFL = erbium-doped fiber laser, PC = polarization controller, P = polarizer, DSF = dispersion-shifted fiber, EDFA = erbium-doped fiber amplifier.

Figure 11. Cross correlation results of the self-synchronization scheme. (a) Input data packet. (b) Output data packet from the SOA. (c) Extracted single pulse from the unbalanced loop mirror intensity discriminator. The extracted single pulse has a >20dB contrast ratio to the rest of the bits in the input packet.

Figure 12. (a) Auto-correlation and (b) spectra of the extracted pulse from the self-synchronization unit. There is minimal pulse distortion and the slight wavelength shift is due to gain dispersion in the semiconductor optical amplifier.

Figure 13. Experimental setup for demonstration of two cascaded logic gates. EDFL = erbium-doped fiber laser, PLL = phase-locked-loop, EDFA = erbium-doped fiber amplifier, LOW-BI NOLM = low-birefringence nonlinear optical loop mirror.

Figure 14. Cross correlation results of the header processor. (a) Input data packet. (b) Output of the inverter. (c) Output at the XOR gate when the headers match. (d) Output at the XOR gate when the headers do not match (the inverted incoming header is '010' and the local header is '100').

Figure 15. Experimental setup for 2λ-NOLM demonstration. The high-nonlinearity fiber has a length of 1.64km, λ_0 = 1530.5nm, and nonlinearity about 4.5 times that of normal dispersion-shifted fibers. EDFL = erbium-doped fiber laser. EDFL #1 (λ = 1535nm) and EDFL #2 (λ = 1542nm) are synchronized using a phase-locked-loop (PLL).

Figure 16. (a) Switching timing window 2λ-NOLM measured at 0.8pJ/pulse switching energy. Dots are experimental data, and the solid curve is the simulated result based on the nonlinear Schrödinger equation without inclusion of timing jitter. (b) Nonlinear transmission of the 2λ-NOLM measured as a function of switching energy. At a switching energy of 0.8pJ/pulse, the nonlinear transmission is 90%.

Figure 17. Auto-correlation of the 2λ-NOLM input and output pulses. Note that there is minimal pulse distortion through the device.

Figure 18. Schematic of erbium/ytterbium (Er/Yb) doped fiber laser configuration. The dashed box shows the phase correction setup. WDM = wavelength division multiplexer, SA = saturable absorber, P = polarizer, AOM = acousto-optic modulator.

Figure 19. (a) Power spectra measured at the 10^{th} harmonic of the laser fundamental. (b) Timing jitter of the laser calculated from the power spectra. The "PLL OFF" marks when the laser is free running, and the "PLL ON" marks when the laser is synchronized to an electronic synthesizer.

Figure 20. Schematic diagram of phase error detection. The solid lines refer to optical paths and dotted lines are electronic circuits. LPF = low pass filter. EDFL = erbium-doped fiber laser.

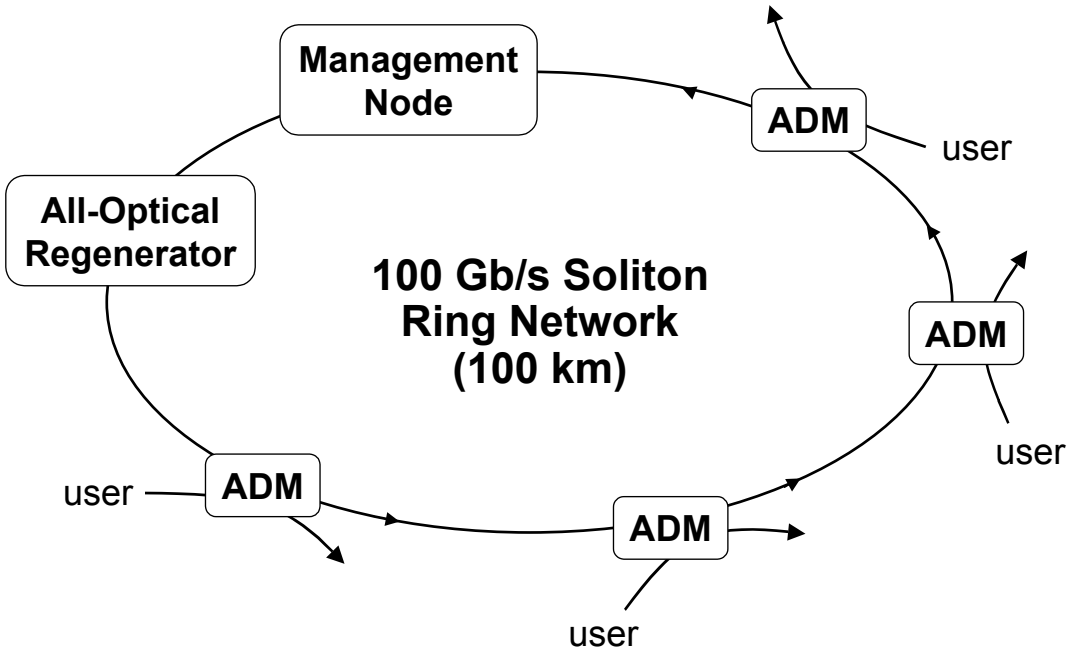
Management Node
ADM
user
All-Optical Regenerator
100 Gb/s Soliton Ring Network (100 km)
ADM
user
user
ADM
ADM
user

Figure 1

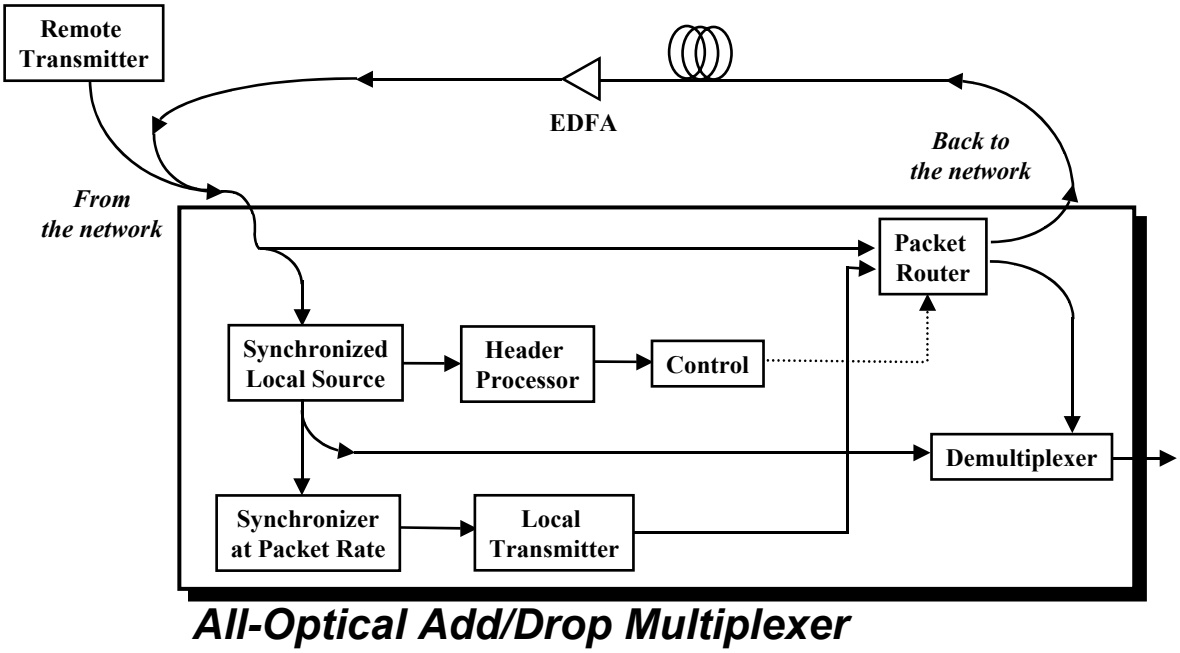
Remote Transmitter
EDFA
Back to the network
From the network
Packet Router
Synchronized Local Source
Header Processor
Control
Demultiplexer
Synchronizer at Packet Rate
Local Transmitter
All-Optical Add/Drop Multiplexer

Figure 2

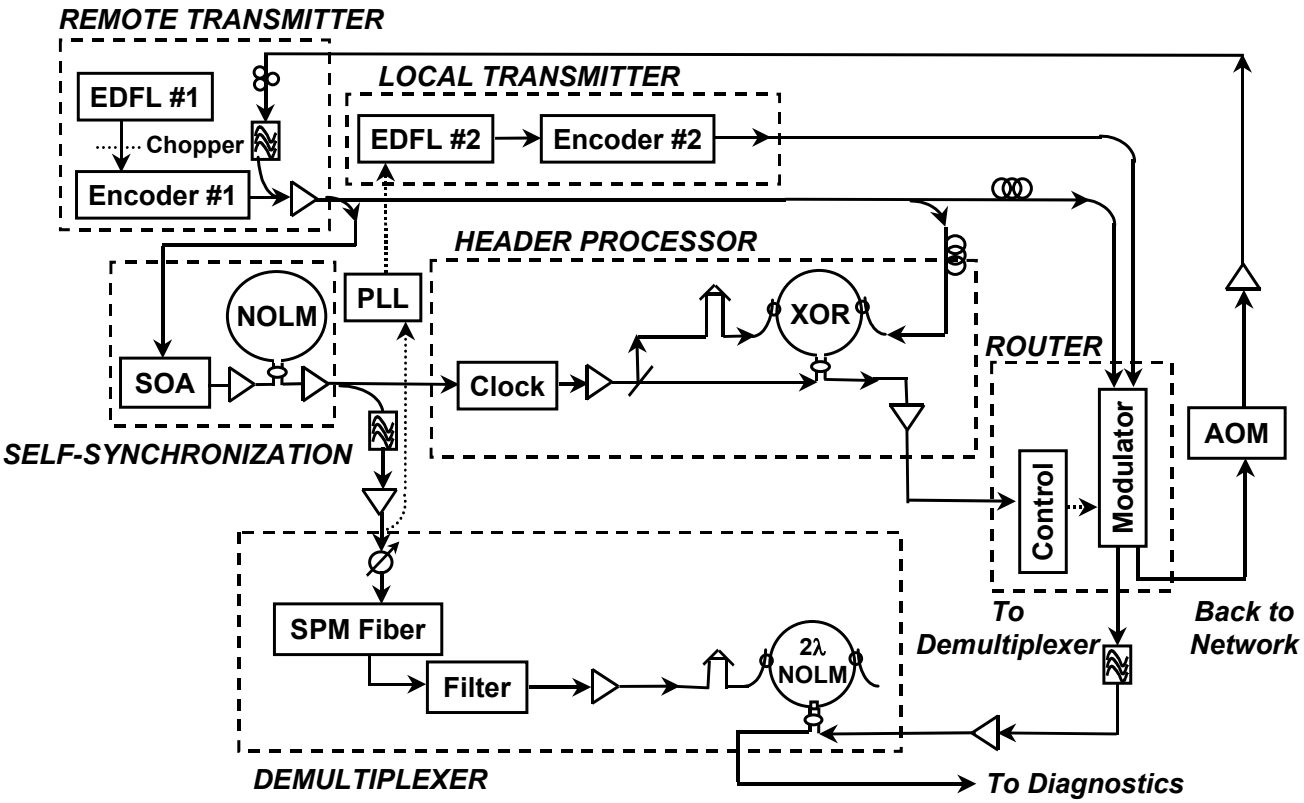
REMOTE TRANSMITTER
EDFL #1
Chopper
Encoder #1
LOCAL TRANSMITTER
EDFL #2
Encoder #2
HEADER PROCESSOR
NOLM
PLL
XOR
SOA
Clock
ROUTER
SELF-SYNCHRONIZATION
Control
Modulator
AOM
SPM Fiber
Filter
2λ
NOLM
To
Demultiplexer
Back to
Network
DEMULTIPLEXER
To Diagnostics

Figure 3

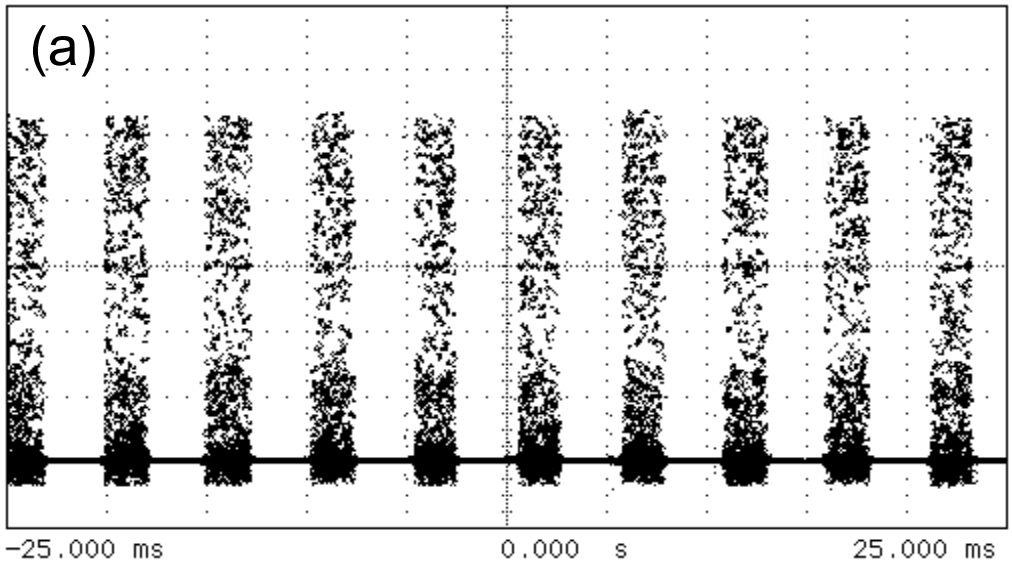

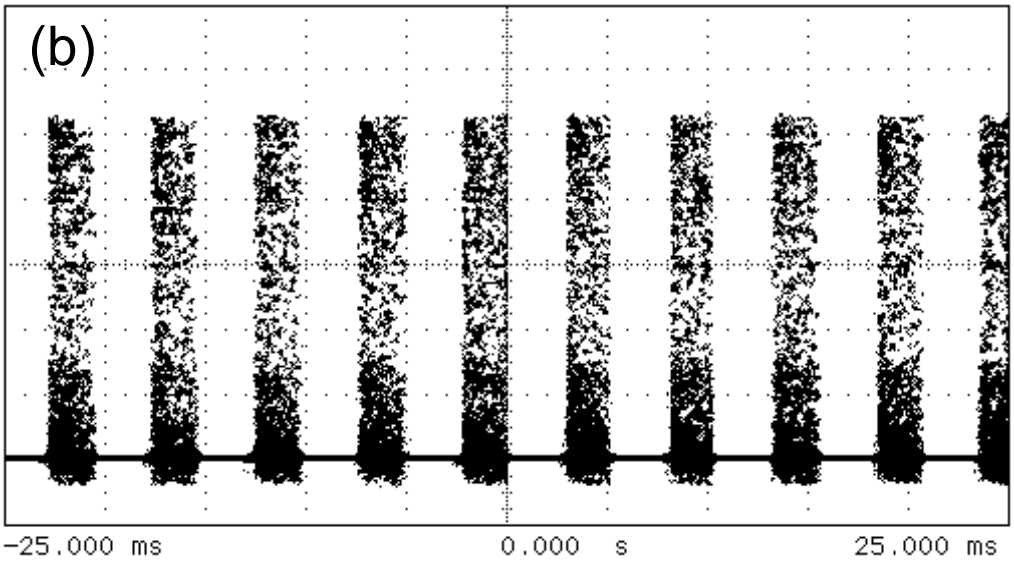

Figure 4

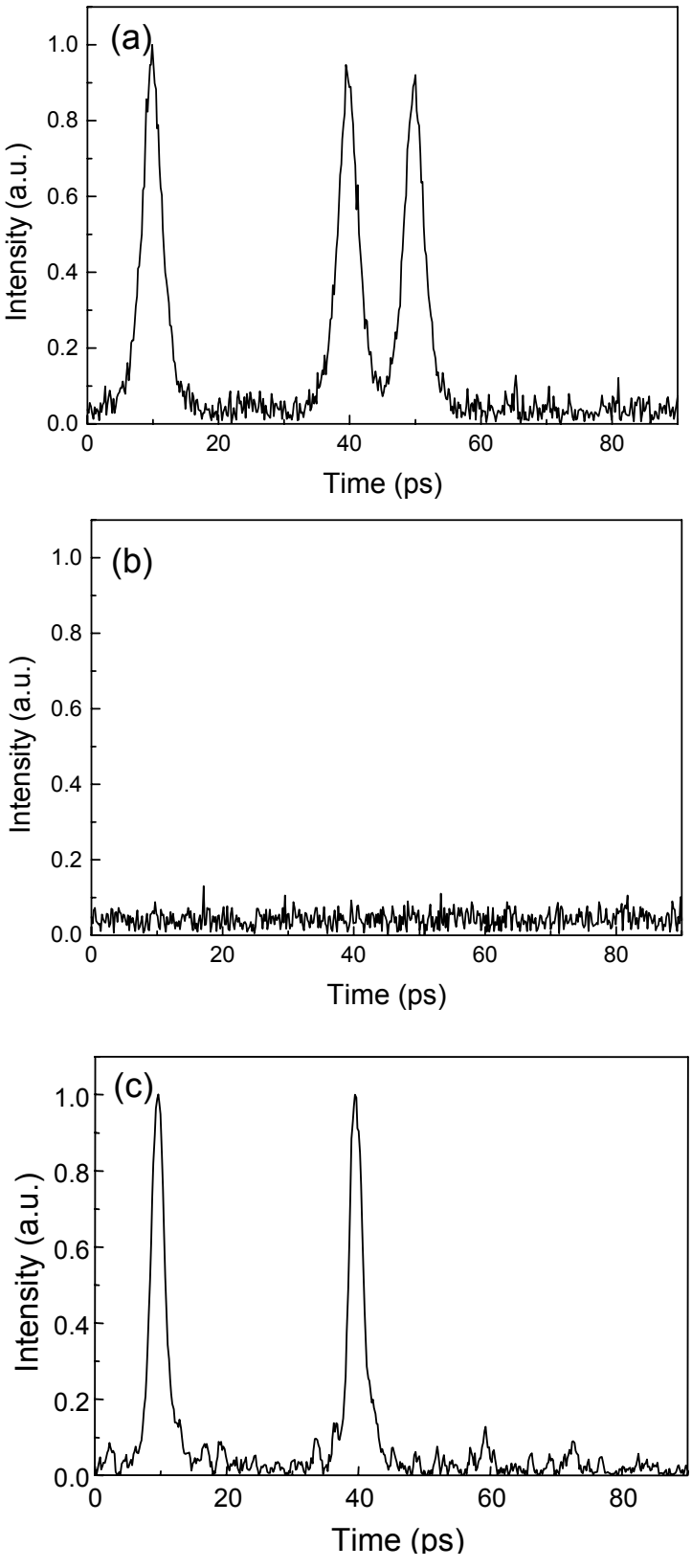
(a)
Intensity (a.u.)
Time (ps)
(b)
Intensity (a.u.)
Time (ps)
(c)
Intensity (a.u.)
Time (ps)

Figure 5

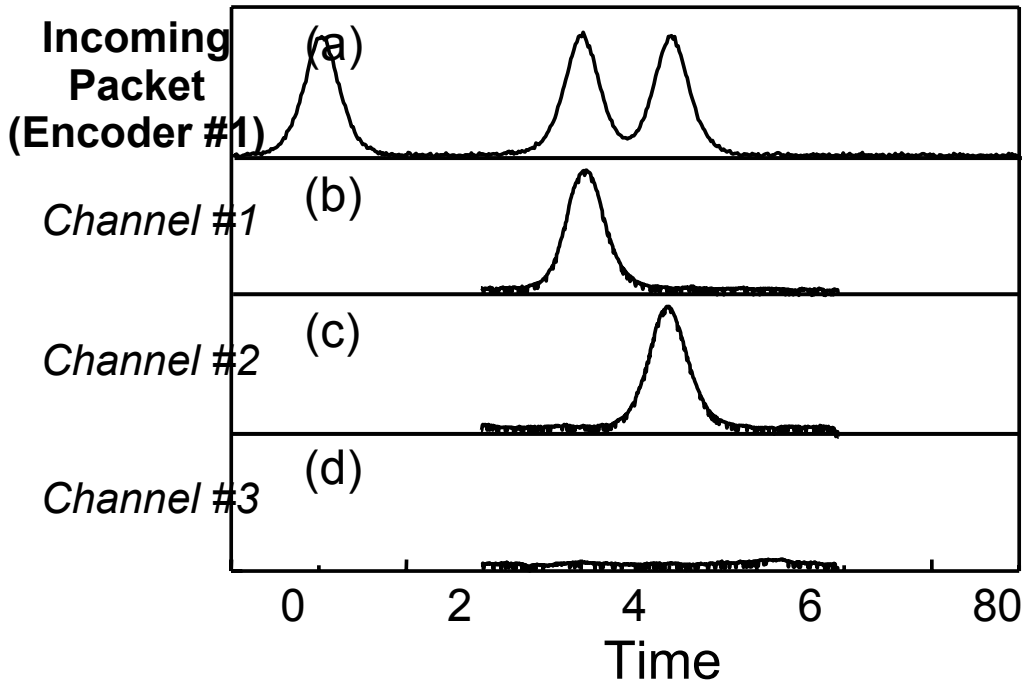
Incoming Packet (Encoder #1)
(a)
Channel #1
(b)
Channel #2
(c)
Channel #3
(d)
0
2
4
6
80
Time

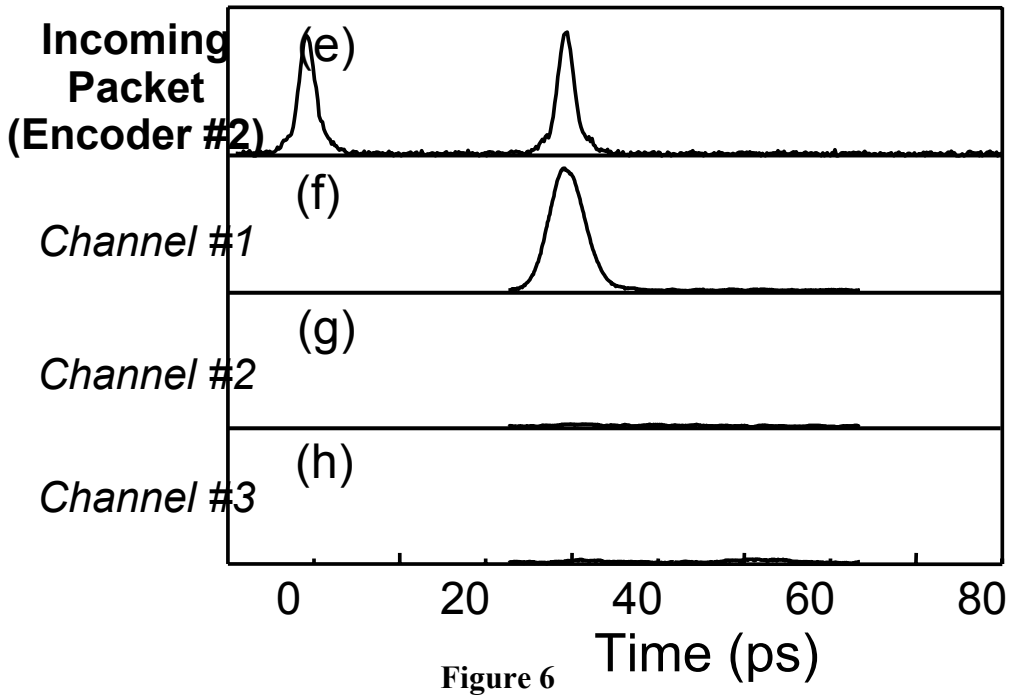
Incoming Packet (Encoder #2)
(e)
(f)
Channel #1
(g)
Channel #2
(h)
Channel #3
0
20
40
60
80
Time (ps)

Figure 6

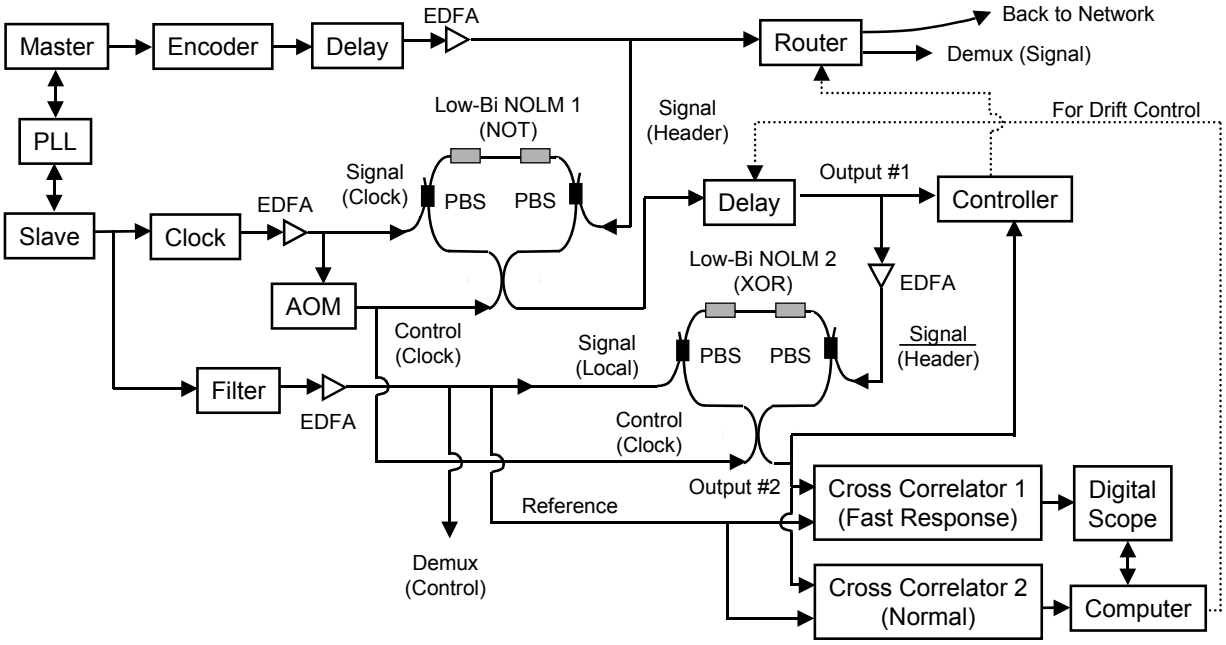
Master
Encoder
Delay
EDFA
Router
Back to Network
Demux (Signal)
PLL
Low-Bi NOLM 1
(NOT)
Signal
(Header)
For Drift Control
Signal
(Clock)
PBS
PBS
Delay
Output #1
Controller
Slave
Clock
EDFA
Low-Bi NOLM 2
(XOR)
AOM
EDFA
Control
(Clock)
Signal
(Local)
PBS
PBS
Signal
(Header)
Filter
EDFA
Control
(Clock)
Output #2
Cross Correlator 1
(Fast Response)
Digital
Scope
Reference
Demux
(Control)
Cross Correlator 2
(Normal)
Computer

Figure 7

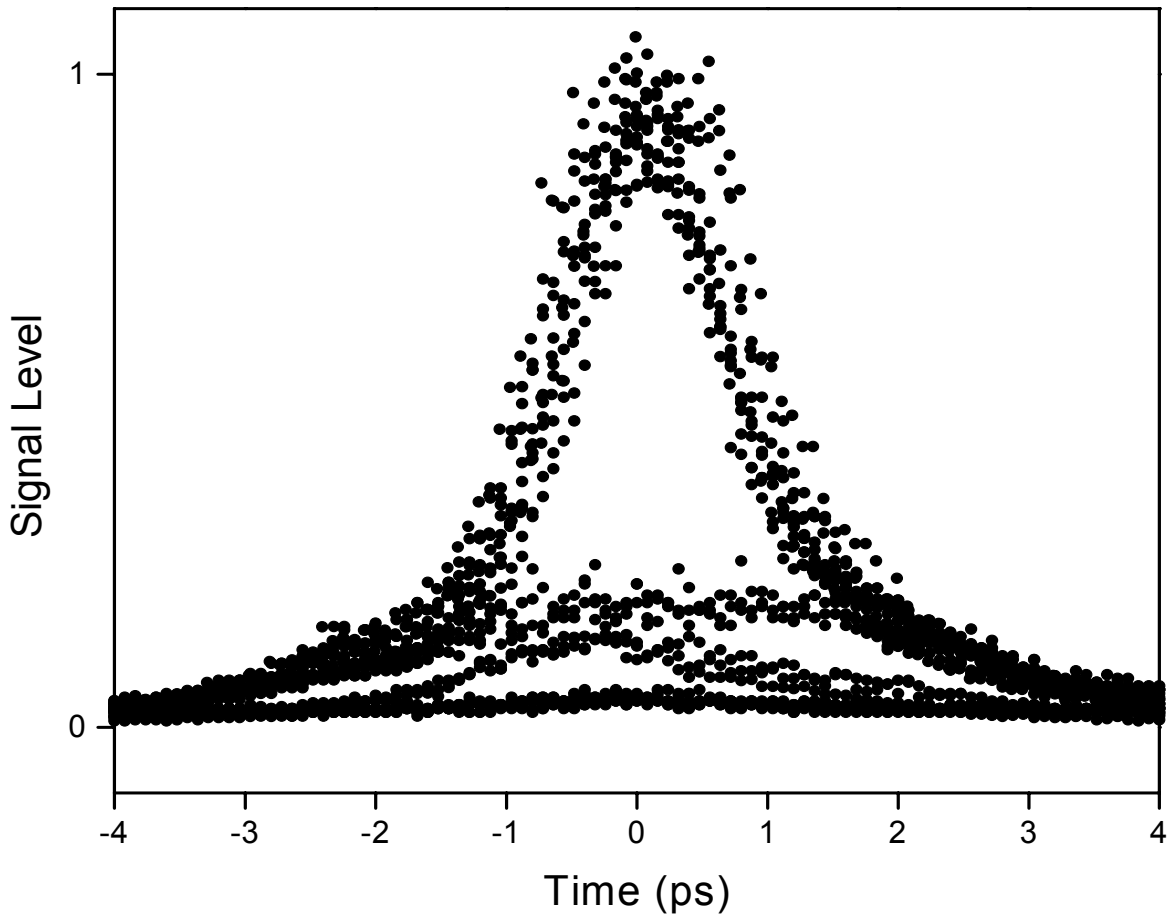

Figure 8

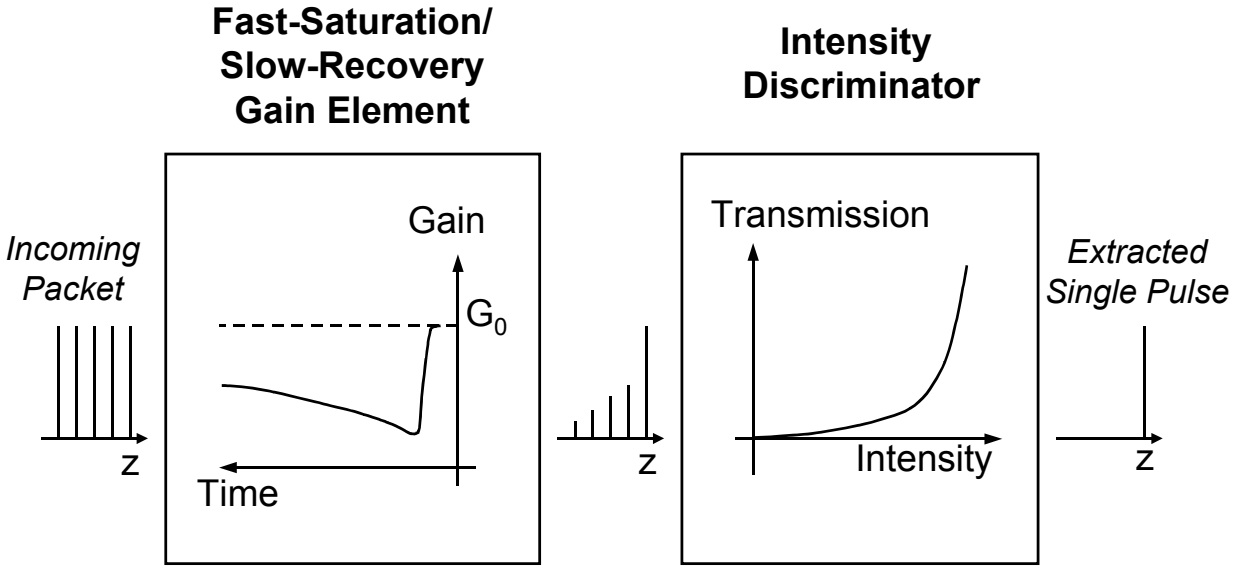
Fast-Saturation/
Slow-Recovery
Gain Element
Intensity
Discriminator
Incoming
Packet
z
Gain
G_0
Time
z
Transmission
Intensity
Extracted
Single Pulse
z

Figure 9

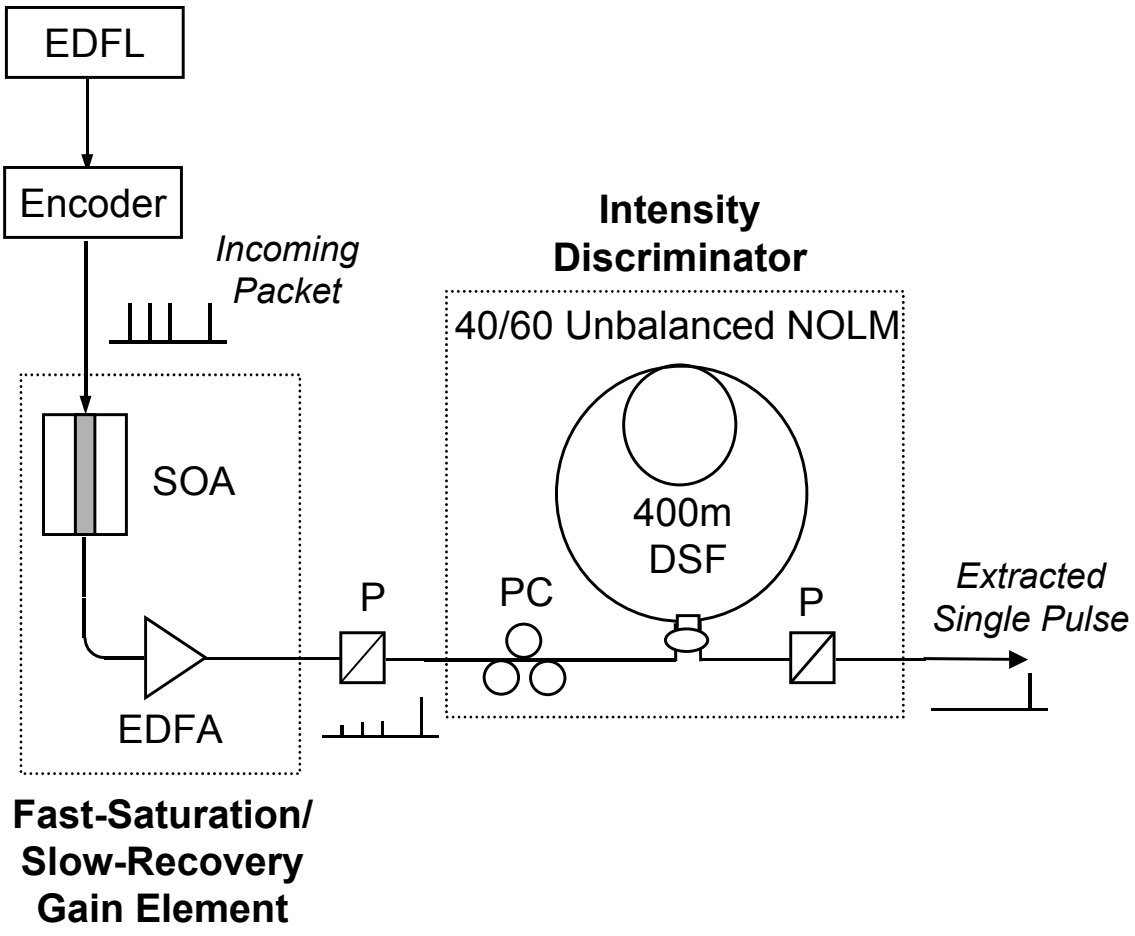
EDFL
Encoder
Incoming
Packet
Intensity
Discriminator
40/60 Unbalanced NOLM
SOA
400m
DSF
P
PC
P
Extracted
Single Pulse
EDFA
Fast-Saturation/
Slow-Recovery
Gain Element

Figure 10

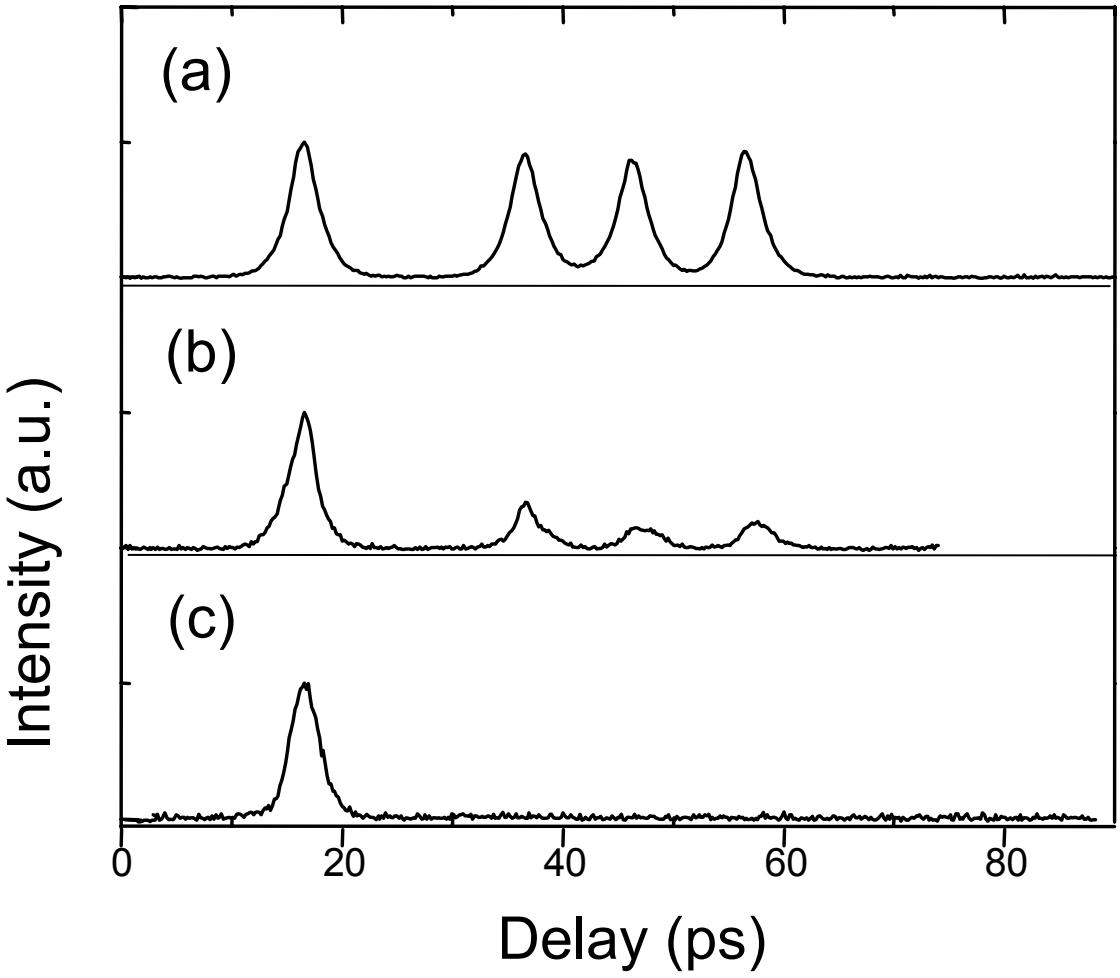

Figure 11

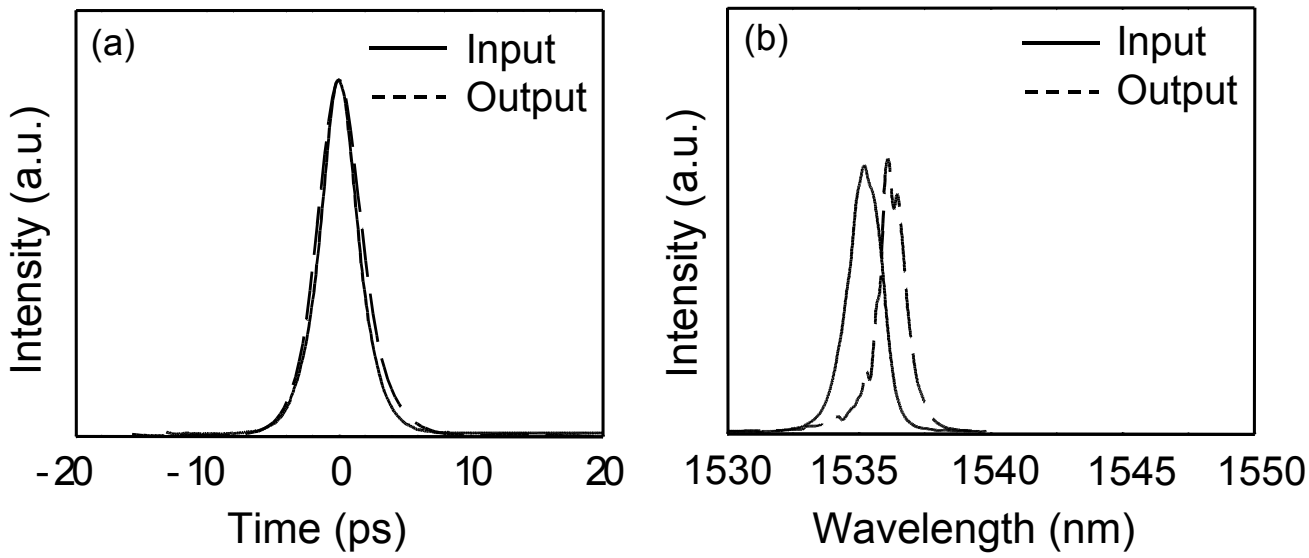
(a)
Input
Output
Intensity (a.u.)
-20
-10
0
10
20
Time (ps)
(b)
Input
Output
Intensity (a.u.)
1530
1535
1540
1545
1550
Wavelength (nm)

Figure 12

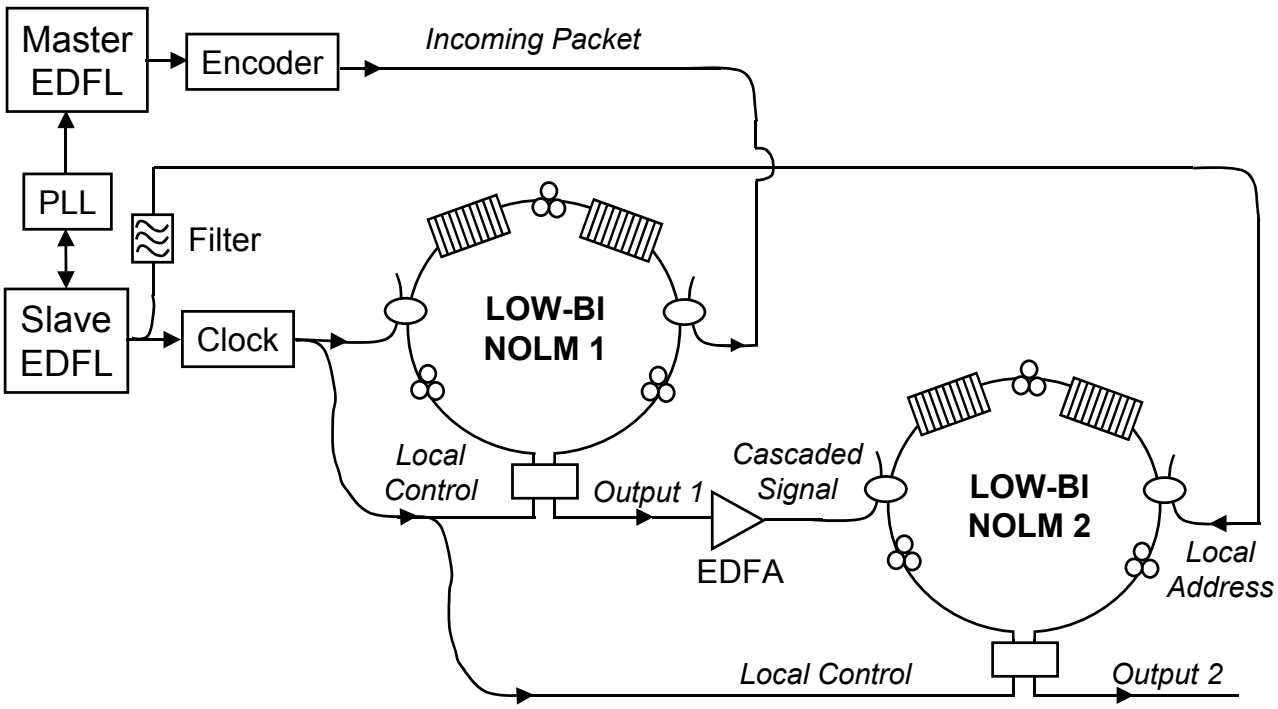
Master EDFL
Encoder
Incoming Packet
PLL
Filter
Slave EDFL
Clock
LOW-BI NOLM 1
Local Control
Output 1
Cascaded Signal
EDFA
LOW-BI NOLM 2
Local Address
Local Control
Output 2

Figure 13

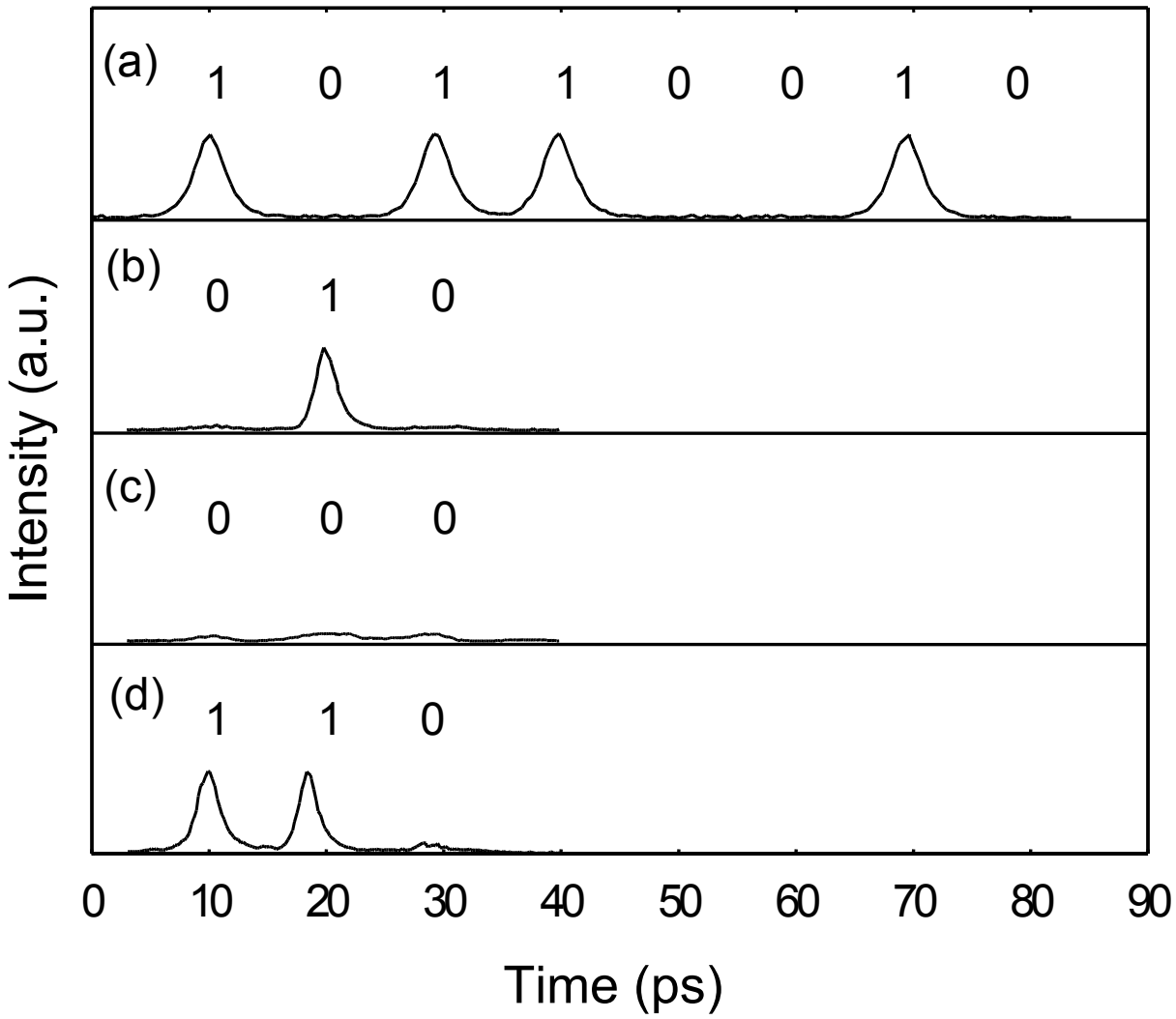
(a)
1 0 1 1 0 0 1 0
(b)
0 1 0
(c)
0 0 0
(d)
1 1 0
Intensity (a.u.)
0 10 20 30 40 50 60 70 80 90
Time (ps)

Figure 14

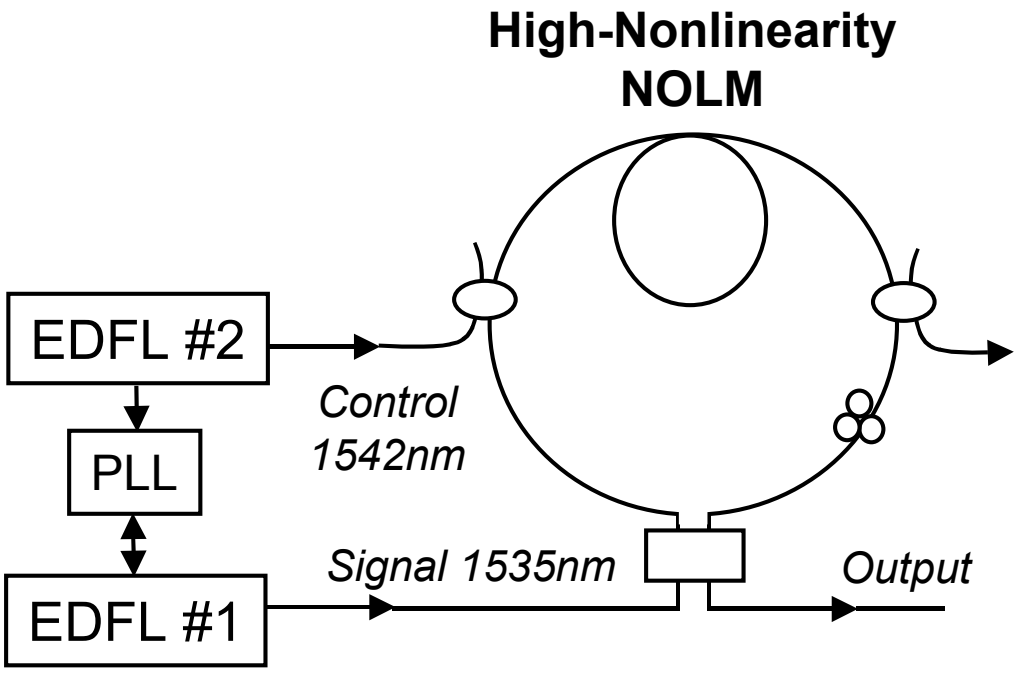
High-Nonlinearity
NOLM
EDFL #2
PLL
EDFL #1
Control
1542nm
Signal 1535nm
Output

Figure 15

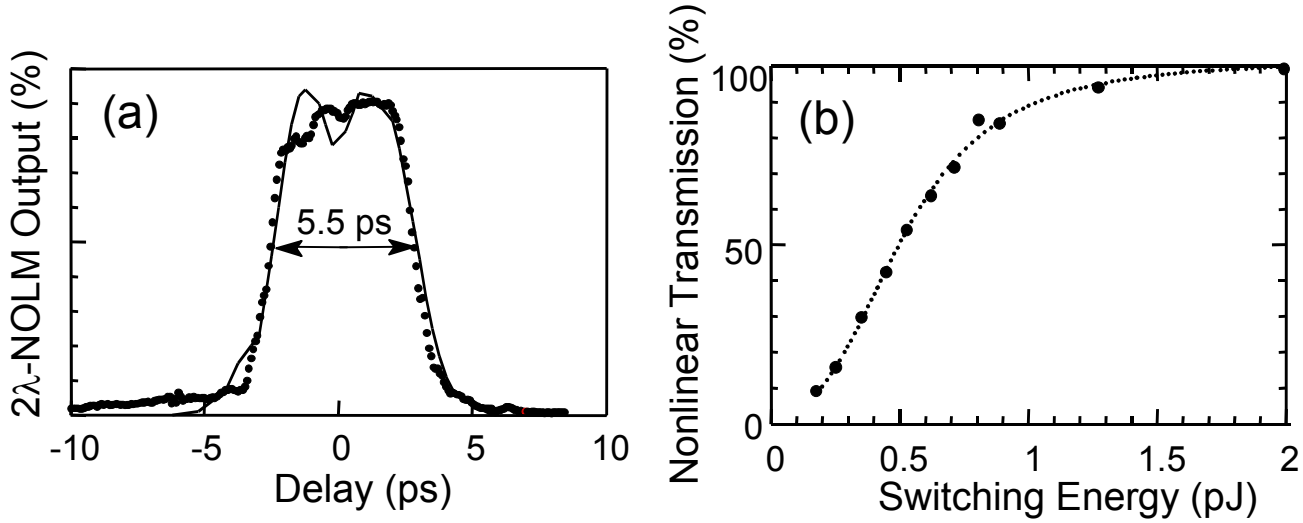
(a)
5.5 ps
2λ-NOLM Output (%)
-10
-5
0
5
10
Delay (ps)
(b)
Nonlinear Transmission (%)
100
50
0
0
0.5
1
1.5
2
Switching Energy (pJ)

Figure 16

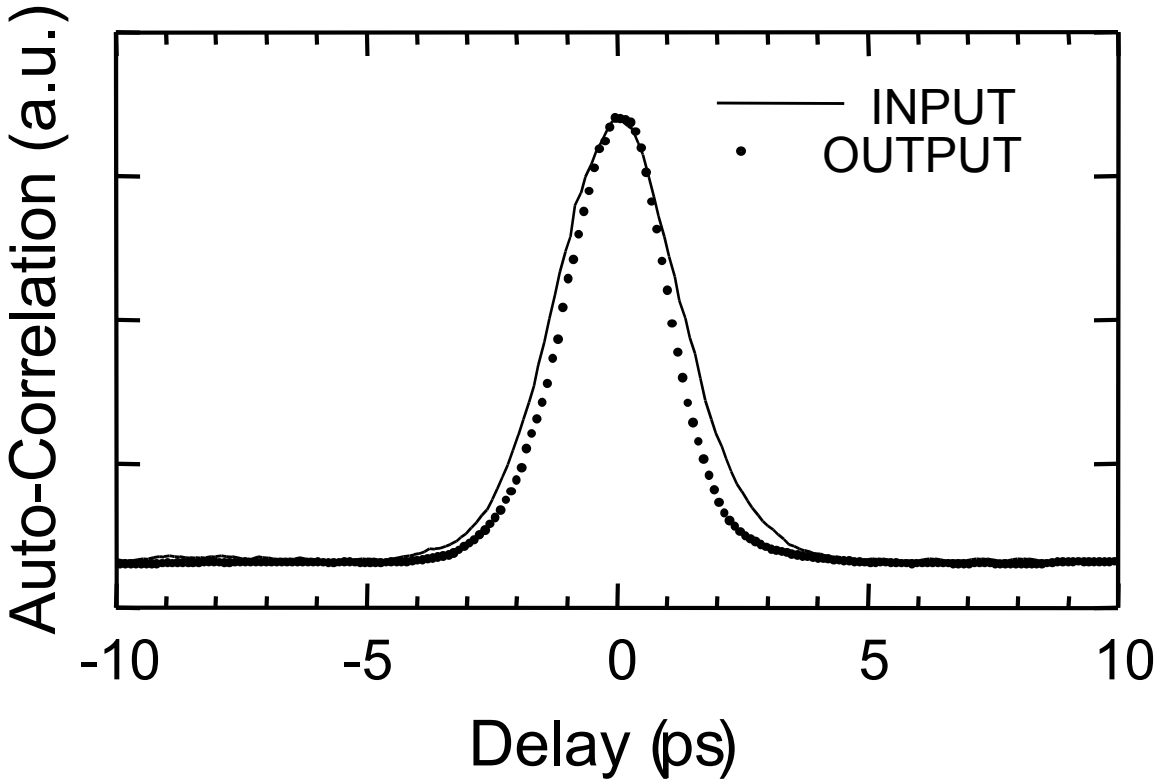

Figure 17

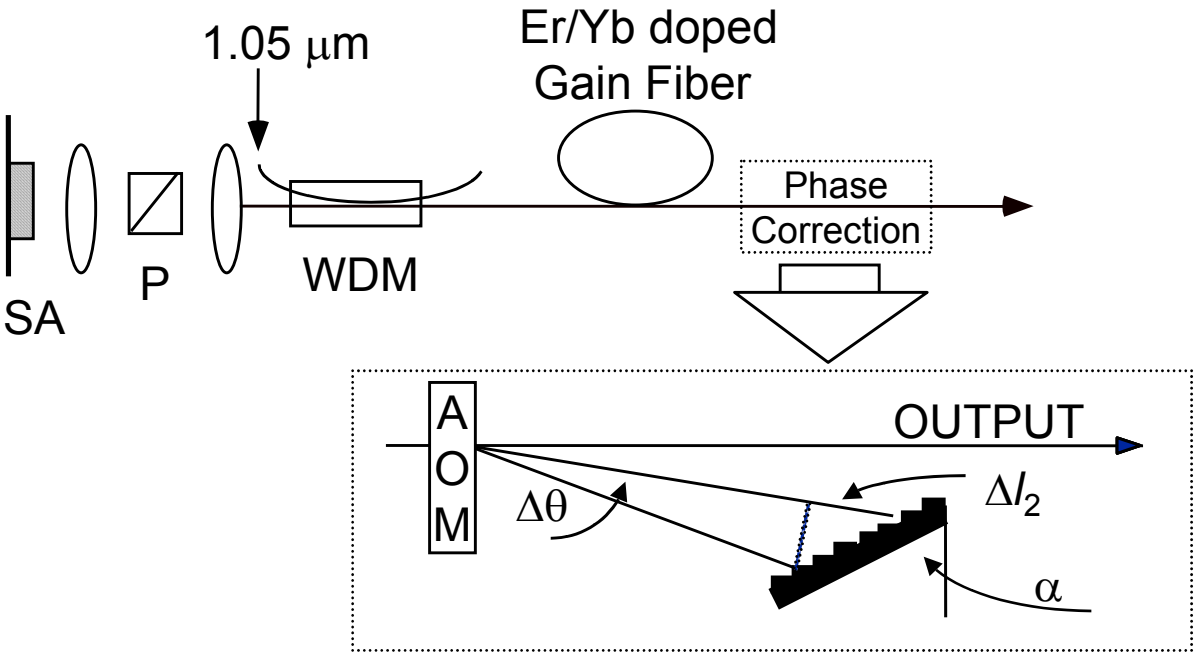
1.05 μm
Er/Yb doped
Gain Fiber
Phase
Correction
SA
P
WDM
A
O
M
OUTPUT
Δθ
Δl2
α

Figure 18

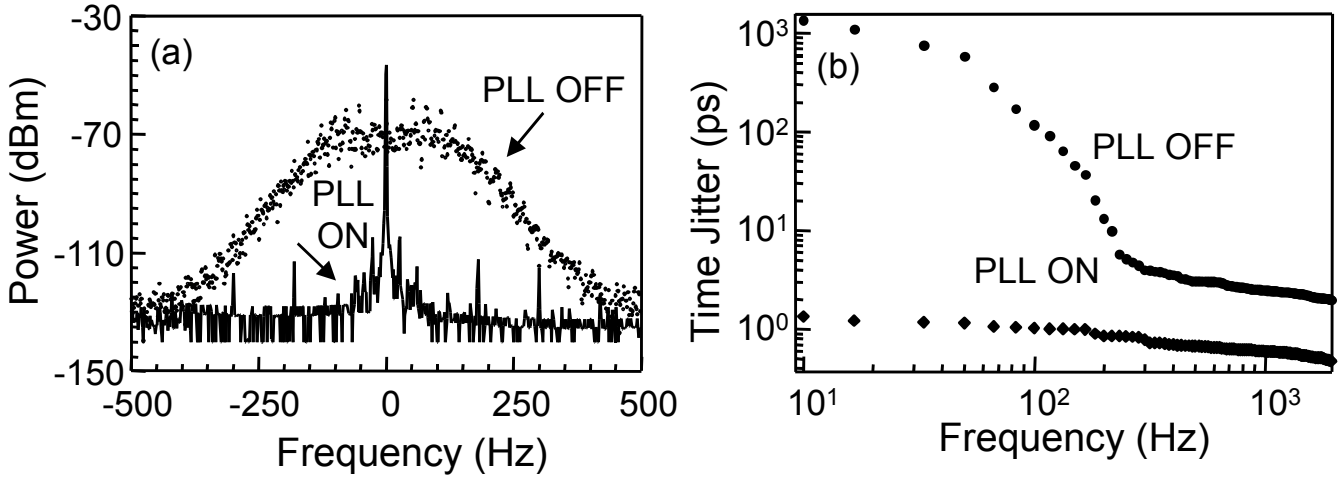
(a)
Power (dBm)
-30
-70
-110
-150
-500
-250
0
250
500
Frequency (Hz)
PLL OFF
PLL
ON
(b)
Time Jitter (ps)
10^3
10^2
10^1
10^0
10^1
10^2
10^3
Frequency (Hz)
PLL OFF
PLL ON

Figure 19

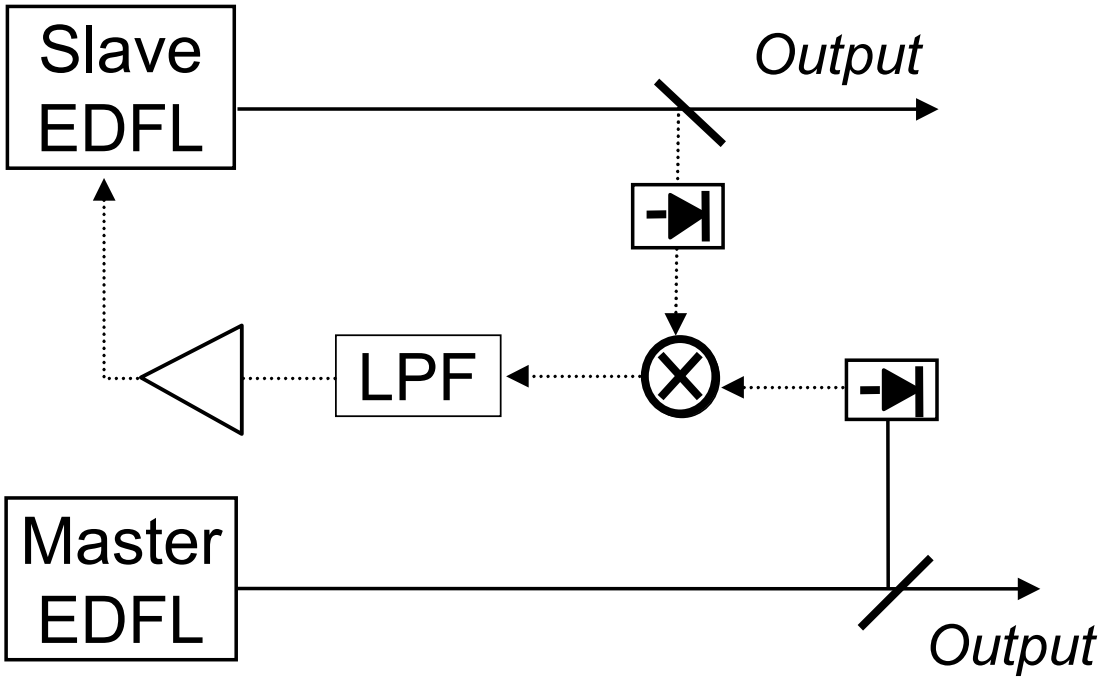

Figure 20

Appendix G

80 Gb/s to 10 Gb/s Polarization-Insensitive Demultiplexing with Circularly Polarized Spun Fiber in a Two-Wavelength Nonlinear Optical Loop Mirror

J. W. Lou*, *Student Member,* **K. S. Jepsen, D. A. Nolan,** *Member*, **S. H. Tarcza, W. J. Bouton, A. F. Evans**
SP-AR-01-2
Science & Technology Division
Corning Incorporated
Corning, NY 14831
*Also with: Electrical Engineering and Computer Science Department
The University of Michigan
Ann Arbor, MI 48109
M. N. Islam, *Senior Member*
Electrical Engineering and Computer Science Department
The University of Michigan
Ann Arbor, MI 48109

Abstract

We demonstrate the first polarization insensitive demultiplexing of 10 Gb/s channels from 80 Gb/s pseudo-random bit streams using a two-wavelength nonlinear optical loop mirror with circularly polarized spun fiber. The polarization sensitivity of the device is reduced to <1dB for >90% transmission, and bit-error-rate measurements show that the remaining polarization sensitivity leads to a power penalty difference of 1.5 dB. The nonlinear transmission is 91% for a switching energy of 4 pJ/pulse, and the full-width-half-maximum timing window is 9.6 ps. The circularly polarized spun fiber has a λ_0 of 1541 nm, a length of ~1 km, and ~4.5 times higher nonlinearity than that of conventional dispersion-shifted fiber. The spin rate is 16 turns/m and the birefringence is $\Delta n \sim 1 \times 10^{-6}$, corresponding to 25 turns/beat length.

Index Terms – demultiplexing, optical fiber communications, optical fibers, optical receivers, optical fiber devices, optical data processing

Introduction

All-optical demultiplexing is necessary to increase the aggregate rate of time-division-multiplexed systems beyond the speed of electronics. We demonstrate a polarization-insensitive (<1 dB for >90% transmission) nonlinear optical loop mirror (NOLM) using high-nonlinearity, circularly-polarized, spun fiber. The residual polarization dependence leads to 1.5dB power penalty in the bit-error-rate (BER) measurements between the maximum- and minimum-output signal input polarizations. The spin rate of the fiber is 16 turns/m and the birefringence is $\Delta n \sim 1 \times 10^{-6}$, corresponding to ~25 turns/beat length. Since the spin rate is greater than 10 times the beat length, the fiber becomes more circularly polarized, implying that the spun fiber has an intrinsic circular birefringence [1]. The nonlinear phase shift induced by the control wavelength is independent of the input signal polarization in circularly-polarized fiber. In linearly-polarized fiber, the difference in the induced nonlinear phase shift can lead to 5 dB of polarization sensitivity [2]. Thus, the circularly-polarized spun fiber is ideal for reducing the polarization sensitivity of the two-wavelength NOLM.

Several polarization-insensitive NOLM demultiplexers have been demonstrated. A polarization diversity scheme has been used to demultiplex 80 Gb/s bit streams [3,4]. Using a twisted fiber NOLM, demultiplexing from short 100 Gb/s fixed-words has been demonstrated [5]. In contrast to other NOLM demultiplexers, we achieve polarization insensitivity by spinning high-nonlinearity fiber preform at 16 turns/m during the drawing process so that the fiber is intrinsically circularly polarized. The built-in twist of the fiber makes the fiber more rugged and environmentally stable. In addition, the spun fiber NOLM is much simpler to construct than other polarization diversity schemes.

Experimental Setup

Figure 1 shows a block diagram of the experimental setup with the two-wavelength NOLM demultiplexer. The output of a 10 Gb/s pulsed laser source ($\Delta\tau$=1.6ps, $\Delta\lambda$=2.3nm, λ_1=1554nm) is modulated with a 2^{31}-1 pseudo-random bit sequence using a $LiNbO_3$ modulator, driven by a pattern generator. An 80 Gb/s signal source is generated by passively multiplexing the 10 Gb/s modulated output using fiber couplers and delay lines. The output of a continuous-wave source is modulated with a 10 GHz clock, using an electro-absorption modulator, and then compressed through 12.2 km of dispersion-decreasing fiber (D=11.4 to 2 ps/nm/km) to generate the control pulse source (λ_2=1550nm). The control pulses to the NOLM have a pulse width of 7.9 ps and an extinction ratio of 13 dB. The 80 Gb/s signal is coupled into the NOLM through a 50/50 splitter, and the loop is biased to totally reflect the signal in the absence of the control. The 10 GHz control pulses are introduced into the loop through a 3 dB coupler and set to one of the eigenmodes of the fiber to reduce the effect of shadow energy [2]. The output of the NOLM is filtered to remove the control wavelength, amplified, filtered again to remove excess amplified spontaneous emission, and sent to a detector followed by a BER tester.

The high-nonlinearity fiber preform is spun at 16 turns/m during the drawing process to induce a circular birefringence, while reducing the linear birefringence and making the fiber more circularly polarized (*i.e.*, the eigenmodes of the fiber are circular). In linearly polarized fiber, the nonlinear phase shift coefficients due to cross-phase-modulation between the control and signal wavelengths are 2 and 2/3 for parallel and orthogonal polarizations, respectively.

However, in circularly-polarized fiber, the nonlinear phase shift coefficient is 4/3 for all polarizations. Thus, the amount of nonlinear phase shift induced by the control pulses on the signal pulses and, therefore, the nonlinear transmission of the NOLM are independent of the input signal polarization. The ~1 km fiber has λ_0 = 1541nm (D=0.32 ps/nm/km at 1550 nm), ~4.5 times the nonlinearity of conventional dispersion-shifted fiber, and loss of 3.8 dB/km. The measured birefringence is $\Delta n \sim 1 \times 10^{-6}$, which implies a beat length of L_B~1.6 m and a spin rate of ~25 turns/L_B. For a sufficiently high twist rate (>10 turns/L_B), the polarization mode dispersion is reduced and a high degree of polarization is maintained for any input polarization [6].

Polarization-Insensitive Demultiplexing Results

The pre-amplified back-to-back BER as well as the BER of the demultiplexed bits for the maximum- and minimum-output polarizations are shown in Fig. 2. The received power per channel is calculated by measuring the total average power and assuming 8×10Gb/s channels are inputted to the NOLM demultiplexer/receiver. For a BER of 10^{-9}, there is an ~6 dB power penalty for demultiplexing from signals with input polarizations corresponding to the maximum output. However, the BER is degraded by the multiplexer as well as the NOLM demultiplexer and several decibels may be attributable to penalty acquired in multiplexing up to 80 Gb/s. The demultiplexer has a measured full-width-half-maximum timing window of 9.6 ps, but adjacent channels may still have been partially switched out by the tails of the control pulses and degraded the BER. Cross-talk induced by the control pulse on the counter-propagating signal pulses may also have a detrimental effect on the BER [7]. The slight floor in the BER curve of the maximum transmission case is attributed to the instability of the pulse laser source and is not observed for the minimum transmission case. The power penalty is increased by 1.5 dB for the minimum-output case because the signal level into the amplifier after the NOLM is lower and more noise is added. In linearly-polarized fiber, the increase in power penalty for the minimum-output case is at least 5 dB. This is because the nonlinear phase shift coefficients are 2 and 2/3 in linearly-polarized fiber, which leads to a 6 dB difference in the switched out power when the maximum-output case corresponds to a π-phase shift.

The measured nonlinear transmission curves versus the control (switching) power for the maximum- and minimum-output polarizations are shown in Fig. 3(a). Note that the polarization sensitivity is ~1 dB at our 43 mW (4 pJ/pulse after the coupler) operating point where we obtain 91% nonlinear transmission. Beyond ~50 mW, the broadening of the control pulse spectrum due to self-phase-modulation causes significant leakage into the signal pulse bandwidth so that an accurate measurement of the signal transmission could not be obtained. While the high-nonlinearity of the fiber reduces the necessary switching energy, the high loss of the fiber, due to the tail of the water absorption peak at 1380 nm in this prototype fiber, counteracts some of that benefit. Additionally, the ~2 dB splice and connector losses to the fiber also raises the switching energy requirement. However, tapered splices may be used to reduce this loss.

Discussion

Residual polarization dependence implies that the spun fiber is not perfectly circularly-polarized and that the nonlinear phase shift coefficients are not the same for the two orthogonal modes. In an ideal circularly-polarized fiber, there is no polarization dependence in the induced nonlinear phase shift or in the nonlinear transmission. However, in a non-ideal circularly-polarized fiber, the maximum and minimum nonlinear transmissions are sine-squared functions of the maximum and minimum induced phase shifts, respectively. The amount of phase shift is

proportional to the product of the nonlinear phase shift coefficient and the power of the switching pulse [8]. Small differences in the nonlinear phase shift coefficients are reflected as polarization sensitivity, which is dependent on the switching energy. As the fiber deviates from the ideal circularly-polarized fiber, the periodicity of the maximum and minimum transmission curves change. The nonlinear transmission level at which the two curves cross may have a reduced polarization sensitive, but the absolute transmission at that point will be less than 100%.

The expected transmission curves and thus, the corresponding polarization sensitivity can be calculated by assuming a sine-squared transmission function from the NOLM [8]. The polarization sensitivity is defined as $-10*\log(T_{min}/T_{max})$, where T_{min} and T_{max} are the minimum and maximum transmissions, respectively. The expected transmission curves for linearly-polarized fiber and the fits to the measured spun fiber data are shown in Fig. 3(b). Using these transmission curves, we calculate the expected polarization sensitivities for linearly-polarized fiber and for this spun fiber (shown in Fig. 4). The measured polarization sensitivity for this spun fiber is also shown in Fig. 4. Using the fits to the data, we calculate the induced phase shift corresponding to the maximum (ϕ_1) and minimum (ϕ_2) transmissions. We find that $\phi_2/\phi_1=0.8$ for this spun fiber (corresponding to nonlinear phase shift coefficients of 1.45 for ϕ_1 and 1.16 for ϕ_2). The ratio for ideal circularly-polarized fiber is 1 and for linearly-polarized fiber is 0.33. For a given difference in the nonlinear phase shift coefficients, the difference in the nonlinear transmissions varies with the switching energy. The calculated transmission curves for our spun fiber show that the maximum and minimum curves cross at ~97% transmission and that the polarization sensitivity is less than 1 dB over a switching energy variation range of 2 dB for >70% transmission. In contrast, for linearly-polarized fiber, the transmission curves cross at ~50% transmission and the polarization sensitivity is less than 1 dB over a 0.32 dB range (corresponding to 40-60% transmission). The ideal circularly-polarized fiber has only one transmission curve and is polarization insensitive for all transmission levels. The experimentally measured polarization sensitivities at low transmission levels deviate from the calculated expectations because polarization dependent leakage (due to polarization dependent loss in the loop) has a greater effect on the measured transmissions. Thus, in comparison to linearly-polarized fiber for polarization sensitivity <1dB, the spun fiber allows for a 1.68 dB wider switching energy range with nonlinear transmission that is 10-40% higher.

Conclusion

We achieve polarization-insensitive (< 1 dB for > 90% transmission) demultiplexing of 10 Gb/s channels from a fully-populated 8×10 Gb/s 2^{31}-1 pseudo-random bit-stream using a NOLM with ~1 km of high-nonlinearity, circularly-polarized, spun fiber. The spun fiber has a nonlinearity ~4.5 times that of conventional dispersion-shifted fiber and a spin rate of 16 turns/m. The inherent circular birefringence of the spun fiber makes the cross-phase-modulation between the control and signal wavelengths polarization independent. The ratio of the nonlinear phase shift coefficients of the input polarizations corresponding to the maximum and minimum outputs of this spun fiber NOLM is 0.8. For linearly-polarized fiber, this ratio is 0.33. Calculations show that, for polarization sensitivity less than 1 dB, the spun fiber gives 10-40% higher nonlinear transmission and a switching energy variation range that is 1.68 dB wider than linearly-polarized fiber. BER measurements show a 1.5 dB power penalty difference due to the residual polarization dependence. The maximum-output power penalty of ~6 dB is largely due to cross-talk between adjacent channels during the multiplexing stage and control pulse induced cross-talk.

Acknowledgement

This work is supported by DARPA.

References

1. R. Dändliker, "Rotational effects of polarization in optical fibers" in Anisotropic and Nonlinear Optical Waveguides, C.G. Someda and G. Stegeman, ed., Elsevier Science, New York, 1992.
2. Y. Liang, J. W. Lou, J. K. Andersen, J. C. Stocker, O. Boyraz, M. N. Islam, D. A. Nolan, "Polarization-insensitive nonlinear optical loop mirror demultiplexer with twisted fiber", *Opt. Lett.*, vol. 24, no. 11, pp.726-728, 1999.
3. B.-E. Olsson, P. A. Andrekson, "Polarization Independent Demultiplexing in a Polarization Diversity Nonlinear Optical Loop Mirror", *IEEE Photon. Technol. Lett.*, vol. 9, no. 6, pp.764-766, 1997.
4. J. Hansryd, B. Bakhshi, B. E. Olsson, P. A. Andrekson, J. Brentel, E. Kolltveit, "80 Gbit/s single wavelength soliton transmission over 172km installed fibre", *Electron. Lett.*, vol. 35, no. 4, pp.313-315, 1999.
5. J. W. Lou, J. K. Andersen, J. C. Stocker, M. N. Islam, D. A. Nolan, "Polarization Insensitive Demultiplexing of 100-Gb/s Words Using a Twisted Fiber Nonlinear Optical Loop Mirror", *IEEE Photon. Technol. Lett.*, vol. 11, no. 12, pp. 1602-1604, 1999.
6. S. Machida, J. Sakai, T. Kimura, "Polarization Preservation in Long-Length Twisted Single-Mode Optical Fibers", *Trans. IECE Japan (Section E)*, vol. E65, no. 11, pp. 642-648, 1982.
7. B.-E. Olsson, A. Boyle, P. A. Andrekson, "Control Pulse-induced Crosstalk in Propagation Diversity and Conventional Nonlinear Optical Loop Mirrors", *IEEE Photon. Technol. Lett.*, vol. 10, no. 11, pp.1632-1634, 1998.
8. G. P. Agrawal, *Nonlinear Fiber Optics*, Academic Press, New York, pp. 122-125 and pp. 239-247, 1995.

Figure Captions

Figure 1: (a) Experimental setup for testing the two-wavelength NOLM demultiplexer. The 80 Gb/s signal is multiplexed from a 10 Gb/s 2^{31}-1 pseudo-random bit stream. The 10 Gb/s control source is the compressed output of a modulated continuous (CW) source. The control pulses are coupled in through a 3 dB coupler. BPF = bandpass filter. EDFA = erbium-doped fiber amplifier. BER = bit-error-rate.

Figure 2: Comparison of back-to-back and demultiplexed bit-error-rates. The BER of the maximum transmission case shows an ~6 dB power penalty with 1.5 dB further degradation for the minimum transmission case. This measured penalty is a combination of the penalty due to demultiplexing, adjacent channel cross-talk after multiplexing, and control pulse induced cross-talk.

Figure 3: (a) Measured nonlinear transmission vs. control power to the fiber. For a control power of 43 mW, the polarization sensitivity is ~1 dB and the nonlinear transmission is 91%. (b) Calculated nonlinear transmission vs. control power to the fiber. The calculated transmission curves for linear fiber cross at ~50% transmission and for the fits to the measured data (spun fiber), cross at ~97%.

Figure 4: Calculated and measured polarization sensitivity vs. control power to the fiber. The power ranges over which the polarization sensitivity is <1 dB are 2 dB for spun fiber and 0.32 dB for linear fiber.

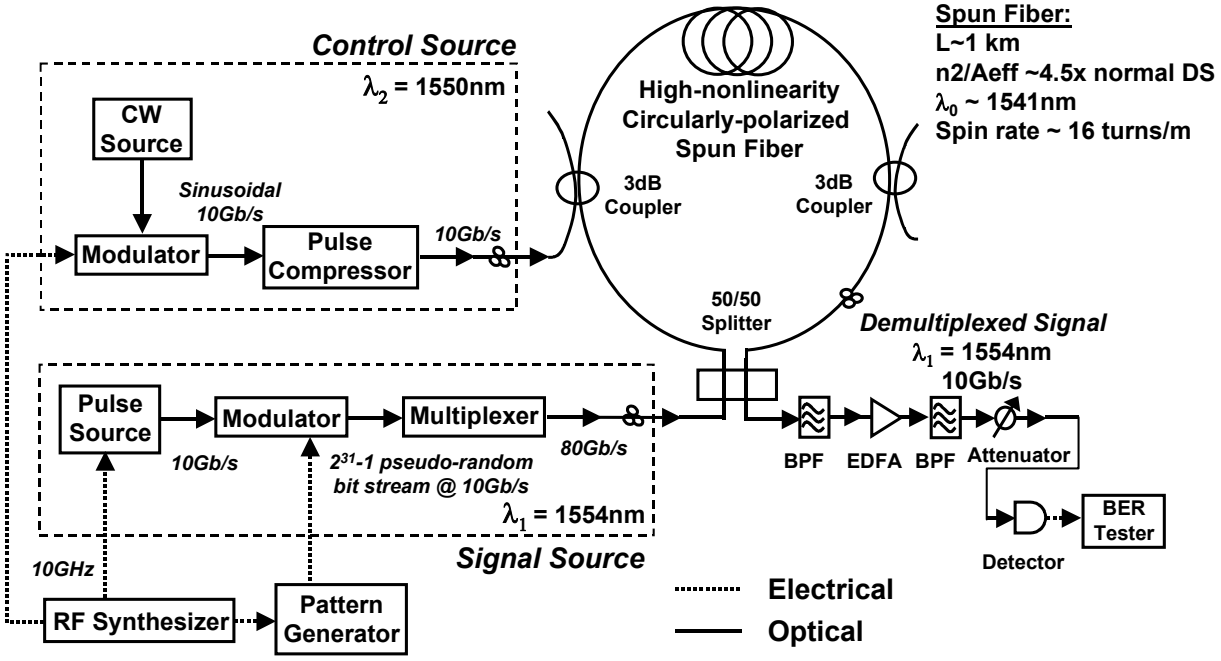
Control Source
λ2 = 1550nm
CW Source
Sinusoidal 10Gb/s
Modulator
Pulse Compressor
10Gb/s
High-nonlinearity Circularly-polarized Spun Fiber
3dB Coupler
3dB Coupler
50/50 Splitter
Spun Fiber:
L~1 km
n2/Aeff ~4.5x normal DS
λ0 ~ 1541nm
Spin rate ~ 16 turns/m
Demultiplexed Signal
λ1 = 1554nm
10Gb/s
Pulse Source
Modulator
Multiplexer
10Gb/s
2^31-1 pseudo-random bit stream @ 10Gb/s
80Gb/s
λ1 = 1554nm
Signal Source
BPF
EDFA
BPF
Attenuator
BER Tester
Detector
10GHz
RF Synthesizer
Pattern Generator
Electrical
Optical

Figure 1

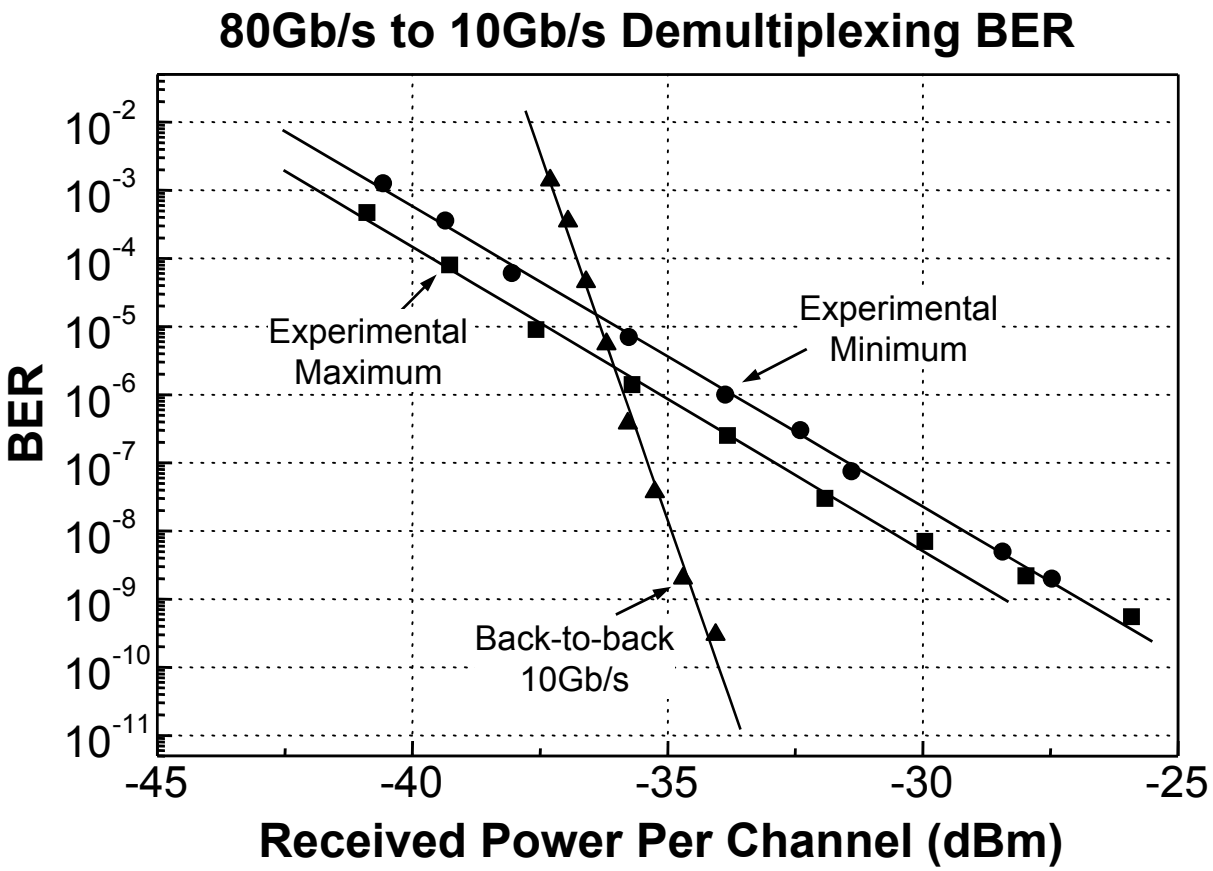
80Gb/s to 10Gb/s Demultiplexing BER
BER
10-2
10-3
10-4
10-5
10-6
10-7
10-8
10-9
10-10
10-11
-45
-40
-35
-30
-25
Received Power Per Channel (dBm)
Experimental Maximum
Experimental Minimum
Back-to-back 10Gb/s

Figure 2

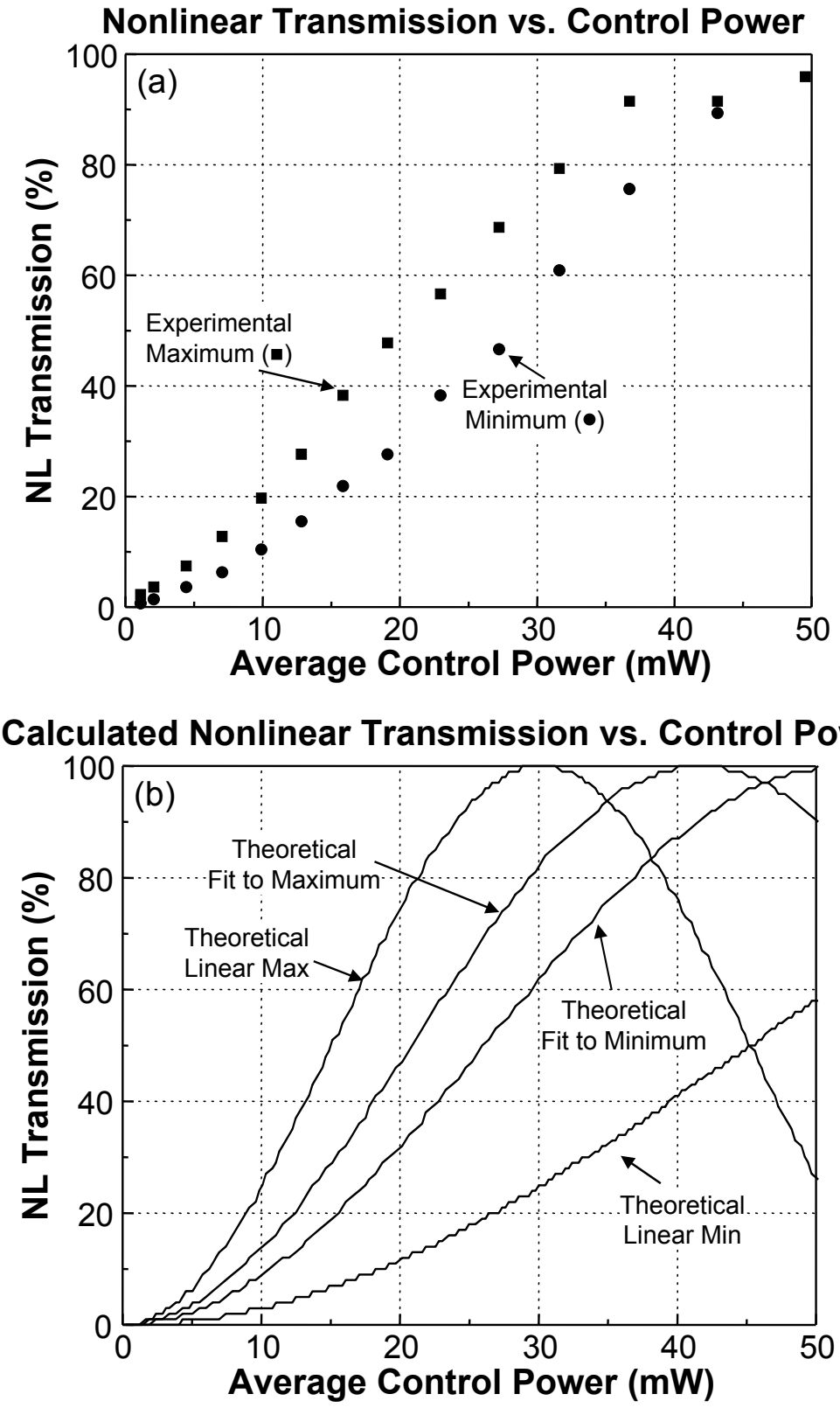
Nonlinear Transmission vs. Control Power
(a)
NL Transmission (%)
Average Control Power (mW)
Experimental
Maximum (■)
Experimental
Minimum (●)
Calculated Nonlinear Transmission vs. Control Power
(b)
NL Transmission (%)
Average Control Power (mW)
Theoretical
Fit to Maximum
Theoretical
Linear Max
Theoretical
Fit to Minimum
Theoretical
Linear Min

Figure 3

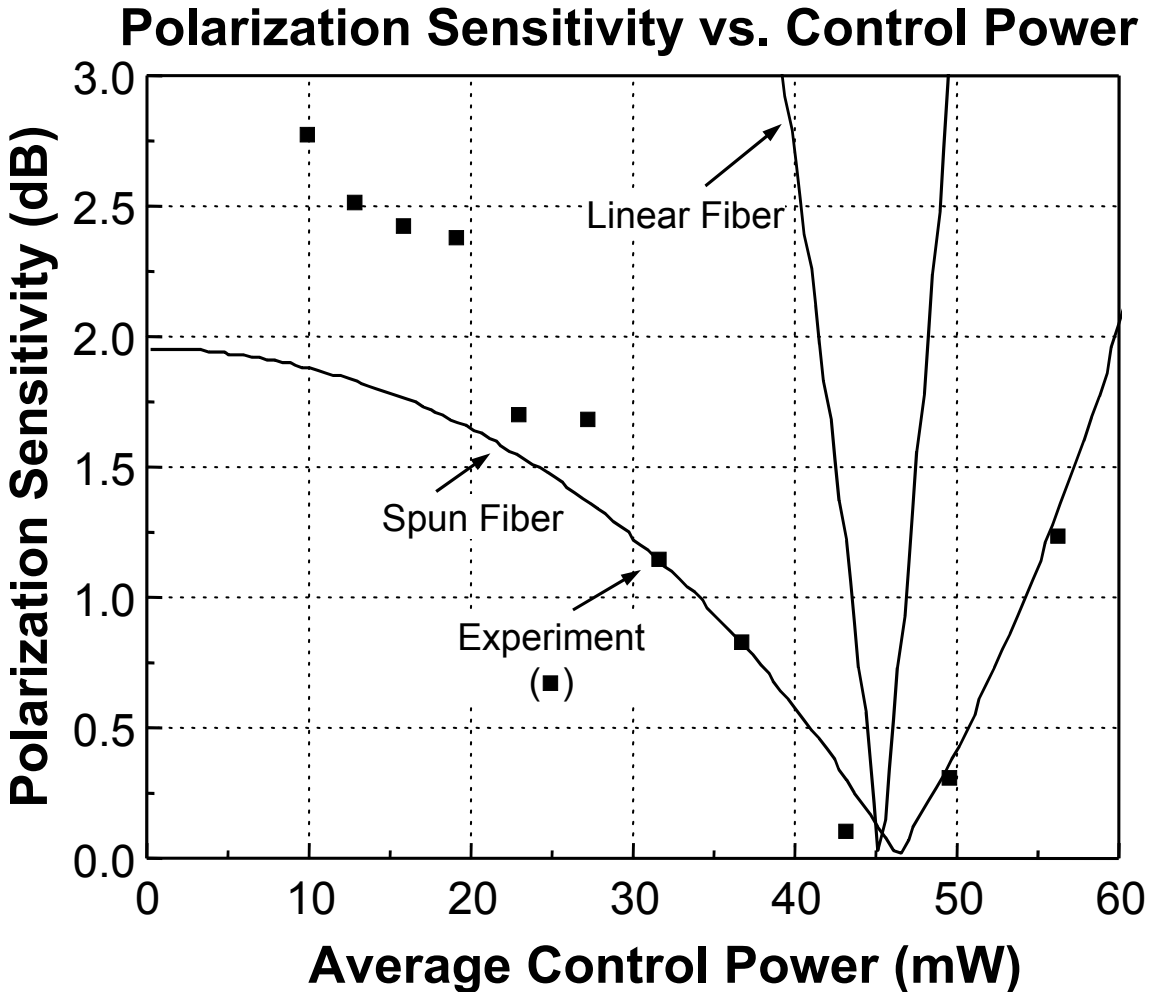
Polarization Sensitivity vs. Control Power
Polarization Sensitivity (dB)
Average Control Power (mW)
Linear Fiber
Spun Fiber
Experiment
(■)
0.0
0.5
1.0
1.5
2.0
2.5
3.0
0
10
20
30
40
50
60

Figure 4

Appendix H

Experimental Measurement and Simulation of Circularly Polarized Spun Fiber in a Two-Wavelength Nonlinear Optical Loop Mirror Polarization Insensitive Demultiplexer

J. W. Lou*, *Student Member*, K. S. Jepsen, D. A. Nolan, S. H. Tarcza,
W. J. Bouton, A. F. Evans
SP-AR-01-2, Science & Technology Division
Corning Incorporated, Corning, NY 14831

*Also with: Electrical Engineering and Computer Science Department
The University of Michigan, Ann Arbor, MI 48109

M. N. Islam, *Senior Member*
Electrical Engineering and Computer Science Department
The University of Michigan, Ann Arbor, MI 48109

Abstract

We present experimental demonstration and computer simulation of a polarization insensitive two-wavelength nonlinear optical loop mirror demultiplexer with circularly polarized spun fiber. Demultiplexing of 10Gb/s channels from 80Gb/s pseudo-random bit streams shows the polarization sensitivity of the device is reduced to <1dB for >90% transmission and is confirmed by simulations based on the nonlinear Schrödinger equation. Bit-error-rate measurements show that the remaining polarization sensitivity leads to a power penalty difference of 1.5dB. The power penalty is due to a combination of timing window induced amplitude fluctuations and cross-talk between the control and the unwanted channels of the counter-propagating signal. The nonlinear transmission is 91% for a switching energy of 3.4pJ/pulse and the full-width-half-maximum timing window is 9.6ps. Simulations show that for the perfectly circularly-polarized fiber NOLM, the range of switching energy where polarization sensitivity is <1dB is at least 7.3dB. This demultiplexer is measured to have a polarization sensitivity <1.3dB for □□ between control and signal up to 20nm, which is in good agreement with simulation results showing <1dB polarization sensitivity. In contrast, simulation of a linear fiber nonlinear optical loop mirror shows that it has polarization sensitivity >5dB.

A short pulse laser (□□=1.53ps) at 1554nm is used to generate the 10Gb/s bit stream input to a LiNbO3 modulator. A pseudo-random pattern generator is used to drive the modulator to encode the bit stream, and the 80Gb/s bit stream is created by optically multiplexing the encoded bit stream. The local source is generated by modulating the output of a continuous-wave source (□=1550nm) with an electro-absorption modulator. The modulated output is propagated through 12.2km of dispersion-decreasing fiber to compress the pulses. The resulting pulse stream has a pulse width of 7.7ps and an extinction ratio of 13dB. The circularly-polarized spun fiber has a □0 of 1541nm, a length of ~1km, and ~4.1 times higher nonlinearity than that of conventional dispersion-shifted fiber. The linear birefringence before spinning is □n=1×10-6, and the spin rate is 16 turns/m, corresponding to 25 turns/beat length.

Introduction

All-optical demultiplexing is necessary when the aggregate rate of time-division-multiplexed systems is increased beyond the speed of electronics. We experimentally demonstrate a polarization-insensitive (<1dB for >90% transmission) nonlinear optical loop mirror (NOLM) using high-nonlinearity, circularly-polarized, spun fiber. The residual polarization dependence leads to 1.5dB power penalty in the bit-error-rate (BER) measurements between the maximum and minimum transmission levels. The linear birefringence before spinning is $\Delta n=1\times10^{-6}$, and the spin rate of the fiber is 16 turns/m, corresponding to 25 turns/beat length. This makes the fiber intrinsically circularly polarized rather than externally biased as with twisted fiber [1]. The polarization sensitivity is reduced because the nonlinear phase shift induced by the control wavelength is the same for all input signal polarizations in circularly-polarized fiber. In linearly-polarized fiber, the difference in the induced nonlinear phase shift can lead to 5dB of polarization sensitivity [2]. Thus, the circularly-polarized spun fiber is ideal for reducing the polarization sensitivity of the two-wavelength NOLM.

Demultiplexing using nonlinear optical loop mirrors has been demonstrated by several groups. A time-dilation method has been used to demultiplex an 80Gb/s 32-bit word using a NOLM cross-correlator [3]. Other polarization-insensitive NOLM demultiplexer configurations have also been demonstrated. A polarization diversity scheme has been used to demultiplex 80Gb/s bit streams [4,5]. Using a twisted fiber NOLM, demultiplexing from short 100Gb/s fixed-words has been demonstrated [6]. In contrast to other NOLM demultiplexers, we achieve polarization insensitivity by spinning high-nonlinearity fiber preform at 16 turns/m during the drawing process so that the fiber is intrinsically circularly polarized and environmentally stable. There is no concern that the fiber will unwind or relax with time.

In this paper, we present the experimental results as well as computer simulation results of a polarization insensitive NOLM demultiplexer with circularly-polarized, spun fiber. In Section II, we discuss the experimental setup for the 80Gb/s to 10Gb/s demultiplexing demonstration. Section III shows the results of the demultiplexing experiment as well as the transmission characteristics of the NOLM device. Then, in Section IV, an analysis of the sources of the power penalty is presented. The limits of the polarization sensitivity of this device are discussed in Section V, while design trade-offs between the bandwidth of operation and power penalty are discussed in Section VI. Finally, Section VII presents the conclusions.

Experimental Setup

Figure 1(a) shows a block diagram of the experimental setup. The output of a 10Gb/s pulsed laser source is modulated with a 2^{31}-1 pseudo-random bit sequence (mark ratio = ½) using a $LiNbO_3$ modulator, driven by a pattern generator. The auto-correlation and spectrum ($\Delta\tau$=1.53ps, $\Delta\lambda$=2nm, λ_1=1554nm) are shown in Fig. 1(b). The 80Gb/s signal source is generated by passively multiplexing the 10Gb/s modulated output using fiber couplers and delay lines. The output of a continuous-wave source is modulated using an electro-absorption modulator and then compressed through 12.2km of dispersion-decreasing fiber (D=11.4 to 2ps/nm/km) to generate the 10GHz control source. Fig. 1(c) shows the control pulse auto-correlation and spectrum (λ_2=1550nm). The control pulses to the NOLM have a pulse width of 7.7ps, spectral width of 0.6nm, and an extinction ratio of 13dB. An RF synthesizer is used to drive the 10Gb/s pulse source, the pattern generator, and the $LiNbO_3$ modulator so that these components are all synchronized.

Figure 2 shows the two-wavelength NOLM demultiplexer and the diagnostics setup. The 80Gb/s signal is coupled into the NOLM through a 50/50 splitter, and the loop is biased to totally reflect the signal in the absence of the control. The control pulses are introduced into the loop through a 3dB coupler and set to one of the eigenmodes of the fiber to reduce the effect of shadow energy [2]. The output of the NOLM is filtered with a 0.8nm bandpass filter to remove the control wavelength, amplified with an erbium-doped fiber amplifier, and filtered with a 3nm bandpass filter to remove excess amplified spontaneous emission. The detection system consists of a detector, an RF amplifier, and a BER tester. The detector has a responsivity of 300mV/mW and thermal noise current approximately 35pA/$\sqrt{\text{Hz}}$.

The high-nonlinearity fiber preform is spun at 16 turns/m during the drawing process to induce a circular birefringence, while reducing the linear birefringence and making the fiber more circularly polarized (*i.e.*, the eigenmodes of the fiber are circular). In linearly-polarized fiber, the nonlinear phase shift coefficients due to cross-phase-modulation between the control and signal wavelengths are 2 and 2/3 for parallel and orthogonal polarizations, respectively. However, in circularly-polarized fiber, the nonlinear phase shift coefficient is 4/3 for all polarizations. Thus, the amount of nonlinear phase shift induced by the control pulses on the signal pulses and therefore, the nonlinear transmission of the NOLM are independent of the input signal polarization. The ~1km fiber has λ_0 = 1541nm (D=0.32ps/nm/km at 1550nm), ~4.1 times the nonlinearity of conventional dispersion-shifted fiber, and loss of 3.8dB/km at 1550nm. The measured linear birefringence before spinning is $\Delta n=1\times10^{-6}$, which implies a beat length of L_B=1.55m and a spin rate of 25 turns/L_B. For a sufficiently high twist rate (>10 turns per beat length), the polarization mode dispersion is reduced and a high degree of polarization is maintained for any input polarization [7]. The high-nonlinearity is achieved by a combination of increased germanium doping (n_2 increased by a factor of ~1.5) and decreased effective area (A_{eff} = 18.4μm^2).

Experimental Demonstration of 80 Gb/s to 10 Gb/s Demultiplexing

Eye Diagrams and Bit-Error-Rate Measurements

Figure 3(a) shows the eye diagrams of the 10Gb/s signal, the 80Gb/s input, and the demultiplexed 10Gb/s signal. The eye diagrams are measured with a 45GHz detector and a 40GHz bandwidth digital oscilloscope. The figures show a ringing effect after each detected pulse that is due to the limited bandwidth of the detector. This ringing does not effect the measured BER because the BER is measured at an optimized position within the eye opening.

The pre-amplified back-to-back BER as well as the BER of the demultiplexed bits for the maximum- and minimum-output polarizations are shown in Fig. 3(b). The received power per channel is calculated by measuring the total average power and assuming 8×10Gb/s channels are inputted to the NOLM demultiplexer/receiver. For a BER of 10^{-9}, there is a 6dB power penalty for demultiplexing from signals with input polarizations corresponding to the maximum transmission. The slight floor in the BER curve of the maximum transmission case is attributed to the instability of the pulse laser source, and is not observed for the minimum transmission case. The power penalty is increased by 1.5dB for the minimum-output case because the signal level into the pre-amplifier is lowered.

Nonlinear Transmission of Spun Fiber NOLM

The nonlinear transmission curves for the parallel and orthogonal input polarizations are shown in Fig. 4(a). Note that the polarization sensitivity is ~1dB for our operating point at an average control power of 25.4mW in the spun fiber. This power corresponds to a switching pulse energy of 3.4pJ/pulse for a maximum nonlinear transmission of 91%. Beyond ~31mW, the broadening of the control pulse spectrum due to self-phase-modulation causes significant leakage into the signal pulse bandwidth so that an accurate measurement of the switched out power could not be obtained. While the high-nonlinearity of the fiber reduces the necessary switching energy, the high loss of this prototype fiber, due to the tail of the water absorption peak at 1380nm, counteracts some of that benefit.

Polarization Sensitivity versus Wavelength Separation

Figure 4(b) shows the measured polarization sensitivities as a function of the wavelength separation between the control and signal. The measured difference between the maximum and the minimum transmission levels remains below 1.3dB for $\Delta\lambda$ up to 20nm. For even larger wavelength separations, the measured polarization sensitivity is dominated by the polarization dependent leakage (due to polarization dependent loss in the components).

Sources of Power Penalty

In order to understand the sources of the power penalty, we first define the sources of noise in the system [8]. The variance of the received signal is

where p=1 for a '1' bit and p=0 for a '0' bit. The first two terms on the right hand side of

$$\sigma_p^2 = \sigma_{th}^2 + \sigma_{ase}^2 + \sigma_{sig,p}^2 + \sigma_{ampl,p}^2,$$

Eqn. (1) exist regardless of whether the demultiplexed bit is a '1' or '0'. The first term comes from the thermal noise of the detector, and the second term comes from the spontaneous-spontaneous noise of the pre-amplifier. The latter two terms on the right hand side of Eqn. (1) vary depending on whether the bit is a '1' or '0'. The third term comes from the signal-spontaneous noise, and the last term comes from the amplitude fluctuations induced by the

$$\sigma_{th}^2 = \frac{4kTB}{R_L} + i_a^2 B,$$

source and the NOLM (due to the non-square timing window). The thermal noise term is defined as

where k is Boltzmann's constant, T is the temperature, R_L is the load resistance of the detector, i_a is the spectrum density of the noise current from the electric amplifier ($A/\sqrt{Hz}$), and B is the bandwidth of the electrical detection system. The spontaneous-spontaneous noise is

$$\sigma^2_{ampl,1} = (q\eta G)^2\left(\Delta I_{source}\cdot < N_1 >^2 + \Delta I_{nolm}\cdot < N_i >^2\right),$$
$$\sigma^2_{ampl,0} = (q\eta G)^2\left(\Delta I_{source}\cdot < N_0 >^2 + \Delta I_{nolm}\cdot r\cdot < N_i >^2\right),$$

$$\sigma^2_{ase} = 4\cdot(q\eta G)^2\cdot n^2_{sp}\cdot \Delta f\cdot B,,$$

$$\sigma^2_{sig,p} = 4\cdot(q\eta G)^2\cdot n_{sp}\cdot B\cdot < N_p >,$$

defined as

where Δf is the optical bandwidth, n_{sp} is the population inversion parameter of the pre-amplifier, q is the electron charge, η is the quantum efficiency of the detector, and G is the gain of the pre-amplifier. The signal-spontaneous noise is

where $<N_p>$ is the mean number of photons in a received '1' (p=1) and '0' (p=0). Finally, the amplitude fluctuations due to the source and the NOLM are defined as ΔI_{source} and ΔI_{nolm}, respectively. Thus, the noise due to amplitude fluctuations is

where $<N_i>$ is the mean number of photons in a '1' bit without noise, and r is extinction ratio of the transmitter modulator so that $r\times<N_i>$ is the mean number of photons in a '0' bit.

The total power penalty can be calculated as the ratio of the number of photons necessary for the desired BER, with and without cross-talk and the effects of the NOLM. While the effects of the NOLM are clearly included in the noise variances, $\sigma^2_{ampl,p}$, the effect of cross-talk appears only in the definitions of $<N_p>$ [8]. Specifically,

$$< N_1 >=< N_i > \{1 + \alpha(N-1)[R_m + r(1-R_m)]\},$$
$$< N_0 >=< N_i > \{r + \alpha(N-1)[R_m + r(1-R_m)]\},$$

where R_m is the mark-ratio, N is the number of multiplexed channels, and α is the magnitude of the cross-talk between the control and the unwanted channels of the counter-propagating signal. The Q corresponding to the desired $BER = 1/2\times \mathrm{erfc}(Q/\sqrt{2})$ is defined as $Q = (I_1-I_0)/(\sigma_1+\sigma_0)$, where I_1 and I_0 are the mean current values of '1' and '0', respectively, and

Thus, the power penalty for a given Q is

Table 1 contains the values corresponding to our experiments. In our calculations, we

$$I_1 = q\eta G N_1,$$

$$I_0 = q\eta G N_0.$$

$$PP = \frac{< N_i >|\alpha \neq 0, \Delta I_{NOLM} \neq 0}{< N_i >|\alpha = 0, \Delta I_{NOLM} = 0}.$$

use Q = 6 for BER = 10^{-9} and we obtained a power penalty of 6dB by assuming a source fluctuation of $\sigma_1=0.103\times I_1$ and a NOLM induced fluctuation of $\sigma_1=0.095\times I_1$. The source fluctuation is approximated by using the statistical calculations of a histogram obtained by a digital oscilloscope. The NOLM induced fluctuations is due to the non-square timing window, where timing jitter between the control and signal pulses is translated into amplitude fluctuations. According to our calculations, the power penalty due to this effect (without cross-talk) is 4.09dB.

Another source of power penalty is the unwanted cross-phase-modulation of the control pulse on the counter-propagating pulses. Following the analysis by Uchiyama, *et al.* [8], the magnitude of the cross-talk from unwanted cross-phase-modulation of a single channel is:

where k is the power coupling ratio. By using the measured extinction ratio of the NOLM

$$\alpha = 1 - 4k(1-k)\cos^2\left[\frac{\pi}{2(\xi-1)}\right],$$

(30dB), the power coupling ratio is calculated to be k = 0.516. ξ is defined as:

$$\xi = \frac{1}{f_c \tau_G}\,\mathrm{erf}\left(\frac{\tau_G\sqrt{\ln(2)}}{t_c}\right), \qquad (1)$$

where f_c is the frequency of the control source, τ_G is the walk-off time between the control and signal pulses, and t_c is the full-width-half-maximum pulse width of the control. For our case, f_c = 10GHz, τ_G = 1.83ps, t_c = 7.7ps, and thus, α is approximately –16.76dB. Note that for 80Gb/s to 10Gb/s demultiplexing, there are actually (N-1)=7 unwanted channels. Thus, the total magnitude of the unwanted cross-talk is $(N-1)\times\alpha$ = –8.31dB. Using the values for our experiment, we calculate the power penalty due only to the unwanted cross-phase-modulation (*i.e.*, $\Delta I_{NOLM} = 0$) to be 0.51dB.

Finally, for the minimum transmission case, the power penalty is increased because the optical power to the pre-amplifier is lowered. Although the pre-amplifier partially compensates for the lower input power, the output of the pre-amplifier still does not have the same power as in the maximum transmission case. Using the same parameters, we note that a decrease of 0.55dB in the switched out bit (*i.e.*, N_1 decreased by 0.55dB) leads to a 1.52dB increase in the power penalty. Thus, even a small polarization sensitivity can lead to a measurable power penalty.

Limits of Polarization Insensitivity

Switching Energy Range of Polarization Insensitive Behavior

Using simulations based on the nonlinear Schrödinger equation, we show the expected maximum and minimum transmissions for a linearly-polarized fiber NOLM and for a perfectly circularly-polarized fiber NOLM in Fig. 5(a). These transmission curves accent two important behaviors. First, the linearly-polarized fiber NOLM is highly sensitive to the input polarization, while the perfectly circularly-polarized fiber NOLM is much less sensitive. Second, even in the case of the perfectly circularly-polarized fiber NOLM, there is residual polarization sensitivity. In fact, at high power levels, the perfectly circularly-polarized fiber NOLM transmission closely

matches the measured transmissions of our spun fiber NOLM. As we expected for this spin rate, our spun fiber is close to a perfectly circularly-polarized fiber. The remaining polarization sensitivity is caused by shadow energy generation [2].

To quantify the polarization sensitivity of the different NOLMs, we simulate and compare the range of switching energies and corresponding transmissions for a polarization sensitivity variation of 1dB. The simulated polarization sensitivities of the linearly- and circularly-polarized fiber NOLMs are shown in Fig. 5(b). For the linearly-polarized fiber, the polarization sensitivity varies from 5dB to 6dB over a 0.35dB range. At the lowest polarization sensitivity, the transmission varies from 29% to 99%. The perfectly circularly-polarized fiber has polarization insensitive <1dB for >6.3% transmission corresponding to at least 7.3dB switching energy variation. Thus, in comparison to the linearly-polarized fiber NOLM, the polarization sensitivity of the spun fiber NOLM is reduced by more than 4dB, while allowing for at least 7dB wider switching energy range. For the highest nonlinear transmission with polarization sensitivity <1dB, the transmission varies from 80% to 98%.

Shadow Energy

Shadow energy refers to the energy that is moved from one eigenmode to the orthogonal eigenmode after dispersive walk-off between two wavelengths [9]. The amount of shadow energy is dependent on the relative polarizations of the two wavelengths. When the co- and counter-propagating signal pulses recombine at the 50/50 splitter, the interference and the transmission is dependent on the amount of shadow energy. This leads to polarization sensitivity in the demultiplexer. Figure 6 shows the simulated amount of shadow energy, as a percent of the total energy in one propagation direction, versus the input polarization. The average control power is 25.4mW and as the control power increases, the shadow energy increases relative to the total energy. The highest level of shadow energy, 11.6%, occurs when the control and signal are polarized 45^{o} relative to each other. The presence of the shadow energy is a fundamental limit to the polarization-insensitivity of the perfectly circularly-polarized fiber NOLM.

Trade-off Between Bandwidth of Operation and Polarization Sensitivity

Simulation results, shown in Fig. 7, confirm the broad bandwidth of polarization insensitive operation for a circularly-polarized fiber NOLM. We choose to use the control power for which the parallel- and orthogonally-polarized control and signal pulses give the same nonlinear transmission. In the case of the perfectly circularly-polarized fiber NOLM, the average control power is 33.15mW, and for the linearly-polarized fiber NOLM, the average control power is 28mW. We simulate and calculate the expected bandwidth of polarization insensitive operation for the perfectly circularly-polarized fiber NOLM and for the linearly-polarized fiber NOLM. The simulated results show that the perfectly circularly-polarized fiber NOLM is polarization-insensitive (<1dB) for $\Delta\lambda$ at least up to 20nm. The linearly-polarized fiber NOLM has a much narrower range of operation, with polarization sensitivity from 5.4dB to 6.4dB for $\Delta\lambda$ = 3nm.

A trade-off exists when the wavelength separation between control and signal is increased. A larger wavelength separation leads to faster walk-off between the pulses and thus, lowers nonlinear transmission, which leads to a higher power penalty. Figure 8 shows the maximum and minimum nonlinear transmissions as a function of the wavelength separation. Note that in the experimental demonstration, most of the power penalty is due to the NOLM induced fluctuations. A faster walk-off implies a wider timing window and this would reduce

the detrimental effects of timing jitter between the control and signal. A shorter control pulse may also be necessary to avoid switching out adjacent channels. Because of the high losses in the current system, we can not take the penalty of the reduced nonlinear transmission due to wavelength separation. However, with lower losses, it may be advantageous to go to larger wavelength separation to reduce the NOLM-induced power penalty.

Conclusion

We achieve polarization-insensitive (<1dB for >90% transmission) demultiplexing of 10Gb/s channels from a fully-populated 8×10Gb/s 2^{31}-1 pseudo-random bit-stream using a NOLM with ~1km of high-nonlinearity circularly-polarized spun fiber. BER measurements show a 1.5dB power penalty difference due to the residual polarization dependence. The NOLM has a timing window of 9.6ps and 91% nonlinear transmission for a switching energy of 3.4pJ/pulse. The maximum-output power penalty of 6dB is due to the combination of NOLM induced amplitude fluctuations and cross-talk between the control and unwanted channels of the counter-propagating signal. The NOLM maintains polarization sensitivity <1.3dB for $\Delta\lambda$ between control and signal up to 20nm.

The 80Gb/s to 10Gb/s demultiplexing testbed consists of an 80Gb/s pseudo-random signal source at λ_1 = 1554nm, a 10GHz control source at λ_2 = 1550nm, and a NOLM with high-nonlinearity circularly-polarized spun fiber. The signal source is generated by modulating 10Gb/s pulses with a $LiNbO_3$ modulator, driven by a 2^{31}-1 pseudo-random pattern generator, and then passively multiplexing up to 80Gb/s using couplers and fiber delay lines. The control source is generated by modulating a continuous-wave source output and then compressing the pulse through 12.2km of dispersion-decreasing fiber. The pulses are inputted to the NOLM through a 3dB coupler and aligned to one of the eigenmodes of the fiber. The spun fiber has nonlinearity ~4.1 times that of conventional dispersion-shifted fiber and a spin rate of 16 turns/m. The inherent circular birefringence of the spun fiber makes the cross-phase-modulation between the control and signal wavelengths polarization independent.

Simulations show that the residual polarization sensitivity is due to the generation of shadow energy and that this spun fiber is close to a perfectly circularly-polarized fiber. For the control power where the polarization sensitivity is lowest, the perfectly circularly-polarized fiber NOLM has at least 50% higher nonlinear transmission than the linearly-polarized fiber NOLM. The perfectly circularly-polarized fiber NOLM also has a switching energy variation range that is 7dB wider than linearly-polarized fiber NOLM for a 1dB change in polarization sensitivity. We also show through simulations that the bandwidth of the perfectly circularly-polarized fiber NOLM, where polarization sensitivity is <1dB, is at least 20nm.

Acknowledgement

This work was supported by DARPA.

References

R. Dändliker, "Rotational effects of polarization in optical fibers" in Anisotropic and Nonlinear Optical Waveguides, C.G. Someda and G. Stegeman, ed., Elsevier Science, New York, 1992.

Y. Liang, J. W. Lou, J. K. Andersen, J. C. Stocker, O. Boyraz, M. N. Islam, D. A. Nolan, "Polarization-insensitive nonlinear optical loop mirror demultiplexer with twisted fiber", *Opt. Lett.*, vol. 24, no. 11, pp.726-728, 1999.

N. S. Patel, K. L. Hall, K. A. Rauschenbach, "Optical Rate Conversion for High-Speed TDM Networks", *IEEE Photon. Technol. Lett.*, vol. 9, no. 9, pp.1277-1279, 1997.

B. E. Olsson, P. A. Andrekson, "Polarization independent demultiplexing in a polarization diversity nonlinear optical loop mirror", *IEEE Photon. Technol. Lett.*, vol. 9, no. 6, pp.764-766, 1997.

J. Hansryd, B. Bakhshi, B. E. Olsson, P. A. Andrekson, J. Brentel, E. Kolltveit, "80 Gbit/s single wavelength soliton transmission over 172km installed fibre", *Electron. Lett.*, vol. 35, no. 4, pp.313-315, 1999.

J. W. Lou, J. K. Andersen, J. C. Stocker, M. N. Islam, D. A. Nolan, "Polarization insensitive demultiplexing of 100Gb/s words using a twisted fiber nonlinear optical loop mirror", *IEEE Photon. Technol. Lett.*, vol. 11, no. 12, pp.1602-1604, 1999.

S. Machida, J. Sakai, T. Kimura, "Polarization Preservation in Long-Length Twisted Single-Mode Optical Fibers", *Trans. IECE Japan (Section E)*, vol. E65, no. 11, pp.642-648, 1982.

K. Uchiyama, T. Morioka, S. Kawanishi, H. Takara, M. Saruwatari, "Signal-to-Noise Ratio Analysis of 100 Gb/s Demultiplexing Using Nonlinear Optical Loop Mirror", *IEEE J. Lightwave Technol.*, vol. 15, no. 2, pp.194-201, 1997.

C.-J. Chen, P. K. A. Wai, C. R. Menyuk, "Soliton switch using birefringent optical fibers", *Opt. Lett.*, vol. 15, no. 9, pp.477-479, 1990.

Table Captions

Table 1: Table of Parameters used in Power Penalty Calculations.

Parameter	Value
T	298 K
R_L	50 Ω
Δf	3 nm
B	10 GHz
r	30 dB
G	12 dB
n_{sp}	2

Table 1

Figure Captions

Figure 1: (a) Block diagram of the experimental setup. The 80Gb/s signal is multiplexed from a 10Gb/s 2^{31}-1 pseudo-random bit stream. The 10Gb/s control source is the compressed output of a modulated continuous (CW) source. (b) Auto-correlation and spectrum of signal pulses. (c) Auto-correlation and spectrum of control pulses.

Figure 2: Diagram of the two-wavelength NOLM demultiplexer and the diagnostic setup. The control pulses are coupled in through a 3dB coupler. BPF = bandpass filter. EDFA = erbium-doped fiber amplifier. BER = bit-error-rate.

Figure 3: (a) Eye diagrams of the 10Gb/s signal input, the 80Gb/s signal input, and the 10Gb/s demultiplexed signal output. The ringing effect is due to the limited bandwidth of the detector. (b) Comparison of back-to-back and demultiplexed bit-error-rates. The BER of the maximum transmission case shows a 6dB power penalty with 1.5dB further degradation for the minimum transmission case. This measured penalty is a combination of the penalty due to NOLM-induced amplitude fluctuations and cross-talk between the control and the unwanted signal channels in the counter-propagating direction.

Figure 4: (a) Measured nonlinear transmissions for parallel- and orthogonally-polarized control and signal vs. control power. For a control power of 25.4mW, the polarization sensitivity is ~1dB and the nonlinear transmission is 91%. (b) Measured polarization sensitivity versus wavelength separation between control and signal. The polarization sensitivity remains below 1.3dB for up to 20nm separation although the absolute transmitted power decreases due to the decreased walk-off length.

Figure 5: (a) Simulated maximum and minimum nonlinear transmissions vs. control power. The minimum transmission of the CPF NOLM is 80% as opposed to that of the LPF NOLM, which is 29%. (b) Simulated polarization sensitivity vs. control power. LPF = linearly-polarized fiber. CPF = circularly-polarized fiber. NOLM = nonlinear optical loop mirror. The control power for the CPF NOLM simulation is 33.15mW and for the LPF NOLM is 28mW. The power range over which the polarization sensitivity is <1dB for the CPF NOLM is 7dB. For the LPF NOLM, the polarization sensitivity is >5dB and increases to 6dB over a range of 0.35dB.

Figure 6: Simulated shadow energy levels, as a percent of total signal power in one propagation direction, for a circularly-polarized fiber NOLM with control power of 33.15mW. The maximum shadow energy is 11.6% of the signal energy in one direction and occurs when the control and signal pulses are polarized 45^{o} relative to each other.

Figure 7: Simulated polarization sensitivity versus wavelength separation. The polarization sensitivity remains below 1.2dB for $\Delta\lambda$ at least 20nm separation in the circularly-polarized fiber NOLM. The polarization sensitivity is >5dB for the linearly-polarized fiber NOLM.

Figure 8: Simulated nonlinear transmission versus wavelength separation. Increased wavelength separation leads to faster walk-off between the control and signal pulses and reduces the nonlinear transmission. However, the circularly-polarized fiber NOLM maintains a higher minimum nonlinear transmission as well as low polarization sensitivity, for $\Delta\lambda$ at least up to 20nm.

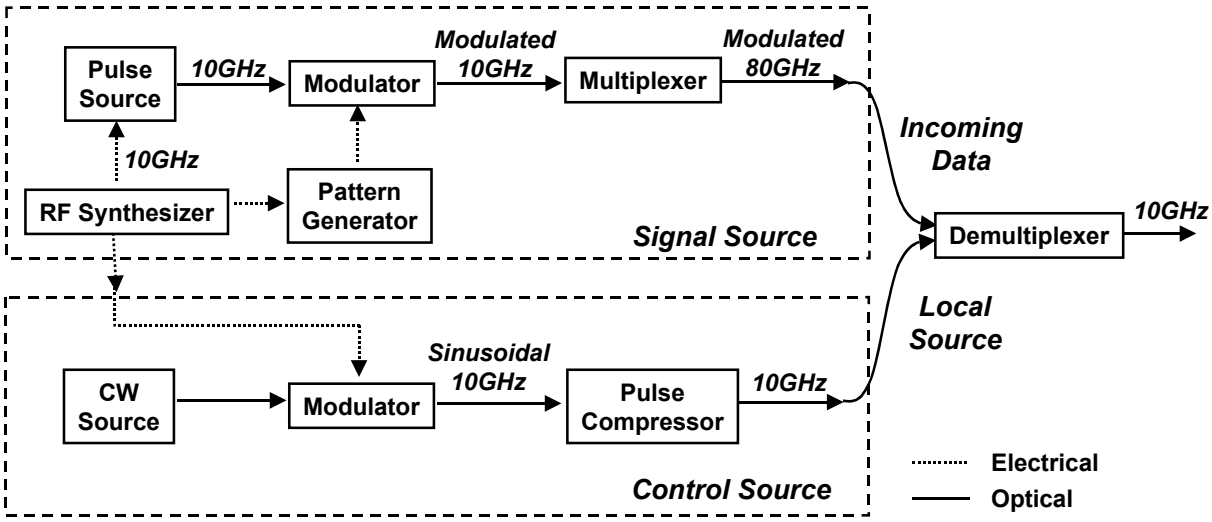
Pulse Source
10GHz
Modulator
Modulated 10GHz
Multiplexer
Modulated 80GHz
Incoming Data
10GHz
RF Synthesizer
Pattern Generator
Signal Source
Demultiplexer
10GHz
Local Source
Sinusoidal 10GHz
CW Source
Modulator
Pulse Compressor
10GHz
Control Source
Electrical
Optical

(a)

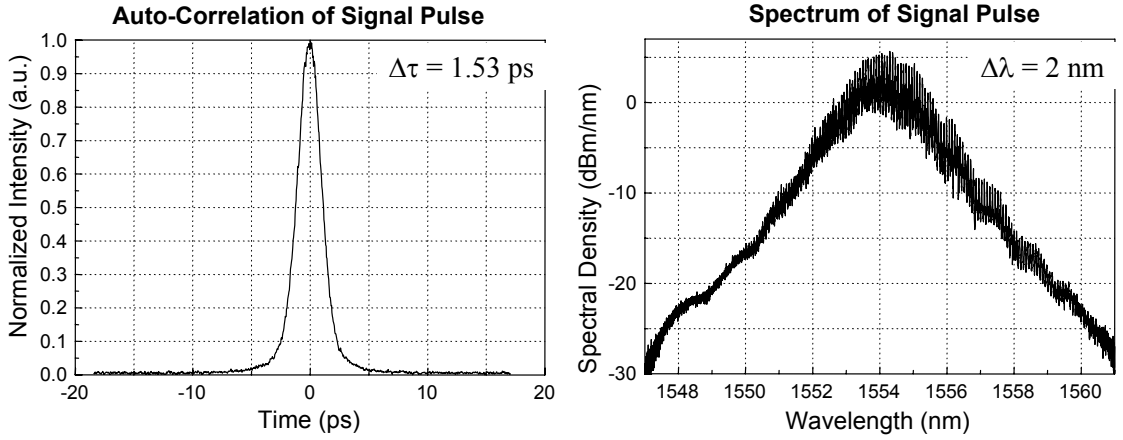
Auto-Correlation of Signal Pulse
Δτ = 1.53 ps
Normalized Intensity (a.u.)
Time (ps)
Spectrum of Signal Pulse
Δλ = 2 nm
Spectral Density (dBm/nm)
Wavelength (nm)

(b)

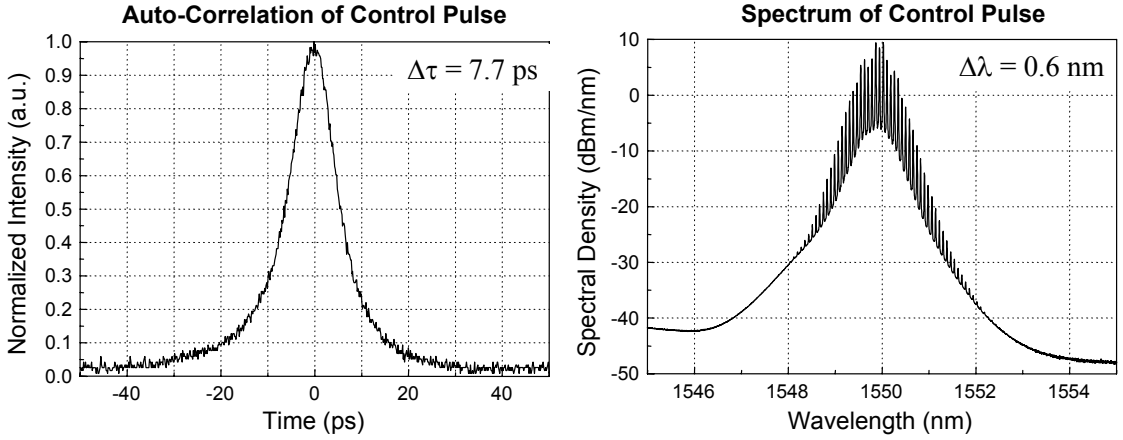
Auto-Correlation of Control Pulse
Δτ = 7.7 ps
Normalized Intensity (a.u.)
Time (ps)
Spectrum of Control Pulse
Δλ = 0.6 nm
Spectral Density (dBm/nm)
Wavelength (nm)

(c)

Figure 1

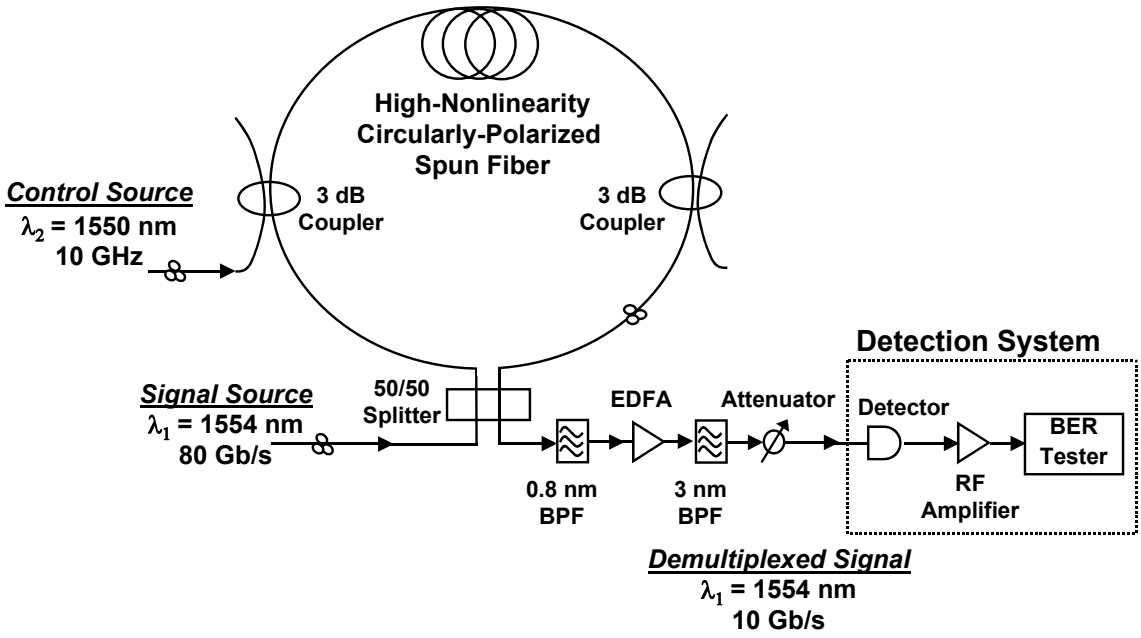
High-Nonlinearity
Circularly-Polarized
Spun Fiber
Control Source
λ2 = 1550 nm
10 GHz
3 dB
Coupler
3 dB
Coupler
Detection System
Signal Source
λ1 = 1554 nm
80 Gb/s
50/50
Splitter
EDFA
Attenuator
Detector
BER
Tester
0.8 nm
BPF
3 nm
BPF
RF
Amplifier
Demultiplexed Signal
λ1 = 1554 nm
10 Gb/s

Figure 2

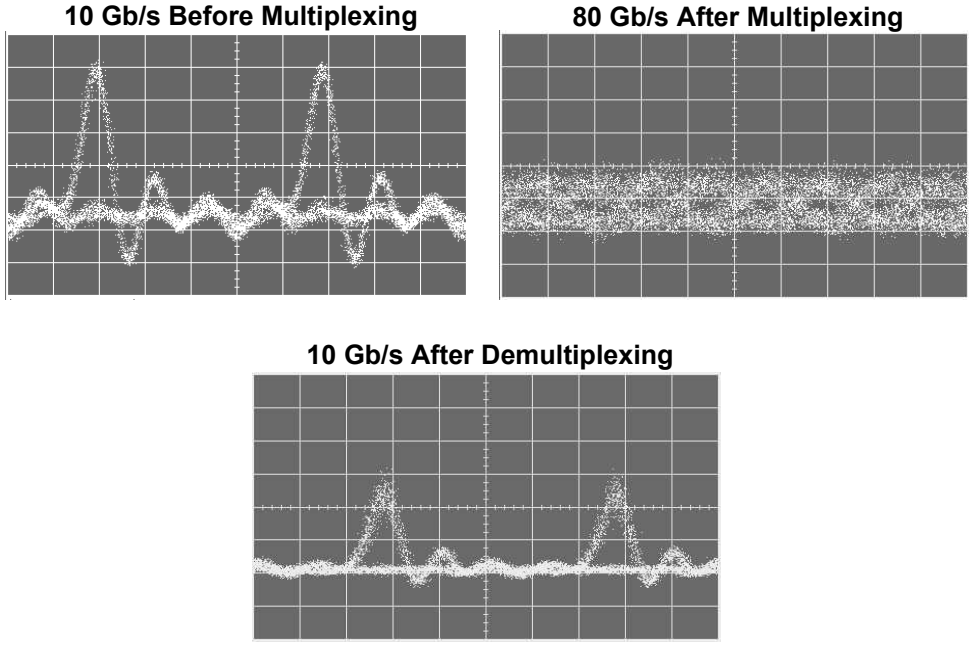
10 Gb/s Before Multiplexing
80 Gb/s After Multiplexing
10 Gb/s After Demultiplexing

(a)

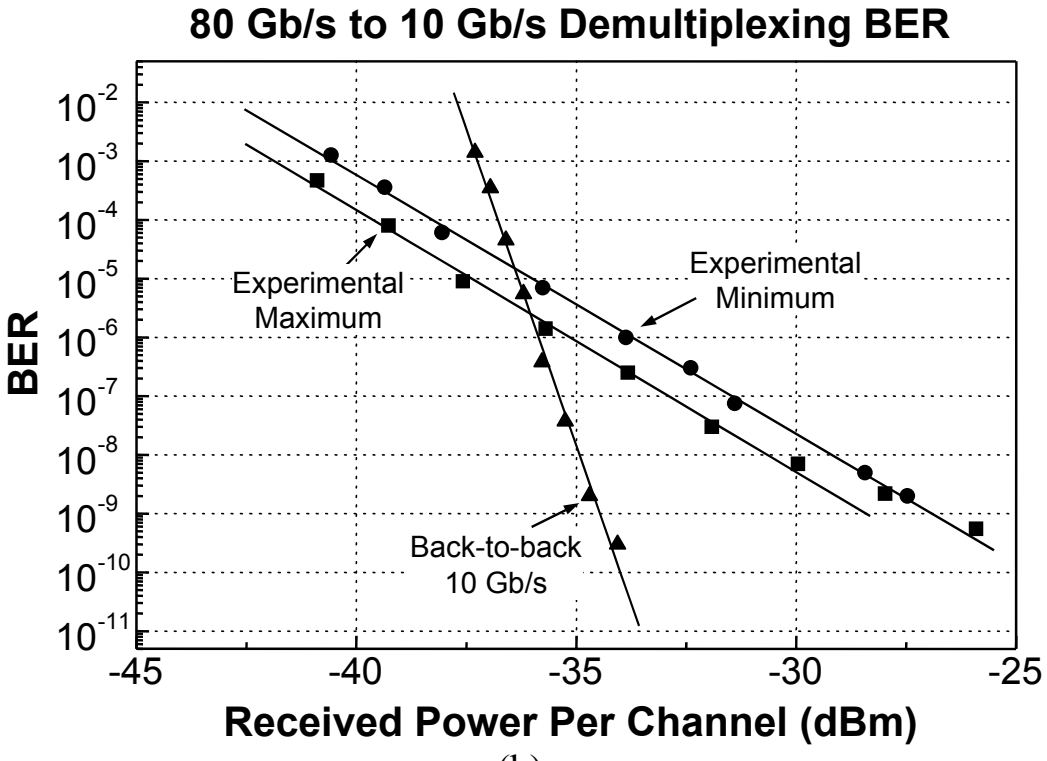
80 Gb/s to 10 Gb/s Demultiplexing BER
BER
10-2
10-3
10-4
10-5
10-6
10-7
10-8
10-9
10-10
10-11
Experimental
Maximum
Experimental
Minimum
Back-to-back
10 Gb/s
-45
-40
-35
-30
-25
Received Power Per Channel (dBm)

(b)

Figure 3

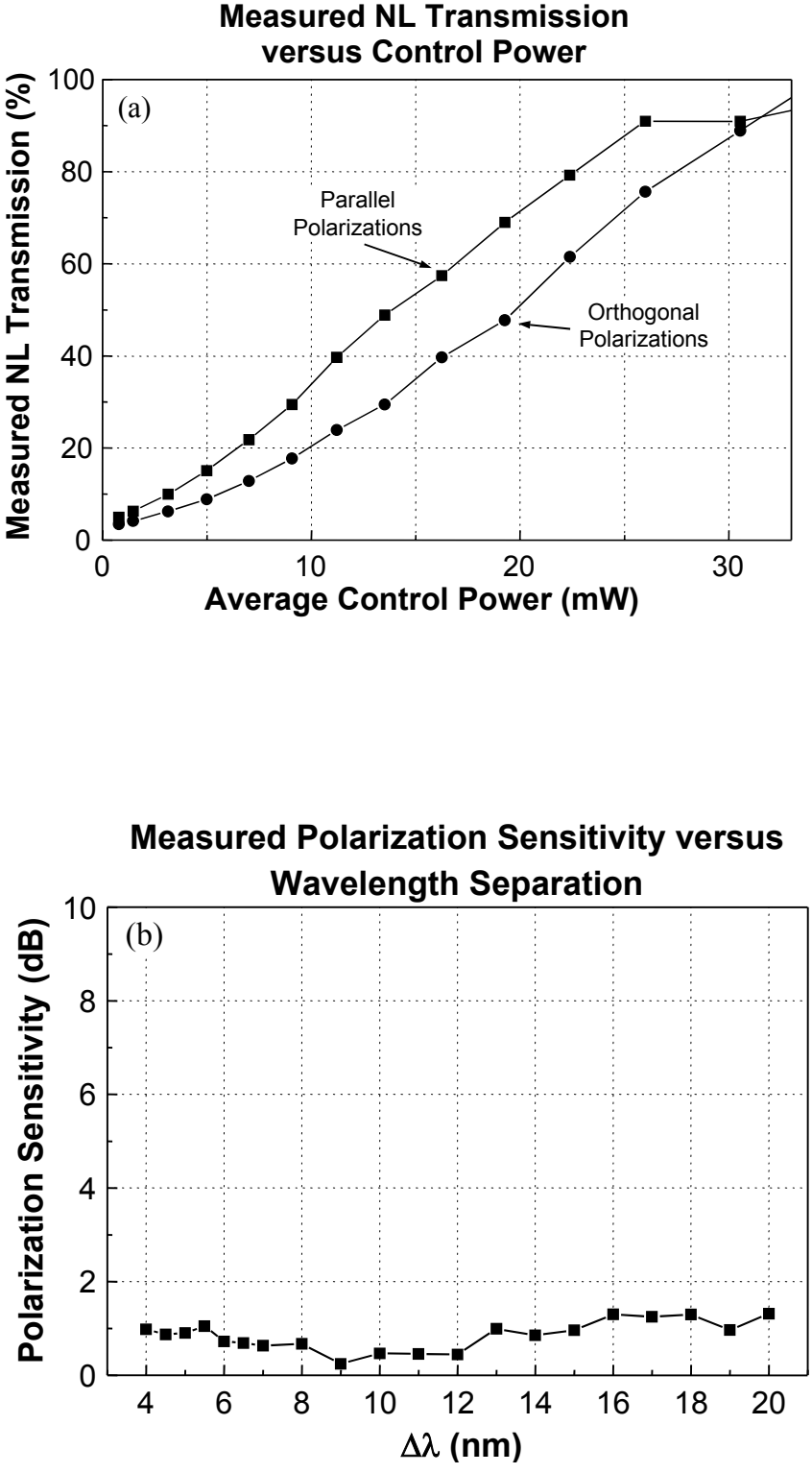
Measured NL Transmission
versus Control Power
(a)
Parallel
Polarizations
Orthogonal
Polarizations
Measured NL Transmission (%)
Average Control Power (mW)
0
20
40
60
80
100
0
10
20
30
Measured Polarization Sensitivity versus
Wavelength Separation
(b)
Polarization Sensitivity (dB)
Δλ (nm)
0
2
4
6
8
10
4
6
8
10
12
14
16
18
20

Figure 4

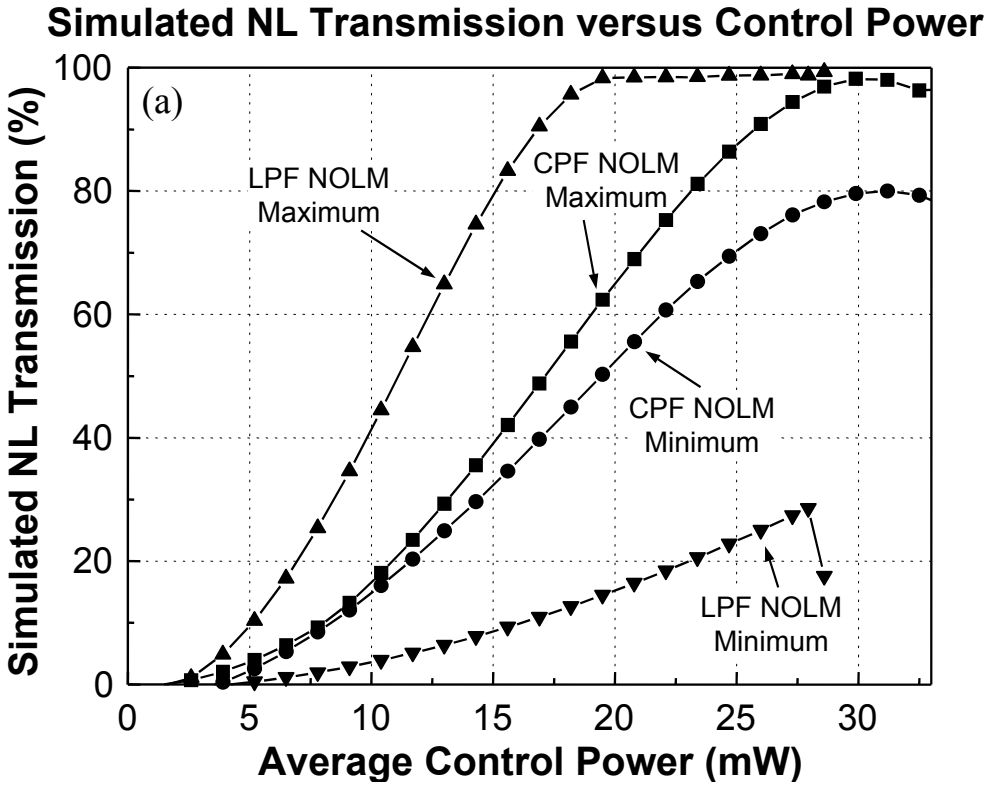
Simulated NL Transmission versus Control Power
(a)
LPF NOLM
Maximum
CPF NOLM
Maximum
CPF NOLM
Minimum
LPF NOLM
Minimum
Simulated NL Transmission (%)
Average Control Power (mW)
0
20
40
60
80
100
0
5
10
15
20
25
30

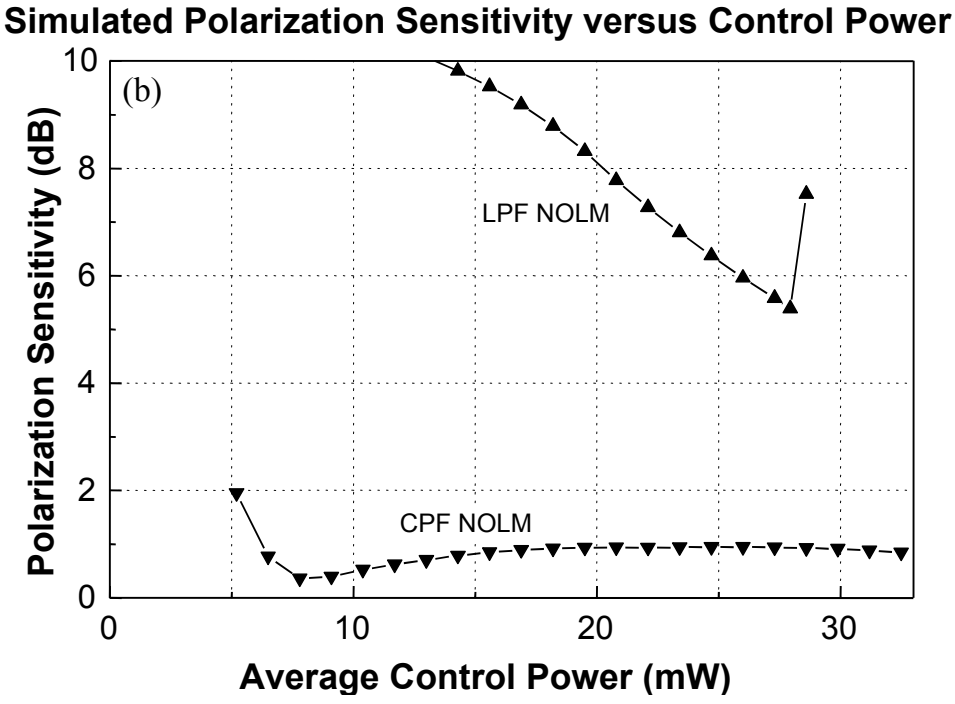
Simulated Polarization Sensitivity versus Control Power
(b)
LPF NOLM
CPF NOLM
Polarization Sensitivity (dB)
Average Control Power (mW)
0
2
4
6
8
10
0
10
20
30

Figure 5

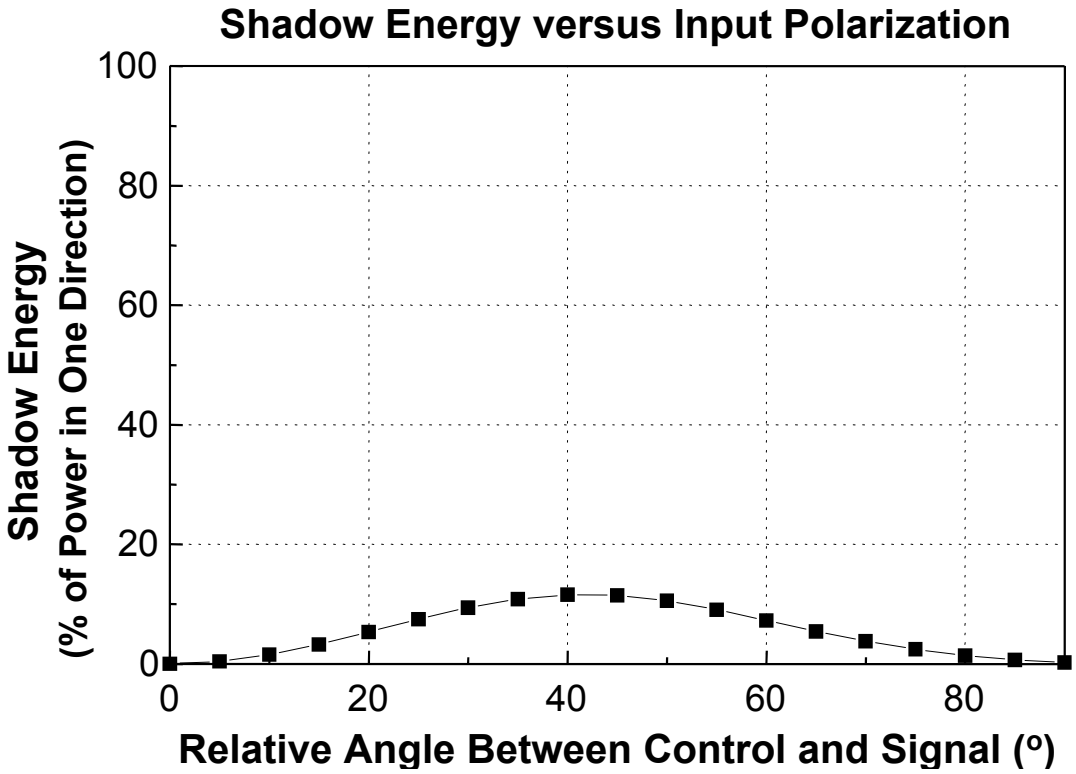
Shadow Energy versus Input Polarization
Shadow Energy
(% of Power in One Direction)
100
80
60
40
20
0
0
20
40
60
80
Relative Angle Between Control and Signal (º)

Figure 6

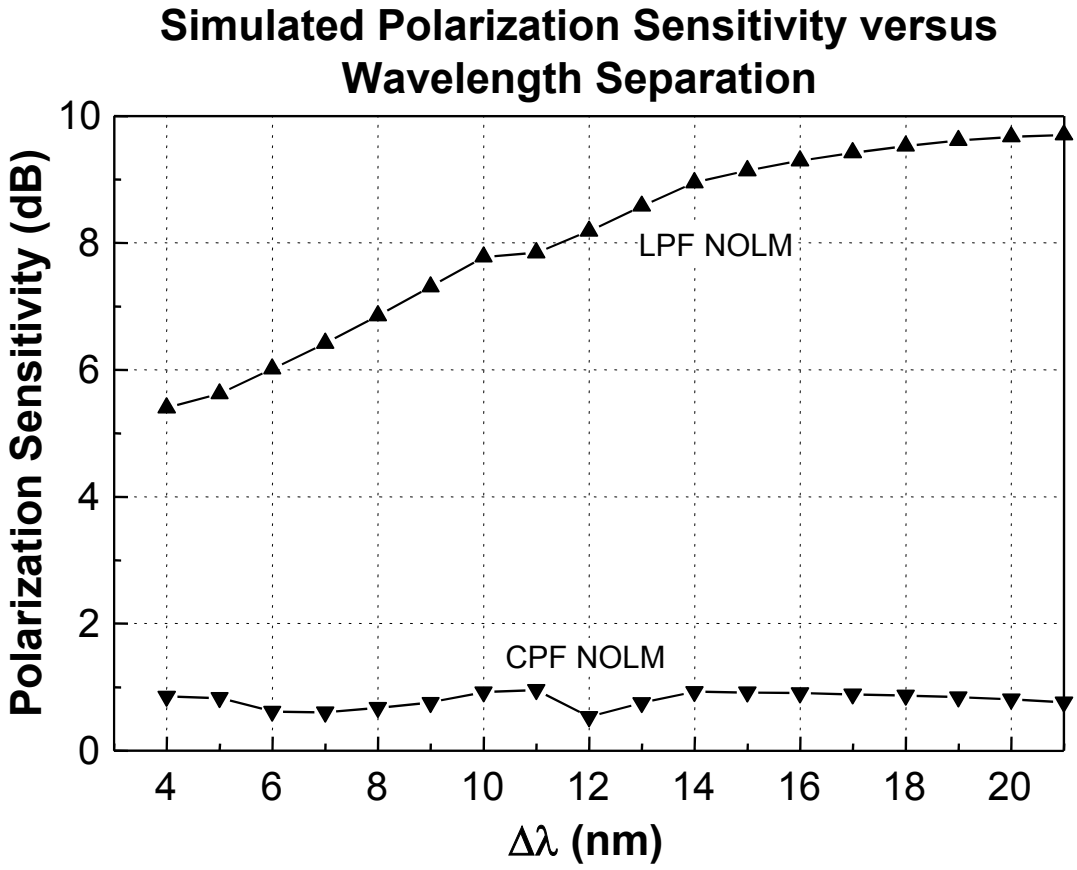
Simulated Polarization Sensitivity versus Wavelength Separation
Polarization Sensitivity (dB)
Δλ (nm)
LPF NOLM
CPF NOLM
0
2
4
6
8
10
4
6
8
10
12
14
16
18
20

Figure 7

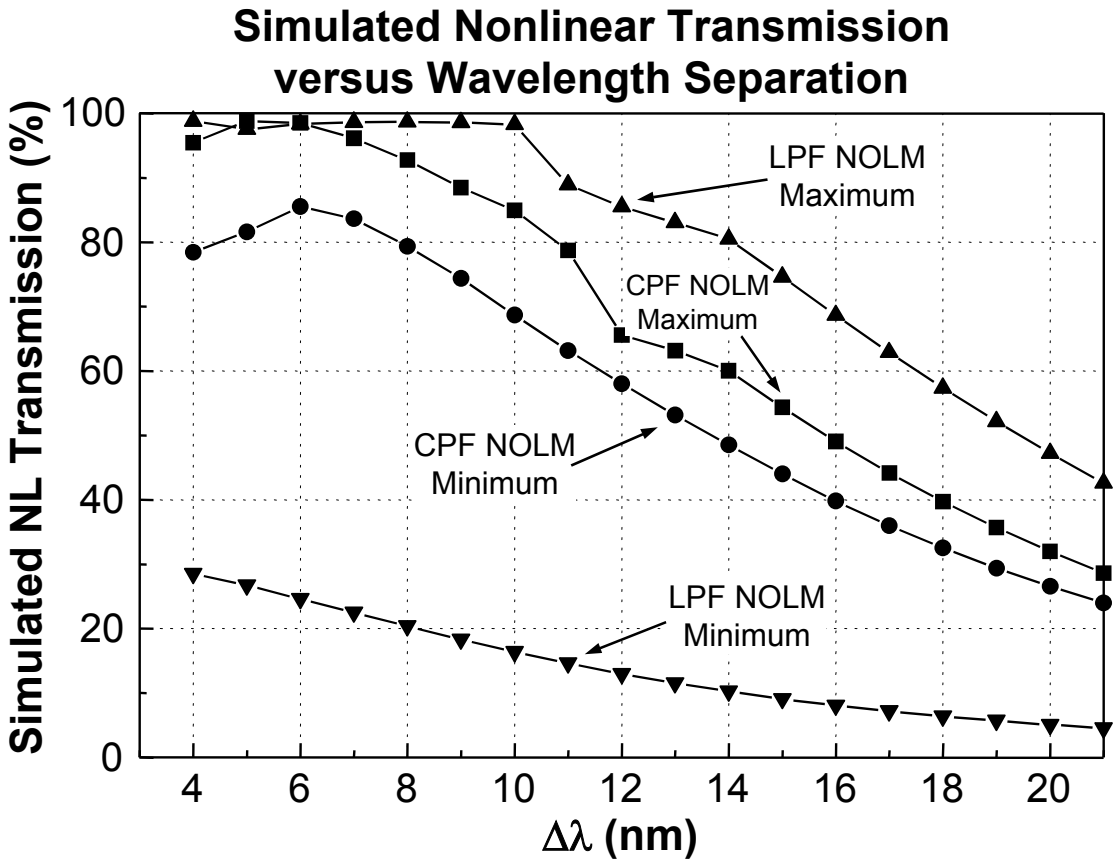
Simulated Nonlinear Transmission
versus Wavelength Separation
Simulated NL Transmission (%)
100
80
60
40
20
0
4
6
8
10
12
14
16
18
20
Δλ (nm)
LPF NOLM
Maximum
CPF NOLM
Maximum
CPF NOLM
Minimum
LPF NOLM
Minimum

Figure 8

Appendix I

Gain Enhancement in Cascaded Fiber Parametric Amplifier with Quasi-Phase Matching: Theory and Experiment

J. Kim, Ö. Boyraz, J. H. Lim, and M. N. Islam
Optical Sciences Laboratory
Department of Electrical Engineering and Computer Science
University of Michigan, Ann Arbor, MI 48109-2122. USA

Abstract

We report a novel gain enhancement scheme for fiber-optic parametric amplifiers utilizing cascaded amplification and quasi-phase matching. The theory and method of quasi-phase matching for four-wave mixing are developed for the first time to our knowledge. In experimental implementations of the theory, we achieve > 12 dB gain improvement in a 3-stage dispersion-shifted fiber parametric amplifier. 16 dB overall gain is obtained with 11 nm separation between zero-dispersion wavelength and pump wavelength. The experimental results show good agreement with theory and simulations. The influence of quasi-phase matching on spectral characteristics of parametric gain is investigated with numerical simulations.

Indexing Terms: Nonlinear optics, Nonlinear wave propagation, Optical fiber amplifiers, Optical fiber communication, Optical fibers, Optical frequency conversion, Optical parametric amplifiers, Optical propagation in nonlinear media

1. Introduction

Optical amplifiers operating outside of Erbium-doped fiber amplifier (EDFA) gain bandwidth are important for future broadband WDM systems. The parametric amplification (PA) process has been under intense research because it can amplify optical signals at arbitrary wavelengths [1,2]. In addition, the generation of phase-conjugate wave during PA process is a promising method for wavelength conversion that will play an important role in multi-wavelength optical networks. In practice, the low PA gain resulting from the weak nonlinearity of optical fiber and the requirement for phase matching have hindered its applications. Pumping near zero-dispersion wavelength (λ_o) [2] or the use of high nonlinearity fiber [3,4] have been proposed to enhance the gain. However, the unavoidable fluctuation of λ_o turns out to be detrimental to near-λ_o pumping scheme [5,6]. To avoid the resultant gain fluctuation, a large separation (> 10 nm) between λ_o and pump wavelength (λ_p) is preferred at the expense of higher dispersion and lowered gain. High nonlinearity fiber is not readily available for a variety of wavelengths and often causes extra loss and handling problems.

In present work, we enhance the low PA gain by cascading the PA processes. Simply extending the length of PA gain fiber results in phase mismatch and periodic fluctuation of the gain. To overcome the problem, we utilize the quasi-phase matching (QPM) concept that is popular in second-harmonic generation. For the first time to the best knowledge of the authors, we have developed the QPM theory for four-wave mixing (FWM) case. The theory gives information on the proper phase relation for maximum gain, the changes in phase relation during PA process, and its compensation. Similar theories have been reported in [4,7] for limited applications. We generalize them by obtaining explicit QPM conditions for single wavelength (called "QPM target wavelength") that can be applied to all wavelengths. The validity of the theory is verified experimentally and the effects of QPM on a broad range of wavelengths are investigated with simulations.

This paper is organized as follows: In section 2, we develop the theory and method for QPM in FWM. In section 3, the implementation and experimental results of QPM PA are presented and compared with theoretical predictions. Discussions on the spectrum and other properties of QPM PA follow in section 4.

2. Theory

The QPM by periodic inversion of domain has long been utilized in $\chi^{(2)}$ media to enhance the conversion efficiency. In inversion-symmetric $\chi^{(3)}$ media, including optical fiber, QPM requires change of a parameter other than domain polarity. The theory and experiment of QPM by periodic changes in optical power are reported in [8] and [9] emphasizing the generation of multiple-order sidebands rather than gain enhancement. The periodic change of fiber dispersion is utilized in FWM process for sideband suppression in fiber links [7] and compensation of dispersion in PA [4,6]. However, the detailed theory and method of QPM for cascading PA processes have not been reported yet.

The basic concept of cascaded PA with QPM is summarized in Fig. 1. The dotted curve shows the parametric gain of a non-QPM PA as a function of fiber length. Similar to second-

harmonic generation process in $\chi^{(2)}$ medium, the signal gain oscillates depending on the phase relation among the waves. To enhance the parametric gain, it is necessary to stop PA processes at each maximum gain point and introduce additional phase shift $\Delta\varphi_{add}$ to restore the phase relation as described in Fig. 2. The solid curve in Fig. 1 shows the enhanced gain of cascaded PA when adequate phase adjustment is introduced at each maximum gain point.

Implementation of QPM PA requires the knowledge of two parameters: the amount of relative phase shift $\Delta\varphi_{add}$ and the point of its introduction. In this work, we theoretically find them under the assumptions of a FWM process within periodic gain regime ($\lambda_p < \lambda_o$) in which three wavelength components are involved without pump depletion. Nonlinear effects caused by signal and conjugate waves are also ignored. The coupled-wave equations that govern the interactions are [1]

(1a)

$$\frac{dA_{s,c}}{dz} = i\cdot\left[\left(\Delta k + 2\cdot\gamma P_p\right)\cdot A_{s,c} + \gamma P_p e^{i\cdot 2\cdot\Phi_{po}}\cdot A^*_{c,s}\right]$$

(1b)

$$\frac{dA_p}{dz} = i\cdot\gamma P_p\cdot A_p$$

where γ is the nonlinear factor of the fiber, P_p is the peak pump power, and Φ_{po} is the initial phase of the pump wave. A_s, A_c, and A_p stand for signal, conjugate, and pump wave, respectively. Equation (1) has exact solution that can be best expressed in matrix form

$$\begin{bmatrix} A_s(z) \\ A^*_c(z) \end{bmatrix} = \begin{bmatrix} e^{i\cdot\Phi_p} & 0 \\ 0 & e^{-i\cdot\Phi_p} \end{bmatrix}\cdot\begin{bmatrix} a & b \\ b^* & a^* \end{bmatrix}\cdot\begin{bmatrix} |A_{so}|\cdot e^{+i\cdot\varphi_{so}} \\ |A_{co}|\cdot e^{-i\cdot\varphi_{co}} \end{bmatrix} \qquad (2)$$

where

$$\begin{aligned} a &= \cosh(g\cdot z) + i\cdot\frac{\kappa}{2g}\cdot\sinh(g\cdot z) \\ b &= i\cdot\frac{\gamma P_p}{g}\cdot e^{i\cdot 2\Phi_{po}}\cdot\sinh(g\cdot z) \\ \kappa &= \Delta k + 2\cdot\gamma P_p \\ g &= \sqrt{(\gamma P_p)^2 - \left(\frac{\kappa}{2}\right)^2} \end{aligned} \qquad (3)$$

and Φ_p is the nonlinear phase of the pump wave accumulated in the PA process and $|A_{so,co}|$ and $\varphi_{so,co}$ are the initial magnitude and phase of the signal and the conjugate wave, respectively [4]. The matrix elements a and b are complex numbers that determine the changes in amplitude and phase of signal and conjugate waves. They can also be represented by their magnitudes |a|, |b| and phases φ_a, φ_b, respectively. g is the parametric gain of the PA. In periodic gain regime ($\lambda_p < \lambda_o$), Δk is always positive and consequently g is always purely imaginary. Therefore the hyperbolic functions in (3) can be converted to corresponding trigonometric functions.

The maximum gain point for introduction of additional phase shift can be calculated by obtaining $|A_s(z)|^2$ in (2)

$$|A_s(z)|^2 = |a|^2 \cdot |A_{so}|^2 + |b|^2 \cdot |A_{co}|^2 + 2 \cdot |a||b||A_{so}||A_{co}| \cdot \cos(\varphi_a + \varphi_{so} - \varphi_b + \varphi_{co}). \qquad (4)$$

The first two terms are maximized at the point where $|a|^2 = 1 + [(\kappa/2|g|)^2 - 1] \sin^2 |g|z$ and $|b|^2 = (\gamma^2 P_p^2 / |g|^2) \sin^2 |g|z$ reach the maximum. They can be maximized simultaneously at L_{max} defined as

$$L_{max} = \pi/2|g| \qquad (5)$$

provided that $\kappa^2 > 4|g|^2$. Knowing that $|g|^2 = (\Delta k/2 + \gamma P)^2 - \gamma P^2$ when $\lambda_p < \lambda_o$ and using the definition of κ, it is straightforward to show that $\kappa^2 > 4|g|^2$ regardless of the magnitude of κ. L_{max} is analogous to the coherence length of second-harmonic generation. Due to the symmetric nature of the solution, the conjugate is maximized at the same length.

To determine the amount of additional phase shift, we first need to know both the initial phase relation that maximizes the signal power and then the change in phase relation caused by propagation and PA process. $\Delta\varphi_{add}$ is determined from the difference between them. The former can be obtained directly from the third term of (4). The expression is complicated in general. It can be simplified, however, by setting $z = L_{max}$. The resultant initial phase relation that maximizes the PA gain at L_{max} is

$$\Delta\varphi_o \equiv \varphi_{so} + \varphi_{co} - 2 \cdot \Phi_{po} = \pm 2n \cdot \pi \qquad (6)$$

where n is an integer. The induced change in phase relation is obtained by calculating $\varphi_s + \varphi_c - 2 \cdot \Phi_p$ at $z = L_{max}$ using (2) and (3). φ_s, φ_c, and Φ_p are phase angles of signal, conjugate, and pump wave, respectively. The result depends on the initial phases of signal and conjugate. Under the assumption that $\Delta\varphi_o = \pm 2n \cdot \pi$initially, it is easy to show that $\varphi_s + \varphi_c - 2 \cdot \Phi_p$ becomes $-\pi$ at L_{max}. In practice, $\Delta\varphi_o = \pm 2n \cdot \pi$ can be accomplished by fine-tuning of polarization controllers at the input of the PA.

We can conclude that the QPM in FWM is achieved by ensuring that input waves are in proper phase relation and subsequently introducing additional relative phase difference of

$$\Delta\varphi_{add} \equiv \Delta\varphi_s + \Delta\varphi_c - 2 \cdot \Delta\Phi_p = \pm\pi \qquad (7)$$

at each $L_{max} = \pi/2|g|$. $\Delta\varphi_s$, $\Delta\varphi_c$, and $\Delta\Phi_p$ are added phase shifts in signal, conjugate, and pump, respectively. $\Delta\varphi_{add}$ can be achieved by splicing a short section of high-dispersion fiber or a proper choice of phase response in all-pass optical filters. Note that the gain enhancement occurs only at QPM target wavelength that satisfies the condition of (5). The influences of QPM on other wavelength components will be discussed in section 4. It is also important to note that the gain maximization conditions are distinct from previous experimental [10] and numerical [11] results due to differences in problem definition. Perfect phase matching is assumed in [10] and pump depletion is considered in [11].

3. Experiment

We experimentally verify the enhancement of the gain in QPM PA. Figure 3 shows the experimental setup. For PA gain fiber, sections of dispersion-shifted (DS) fiber with λ_o = 1561 nm and dispersion-slope of 0.07 ps/nm^2-km are used. For both fibers, the value of nonlinear factor γ is 2.2 W^{-1}km^{-1}. We set the λ_o-λ_p separation to 11 nm to avoid the detrimental effect of λ_o fluctuation. Two laser diodes with wavelength of 1550 nm and 1556 nm are used as pump and signal, respectively. To maximize the peak pump power at the EDFA output, the pump wave is modulated to have 50 nsec width with 50:1 duty-cycle by an electro-optic modulator. The two waves are combined by a 70:30 coupler and amplified by a high power EDFA with 1 W saturation power. At the input to the PA gain fiber, the quasi-CW pump has 16 W peak power. The fact that the signal power is only 0.7% of the pump power justifies the assumptions made in the previous section.

Given the QPM target wavelength at 1556 nm, we set the length of PA gain fiber section to 50 m that is the maximum gain point according to (5). To introduce $\Delta\varphi_{add}$, we choose to use a section of SMF-28 fiber for its simplicity and availability. In highly dispersive SMF-28 fiber, only the linear phase shift is considered while the effect of nonlinear phase shift is ignored. The length of SMF-28 to introduce $\Delta\varphi_{add} = \pm\pi$ is calculated from the relation $\Delta\varphi_{add} \equiv \Delta k \cdot L_{SMF\text{-}28}$ and the standard linear phase mismatch formula

$$\Delta k = k_s + k_c - 2\cdot k_p = -2\pi c \cdot D_p \cdot (\lambda_p/\lambda_s - 1)^2$$

where D_p is the dispersion of the fiber at the pump wavelength. Substitution of experimental parameters shows that $\Delta k \cong -0.475$ [m^{-1}] and $\Delta\varphi_{add} = -\pi$ is obtained with 6.6 meters of SMF-28 fiber. With the basic information obtained so far, we implement a 2-stage (one SMF-28 section) and a 3-stage (two SMF-28 sections) QPM PA. At the output of PA, the signal portion is selected by an optical bandpass filter and detected with a photodetector. Since PA occurs only when the pump is present, the gain is calculated as a ratio of the peak and the trough. The contributions of ASE and residual pump are also measured and excluded from gain calculations. Along with the experiments, we have also simulated the PA processes using the matrix solution (2). The propagation loss of the fiber is not considered because of the shortness of the fiber in the setup (< 200 m). However, the splicing losses between two different types of fibers are included in the simulations as a power loss. Due to the technical difficulty in measuring the splicing loss, it is the only assumed variable in our simulations. For most cases, we use 0.4 dB power loss.

Figure 4 shows the gain enhancement of the 2-stage QPM PA as a function of SMF-28 fiber length that is varied from 0 to 18 m. The corresponding values of $\Delta\varphi_{add}$ are also plotted for reference. The maximum gain enhancement of 6.1 dB is achieved with 6 m of SMF-28 that sets $\Delta\varphi_{add}$ to $-\pi$ radian approximately. The gain enhancement is a periodic function of SMF-28 length since the integer multiple of 2π in $\Delta\varphi_{add}$ does not contribute to QPM. The mismatch between simulation and experimental data can be explained by high splicing loss between DS and SMF-28 fiber. Figure 5 shows the measured gain along the fiber. Two circles near the dotted-curves show the effect of QPM when 6 m or 10 m sections of SMF-28 is inserted at the 50 m point. While the insertion of 6 m SMF-28 enhances gain by 6.1 dB, the 10 m SMF-28 results in much less enhancement due to improper phase adjustment. Simulation and experimental data of non-QPM PA using the same setup is included for comparison.

The experimental results of 3-stage QPM PA are shown in Fig. 6 along with the simulation curve. Considering the higher loss from multiple splicing, we increase P_p to 17 W and accordingly reduce the length of the 2nd stage DS fiber to 40 m. The measured gain shows good agreement with the simulation. At the peak point near 140 m, the gain enhancement reaches 12.1 dB resulting in 15.9 dB overall parametric gain. The drop in gain near the peak point can be ascribed to the increased polarization effect from extended fiber length. In both 2- and 3-stage cases, the contribution of gain from a SMF-28 fiber section is less than 1 dB. Note that the gain in 2nd or 3rd stages (~6 dB) is almost twice the maximum achievable gain of the 1st stage (~3.5 dB) in log scale. This increase in maximum achievable gain results from the involvement of conjugate wave, which is absent at the input of the 1st stage, in the parametric amplification process.

4. Discussion

We numerically investigate the influence of QPM on PA gain spectrum for future applications in multi-wavelength systems. The simulation parameters are chosen in accordance with the experiment (QPM target wavelength at 5 nm away from λ_p). Perfect QPM is enforced by resetting the relative phase difference of the target wavelength component to zero at each L_{max}. We simulate up to the 5th stage and present the results in Fig. 7. At 5 nm wavelength offset, we obtain 28 dB gain enhancement with 5 stages. The gain spectra retain the original profile with only 3.2 nm reduction in 3 dB gain bandwidth.

Comparisons with previously reported experimental results are also performed to estimate the usefulness of the scheme. The 15.9 dB overall gain obtained with 17 W pump power, 150 m of DS fiber, and 11 nm λ_o-λ_p separation is comparable to the 18 dB maximum gain in [2] achieved with 7 W pump power, 200 m of DS fiber, and 0.8 nm λ_o-λ_p separation. Our result is also comparable to 20 dB maximum gain in [4] obtained with 8 W pump power, 40 m of high nonlinearity fiber, and 49 nm λ_o-λ_p separation when an order of magnitude difference in fiber γ is taken into consideration. The comparison shows that it is possible to enhance PA gain with large λ_o-λ_p separation by utilizing QPM technique.

The validity and limitation in theory are also examined based on experimental results. Figure 4 and 6 show good agreement between theory and experiment at output points and along the fiber, respectively. Main deviation occurs near the end of the 3rd stage (See Fig. 6). The limiting factors include: the loss from splicing two different types of fibers, the polarization effect, and technical difficulty of setting the initial phase relations between the pump and signal waves. Experimental investigation for the plausibility of 4~5 stage QPM PA is a natural extension of this work. The validity of the theory implies that the phase relations in parametric processes can be accurately tracked and manipulated. This QPM technique may be adopted in modulation instability regime (where $\lambda_p > \lambda_o$) to cope with the deviation from self-phase matched regime cause by pump depletion.

5. Conclusion

We have studied the theory and implementation of QPM PA. The theory of QPM in FWM developed in this work reveals that the QPM can be achieved by ensuring the proper initial phase relation and then by introducing additional relative phase difference $\pm\pi$ at every $L_{max} = \pi/2|g|$. We experimentally show the validity of the theory with 2- and 3-stage QPM PA. The 2-stage QPM PA experiments with varied amount of relative phase difference verify the theory. The 3-stage QPM PA experimental results also corroborate the theory by showing good agreement with the simulation. We achieve 15.9 dB overall gain and 12.1 dB gain enhancement over non-QPM PA with the 3-stage QPM PA. The simulation of gain spectrum shows that the QPM induces only 3.2 nm reduction in 3 dB gain bandwidth even with > 20 dB enhancement in parametric gain.

We suggest that QPM is a simple and effective method for enhancing the gain of fiber-optic PA while maintaining a wide separation between pump and zero-dispersion wavelength. Since the QPM results in flat gain spectrum between QPM target wavelengths, it can find the best application for wide band optical amplification in multi-wavelength communication systems

This work is supported by HRLD Foundation.

References

[1] R. H. Stolen and J. E. Bjorkholm, "Parametric amplification and frequency conversion in optical fibers," IEEE J. Quantum Elec., QE-18, pp. 1062-1072, Jul. 1982.

[2] M. E. Mahric, N. Kagi, T.-K. Chiang, and L. G. Kazovsky, "Broadband fiber optical parametric amplifiers," Opt. Lett., vol. 21, pp. 573-575, Apr. 1996.

[3] G. A. Nowak, Y.-H. Kao, T. J. Xia, and M. N. Islam, "Low-power high-efficiency wavelength conversion based on modulational instability in high nonlinearity fiber," Opt. Lett., vol. 23, pp. 936-938, Jun. 1998.

[4] M. E. Mahric, F. S. Yang, M.-C. Ho, and L. G. Kazovsky, "High-nonlinearity fiber optical parametric amplifier with periodic dispersion compensation," IEEE J. Lightwave Technol., LT-17, pp. 210-215, Feb. 1999.

[5] M. Karlsson, "Four-wave mixing with randomly varying zero-dispersion wavelength," J. Opt. Soc. Amer. B, vol. 15, pp. 2269-2275, Aug. 1998.

[6] K. Inoue, "Arrangement of fiber pieces for a wide wavelength conversion range by fiber four-wave mixing," Opt. Lett., vol. 19, pp. 1189-1191, Aug. 1994.

[7] H. Takahashi and K. Inoue, "Cancellation of four-wave mixing by use of phase shift in a dispersive fiber inserted into a zero-dispersion transmission line," Opt. Lett., vol. 20, pp. 860-862, Apr. 1995.

[8] F. Matera, A. Mecozzi, M. Romagnoli, and M. Settembre, "Sideband instability induced by periodic power variation in long-distance fiber links," Opt. Lett., vol. 18, pp. 1499-1501, Sept. 1993.

[9] K. Kikuchi, C. Lorattanasane, F. Futami, and S. Kaneko, "Observation of quasi-phase matched four-wave mixing assisted by periodic power variation in a long-distance optical amplifier chain," IEEE Photon. Technol. Lett., vol. 7, pp. 1378-1381, Nov. 1995.

[10] I. Bar-Joshep, A. A. Friesem, R. G. Waarts, and H. H. Yaffe, "Parametric interaction of a modulated wave in a single-mode fiber," Opt. Lett., vol. 11, pp. 534-536, Aug. 1986
[11] A. Vatarescu, "Light conversion in nonlinear monomode optical fibers," IEEE J. Lightwave Technol., LT-5, pp. 1652-1659, Dec. 1987.

Figure Captions

Figure 1: Concept of gain enhancement by cascading PA processes with QPM (Dashed: Parametric gain of non-QPM PA, Solid: Parametric gain of QPM PA)

Figure 2 : Concept of Phase Adjustment for QPM in FWM case

Figure 3: Experimental Setup (PC: Polarization Controller, LD: Laser Diode, EOM: Electro-Optic Modulator, OBPF: Optical Bandpass Filter, Det: Detector, OSC: Oscilloscope)

Figure 4 : Gain Enhancement vs. SMF-28 fiber length. The gain enhancement is maximized at a length that makes $\Delta\varphi_{add} = -\pi$. 0.4 dB splicing loss is assumed in simulations.

Figure 5 Experimental and simulation results of a 2-stage PA (Solid: PA gain without QPM, Dotted: PA gain with QPM)

Figure 6 : Experimental and simulation results of 3-stage QPM PA

Figure 7 : Gain Spectra of QPM PA with various numbers of stage

Appendix J

A Multi-Wavelength CW Source BASED on longitudinal mode carving of supercontinuum generated in fibers and noise performance

Özdal Boyraz, and Mohammed N. Islam

The University of Michigan, EECS Department Room # 1214, Ann Arbor MI 48109

Abstract

We experimentally demonstrate novel multiple wavelength continuous wave (CW) sources based on longitudinal mode carving of supercontinuum (SC) generated in optical fibers. We show that by longitudinal mode carving of the SC we can generate > 600 wavelength channels with 10 GHz precise channel spacing and -6 dBm/Ch power level at the > 48 nm flat region (±0.5 dB spectral uniformity) of the SC. By full utilization of the generated SC, the channel count exceeding 1600 can be accomplished. Moreover, we study the noise performance of the carved CW signals experimentally and theoretically. Experimentally, we measure the relative intensity noise (RIN) to characterize the noise performance of the generated CW signals. An average RIN value of –107 dB/Hz is obtained. Compared to the CW sources carved directly from the pump laser a 4 dB/Hz RIN degradation is measured. The two main reasons behind the high RIN values are determined to be the frequency instability and the low side-mode suppression ratio of the pump laser. Experimentally we confirm that combined effect of the frequency instability and the low side-mode suppression ratio of the pump laser can degrade the RIN as much as ~30 dB/Hz. Theoretically, we estimate the lowest achievable RIN values as -160 dB/Hz and -144 dB/Hz RIN after the EDFA and the SC fiber, respectively. These results indicate that starting with a stable pump laser, CW lasers with <-140 dB/Hz RIN can be achieved.

A Multi-Wavelength CW Source BASED on longitudinal mode carving of supercontinuum generated in fibers and noise Performance

Özdal Boyraz, and Mohammed N. Islam
The University of Michigan, EECS Department Room # 1214, Ann Arbor MI 48109

Introduction

Wavelength division multiplexing (WDM) systems with very dense channel spacing is an attractive option for providing increased capacity in both short distance and long distance lightwave transmission systems. As the current demand moves toward building dense WDM (DWDM) systems with 25 GHz or less channel spacing, providing a low noise multiple wavelength continuous wave (CW) source with very high wavelength accuracy, high amplitude stability, and high brightness is the key challenge. Since passive filters set its wavelength stability, WDM sources carved from a broadband light source can satisfy current demand in wavelength stability. In our experiments, we show that novel CW WDM sources based on longitudinal mode carving of supercontinuum (SC) generated in optical fibers will be a strong candidate for future optical networks because of its low amplitude noise degradation (<4 dB/Hz), broad bandwidth (>140 nm), high brightness (>-6 dBm/Ch), high amplitude uniformity (±0.5 dB), high wavelength stability and periodicity.

The spectrum-slicing scheme for generating a continuous wave (CW) source, which is compatible to operate in NRZ formats, has been searched by several groups. By spectral slicing of 40 nm amplified spontaneous emission (ASE) spectra 1.7 Gb/s data transmission over 165 km dispersion shifted fiber has been demonstrated [1]. In a similar approach, Holloway *et al*. has demonstrated CW generation by spectral slicing of ASE from a Fabry-Perot laser, which is biased below threshold [2]. However, the performance of CW sources generated by these two techniques is limited by the intrinsic spontaneous-spontaneous beat noise due to incoherent nature of the ASE. This beat noise increases with decreasing channel bandwidth and limits the channel density of the communication system. In a different approach, Sanjoh *et al.* has demonstrated CW generation by spectral slicing of longitudinal modes of modelocked semiconductor laser [3]. However, the bandwidth and the spectral shape of the modelocked laser limit maximum achievable channel count and spectral uniformity, respectively. In a similar approach, 13 channel CW carving with 10 dB spectral uniformity and 64 GHz channel spacing has been demonstrated by using an externally modulated DFB laser followed by 31 km dispersion shifted fiber to generate spectral broadening [4]. Similar to the previous method the channel count and spectral uniformity is limited by the amount of self-phase modulation (SPM) in the dispersion-shifted fiber.

In this paper, we present the novel CW generation scheme for DWDM applications by utilizing the longitudinal modes of the SC generated in optical fibers and its noise performance. Previously, we have demonstrated the pulsed WDM source and its coherence properties by using the similar SC setup [5]. In the current experiment, we demonstrate that by longitudinal mode carving of SC spectra up to 1600 CW channels can be achieved with 10 GHz precise channel spacing over 140 nm spectral bandwidth, where

the wavelength stability and the channel spacing of the carved signals are set by the wavelength stability and the repetition rate of the pump laser, respectively [6]. By using the flat region of the SC, >600 CW channels with ±0.5 dB spectral uniformity and –6 dBm per channel power level are achievable. As a figure of merit, we measure the relative intensity noise (RIN) of the generated CW. We start with RIN measurement of the CW signals before and after the SC fiber by using the conventional RIN and measurement technique. Experimentally, we measure the average RIN value of –107 dB/Hz for the CW signals carved from the SC spectra. Compared to the CW signal carved from the pump laser, RIN degradation of <4 dB/Hz is measured. Sources of high RIN values are also investigated.

The frequency stability and side mode suppression ratio of the pump laser, ASE generation in the EDFA and the amplification of the ASE in the SC fiber are found to be the four reasons for the high RIN values. Based on the experimental research on the actively modelocked fiber lasers, we show that the RIN is mainly limited by the frequency instability and the low side mode suppression ratio of the modelocked laser used for SC generation. After frequency stabilization of the modelocked laser, RIN value of the CW carved directly from the pump laser is decreased to –120 dB/Hz from –111 dB/Hz at the frequency values coincide with the fundamental cavity modes. However, RIN values as low as ~ -148 dB/Hz are measured at frequencies between fundamental cavity modes of the laser. These result shows that side mode suppression ratio of the modelocked laser has significant contribution in high RIN values. Since the coherence of the SC is preserved, we expect that, signal-spontaneous and spontaneous-spontaneous beat noise will have tolerable effect on RIN values [5]. In a theoretical study, we show that the lowest RIN value of –160 dB/Hz is achievable after the amplifier. We also show that amplification of ASE by modulational instability during SC generation degrades RIN values. The results indicate that coherence degradation raises the minimum RIN value to –144 dB/Hz. The results also show that starting with a stable pulse source with RIN <-150 dB/Hz, a stable multiple wavelength CW source with < -140 dB/Hz RIN value, which is an acceptable level for commercial applications, is achievable.

The outline of the paper is as follows. In section II, we will describe the experimental setup used for SC generation and CW carving. The experimental results including the generated SC and RIN measurements will be presented. In section III, the effect of laser stabilization on RIN will be discussed. Limitations of harmonically modelocked lasers will also be presented in the same section. Theoretical results of RIN degradation in EDFA and in SC fiber will be presented in section IV. Section V contains a discussion of possible system applications of the short fiber SC generation as a DWDM source as well as its advantages. Finally, section VI summarizes our findings.

Experimental Results of CW Generation

The experimental setup used in multi-wavelength CW generation by longitudinal mode carving is shown in Fig 1. As a pump laser, we use an actively mode-locked fiber laser, which generates 10 GHz train of squared hyperbolic secant pulses with 1.2 psec pulsewidth and $\Delta\tau\Delta\nu = 0.32$ at 1552 nm. By using a high power EDFA, the pulse train is amplified to an average power of 800 mW. Following the EDFA, three sections of fibers are used for SC generation [7,5]. The first two sections are mainly used for pulse compression by soliton effect pulse compression scheme. The combined effect of third

order dispersion and SPM is utilized in the last section to generate the SC. The fibers used for SC generation are 6.8 meters of SMF-28 fiber followed by 15.7 meters of dispersion shifted fiber with λ_0 = 1492 nm. The last section is 6.6 meters of another dispersion shifted fiber with λ_0 = 1546 nm. Due to difficulty in finding narrow band optical filters with <10 GHz bandwidth, longitudinal mode spacing of the SC increased to 40 GHz by using a pulse interleaver. The pulse interleaver is made of two 1X4 couplers spliced to each other with 25 ps relative delay in each arm. As a band-pass filter, we use a monochromator to carve out the longitudinal modes of the generated SC. The resolution of the monochromator is ~6. The bandwidth of the filter is 30 GHz at 20 dB level. An optical spectrum analyzer is used to characterize the spectral features of the generated SC and the carved CW signal. We use a 10 MHz low noise optical detector to detect the carved CW. Noise performance of the carved CW signals is characterized by using an RF spectrum analyzer and a scope after the detection.

Figure 2a shows the normalized 10 Gb/s SC spectra generated in three sections of conventional dispersion-shifted fibers. The 20 dB bandwidth measured from the peak is 140 nm. On anti-Stokes side, we obtain ±0.5 dB flatness over 48 nm (6.34 THz). The average power spectral density over the flat region is measured to be 4.2 dBm/nm. On Stokes side, a spectral peak with 30 nm bandwidth (3.59 THz) at 3 dB point is obtained. The power spectral density of 7.48 dBm/nm or higher is measured on the Stokes side. By using a different configuration of SC fibers, the power spectral density of the SC can be increased to > 7 dBm/nm over the flat region. Similarly, 20 dB bandwidth of the SC can be increased to >250 nm with ±0.5 dB spectral uniformity over 80 nm by using high nonlinearity fibers [5].

CW generation by longitudinal mode carving is done after quadrupling the repetition rate to 40 Gb/s by 4 bit interleaver. Magnified SC spectra after the bit interleaver is shown in Fig 3a. A ~13 dB of modulation depth is obtained, and this modulation depth of the longitudinal modes is mainly set by the resolution of the optical spectrum analyzer (~6.3 GHz) and the polarization sensitivity of the bit interleaver. By using the monochromator as a bandpass filter, we carve out each individual mode to generate a CW signal. Figure 3b shows the typical CW spectrum obtained by spectral slicing of the SC. The line width of the CW signal is also set by the resolution of the optical spectrum analyzer used in the experiment.

Relative intensity noise (RIN) is one of the measurements used for characterizing the noise performance of the CW signals. RIN defines the ratio of noise power at every frequency to the average DC power level and it is formulated as

$$RIN = 10*\mathrm{Log}\left(\Delta P / P_{ave} \right) \quad [\mathrm{dB/Hz}]$$

where ΔP [W/Hz] describes the power spectral density of the amplitude noise and P_{ave} describes the average DC power obtained from the CW signal [8]. RIN values across the SC spectra are calculated after measuring ΔP and P_{ave} values experimentally. Average DC power level is measured by using a scope with a 50 ohm input impedance after detecting the generated CW signal by a 10 MHz low noise detector. The power spectral density of the noise distribution (ΔP) is measured by using an RF spectrum analyzer with a bandwidth of 6 GHz. Figure 4 shows the calculated RIN values at different wavelengths across the SC spectra. The results show that the carved CW signals have average RIN of –107 dB/Hz with variation of a ~4 dB/Hz. We also measure the RIN of a CW signal carved

directly from the pump without SC fiber. The results indicate that -111 dB/Hz RIN is achievable by CW carving from a modelocked laser, and <4 dB/Hz RIN degradation occurs during the SC generation. Since the experiment has started with a noisy laser, the effect of the EDFA noise figure on RIN is calculated to be ~2.5 dB degradation. The 1.5 dB degradation can be attributed to ASE amplification due to four wave mixing process during the SC generation. The RIN degradation in the case of stable laser will be calculated in following sections. In any case, the results confirm that the pump laser used for SC generation ultimately sets the lowest limit of the achievable RIN value.

Effect of Laser Stabilization

In the second phase of the experiment, we study the effect of the laser stability on relative intensity noise. In our experiment, we are using an actively modelocked fiber laser with σ cavity configuration [9]. Recently, the amplitude stability and the pulse dropout characteristics of the σ lasers have been studied theoretically and experimentally [10,11]. Since we are using longitudinal mode carving technique to generate CW signal, frequency (mode) stability of the fiber laser is the main concern. Since the filter position is fixed to certain frequency to carve out a CW signal in the experiment, any changes in the laser frequency translates into amplitude noise by the fixed CW carving filter. Experimentally, we measure the highest RIN value as -107 dB/Hz RIN at frequencies between 20 kHz to 400 kHz. This peak RIN value moves to different frequencies randomly. The same RIN pattern repeats itself for the CW signals carved from the pump laser as well. This result shows that random changes in laser frequency translate into RIN during the CW carving. Theoretically, the frequency instability of the laser arises from the fact that the laser cavity has the fundamental repetition rate of ~2.3 MHz. To obtain a pulse train with 10 GHz repetition rate every ~4300th modes are selected by the harmonic modelocking scheme [12]. Since there is no active component in the cavity to determine which super-modes will be selected during the modelocking, lasing modes change randomly with any perturbation in the cavity. This frequency instability can also cause amplitude noise through beating of different frequencies [12].

Frequency stabilization of the pump laser is realized by inserting a Fabry-Perot filter with fixed free spectral range into the laser cavity. Figure 5 shows the modified laser cavity. A solid etalon with free spectral range of 10 GHz and finesse of ~67, is placed in the unidirectional ring portion of the laser cavity in order to eliminate the back reflection from the etalon going back into the laser cavity. By placing the etalon, we observe stable pulse train with 100 ps separation and higher frequency stability, which is set by the finesse of the etalon. Figure 6 shows the RF spectrum of the detected pulse train. The side mode suppression ratio of the pulse train is measured to be ~65 dB for the best case. However, due to 4 dB insertion loss of the etalon used in the experiment, output pulse width is increased to 8 ps from 1.2 ps. By choosing low loss components, stable short pulses can be generated. Although the pulse broadening due to high loss makes it difficult to generate SC in short fibers without additional pulse compression before the SC generation, it makes easy to understand RIN degradation due to frequency instability of the laser.

The amplitude noise distribution of the CW signal carved from the pump laser is shown in Fig 7. To calculate the RIN values, the average signal power at the detector output is measured by an oscilloscope and the noise power distribution is measured by an

RF spectrum analyzer. Mainly we obtain two different RIN values: RIN at the frequencies the same as the harmonics of the fundamental laser cavity frequency and at the frequencies in between. When the side mode suppression ratio is about 63 dB, RIN values at the frequencies the same as the super modes of the laser cavity are calculated to be –120 dB/Hz. This result shows only 9 dB/Hz improvement compare to the previous results. However, at the frequencies in between super modes RIN value goes down to as low as –148 dB/Hz. Moreover, by adjusting the quality of the modelocking, we observe that side mode suppression ratio of the laser changes the RIN values. Higher RIN values are obtained with a modelocking position with lower side mode suppression ratio. These results indicate that the low side mode suppression ratio of the active modelocking is the second limitation of obtaining a stable CW signal by longitudinal mode carving. However, obtaining as low as –148 dB/Hz RIN value at frequencies between the cavity modes indicates that stable CW sources can be obtained by using a stable pulsed laser by longitudinal mode carving. Since it will not have a problem of side mode suppression ratio like in modelocked lasers, an externally modulated short pulse source will be the best approach for a pump source.

RIN Degradation in EDFA and SC Fiber

RIN degradation due to amplification and SC generation is also studied theoretically. To calculate the RIN degradation, we estimate the amount of ASE accumulation after the EDFA and the SC fiber. From the estimated ASE power, we can calculate the amount of the photocurrent generated due to noise and the signal. Mainly we focus on the two effects; noise current due to spontaneous-spontaneous beating and noise current due to signal-spontaneous beating [13]. For calculation purposes, we assume an ideal detection system with negligible circuit noise. We also ignore the effect of side mode suppression ratio and assume that we start with an externally modulated laser source. The photocurrents generated by the noise and the signal are formulated as

$$I_{ASE} = e.\eta.m.n_{sp}.(G-1).B_o$$

$$I_i = e.\eta.G.P_i / h\nu_s$$

$$I^2_{s-sp} = 4I_{ASE} I_i B_e /(m.B_o)$$

$$I^2_{sp-sp} = 2I^2_{ASE} B_e /(m.B_o)$$

where I_{ASE} defines the generated DC current due to ASE, I_i defines DC photocurrent due to signal, $I_{s\text{-}sp}$ defines the noise current generated due to signal-spontaneous beating and $I_{sp\text{-}sp}$ defines the generated noise current due to spontaneous-spontaneous beating [13]. The parameter η is quantum efficiency of the detector, e is electron charge, G is gain, n_{sp} is the spontaneous emission factor of the amplifier, m is the number of amplifier modes, and P_i is the optical input power to the amplifier. B_e and B_o defines the electrical bandwidth of the detector and the optical bandwidth of the filter, respectively. The noise and signal power levels are calculated by using the formula

$$\Delta P = (I_{sp-sp}^2 + I_{s-sp}^2).R$$

$$P = (I_{ASE}^2 + I_i^2).R$$

where R is the input impedance of the diagnostics.

Figure 8 shows the changes in RIN values due to ASE accumulation in the EDFA. For calculations we use m = 2, n_{sp} = 1.7, G = 80, P_i = 10 mW, B_e = 10 MHz, and B_o = 30 GHz. The analytical calculations indicate that for low initial RIN values, the ASE power limits the lowest achievable RIN value. RIN values as low as –160 dB/Hz can be achieved by spectral slicing of longitudinal modes when we start with a very stable source. Since the generated ASE will dominate the source noise after the EDFA, the saturation near –160 dB/Hz occurs. As the RIN of the pump laser increases, the RIN of the EDFA output is set by the initial RIN value of the source and the ASE generation inside the EDFA has a minimal effect on RIN values. According to Fig 8, the experimental RIN value of –148 dB/Hz at the frequencies in between the fundamental cavity modes indicates that our source laser has the initial RIN of ~-150 dB/Hz.

We also calculate the RIN degradation due to SC generation. In our previous work, we have demonstrated that SNR of the generated SC is degraded ~20 dB at 60 nm away from the pump wavelength due to amplification of ASE noise by modulational instability [5]. For the purpose of RIN degradation modeling, we consider a noise free SC source followed by an EDFA with unity gain and 20 dB noise figures. This 20 dB noise figure is the extreme case for RIN degradation and it increases the spontaneous emission factor n_{sp} by nearly 25 times [14]. Therefore, an n_{sp} value of 50 is a conservative estimation in this case. Figure 9 shows the variation of RIN values due to amplification and the SC generation. The results indicate that ultimate value of the RIN is set by the coherence degradation during the SC generation. Even though we start with a very stable laser, the ASE generation in the EDFA and the ASE amplification during the SC generation will saturate the RIN value. According to the results, RIN values as low as –144 dB/Hz are still achievable when we start with a laser with initial the RIN < -150 dB/Hz to generate the SC. For the initial RIN values of >-145 dB/Hz, the quality of the CW source generated by the longitudinal mode carving is limited by the pump laser.

Discussion

The experimental results show that, because of its large bandwidth, >140 nm, and uniformity, ±0.5 dB over 48 nm, the SC generation is a potential multiple wavelength CW source with precise channel spacing, where the channel spacing is set by the repetition rate of the pump laser and low noise degradation. However, the noise performance is the main limitation for using the longitudinal mode carving of SC in communication systems. In general, RIN value of -110 dB/Hz is considered high for a communication system with long distance propagation. However, this value is not an intrinsic limitation of the method we are using, it is a limitation of the laser used in the current experiment. Moreover, since the propagation of incoherent CW signals with 1.3 nm bandwidth carved from ASE spectra through 165 km of dispersion shifted fiber have already been shown, the coherent CW signal from coherent SC generation can be used in long distance propagation systems [1]. When we start with a stable pulse source like an externally modulated CW source to obtain

a short pulse pump source, CW signals with RIN values as low as -144 dB/Hz are achievable and it can accommodate any channel spacing, which is set by the repetition rate of the pump laser. On the other hand, RIN of the incoherent sources are intrinsically limited by the spontaneous-spontaneous beat noise. The maximum capacity is also estimated as 47 Gb/s for 40 nm ASE source, as opposed to 140 nm SC source. Moreover, the RIN value also increases drastically due to incoherent nature of the ASE source with decreasing filter bandwidth and channel spacing. For example, the lowest theoretical achievable RIN values by using a 0.08 nm and 1.3 nm rectangular filter are estimated as -100 dB/Hz and -112 dB/Hz, respectively [8].

For lower RIN values, starting with a stable coherent source is a necessity to overcome the high RIN value problem. The actively modelocked lasers has intrinsic limitations of frequency instability and low side mode suppression ratio when they are used for generating SC. In the first limitation of frequency instability, any random changes in the laser wavelength are translated into the amplitude noise due to fixed CW carving filter. However, this limitation can be solved by using broadband filters at the expense of high channel count. The side-mode suppression ratio is also an intrinsic property of modelocked lasers. The beating of the carved CW signal and these totally unsuppressed side modes are the second largest sources of high RIN values (-120 dB/Hz). Using an externally modulated DFB laser with low RIN can be a solution to pump limitations if short pulses are obtained after the external modulation to generate SC. Although coherence degradation during the SC generation is the other limitation due to signal-spontaneous beat, RIN values of -144 dB/Hz at 60 nm away from the pump source shows that commercial CW sources can be generated despite the coherence degradation. Therefore, starting with a stable pump source >1600 WDM channels with precise 10 GHz spacing and <-140 dB/Hz RIN vales can be obtained for commercial applications.

Summary

In summary, we experimentally demonstrate that longitudinal modes of the SC generated in optical fibers can be used as a CW source. Because of its large bandwidth, >140 nm at 20 dB point, uniformity, ±0.5 dB over 48 nm, SC sources can generate a multiple wavelength CW source with high wavelength stability and perfect channel spacing, which is set by the repetition rate of the pump laser. Based on the 10 GHz repetition rate, >600 wavelength CW channels can be carved with –6 dBm/ch power level and 10 GHz exact channel separation. With full utilization of the whole SC spectra, channel count exceeding 1600 can be achieved. In our experiments, we study the noise performance of the carved CW signals and we measure the average RIN value of –107 dB/Hz with 4 dB/Hz degradation compared to the pump laser. Experimental results show that the frequency instability and the low side mode suppression ratio of the pump laser are the main sources of the RIN. Frequency stabilization of the laser reveals that as low as –148 dB/Hz RIN values can be achieved after the EDFA. These results show that using a stable pump source for SC generation is essential for low noise CW source generation. Numerical results indicate that the EDFA and the coherence degradation during the SC generation also increase the RIN values. However, the spontaneous-spontaneous and signal-spontaneous beat noises are not main limitation of CW sources by longitudinal mode carving. The lowest achievable RIN values after the EDFA and the SC fiber are calculated to be –160 dB/Hz and –144 dB/Hz, respectively.

References:

1. Y. C. Chung, J. S. Lee, R. M. Derosier, and D. J. DiGiovanni, "1.7 Gbit/s transmission over 165 km of dispersion-shifted fiber using spectrum sliced fiber amplifier light source," *Electronics Lett.,* vol. 30, No. 17, pp. 1427-1428, 1994.
2. Warwick T. Holloway, Adrian J. Keating, and David D. Sampson, " Multiwavelength source for spectrum-sliced WDM access networks and LAN's," *IEEE Photonics Technology Lett.,* vol. 9, No. 7, pp. 1014-1016, 1997.
3. Hiroaki Sanjoh, Hiroshi Yasaka, Yoshihisa Sakai, Kenji Sato, Hiroyuki Ishii, and Yuzo Yoshikuni, "Multiwavelength light source with precise frequency spacing using a mode-locked semiconductor laser and arrayed waveguide grating filter," *IEEE Photonics Technology Lett.,* vol. 9, No. 6, pp. 818-820, 1997.
4. J. J. Veselka, and S. K. Korotky, "A multiwavelength source having precise channel spacing for WDM systems," *IEEE Photonics Technology Lett.,* vol. 10, No. 7, pp. 958-960, 1998.
5. Ö. Boyraz, J. Kim, M. N. Islam, F. Coppinger, and B. Jalali, "10 Gb/s multiple wavelength, coherent short pulse source based on spectral carving of supercontinuum generated in fibers," *Journal of lightwave Technology,* vol. 18, No. 12, pp. 2167-2175, 2000
6. Jaeyoun Kim, Özdal Boyraz, and Mohammed N. Islam, "150^{+} Channel Ultra-DWDM Source with Nx10 GHz Spacing Utilizing Longitudinal Mode Slicing of Supercontinuum," *OFC'00*, paper ThA2, 2000.
7. G. A. Nowak, J. Kim, and M. N. Islam, "Stable supercontinuum generation in short length of conventional dispersion-shifted fiber,", *Applied Optics*., vol. 38, No. 36, pp. 7364-7369, 1999.
8. Dennis Derickson, *Fiber Optic Test and Measurement,* New Jersey: Prentice Hall PTR, 1998.
9. Thomas F. Carruthers, and Irl N. Duling III, "10 GHz, 1.3 ps erbium fiber laser employing soliton pulse shortening," *Optics Lett.,* vol. 21, No. 23, pp. 1927-1929, 1996.
10. Moshe Horowitz, and Curtis R. Menyuk, "Analysis of pulse dropaout in harmonically mode-locked fiber lasers by use of the Lyapunov method," *Optics Lett.,* vol. 25, No. 1, pp. 40-42, 2000.
11. Thomas F. Carruthers, Irl N. Duling III, Moshe Horowitz, and Curtis R. Menyuk, "Dispersion management in a harmonically mode-locked fiber soliton laser," *Optics Lett.,* vol. 25, No. 3, pp. 153-155, 2000.
12. G. T. Harvey, and L. F. Mollenauer, "Harmonically mode-locked fiber ring laser with an internal Fabry-Perot stabilizer for soliton transmission," *Optics Lett.,* vol. 18, No. 2, pp. 107-109, 1993.
13. C. R. Giles, E. Desurvire, J. L. Zyskind, and J. R. Simpson, "Erbium-doped fiber amplifiers for high speed fiber optic communication systems," *SPIE conf. Fiber Lasers Amplifiers*, (Boston, MA), Paper 1171-32, 1989
14. C. R. Giles, E. Desurvire, J. L. Zyskind, and J. R. Simpson, "Noise performance of erbium doped fiber amplifier pumped at 1.49 μm, and application to signal pre-amplification at 1.8 Gbits/s," *IEEE Photonics Technology Lett.,* vol. 1, No. 11, pp. 367-369, 1989.

Figure Captions:

Figure 1. The experimental setup used for CW generation by longitudinal mode carving. The longitudinal modes of the 10 GHz SC is carved by a monochromator to obtain a multiple wavelength CW source. Relative intensity noise (RIN) is measured to characterize the noise performance of the CW signals.

Figure 2. The normalized supercontinuum spectra generated in conventional DS fibers. We measure 140 nm bandwidth with ±0.5 dB uniformity over 48 nm. Power spectral density is measured to be 4.2 dBm/nm over the flat region.

Figure 3. a) The magnified SC spectra after the interleaver. The repetition rate of the generated SC is increased to 40 Gb/s to eliminate difficulty in filtering the modes 10 GHz apart. b) Typical spectrum of the generated CW signals after the longitudinal mode carving.

Figure 4. Relative intensity noise (RIN) values of the carved CW signals. The noise performance of the generated CW signals is characterized by RIN measurement. Average RIN value of –107 dB/Hz is obtained. <4 dB/Hz RIN degradation is measured compared to the CW carved directly from the pump laser.

Figure 5. The pump laser is modified increase frequency stability. By inserting a solid etalon with 10 GHz free spectral range and finesse of 67, mode shifting of the laser is eliminated.

Figure 6. RF spectrum of the modelocked laser after stabilization is measured. Side mode suppression ratio of ~65 dB is obtained.

Figure 7. RIN distribution of the CW signals carved directly from the pump laser. Maximum RIN value of –120 dB/Hz is measured. RIN value is set by the side mode suppression ratio of the modelocked laser. In between the cavity modes RIN values as low as –148 dB/Hz is obtained.

Figure 8. RIN degradation due to EDFA is calculated. For RIN values <-160 dB/Hz, ASE sets the RIN value to ~-160 dB/Hz. For initial values >-160 dB/Hz the EDFA has minimal effect.

Figure 9. RIN degradation due to SC generation is calculated. Coherence degradation during the SC generation sets the lower limit of the RIN value as –144 dB/Hz. For initial RIN values >-145 dB/Hz the coherence degradation has minimal contribution and the final RIN value is set by the initial condition.

Appendix K

10 Gb/s MULTIPLE WAVELENGTH, COHERENT SHORT PULSE SOURCE BASED ON SPECTRAL CARVING OF SUPERCONTINUUM GENERATED IN FIBERS

Ö. Boyraz, J. Kim, and M.N. Islam

The University of Michigan, EECS Department Room # 1214, Ann Arbor MI 48109

F. Coppinger, and B. Jalali

The University of California, Electrical Engineering Department, Los Angeles CA

90095

Abstract:

We demonstrate a high power, multi-wavelength, short pulse source at 10 Gb/s based on spectral slicing of supercontinuum (SC) generated in short fibers. We show that short fiber SC can be used for dense wavelength division multiplexing applications because of its >7.9 dBm/nm power spectral density, 140 nm spectral bandwidth, and ±0.5 dB spectral uniformity over 40 nm. Pulse carving up to 60 nm away from the pump wavelength and CW generation by longitudinal mode carving indicates that the coherence of the SC is maintained. By using high nonlinearity fibers the spectral bandwidth is increased to 250 nm, which can accommodate >600 wavelength channels with 50 GHz channel spacing and >6 Tb/s aggregate data rate. We also calculate the coherence degradation due to amplification of incoherent energy during the SC generation. Theoretical results show that the SC generation in short fibers has 13 dB higher signal to noise ratio compared to the SC generated in long fiber.

10 Gb/s MULTIPLE WAVELENGTH, COHERENT SHORT PULSE SOURCE BASED ON SPECTRAL CARVING OF SUPERCONTINUUM GENERATED IN FIBERS

Ö. Boyraz, J. Kim, and M.N. Islam

The University of Michigan, EECS Department Room # 1214, Ann Arbor MI 48109

F. Coppinger, and B. Jalali

The University of California, Electrical Engineering Department, Los Angeles CA 90095

Introduction

Due to fast growth in Internet technology, demand for bandwidth is estimated to exceed 1 Tb/s by year 2002 with a further doubling every two years. Utilizing the entire 40 THz low loss transmission window of the silica fibers is one of the ways to answer this growth other than using multiple fiber links. The preferred approach to utilize the low loss transmission window of silica fibers with the current technology is to use the combined techniques of optical time division multiplexing (OTDM) and wavelength division multiplexing (WDM). For a high spectral efficiency, large channel count system, a key enabling technology is a multiple wavelength high repetition rate source with large and uniform bandwidth, accurate wavelength spacing, high coherence and high power spectral density.

Dense wavelength division multiplexing (DWDM) sources based on temporal modulation of chirped short pulse lasers have been demonstrated [1-2]. In this scheme, Knox *et al* encode the data on different wavelengths by modulating a highly chirped laser spectrum that is temporally distributed. Based on the same scheme, in a recent experiment, Boivin *et al*. have demonstrated 110 channels at 2.35 Gb/s data transmission by utilizing pulse interleaving technique to multiply the repetition rate 64 times [3]. However, the spectral width of the seed pulse and the modulator speed (~12 GHz) limit the channel count and the pulse width of the each channel in this scheme. Moreover, due to the requirement of high chirp rate, it can only operate at higher speeds at the expense of the channel count. Since the power spectral density is not uniform across the spectrum, a special equalization technique is required to obtain uniform wavelength channels. In an alternative scheme, Mikulla *et al*. have demonstrated pulse carving from a laser spectrum broadened in normal dispersion fiber [4]. By using this scheme, authors has demonstrated 16 channel pulse carving [5]. Although over forty wavelength channels with 2.5 Gb/s repetition rates and 100 GHz channel spacing is feasible in this scheme, rapid pulse broadening in normal dispersion regime limits reaching higher channel counts and larger spectral broadening. This rapid temporal broadening also limits the SC generation in

normal dispersion regime at higher repetition rates due to interference between adjacent pulses.

Short pulse generation based on spectral slicing of the supercontinuum (SC) generated in optical fibers is another technique to obtain a DWDM source. Although the SC generation has been used for different applications before, only recently has it been proposed as a DWDM source [6-8]. Multiple wavelength pulse sources with more than 100 nm spectral bandwidth generated in specially designed long fibers (>1 km) have been demonstrated by different groups [9-10]. In an updated work, Kawanishi *et al.* has recently demonstrated propagation of 19 wavelength channels carved out of SC through 40 km of dispersion-shifted (DS) fiber at 160 Gb/s [11]. Each 160 Gb/s channel is generated by 16 times multiplication of pulses carved from the SC. However, since these experiments use long lengths of fibers to generate the SC by adiabatic soliton compression effect, low input power is required, and this requirement leads to lower power spectral density and signal to noise ratio (SNR) at the output. Experimental demonstrations reveal that only less than -7 dBm/nm power spectral density is available at the fiber output in long fiber SC generation schemes [12]. In order to compensate low power spectral density, low noise amplifiers are required for long distance propagation. In addition to the issue of power spectral density, Nakazawa *et al.* has shown that the quality of SC generated in long fibers is also limited by the coherence degradation of the channels away from the pump wavelength [13]. In their recent work, the authors show that quality of the SC is correlated with its coherence, and the coherence is degraded by the spreading of amplified spontaneous emission (ASE) noise due to modulation instability (MI) and four wave mixing (FWM) during SC generation.

In this paper, we show that short fiber SC generation has the ability to generate a DWDM source with broad and uniform bandwidth, high power spectral density, and high coherence. Experimentally, we demonstrate a 10 Gb/s multiple wavelength pulse source with >140 nm spectral bandwidth and ±0.5 dB uniformity over 40 nm. The power spectral density is measured to be +7.9 dBm/nm across the flat region. Furthermore, the SC can be improved up to 250 nm bandwidth and ±0.5 dB uniformity over 83 nm by using high nonlinearity fibers. Experimental demonstration of ~1.4 ps transform-limited pulse carving as far as 60 nm away from the pump wavelength, pulse propagation and longitudinal mode carving for CW generation indicates that the coherence of the SC is maintained. Based on the theoretical calculations, we also show that the coherence of the short fiber SC generation is maintained, and it has 13 dB higher modulation depth of longitudinal modes as compared to SC generated in long fibers. The experimental and the theoretical results indicate that by using DWDM source based on short fiber SC generation, >600 channel data transmission with >6 Tb/s capacity is achievable at 50 GHz channel separation.

The outline of the paper is as follows. In section II, we will describe the experimental setup used for SC generation and the experimental results including the generated SC and coherence test based on pulse carving and propagation. We will simulate short fiber SC generation and contrast ratio degradation of longitudinal modes due to noise amplification in section III. Section IV contains a discussion of possible system applications of the short fiber SC generation as a DWDM source and its advantages. Finally, section V summarizes our findings.

Experimental Setup and Results of the SC Generation

The experimental setup used in SC generation is shown in Fig 1. A 10 Gb/s actively modelocked fiber laser generates hyperbolic secant pulses with 1.3 ps temporal width with a time-bandwidth product of 0.32 at 1551 nm. Since the SC is generated in short fibers, ~100 W input peak power is required to achieve enough spectral broadening. We use an erbium doped fiber amplifier with 30 dBm saturated output power to reach an average power level of 1 W. Following the amplifier, three sections of fibers are used to generate the SC. In general, the first two sections are used for pulse compression and the last section is used for SC formation. Specifically, the first section is 10 meters of Corning SMF-28 fiber, where the amplified pulses are compressed via the soliton effect pulse compression. Further pulse compression is obtained by the same effect in DSF1, which is 13 meters of DS fiber with $\lambda_0 = 1492$ nm. The last section is 4.5 m of dispersion shifted fiber (DSF2) with $\lambda_0 = 1546$ nm or 4 m of high nonlinearity dispersion shifted (HNL-DS) fiber with $\lambda_0 \sim 1530$ nm. The third order dispersion is the dominant effect in this section, and spectral flattening accompanied by additional spectral broadening is obtained [14,15]. Since the first two sections of fibers are the same, throughout the paper, we differentiate the two SC setups according to the fiber used in the last section. Table I summarize the fiber parameters used in the experiment. Detailed description of the mechanisms contributing to the SC generation will be discussed in the next section. We demonstrate spectral slicing for short pulse generation both within the EDFA band and at shorter wavelengths by using a 2.3 nm tunable filter. A 25 nm super-Gaussian filter centered at 1490 nm is used for testing the broadband coherence. After the amplification of the pulses carved at short wavelengths by a Raman amplifier, 26 km of Corning SMF-28 fiber is used for propagation. An optical spectrum analyzer with 6.25 GHz spectral resolution and an autocorrelator are used for diagnostics.

Figure 2a shows the 10 Gb/s SC spectra generated in conventional, low nonlinearity, DS fiber. We obtain 140 nm spectral broadening at 20 dB below the spectral peak. The SC has three regions where most of the energy is accumulated: center, Stokes and anti-Stokes regions. The Stokes side has 44 nm bandwidth at 15 dB below the center peak, and 20 nm spectral region with ±0.5 dB uniformity. The power spectral density in this region is measured to be 11 dBm/nm. On the other hand, the anti-Stokes side has 50 nm bandwidth at the same level and 40 nm spectral region with the same uniformity of ±0.5 dB. Unlike the Stokes region, power spectral density in this side is lower, 7.9 dBm/nm. A generated SC with a nearly symmetric spectrum indicates that the spectral broadening mechanism is dominated by self-phase-modulation (SPM) during the SC generation. 6 nm difference in bandwidth and 3 dB difference in power density shows the effect of third order dispersion, which leads to asymmetrical flattening of the anti-Stokes side while lowering the power spectral density. The center part of the SC has the peak spectral density and 16 nm bandwidth.

The spectral broadening is increased to 250 nm by replacing the last section of the SC fiber with HNL-DS fiber. Experimentally, we use 4 meters of HNL-DS fiber with 4.5 times higher nonlinearity and zero dispersion wavelength at 1530 nm to replace DSF2. Similar SC to that obtained from DSF2 is generated, but due to the higher nonlinearity and lower dispersion slope in the HNL-DS fiber, spectral broadening is increased to 250 nm [16]. Figure 2b shows the generated SC spectra with 250 nm bandwidth in high

nonlinearity fiber. The flat region on the anti-Stokes side is increased to 83 nm with the same ±0.5 dB uniformity. However, because of the lower input power requirement due to increased nonlinearity, almost doubled spectral broadening, and higher splice loss, the power spectral density of the flat region is decreased to 0 dBm/nm at the flat portion of the spectrum. The bandwidth of the Stokes region is measured to be 21 nm with ±0.5 dB uniformity and 9 dBm/nm power spectral density.

The coherence of the SC is tested by measuring the pulse quality across the spectrum and by carving longitudinal modes to generate CW light. The SC generation setup with conventional DS fiber is used for pulse carving and coherence measurements. Experimentally, we use two different filters to carve out pulses across the spectrum. The first filter is a tunable Gaussian filter with a tuning range of 70 nm from 1490 nm to 1560 nm and nominally 2.3 nm bandwidth, which varies from 2.4 nm to 2 nm within the tuning range. The second filter is a 25 nm super-Gaussian filter centered at 1490 nm. In the first step of the experiment, we test the coherence of the pulses carved from SC near the EDFA band. We use the tunable filter to carve out a pulse at 1524.8 nm with 2.11 nm 3dB bandwidth as shown in Fig 3a. In order to check the nonlinear behavior of the carved pulses, we propagate it through 12 km of dispersion shifted fiber with $\lambda_0 = 1524$ nm. Figure 3b shows the pulse spectra after the propagation for three different average input power levels of 1 mW, 3 mW and 5 mW. Since the carved pulse is very close to zero-dispersion-wavelength, SPM-dominated propagation characteristics are presented at the output of the fiber. The number of the spectral peaks indicate nonlinear phase shift of $\sim\pi$, and $\sim 2.5\pi$ is obtained for input power levels of 3 mW and 5 mW respectively. The asymmetry in the spectrum is expected due to normal dispersion effect at shorter wavelengths. These results show that the temporal stability and the coherence of the SC within EDFA band are preserved.

In the second step of the coherence test, we carve pulses near 1500 nm and propagate through 26 km SMF fiber after amplification. We use a Raman amplifier to amplify the signal after carving pulses at short wavelengths and before propagation. The Raman amplification is obtained by using two sections of dispersion shifted fibers with 4.4 km length and a CW pump source at 1117 nm. Accumulated chirp in the Raman amplifier is compensated by using a 2.5 km of SMF-28 fiber after the amplifier. Optimum chirp compensation is obtained at ~1504 nm. After compensation, we carve 1.37 ps nearly transform limited Gaussian pulses with $\Delta\tau\Delta\nu$=0.45 at 1504 nm indicated in Fig 4a. The corresponding autocorrelation trace is shown in Fig 4b. The coherence of the pulse is confirmed by the propagation through 26 km of SMF-28 fiber. Because of the very high dispersion, which is more than 700 ps, a higher repetition rate pulse train is observed in the temporal domain at the output end of the SMF-28 fiber. The phenomenon of obtaining high repetition pulses in linear propagation is explained by longitudinal mode beating resulted from high dispersion [17]. Shake *et al.* show that, because of dispersion, a pulse is formed at the time position where longitudinal modes of the several adjacent pulses overlap. With further dispersion, the repetition rate decreases gradually and returns to fundamental operation frequency. The autocorrelation of the propagation results are shown in Fig 5. The separation between adjacent pulses are measured to be ~21 ps, which corresponds a pulse train at 48 GHz repetition rate. The pulse train remains stable as long as environmental fluctuations are isolated. This measurement result indicates that the

longitudinal mode structure of the laser is replicated across the SC instead of incoherent energy spreading, which also shows that the coherence of the SC is preserved.

The pulse carving results across the whole Raman gain bandwidth are shown in Fig 6a. In addition to pulse carving and propagation at single wavelength in Raman gain bandwidth, we demonstrate carvability of the SC spectra wavelengths between 1490 nm and 1511 nm. Since the chirp compensation is optimized for the wavelength 1504 nm, broader pulse widths are measured at wavelengths other than 1504 nm. After subtracting the pulse broadening during the amplification by using the formula $\tau = \tau_{meas} - (\lambda_0 - \lambda_c) \cdot \Delta\lambda \cdot \partial D / \partial\lambda \cdot L$, we calculate the actual width of the carved pulses. The parameter τ_{meas} is the measured pulsewidth, λ_0 is zero dispersion wavelength of the fiber, λ_c is pulse carving wavelength, $\Delta\lambda$ is the filter bandwidth, $\partial D/\partial\lambda$ is the dispersion slope and L is the fiber length in the Raman amplifier. Figure 6a shows the calculated pulse widths after subtracting the effect of the total dispersion accumulated in the amplifier from the measured pulse widths. An average of ~1.5 ps pulse width and $\Delta\tau\Delta\nu$~ 0.46 indicates that the coherence of the SC is preserved up to 60 nm away from the pump wavelength and uniform across the spectrum. As another example, Fig 6b shows the generation of 0.6 ps pulses with 20 nm spectral carving, which also indicates that coherence is preserved even at the edge of the SC. The inconsistency between filter bandwidth and the pulse width arises because the edge of the SC spectrum does not completely fill the filter bandwidth and the pulses are slightly chirped before the autocorrelator.

The coherence of the SC is also confirmed by CW generation by longitudinal mode carving of the generated SC. In an updated experiment, we have demonstrated that longitudinal modes of the SC can be carved to generate CW light [18]. The carving results indicate that the longitudinal modes of the seed pump source is replicated during the SC generation with low noise degradation. As a figure of merit, we measure the noise performance of CW from the SC and CW from seed pump. Figure 7 shows the measured relative intensity noise for CW signals carved from the pump and the SC. The measurement results show that the generated CW source has less than 7 dB/Hz intensity noise degradation across the spectrum compared to the pump. This degradation is attributed to the amplifier noise, ASE noise and MI effects during SC formation. However, the uniformity of the intensity noise shows that coherence of the SC is preserved equally across the spectrum.

Mechanisms of SC Generation and Theoretical Results

We confirm our experimental results by simulating the SC generation. We also focus on the evolution of the SC starting with the amplifier output and discuss the behavior of the spectral broadening with respect to linear and nonlinear effects in the fiber. The generation of SC is modeled by the nonlinear Schrodinger equation, which describes the pulse propagation under the influence of nonlinear and linear effects in the fiber. The equation is formulated as

$$\frac{\partial U}{\partial z} + \frac{i}{2}\beta_2 \frac{\partial^2 U}{\partial t^2} - \frac{1}{6}\beta_3 \frac{\partial^3 U}{\partial t^3} = i\gamma\left[|U|^2 + \frac{2}{3}|U_x|^2 - T_R \frac{\partial |U|^2}{\partial t} \right] U$$

where U defines the normalized envelope function of the electric field at the main axis and U_x defines the component at the orthogonal polarization [19]. The left side of the equation gives the linear pulse propagation under the influence of group velocity dispersion (GVD) and third order dispersion (TOD), where β_2 is the second order dispersion constant (ps^2/km) and β_3 is the TOD constant (ps^3/km). The perturbations caused by the nonlinear effects in the fiber are given by the terms on the right hand side of the equation. The first two nonlinear terms on the right side are SPM and cross phase modulation (XPM) effects, and the stimulated Raman scattering is included as the last term on the right hand side. The nonlinearity constant is defined by γ ($W^{-1}km^{-1}$). Raman gain is defined by the constant T_R, which is set to be 5 fs. We use the split step Fourier method to simulate the SC generation [19].

Figure 8 summarizes the evolution of the SC generation based on fiber parameters used in the experiment. Figure 8a shows the pulse spectrum after the amplifier. Due to >20 meters of gain fiber and patch cords, the spectral width of the pulse at the amplifier output is increased from 2 nm to 3.2 nm, which shows that the pulse compression starts during the amplification. At the end of the 10 meters of SMF-28 fiber, we observe soliton effect pulse compression with a clear indication of SPM as shown in Fig 7b. The double peak on the spectrum indicates that signal acquires nearly $3\pi/2$ nonlinear phase shift in the first section. Figure 8c shows the spectral broadening at the end of the DSF1 fiber. Since the GVD is nearly four times smaller in the second section than the first section, higher nonlinear phase shift is acquired. The contribution of the TOD is also expected to appear with increasing bandwidth in this section and to cause small spectral asymmetry. The spectral flattening occurs in the last section of the fiber, where GVD is as low as 0.3 ps/nm.km. Although the spectral broadening still continues along the fiber in this section, spectral asymmetry also continues to grow with increasing TOD effect due to large bandwidth. Figure 8d shows the shape of the spectrum at one third of the length of the last section, where TOD effects starts to show up more clearly. Starting with the second half of the DSF2, asymmetric pulse break up starts to dominate at the trailing end of the pulse and the rate of the spectral broadening decreases. However, the rate of spectral flattening increases with the pulse breakup and anti-Stokes side becomes wider and flatter. Figure 8e shows the power spectral density distribution at 3 meters of DSF2 fiber. Complete flattening is obtained at the last 1.5 meters of DSF2 fiber as seen in Fig 7f. The simulation results show that the contribution of Raman in SC generation is minimal, and this can be explained by the shortness of the fiber.

We calculate the degradation in phase coherence during the SC generation by using the same simulation. Since there is no direct measurement of coherence for pulsed laser, we use SNR, i.e. the depth of longitudinal modes, as an indicator for the coherence. Our aim is to measure how much the SNR and depth of longitudinal modes degrade compared to input signal due to interaction of ASE noise with signal during supercontinuum generation. Deteriorating SNR values shows increasing randomness in phase and amplitude due to ASE noise. In previous works, this comparison has been demonstrated for different combinations of long fiber SC generation, and it has been shown that the coherence degradation due to ASE amplification is less in dispersion decreasing fibers than in constant dispersion fibers and dispersion flattened fibers [13]. For comparison, we

simulate the SC generation in short fibers with experimental parameters as well as in dispersion-decreasing-dispersion-flattened (DDDF) fiber. The length of DDDF is set to 1 km with dispersion parameters of –10.5 ps^2/km and 0.1 ps^2/km at the beginning and at the end of the fiber, respectively. The soliton order at the beginning of DDDF fiber is set to ~1.6. In order to simulate the ASE, we generate a background noise with random amplitude and phase generated by a Gaussian random number generator. The initial SNR is set to be 45 dB, which corresponds to an amplifier with noise figure of ~7 dB. Since the coherence of the pulse is related to the contrast ratio, modulation depth, of the longitudinal modes, we calculate the contrast ratio at different spectral points along the SC for comparison.

Figure 9 summarizes the calculated contrast ratio at different points along the SC spectra for two different fibers. The simulation results show that the SNR and the modulation depth are degraded more than 20 dB in both fibers due to MI initiated by background ASE. However, the short fiber SC generation shows better contrast ratio compared to the DDDF fiber. Specifically, 13 dB less degradation is calculated in short fiber SC generation at 60 nm away from the pump, where contrast ratio decreases to as low as 9 dB in DDDF fiber. The only exception is that 4-dB better modulation depth is calculated at the vicinity of the pump wavelength, where long fiber SC has a spectral peak. The asymmetry in contrast ratio degradation is caused by the higher power spectral density at longer wavelengths, and the location of the pump wavelength close to the edge of the EDFA band. Nearly flat contrast ratio (~22 dB) around 1500 nm also confirms the transform limited pulse carving and broadband coherence demonstrated experimentally.

Discussion

Our experimental and theoretical results confirm that the DWDM source based on short fiber SC generation satisfies all the requirements of a source used in OTDM/WDM applications. Although synchronization and wavelength accuracy are inherent properties of DWDM sources from a single laser, coherence, bandwidth, uniformity, and high power spectral density are four main properties can be satisfied by DWDM source based on short fiber SC generation. By using multiple wavelength pulse generation based on spectral slicing of short fiber SC, we show that the bandwidth of the source can be more than doubled with ±10% amplitude variation over 80 nm compared to chirped pulse modulation and SC generation in normal dispersion fiber. This bandwidth can be increased up to 250 nm by compromising the spectral uniformity and power spectral density. Moreover, for a single channel DWDM source 10 Gb/s data rate shows nearly two orders-of-magnitude increments in repetition rates without any pulse interleaving circuit compared to sources generated by chirped pulse modulation technique. On the other hand, data encoding on multiple wavelength channels simultaneously by using a single modulator is a unique feature used in chirped pulse modulation technique, where this modulation technique can not be implemented by using high repetition rate SC sources. However, the channel count is proportional to the speed of the modulator and the amount of chirping. This proportionality limits the operation frequency in chirped pulse modulation technique due to availability of high-speed modulators and inter-pulse interference caused by high chirping. In addition to high bit rate operation, by using the short fiber SC generation scheme in conventional dispersion shifted fibers, the power spectral density is improved by more than 15 dB compared to long fiber SC generation, and bandwidth is uniform over 40

nm. This uniform bandwidth can also be improved to 83 nm at the expense of 8 dB decrease in power spectral density, which still gives 7 dB improvement in power level compared to long fiber SC generation scheme.

Since actual coherence measurements of a pulsed laser by interferometric techniques are limited by frequency chirp and pulsed nature of the signal, spectral carvability, SNR, CW generation by longitudinal mode filtering and propagation characteristics can be used as indicator of coherence [13]. In our experiments, we show that the SC generated in short fibers maintains its coherence up to 60 nm away from the pump wavelength by transform limited pulse carving and propagation within and outside the EDFA band. These results are also confirmed theoretically. We calculate that the pulses carved from the short fiber SC have longitudinal modes contrast ratio of 22 dB even at 60 nm away from the pump wavelength for the input signal with SNR of 45 dB. Compared to the contrast ratio of 9 dB at the same point obtained in long fiber SC generation scheme, short fiber SC generation scheme shows 13 dB improvement in modulation depth of longitudinal modes and in coherence. Although essential mechanisms for spectral broadening in both fibers are the same, the difference between contrast ratio can be explained by the difference in the length. In the short fiber SC generation spectral, flattening occurs within a distance less than half soliton period, where optimum compression is obtained. For soliton orders <10, MI perturbation is not as effective as higher order solitons within half soliton period [13]. The stepwise dispersion decreasing pulse compression scheme with relatively high average dispersion (~9.5 ps/nm.km) is also disturbs MI gain in the first two section. Although in DDDF fiber, decreasing dispersion profile reduces MI gain, the average dispersion is low and steady growth of ASE noise with increasing gain bandwidth is still expected along the fiber. Moreover, the pulses propagate multiple soliton periods, where the symmetry of initial soliton disappears due to MI.

CW signal generation based on longitudinal mode carving is also confirm that the coherence is preserved across the spectrum. 7 dB/Hz amplitude noise degradation compare to the pump signal shows that generated SC has similar coherence. This 7 dB/Hz difference confirms the degradation due to amplification and MI during SC generation. However, the uniformity of the intensity noise also shows that the coherence is maintained equally across the whole SC spectra. In addition to coherence, power spectral density of the two scheme is compared. Since SC generation in long fibers depends on adiabatic soliton compression effect, where this compression scheme requires low input power, the low power spectral density (-7 dBm/nm) and low SNR is obtained at the output. These results lead to high amplification requirement at the output, where no single amplifier module is available to cover the whole SC bandwidth.

To understand capacity of SC generation, we calculate the maximum achievable number of channels by assuming 50 GHz (0.4 nm) filter spacing, which is commercially available. Our experimental results indicate that SC generation in high nonlinearity fibers has the capacity of achieving >200 wavelength channels at 10 Gb/s over 83 nm bandwidth with ±0.5 dB amplitude uniformity. Due to overall bandwidth of 250 nm, these capacities can reach up to 6 Tb/s by utilizing the entire SC bandwidth at the expense of amplitude equalization circuit. Compared to the experimental demonstration of 235 Gb/s by using chirped pulse modulation technique, short fiber SC generation has the capability of an order of magnitude improvement without any pulse interleaving circuit.

Summary

In summary, we demonstrate coherent short pulse generation based on spectral slicing of the SC generated in short fibers at 10 Gb/s. By using conventional DS fibers, we generate 140 nm spectral broadening with 7.9 dBm/nm (±0.5 dBm) power spectral density over 40 nm. By using high nonlinearity dispersion shifted fibers, spectral broadening is improved to 250 nm with ±0.5 dB uniformity over >80 nm. Coherence of the SC is tested by pulse carving, propagation and longitudinal mode carving. The results show that the coherence of the short fiber SC generation is maintained up to 60 nm away from the pump wavelength. We confirm our results by calculating the SNR degradation because of interaction of pulses with ASE noise during the SC generation. The simulation results show that the longitudinal mode contrast ratio of the pulses carved from the SC degrades nearly 23 dB at 60 nm away from the pump wavelength. 13 dB improvement in contrast ratio is calculated at 60 nm away from pump compared to the results obtained by using long fiber SC generation. As a DWDM source short fiber SC source can also improve the power spectral density by >15 dB compared to the SC generated in long fibers. Compared to the chirped pulse modulation technique, we obtain doubled uniform spectral bandwidth at >200 times higher repetition rates. Based on the experimental results, we estimate that synchronous 600 wavelength channels with total of >6 Tb/s data rate at 50 GHz channel spacing is achievable by utilizing the 250 nm spectral bandwidth generated in high nonlinearity fibers.

This work is supported by DARPA.

ACKNOWLEDGMENT

The authors wish to thank Dr. Mike Freeman from Xtera Communications Inc. for lending and setting up the Raman amplifier.

Table I.

Fiber	Section	Length (m)	λ_0 (nm)	$\partial D/\partial\lambda$ ($ps^2/nm.km$)	γ ($W^{-1}.km^{-1}$)
SMF-28	1	10.0	1310	0.076	2.3
DSF-1	2	13.0	1492	0.03889	2.3
DSF-2	3	4.5	1546	0.05557	2.3
HNL-DSF	3	4.0	1530	0.0265	9.9

References:

15. E. A. De Souza, M. C. Nuss, W. H. Knox, and D. A. B. Miller, "Wavelength-division multiplexing with femtosecond pulses," *Electronics Lett.*, vol. 20, No. 16, pp. 1166-1168, 1995.
16. M. C. Nuss, W. H. Knox, and U. Koren, "Scalable 32 channel chirped-pulse WDM source," *Electronics Lett.*, vol. 22, No. 20, pp. 1311-1312, 1996.
17. L. Boivin, M. Wegmueller, M. C. Nuss, and W. H. Knox, "110 Channels x 2.35 Gb/s from a single femtosecond laser," *IEEE Photonics Technology Lett.,* vol. 11, No. 4, pp. 466-468, 1999.
18. B. Mikulla, L. Feng, S. Sears, B. C. Collings, M. Arend, and K. Bergman, "Broad-band high-repetition-rate source for spectrally sliced WDM," *IEEE Photonics Technology Lett*., vol. 11, No. 4, pp. 418-420, 1999.
19. B. Mikulla, L. Feng, S. Sears, M. Arend, and K. Bergman, "16 Channel x 2.5 Gbit/s WDM source using an harmonically and passively modelocked Er/Yb fiber laser," *IEEE/LEOS Annu. Meeting'1998*, paper WT1.
20. K. Mori, T. Morioka, and M. Saruwatari, "Group velocity dispersion measurement using supercontinuum picosecond pulses generated in an optical fiber," *Electronics Lett.,* vol. 29, No. 11, pp. 987-989, 1993.
21. H. Takara, S. Kawanishi, T. Morioka, K. Mori, and M. Saruwatari, "100 Gb/s optical waveform measurement with 0.6 ps resolution optical sampling using subpicosecond supercontinuum pulses," *Electronics Lett.,* vol. 30, No. 14, pp. 1152-1153, 1994.
22. T. Morioka, K. Mori, S. Kawanishi, and M. Saruwatari, "Multi-WDM-channel, Gbit/s pulse generation from a single laser source utilizing LD-pumped supercontinuum in optical fibers," *IEEE Photonics Technology Lett.,* vol. 6, No. 3, pp. 365-368, 1994.
23. K. Mori, H. Takara, S. Kawanishi, M. Saruwatari, and T. Morioka, "Flatly broadened supercontinuum spectrum in a dispersion decreasing fibre with convex dispersion profile," *Electronics Lett.,* vol. 33, No. 21, pp. 1806-1807, 1997.
24. T. Okuno, M. Onishi, and M. Nishimura, "Generation of Ultra-broad-band supercontinuum by dispersion-flattened and decreasing fiber," *IEEE Photonics Technology Lett.,* vol. 10, No. 1, pp. 72-74, 1998.
25. S. Kawanishi, H. Takara, K. Uchiyama, I. Shake, and K. Mori, "3 Tb/s (160 Gbit/s x 19 ch) OTDM/WDM Transmission Experiment," *OFC'99*, paper PD1-1, 1999.
26. T. Morioka, S. Kawanishi, , H. Takara, O. Kamatani, M. Yamada, T. Kanomori, K. Uchiyama, and M. Saruwatari, "100 Gbit/s x 4 ch, 100 km repeaterless TDM-WDM transmission using a single supercontinuum source," *Electronics Lett.,* vol. 32, No. 5, pp. 468-470, 1996.
27. M. Nakazawa, H. Kubota, and K. Tamura, "Random evolution and coherence degradation of a higher-order optical soliton train in the presence of noise," *Optics Lett.,* vol. 24, No. 5, pp. 318-320, 1999.
28. G. A. Nowak, J. Kim, and M. N. Islam, "Stable 200 nm TDM/WDM source based on continuum generation in 2m of fiber," *OFC'99*, paper TuB3-1, 1999.
29. G. A. Nowak, J. Kim, and M. N. Islam, "Stable supercontinuum generation in short length of conventional dispersion-shifted fiber,", *Applied Optics*., vol. 38, No. 36, pp. 7364-7369 ,1999

30. J. Kim, G. A. Nowak, O. Boyraz, and M. N. Islam, "Low energy, enhanced supercontinuum generation in high nonlinearity dispersion-shifted fibers," *CLEO'99*, paper CWA7, 1999.
31. I. Shake, H. Takara, S. Kawanishi, and M. Saruwatari, "High-repetition-rate optical pulse generation by using chirped optical pulses," *Electronics Lett.,* vol. 34, No. 8, pp. 792-793, 1998.
32. Jaeyoun Kim, Özdal Boyraz, and Mohammed N. Islam, "150^{+} Channel Ultra-DWDM Source with Nx10 GHz Spacing Utilizing Longitudinal Mode Slicing of Supercontinuum," *OFC'00*, paper ThA2, 2000.
33. G. P. Agrawal, *Nonlinear Fiber Optics,* 2^{nd} ed. New York: Academic Press, 1995.

Figure Captions:

Figure 1. The experimental setup used for 10 Gb/s supercontinuum generation in short fibers. Amplified 10 Gb/s pulse train propagated through three sections of fibers to generate 140 nm SC. Pulse carving followed by amplification and propagation is demonstrated at the EDFA band and at shorter wavelengths. DSF: Dispersion shifted fiber, HNLF: high nonlinearity fiber, OSA: optical spectrum analyzer, AC: autocorrelator.

Figure 2. a) Supercontinuum spectra generated in conventional DS fibers. We measure 140 nm bandwidth with ±0.5 dB uniformity over 40 nm. Power spectral density is measured to be 7.9 dBm/nm over the flat region. b) The spectral broadening improved to 250 nm with ±0.5 dB uniformity over 83 nm by using high nonlinearity DS fibers.

Figure 3. a) Transform limited pulse carving has been demonstrated vicinity of the EDFA band (1524 nm). b) We check the propagation behavior of the carved pulses by propagating through 12 km DS fiber for three different input power levels. SPM dominated spectral modulation indicates that spectral carving of the SC near EDFA band generates soliton like pulses and coherence of the SC is maintained.

Figure 4. a) Transform limited pulse carving is demonstrated near 1500 nm. b) The autocorrelation trace of the carved pulse at 1504 nm. We obtain 1.37 ps nearly transform limited Gaussian pulses with time-bandwidth product of ~0.45.

Figure 5. High repetition rate pulse train is obtained after propagating the carved pulses through 26 km of standard fiber. More than 700 ps dispersion leads to beating of the longitudinal modes at different time position and creates 48 GHz pulse train.

Figure 6. a) Results of the coherent pulse carving after subtracting the total dispersion in the 11 km of DSF at the Raman amplifier. Nearly transform limited pulses are generated with average $\tau \sim 1.5$ ps and $\Delta\tau\Delta\nu \sim 0.46$. The results indicate that the coherence of the SC is maintained up to 60 nm away from the pump and it is uniform across the spectrum. b) 0.6 ps short pulse carving with 20 nm broadband filter shows the coherence of the SC is maintained even at the edge of the SC.

Figure 7. Experimental results of relative intensity noise measurement. The results indicate that the longitudinal modes of the pump are replicated with 7 dB/Hz noise degradation. The results also show that each of the longitudinal modes can be carved to generate a CW signal. Uniformity of relative intensity noise shows that coherence is preserved equally across the SC.

Figure 8. Experimental and simulation results of the SC generation in optical fibers based on the experimental fiber parameters. Figure shows the evolution of SC spectra at fiber lengths of a) after the amplifier, b) 10 m, c) 23 m, d) 24.5 m, e) 26 m and f) 27.5 m. The straight line shows the experimental results and dotted line shows the simulation results.

Figure 9. Simulation results of the coherence degradation in short fiber SC generation and 1 km of dispersion decreasing and dispersion flattened fiber (DDDF). ● Indicate modulation depth (contrast ratio) of longitudinal modes calculated for SC generated in short DS fibers, and ▲ shows the contrast ratio calculated for the SC generated in long DDDF fibers. In average, short fiber SC generation has ~13 dB higher contrast ratio than the one generated in 1 km fiber.

Appendix L

Path Average Measurements of Optical Fiber Nonlinearity Using Solitons

John K. Andersen, Janet W. Lou, George A. Nowak, Tiejun Xia, Mohammed N. Islam
The University of Michigan, Ann Arbor, MI 48109-2122
Rance M. Fortenberry*, and Steve A. Newton
Hewlett-Packard Laboratories, Palo Alto, CA 94304-1392

*Currently at Hewlett-Packard Lightwave Division, Santa Rosa, CA 95403

Abstract

We experimentally demonstrate a new method to determine the optical nonlinearity of single mode optical fiber. The technique takes advantage of the well-known nonlinear response of optical fibers and well-developed models for soliton pulse propagation to extract information about the fiber characteristics. Fiber nonlinearity can degrade the performance of communication systems by, for example, causing crosstalk and signal distortions. Measuring the fiber nonlinearity would greatly aid system designers in building and upgrading communication systems. The method is utilized to determine values for n_2/A_{eff}, where n_2 is the nonlinearity of the glass and A_{eff} is effective area of the core, on various lengths of Corning SMF-28 fiber and Corning SMF-DS fiber. Experimentally measured propagation results for short (≈2 ps) optical pulses are compared to computer simulated models to determine the fiber nonlinearity. The method finds $n_2/A_{eff} = 3.0\text{x}10^{-10}$ W^{-1} values for short lengths (≈400 m) of Corning SMF-28 fiber and values of $2.7\text{x}10^{-10}$ W^{-1} for longer lengths (≈6.5 km and ≈20 km). The difference is expected due to the 8/9 polarization scrambling factor, and the values are in agreement with reported literature[1]. The method also determines $n_2/A_{eff} = 5.6\text{x}10^{-10}$ W^{-1} for a ≈12 km Corning dispersion shifted fiber. The method has two major regimes of operation based on the soliton period, a characteristic length for solitons. For few soliton periods ($Z/Z_o < \sim 4$) the output phase is measured as a function of launched power; for many soliton periods ($Z/Z_o > \sim 4$) the output pulsewidth is measured as a function of launched power. The method's major advantage is its capability to measure long lengths of standard fiber, where it uses only standard diagnostic tools such as autocorrelation and optical power measurements. However, the method is only applicable in the soliton regime of fibers.

Index Terms

Optical fiber, dispersion, nonlinearity, optical communications

Introduction

Increasing the information throughput of the currently deployed optical fiber transmission lines is of great interest. Either increasing the bit rates or adding additional wavelength channels represents the most cost-effective way of upgrading current systems. Also, longer distances between amplifiers are important in lowering costs and increasing system reliability. However, these techniques to upgrade existing communication systems increase the necessary launched power into the transmission fiber. Whereas traditionally the major limitation to fiber networks was fiber dispersion, today the increased launched optical powers are causing fiber nonlinearity to become a significant source of bit error rate degradation. Fiber nonlinearity can generate crosstalk between channels through four wave mixing and cause signal distortion through self-phase modulation. Thus, in building and maintaining these communication networks, it is important to accurately characterize the nonlinearity in the optical fiber.

Recently, a number of different techniques to measure fiber nonlinearity have been explored in the literature [2-7]. Each examines the result of a different nonlinear effect. One technique measures side band generation due to self-phase modulation on a pulsed source[5]. Another technique examines phase changes on one optical beam due to cross phase modulation from another optical beam[2]. Finally, a third technique measures the beat frequency components created through four wave mixing[7]. Each method has disadvantages either in complexity of the experimental setup or limits on the maximum fiber length or on the maximum fiber dispersion that can be tested. The limitations on the length of the fiber or dispersion of the fiber are based on the premise that dispersion does not play a significant role in shaping the signal or cause walk-off between two signals. Consequently, these methods are limited to a fraction of a dispersive length. This limitation is on the order of hundreds of meters. For example, for a 10 ps pulse at 1550 nm, the dispersive length is 4.8 km in standard fiber, and to prevent signal distortion or walk-off between two signals, the propagation distance would need to be even less, perhaps 1/10 of a dispersive length or 480 m.

The technique described here is of particular value in measuring long lengths (i.e., many dispersive lengths) of standard fiber or dispersion shifted fiber. In communication systems, a distributed measurement, one that measures the averaged fiber nonlinearity over the entire length of fiber, is preferred. This would be advantageous in characterizing already deployed fibers. However, to measure the path averaged fiber nonlinearity, the signal should not undergo major distortions along the fiber length, due to either the fiber nonlinearity or the fiber dispersion. Optical solitons use the fiber nonlinearity to balance the fiber dispersion, thereby maintaining a constant signal over long fiber lengths. Solitons also provide a convenient and well-understood framework for examining the effect of nonlinearity on pulse propagation. Thus, by an appropriate choice of input optical powers, the fiber nonlinearity can be used to balance the dispersion and maintain the pulse shape over long distances. Since the amount of optical power necessary to balance a known dispersion is a function of the fiber nonlinearity, the fiber nonlinearity may be determined.

Our method has the advantage of being easy to implement for long lengths of fiber. The method requires only standard optics instrumentation: optical spectrum analyzer (OSA), pulse laser source, power meter, and autocorrelator. For short distances, a more complex experimental setup is necessary; an optical sampling oscilloscope (OSO) is used to measure the phase across the pulse[8]. The OSO uses a cross-correlator with a

synchronized short pulse source. An optical discriminator is added to determine the optical phase across the pulse[9]. A phase measurement is necessary for short fiber lengths, since for different launched powers the optical pulse shape does not completely define the optical pulse, extra information may be included in the optical phase (chirp). For the longer distances, the optical pulses evolve into fundamental solitons, which have the well-known constant phase across them (chirp free)[10]. While the experimental setup necessary to measure short fiber lengths is complicated, the major component is the OSO itself, which has been demonstrated by both Hewlett-Packard and Anritsu as a possible product. Also, the key novelty of this method is its ability to measure long lengths of standard fiber and in that configuration the OSO is not required.

Figure 1 illustrates the regions where our method is applicable and shows how, with a simple experimental setup, the measurable length is extended, especially for standard fiber. The dispersive length, defined by $L_D = \tau_0^2/\beta_2$, where τ_o is the pulse width and β_2 is the fiber dispersion, is related to the soliton period, Z_0, by $Z_0 = (\pi/2)*L_D$. The curves are for constant dispersive lengths, with a pulsewidth, τ_0 = 2 ps, and varying dispersion; the L = 1 L_D and L = 6 L_D lines are shown. It is more convenient to work in dispersive lengths since most methods that rely on the signal distortions being small must operate with fiber links below the 1 L_D line. Our method uses measurements on optical phase up to approximately the 6 L_D line (or ~4 Z_0) and pulsewidth measurements for longer lengths. Note that this break point of six dispersive lengths between the phase regime and the pulsewidth regime is approximate. The upper limit on measurable fiber length is limited by loss, or how far soliton propagation can be maintained. Soliton propagation can be maintained for up to ≈6 db of loss and for optical fibers with 0.25dB/km attenuation, that length is 32 km. The "X"s in Fig. 1 indicate experimental points to be described here.

Soliton Propagation

The propagation behavior of an optical pulse is completely determined by the fiber parameters: dispersion, n_2/A_{eff}, and loss. If any two of these parameters are known, the third is determined. (In this paper, the term nonlinearity refers to n_2/A_{eff}, as it is difficult to determine one of these parameters without knowing the other and, in most cases, it is the quotient that is important to system designers.) The term soliton refers to a description of the propagation behavior defined by the relationship between the optical pulse and the optical fiber properties. A soliton propagating along a fiber maintains its shape over long propagation distances. This provides the constant intensity signal over long lengths of fiber necessary to measure the fiber nonlinearity. This is not completely true for a lossy fiber, but the effect of loss can be accounted for in the simulations. Solitons provide a convenient and well-understood framework for the modeling and the simulation work; this makes them an attractive construct for use as a diagnostic tool.

As an example, assume a well-characterized optical pulse of width τ and peak power P_0, and a lossless test fiber with a well-defined fiber dispersion, D. To launch a fundamental soliton (N=1), it is necessary to know n_2/A_{eff}. Vary P_0 until the output pulsewidth matches the input τ, then for that P_0, n_2/A_{eff} is given by:

$$\frac{n_2}{A_{eff}} = \frac{\beta_2}{P_o \frac{w_o}{c} \tau_o^2},$$

where ω_o is the optical frequency, c is the speed of light, and β_2 is related to dispersion D by $\beta_2 = -\lambda^2 D/2\pi c$. In a similar manner, D can be found once n_2/A_{eff} is known.

The simplified example above has three practical problems. The first is the assumption of a lossless fiber. While this may be valid for short test lengths, for any appreciable length of fiber, the effect of loss is significant, which prevents the use of the standard soliton equations. In that case, it is necessary to use either a more complicated analytical solution or computer simulations to predict the propagation behavior. The second practical issue is the sensitivity of the measurement system. If only one point is measured at the fundamental soliton power level, the final pulsewidth may not be unique. This discrepancy can be caused by dispersive waves that are formed by energy that leaves the pulse but still affect the final pulsewidth for a given P_0. Various levels of launched power can result in different amounts of dispersive wave being shed, thereby resulting in different final pulsewidths. To avoid this error, the output pulse properties are measured for various launched powers and through simulations the fiber parameters that match the measured behavior are found.

The final practical problem with the above example is the importance of an accurate characterization of both the input and output optical pulses to the modeling of the propagation behavior. In the above example, it is assumed that the pulsewidth τ completely characterizes the pulse (i.e., there is no frequency chirp to consider). While this could be set as a condition on the launched pulse into the test fiber, it is not a valid assumption for the output pulse, especially over short propagation distances. The definition of "short" distances is based on the soliton period. The soliton period is proportional to the dispersive length and is a characteristic length for soliton behavior that determines how fast, or over what distance, the soliton will react to different fiber parameters. An ideal soliton has no excess frequency chirp and can be completely defined by the pulsewidth. Optical pulses at various energies near the fundamental soliton level, N = 1, will acquire an excess frequency chirp as each optical pulse reacts to the optical fiber. This excess frequency chirp decreases after only a few soliton periods, and at that point the pulsewidth is a valid way to characterize the optical pulse.

A more schematic illustration of the method is shown in Fig. 2. A well-known optical pulse is launched into a test fiber and the response due to the fiber is measured. The propagation of an optical pulse in a single mode fiber is that of a nonlinear system whose behavior is characterized by the Nonlinear Schroedinger Equation:

$$i\frac{\partial A}{\partial z} = \frac{1}{2}\beta_2 \frac{\partial^2 A}{\partial T^2} - \gamma |A|^2 A,$$

where A is the complex pulse field, β_2 is the fiber dispersion and γ is the nonlinear parameter given by $(n_2/A_{eff})*(\omega_o/c)$, with ω_o and c being center frequency and speed of light, respectively. By changing the launched power, the balance between dispersion and nonlinearity is varied and the subsequent effect on the pulse can be observed. The system response at different power levels is a direct reflection of the fiber characteristics.

To illustrate the propagation behavior over short distances more clearly, Fig. 3 shows how a transform-limited optical pulse launched at various power levels near that of

a fundamental soliton, reacts as it propagates through a fiber. Note that initially the chirp increases rapidly until around one soliton period. Then, the chirp begins to decrease and asymptotically approaches zero. Also note that the pulsewidth deviation continues to increase after one soliton period and becomes a better indicator of the effect the fiber propagation is having on the optical pulse.

The gradual change from a large phase change to a large pulsewidth change necessitates the use of two operating regimes for the fiber measurement system. For short lengths, the phase of the optical pulses must be measured. For longer lengths, $L > 4Z_0$, the pulsewidth may be used. It is more desirable to work in the pulsewidth regime since a simple autocorrelation measurement will suffice, while for the phase regime, a more complicated measurement is necessary. Theoretically, the need to measure phase information could be avoided if the pulsewidth could be made small enough to lower the number of Z_0's relative to the test fiber length. Indeed, for lengths on the order of kilometers, pulsewidth measurements are adequate since a picosecond pulse source is used. Shorter lengths would necessitate pulsewidths below a picosecond at which point other issues begin to complicate both the experiment and the computer simulations. In the experiment, avoiding pulse distortion in the Erbium Doped Fiber Amplifier (EDFA) becomes more difficult when amplifying sub-picosecond pulses. In the simulations, the pulse propagation behavior starts to be effected by other mechanisms such as β_3, Raman, and self-steepening. These effects can be modeled, but they introduce unnecessary complications and uncertainties into the algorithm.

Algorithm/Method

The algorithm is shown schematically in Fig. 4. From experimentally measured input pulse parameters and an initial estimate of the fiber parameters, the propagation of the pulse is simulated using the Nonlinear Schroedinger Equation modeled by the split-step Fourier method[10]. The simulation is repeated for the range of input powers used in the experiment. Then, the simulated response is compared to the measured response. The initial estimate of the fiber parameters is perturbed in subsequent iterations until the sum of the errors is less than the specified tolerance.

Depending on the regime of operation, the algorithm can determine both dispersion and nonlinearity or simply the nonlinearity, given the dispersion. For short lengths, where phase method is appropriate, the algorithm can use the low power points to determine the dispersion and then use the entire curve to determine the nonlinearity. For longer lengths, there is a limitation in the pulsewidth measurement systems, i.e. one that can measure 1 ps pulses may not be well suited to measuring 200 ps pulses. Also, the power sensitivity becomes more of an issue as the pulse broadens. This makes it experimentally difficult to use powers low enough to avoid the nonlinear regime and still obtain an accurate dispersion measurement. Consequently, the dispersion for the long test fibers is measured independently using a commercial instrument, the HP83420A Dispersion Test System. This system provides a measure of the dispersion parameter, D, that is used by the algorithm, to find the fiber nonlinearity.

In order to simulate the propagation behavior, it is preferable to operate near the N = 1 soliton regime where there is relatively little shedding of dispersive energy. But to

define the order of the soliton, the fiber dispersion and the fiber nonlinearity, which is to be measured, must be known. Thus, only an estimate of the soliton order can be used with launched power levels in the range of N = 1. Note that while it is theoretically possible to change the order of the soliton by changing the pulsewidth, this is extremely difficult to achieve experimentally, especially for picosecond pulses, while changing the input power is relatively easy.

Experimental Setup

The experimental setup is shown in Fig. 5. The pulse source is a passively mode-locked, erbium doped fiber ring laser producing ≈ 2 ps pulses[11,12]. The pulse from the laser is amplified and then attenuated with the variable attenuator. The amplifier pump power is held constant throughout the experiment to avoid changes due to nonlinear pulse shaping. The variable attenuator is used to linearly vary the launched power. The power is monitored with a 95:5 coupler before being launched into the test fiber. At this point, the pulse can be completely characterized to provide the parameters for the well-known input pulse required for the simulations. The pulse properties, such as pulse shape and chirp, are determined with either an OSO measurement or with an autocorrelation measurement. The autocorrelation is verified using a fit to the assumed sech^2 pulse shape. At the output, the pulse is measured with either an OSO or an autocorrelator depending on the length regime of the test. The OSO requires an electronic synchronization signal but the OSO is only used for short test lengths where this is feasible. For long test lengths a simple autocorrelator is used.

The OSO consists of a synchronized optical short pulse source, a cross-correlator, and an optical discriminator. The synchronized short pulse source, a fiber ring laser that provides 600 fs pulses, acts as an optical sampler or probe for the cross-correlator. This allows direct measurement of the pulse shape and pulsewidth. The addition of the optical phase discriminator provides the means for determining the phase as a function of time across the pulse. The resolution of the system is about 1 ps and is limited by the timing jitter of the probe laser.

Results

The method is illustrated in both the phase and pulsewidth regimes using different lengths of Corning SMF-28 fiber (λ_o = 1.312 μm) and Corning SMF-DS, dispersion shifted fiber (λ_o = 1.524 μm). The phase regime is demonstrated with a 407 m length of SMF-28. For this test length, both the dispersion and nonlinearity are determined. The low power points, which are completely dominated by dispersion, are used to find the dispersion. To measure longer test fiber lengths in the method's pulsewidth regime, a 6.5 km and 19.9 km length of Corning SMF-28 fiber are used. In addition, an 11.5 km length of Corning SMF-DS fiber is measured. For these long fibers, the dispersion is measured independently and fed into the computer algorithm.

Figure 6 is an example of phase data measured from the OSO for different launched powers in the 407 m test fiber. The optical pulse is shown for reference. Note that

for a low power pulse, N ≈ 0.05, the phase across the pulse is linear, showing little nonlinear effect since the pulse evolution is dominated by linear dispersion. At a high power, N ≈ 0.8, the nonlinearity begins to play a role in forming a soliton and the phase begins to flatten across the pulse.

By fitting a line across the phase between the 1/e intensity points of the launched optical pulse, the slope of the phase as a function of the launched power is obtained. This is shown as the dots in Fig. 7. The solid line is the fit as calculated by the computer algorithm. The dispersion and n_2/A_{eff} are estimated to be 15.5-ps/nm/km and $3.0x10^{-10}$ W^{-1}, respectively. For confirmation, the dispersion is measured independently and found to be 15.9-ps/nm/km for this test fiber.

Figure 8 is the pulsewidth data from autocorrelation fit versus launched power for the 6.5-km test fiber. The dots are the experimentally measured points and the solid line represents the fitted curve calculated by the computer algorithm. The dispersion was first measured by the HP Chromatic Dispersion System to be 15.1-ps/nm/km and input to the computer algorithm. n_2/A_{eff} was then determined to be $2.7x10^{-10}$ W^{-1}. Notice the value is less than the previous measurement made on the 407 m test fiber. This is due to a loss of polarization along the 6.5 km test fiber[13]. As reported in previous literature, there is an 8/9 factor difference between the linearly polarized n_2 and the randomly polarized n_2 and (8/9)* $3.0x10^{-10}$ W^{-1} = $2.67x10^{-10}$ W^{-1} which is in close agreement with the $2.7x10^{-10}$ W^{-1} value. In addition, the measurement was performed on a 19.9 km length of Corning SMF-28 fiber and measured an n_2/A_{eff} of $2.6x10^{-10}$ W^{-1}. This is in good agreement with the 6.5 km test fiber.

Finally, measurements were made on an 11.5 km length of Corning SMF-DS fiber, as shown in Fig. 9. The dispersion for this fiber was measured to be 1.5 ps/nm/km. Since the fundamental soliton powers are much lower for dispersion shifted fiber, the amplifier was not needed before the variable attenuator. The EDFA was placed after the test fiber and just before the diagnostics. This was necessary due to the low signal levels. After the measurements, the n_2/A_{eff} was determined to be $5.6x10^{-10}$ W^{-1}. The larger nonlinearity is expected, since the core size of dispersion shifted fibers are smaller than that of standard fibers. Typically the core size of dispersion shifted fiber is 50 μm^2 while for standard fiber it is 86 μm^2[14].

Discussion

When examining this method, issues such as limits on range of applicability, sensitivity, and accuracy must be carefully considered. One of the limitations of this method is the need for the dispersion to be in the anomalous region. Since the method relies on soliton propagation, the signal wavelength must be above the zero dispersion wavelength so that the nonlinearity can balance the dispersion. Also, the fiber dispersion is assumed to be constant along the fiber, the soliton propagation will average out any perturbation that is shorter than the soliton period. For standard fiber the variations in dispersion should be minimal since the waveguide dispersion is not a factor. Another limitation is imposed by the loss of the fiber, since amplifiers can not be used along the test fiber. Once the pulse has lost enough power to drop below an N = 0.5 soliton, the nonlinear effects diminish. While this does not preclude our simulation models from working, the nonlinearity will no longer be averaged over the remainder of the fiber. The criterion for

the test fiber length limitation is similar to that of optical amplifier spacing where the soliton can not drop below N = 0.5 and still be recovered.

Inaccuracies in the measured input pulse parameters are a possible source of error for this measurement method. For example, the algorithm will be unable to accurately match the experimental propagation behavior if the input pulse is chirped and the algorithm is not aware of it. This sensitivity is illustrated through a simulation of this diagnostic method on a 1 km fiber. The nonlinearity is set at $n_2/A_{eff} = 2.67x10^{-10}$ W^{-1}, and the pulse propagation with various chirps is simulated at five different power levels. The pulse model used in the simulations is: $A*sech(t/T_o)*exp(\phi)$, where A is the amplitude, t is time, T_o is pulsewidth, and ϕ is defined by $\phi = -C\ t^2 / 2*T_o^2$, with C being the chirp parameter. The resulting pulsewidths are then fed into the diagnostic algorithm, which calculates the nonlinearity.

As expected, when the algorithm uses an unchirped initial pulse to fit to the pulsewidths resulting from an unchirped pulse, the algorithm finds the correct nonlinearity with close to zero error in the determined pulsewidths, as shown in Fig. 10. When the algorithm tries to match the propagation behavior of the chirped pulses with a non-chirped initial pulse, an incorrect nonlinearity is determined. The inaccuracy is shown by an error in the match between experimental (in this case simulated) and simulated propagation results which increases with the chirp parameter as shown in Fig. 10. The same holds true for the phase measurement where errors in the initial pulse estimations cause an error in the final determined nonlinearity. This error is apparent to the user by a poor match between the measured and simulated pulsewidth or phase slope. A pulse perturbation of asymmetry has a similar effect as chirp on the method's ability to determine the nonlinearity.

Figures 11 and 12 illustrate the sensitivity of this method by showing how much the simulated results are effected by perturbing the nonlinearity value. They also show why the algorithm can find both dispersion and nonlinearity for short lengths of fiber, and why it is necessary to measure the dispersion independently for long lengths. In Fig. 10, simulation data for a variation in n_2 of ±5% are plotted on top of the experimental points. Notice the low power points are not a strong function of the nonlinearity. In this case, the low power points can be used to find the dispersion while the entire curve is used to find n_2/A_{eff}. In Fig. 11, again the data are for a variation in n_2 of ±5% plotted on top of the experimental points. In this case, the entire curve is effected by the change in nonlinearity.

The simplest check on the accuracy of the method is to use the accepted value for n_2, $2.3x10^{-20}$ m^2/W [10], and A_{eff}, 86.6 μm^2 [14], to calculate n_2/A_{eff}. This results in $n_2/A_{eff} = 2.67x10^{-10}$ W^{-1}, which is in very good agreement with the 6.5 km and 19.9 km test fibers. The expectation is that the 407 m test fiber will have a higher nonlinearity since the polarization will not have scrambled over such a short length. The difference is found to be the expected 8/9 factor. For the dispersion shifted fiber, $n_2 = 2.3x10^{-20}$ m^2/W and $A_{eff} = 50.0$ μm^2 yields $n_2/A_{eff} = 4.6x10^{-10}$ W^{-1}. This is lower than our measured value, but the n_2 value does not account for the increased Ge concentrations in the core of most dispersion shifted fibers.

The uncertainty in the dispersion shifted fibers is one of the reasons for the development of this measurement technique. The parameters of standard fiber, in particular SMF-28, are well known and our results concur with other reported literature. Dispersion

shifted fibers vary more in fiber parameters, as different techniques such as changing the refractive index profile and concentration of core dopants like Ge are used to control the dispersion. These variations can affect the fiber nonlinearity. Even if one has detailed knowledge of the refractive index profile and core dopants, information that is rarely available, it is difficult to translate that information into a fiber nonlinearity value.

Conclusions

In conclusion, a method capable of measuring the path averaged value of fiber nonlinearity over long lengths of optical fiber has been demonstrated. The method is illustrated using various lengths of Corning SMF-28 fiber and Corning SMF-DS fiber. The method finds $n_2/A_{eff} = 3.0\text{x}10^{-10}$ W^{-1} values for short lengths (≈400 m) of Corning SMF-28 fiber and values of $2.7\text{x}10^{-10}$ W^{-1} for longer lengths (≈6.5 km and ≈20 km). The difference is consistent with the 8/9 polarization scrambling factor[1]. The method also determines $n_2/A_{eff} = 5.6\text{x}10^{-10}$ W^{-1} for a ≈12 km Corning SMF-DS fiber. The method's major advantage is its capability to measure long lengths of fiber, where it uses only standard diagnostic tools such as autocorrelation and optical power measurements.

This work is supported by DARPA.

Reference

[1] S.V. Chernikov and J.R. Taylor, "Measurement of normalization factor of n_2 for random polarization in optical fibers," *Opt. Lett.*, vol. 21, pp. 1559-1562, 1996.

[2] T. Kato, Y. Suetsugu, M. Takagi, E. Sasaoka, and M. Nishimura, "Measurement of the nonlinear refractive index in optical fiber by the cross-phase-modulation method with depolarized pump light," *Opt. Lett.*, vol. 20, pp. 988-990, 1995.

[3] A.J. Taylor and G. Rodriguez, and T.S. Clement, "Determination of n_2 by direct measurement of optical phase," *Opt. Lett.*, vol. 21, pp. 1812-1814, 1996.

[4] A. Boskovic, S. V. Chernikov, J. R. Taylor, L. Gruner-Nielsen, and O. A. Levring, "Direct continuous-wave measurement of n_2 in various types of telecommunication fiber at 1.55 μm," *Opt. Lett.*, vol. 21, pp 1966-1969, 1996.

[5] K. S. Kim, R.H. Stolen, W. A. Reed, and K. W. Quoi, "Measurement of the nonlinear index of silica-core and dispersion-shifted fiber," *Opt. Lett.*, vol. 19, pp. 257-259, 1994.

[6] T. Kato, Y. Suetsugu, and M. Nishimura, "Estimation of nonlinear refractive index in various silica-based glasses for optical fiber," *Opt. Lett.*, vol. 20, pp. 2279-2282, 1995.

[7] L. Prigent and J.-P. Hamaide, "Measurement of Fiber Nonlinear Kerr Coefficient by Four-Wave Mixing," *IEEE Photon. Technol. Lett.*, vol. 5, pp. 1092-1095, 1993.

[8] H. Lin, D. M. Baney, K. W. Chang, W.V. Sorin, and S.A. Newton, "Measuring dynamic chirp in optical pulses using frequency discriminators," *in Technical Digest of the Annual Meeting of the Optical Society of America (OSA 95)*, ThYY5, pp 167, Portland, OR, Sept. 10-15, 1995.

[9] W.V. Sorin, K.W. Chang, G. Conrad, and P. Hernday, "Frequency domain analysis of an optical FM Discriminator," *IEEE J. Lightwave Technol.*, vol 10, no. 6, pp 787-793, 1992.

[10] G.P. Agrawal, *Nonlinear Fiber Optics*. New York: Academic Press, 1995.

[11] H. Lin, D. K. Donald, K.W. Chang, S. A. Newton, "Colliding-pulse mode-locked lasers using Er-doped fiber and a semiconductor saturable absorber," in *Technical Digest: Conference on Lasers and Electro-Optics (CLEO 95)*, JtuE1, pp 72-73, Baltimore, MD, May 21-26, 1995.

[12] B. C. Barnett, L. Rahman, M. N. Islam, Y.C. Chen, P. Bhattacharya, W. Riha, K. V. Reddy, A. T. Howe, K. A. Stair, H. Iwamura, S. R. Friberg, and T. Mukai, "High-power erbium-doped fiber laser mode locked by a semiconductor saturable absorber," *Opt. Lett.*, vol. 20, pp 471-473, 1995.

[13] P. K. A. Wai, C. R. Menyak, and H. H. Chen, "Stability of solitons in randomly varying birefringent fibers," *Opt. Lett.*, vol. 16, pp. 1231-1233, 1991.

[14] Corning Product Literature, Pl1036 and Pl1037.

Figure Captions

Figure 1. Range of applicability. The lines are constant number of dispersive lengths (τ = 2 ps), L = 1 L_D and L = 6 L_D. Most nonlinear measurements are limited to below the L = L_D line. Our method is capable of the entire range. The "X"'s indicate experimental points we have demonstrated.

Figure 2. The method consists of using a known optical pulse and propagating it through the unknown test fiber and measuring the effect on the pulse at various power levels. Either the chirp or output pulsewidth is measured as the system response.

Figure 3. Phase and pulsewidth variations for short pulse propagation. The phase provides a more measurable response for short test fibers.

Figure 4. The algorithm consists of propagating a well-characterized pulse through a test fiber with an estimated dispersion (D) and nonlinearity (n_2/A_{eff}), followed by a comparison of the simulated propagation with the experimentally measured values and minimizing errors in a least squares fashion are performed.

Figure 5. Experimental setup. Pulse from erbium doped fiber laser is amplified and then attenuated with the optical attenuator. The 95:5 coupler monitors the launched power into the test fiber. Finally, the output pulse is characterized for various launched power levels.

Figure 6. Optical Sampling Oscilloscope measurements on phase. This illustrates the soliton evolution; the low power case ($N \approx 0.05$) has a linear chirp across the entire pulse while the high power pulse ($N \approx 0.8$) tries to maintain a flat phase.

Figure 7. 407 m test fiber. Slope of the phase fit across the 1/e points plotted against the launched power for 407 m, Corning SMF-28, test fiber. The dots are the experimentally measured points and the line is the computer fit to the propagation behavior which finds $n_2/A_{eff} = 3.0 \times 10^{-10}$ W^{-1} and D = 15.5 ps/nm/km.

Figure 8. 6.5 km test fiber. Output pulsewidth versus the launched power for 6.5 km, Corning SMF-28, test fiber. The dots are the experimentally measured points and the line is the computer fit to the propagation behavior which finds $n_2/A_{eff} = 2.7 \times 10^{-10}$ W^{-1}.

Figure 9. 11.5 km DS test fiber. Output pulsewidth versus the launched power for 11.5 km, Corning DS, test fiber. The dots are the experimentally measured points and the line is the computer fit to the propagation behavior which finds $n_2/A_{eff} = 5.6 \times 10^{-10}$ W^{-1}.

Figure 10. Effect of inaccurate initial pulse characterization. Shows the sum of the squared errors as a function of the unaccounted initial chirp. As the unaccounted chirp increases, the errors in the fit increase along with the difference in the determined nonlinearity.

Figure 11. Sensitivity for phase regime. Shows that a 5% error in n_2/A_{eff} is easily detectable for the phase measurement regime. Note that the low power points still match indicating less dependence on nonlinearity.

Figure 12. Sensitivity for pulsewidth regime. For the pulsewidth measurement regime, 6.5 km test fiber, a 5% error in n_2/A_{eff} is easily detectable. For this case, the entire curve shifts which indicates that each point is strongly effected by nonlinearity.

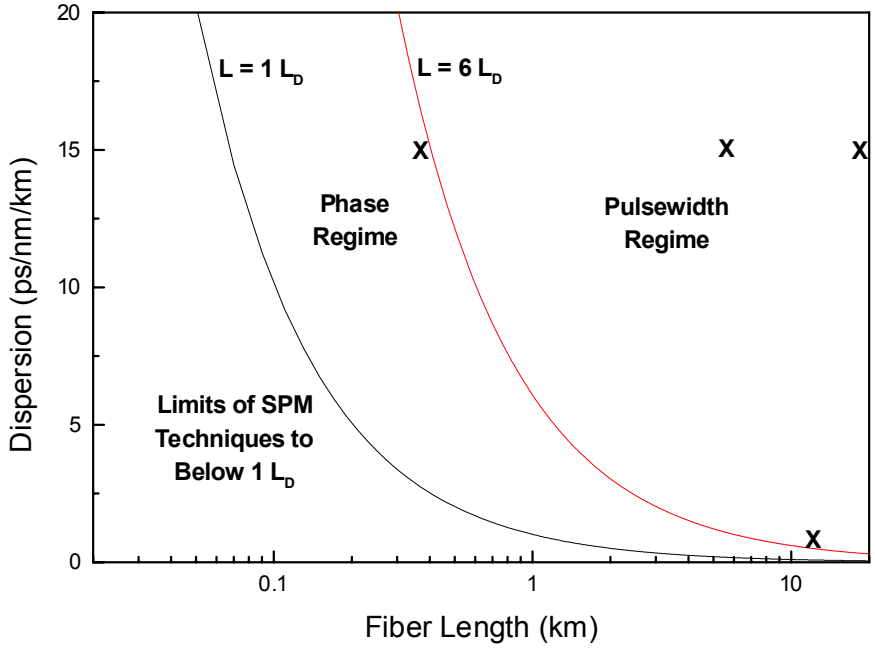

Figure 1

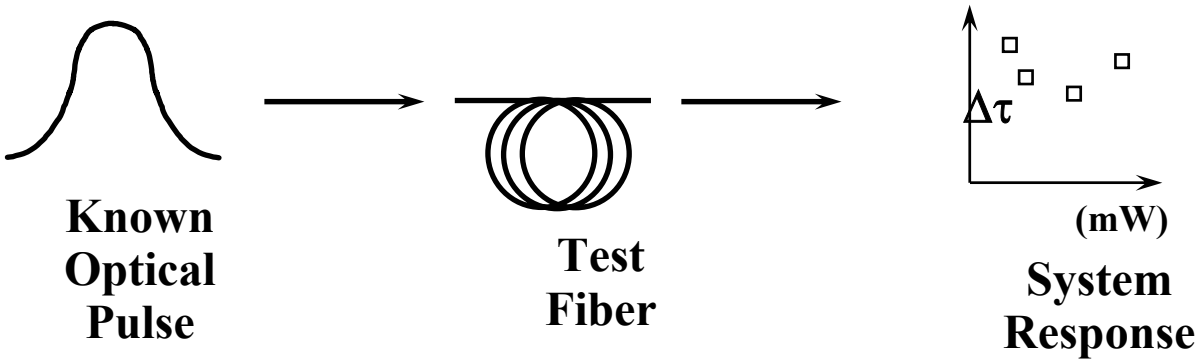

Figure 2

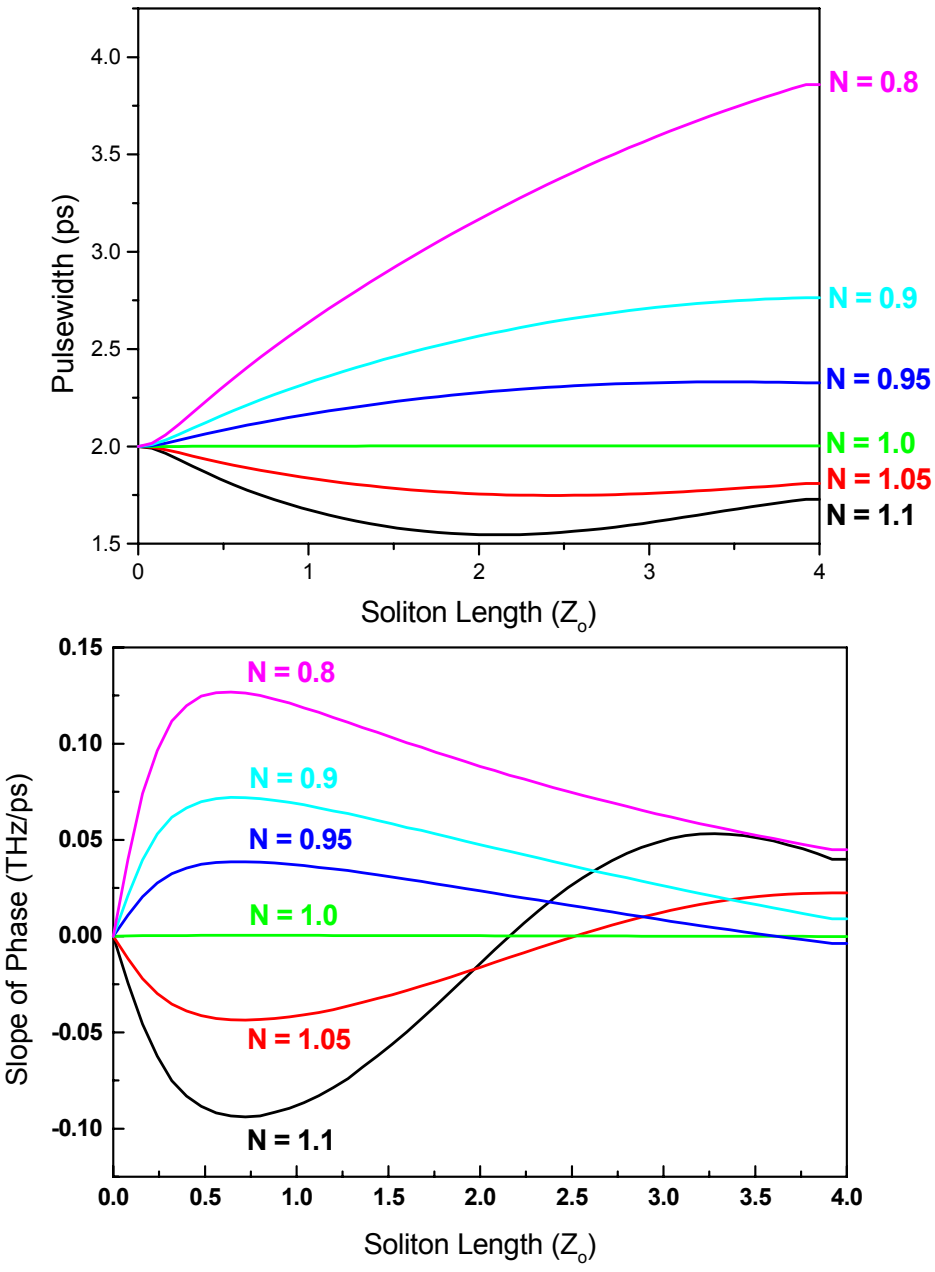
Pulsewidth (ps)
Soliton Length (Z_o)
N = 0.8
N = 0.9
N = 0.95
N = 1.0
N = 1.05
N = 1.1
Slope of Phase (THz/ps)
Soliton Length (Z_o)
N = 0.8
N = 0.9
N = 0.95
N = 1.0
N = 1.05
N = 1.1

Figure 3

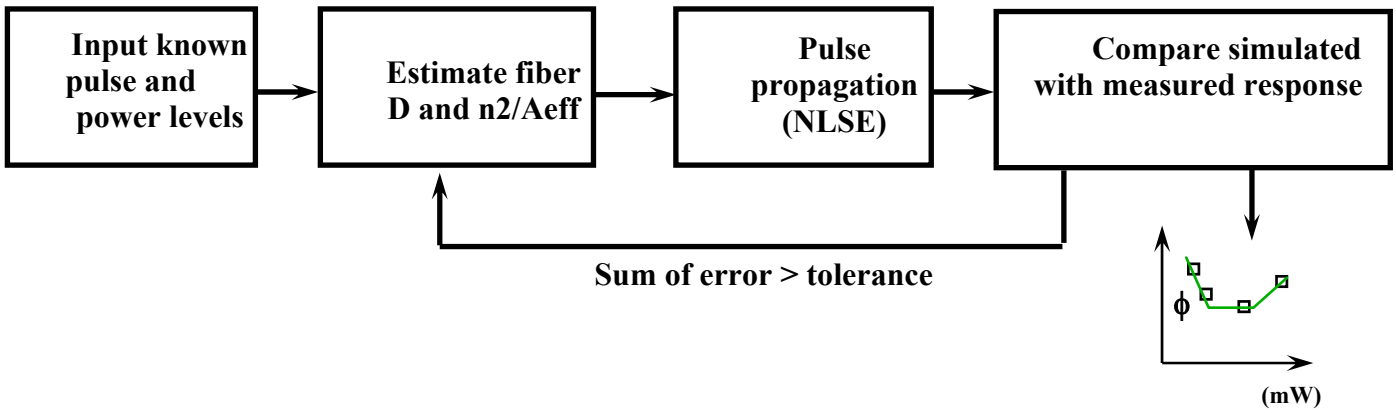

Figure 4

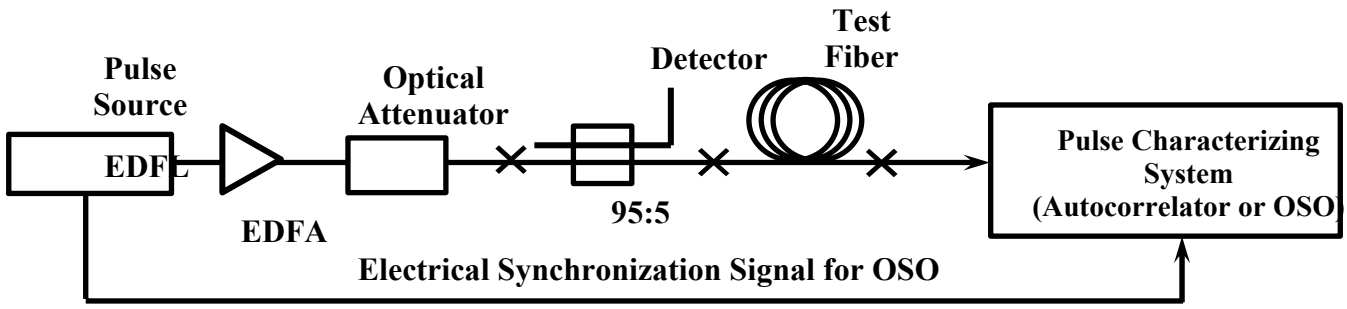

Figure 5

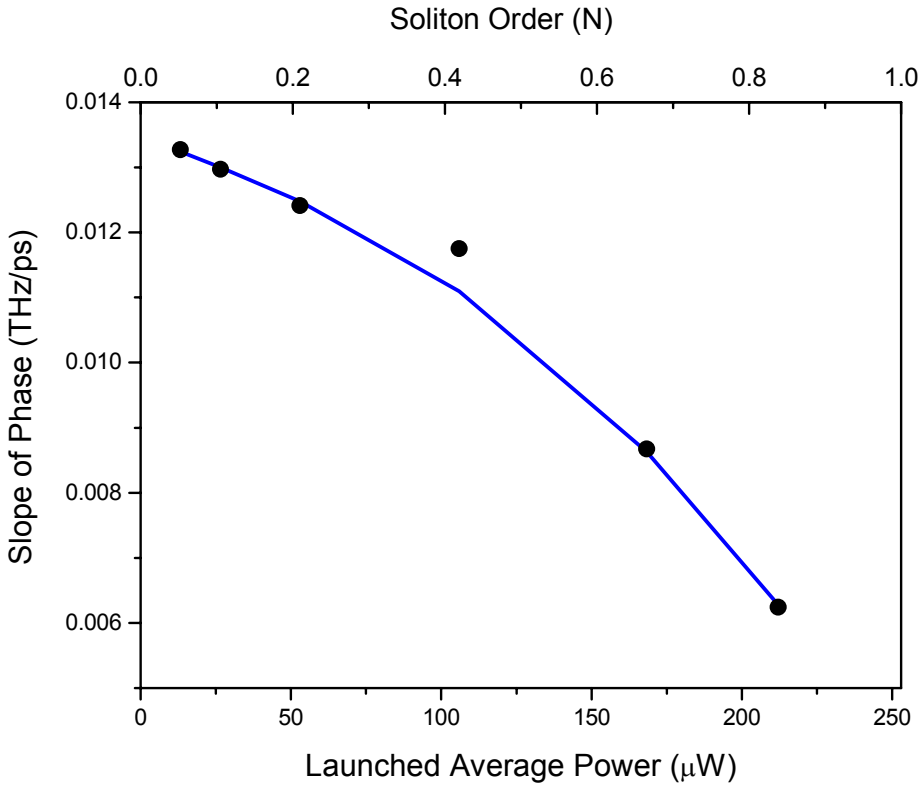
Soliton Order (N)
0.0
0.2
0.4
0.6
0.8
1.0
0.014
0.012
0.010
0.008
0.006
Slope of Phase (THz/ps)
0
50
100
150
200
250
Launched Average Power (μW)

Figure 6

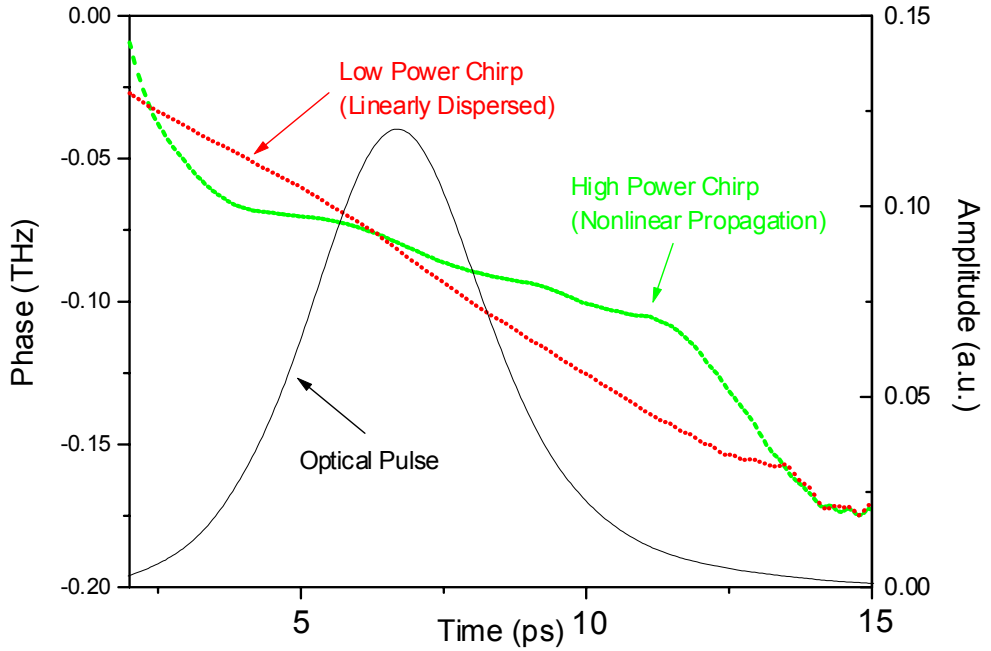

Figure 7

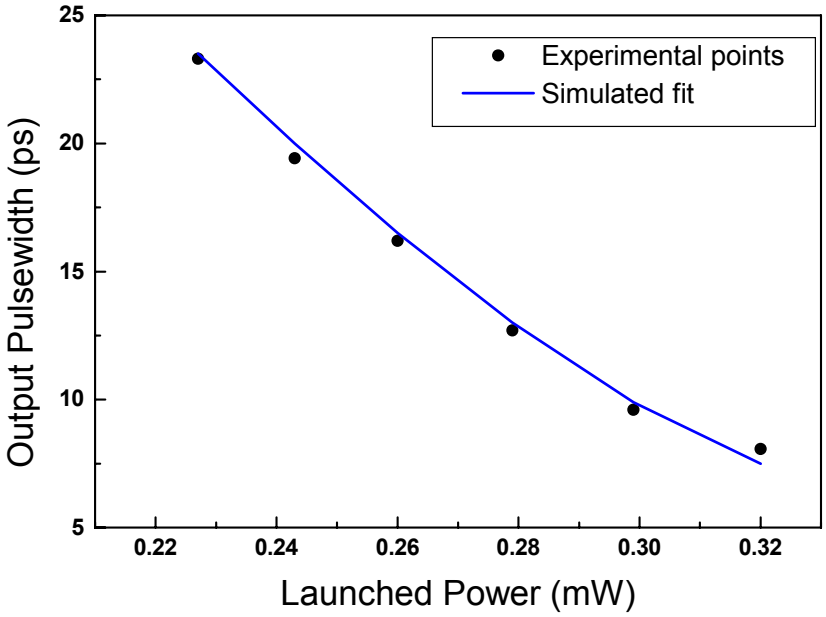

Figure 8

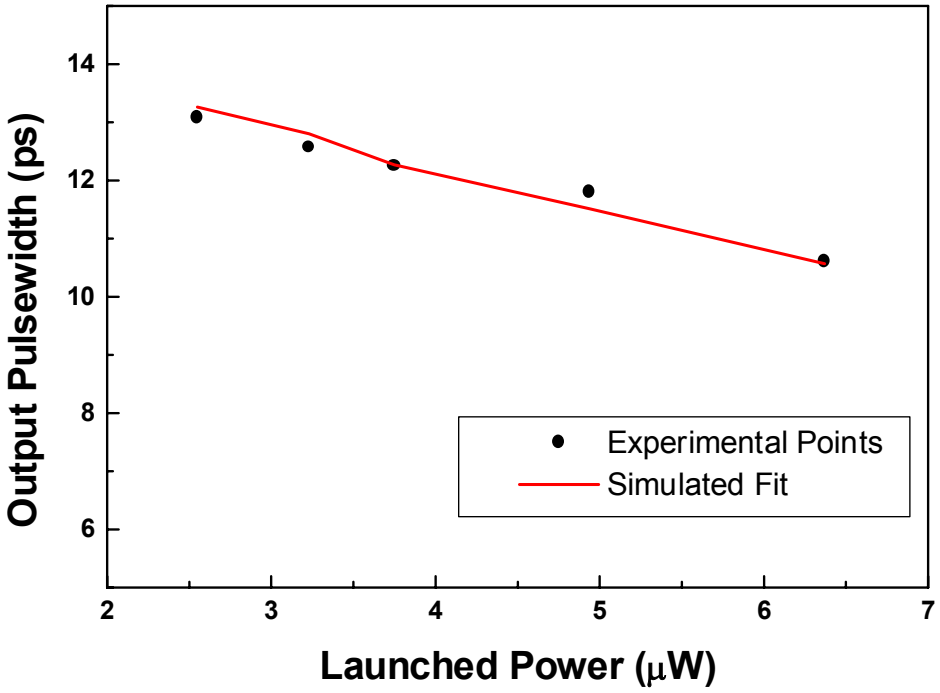

Figure 9

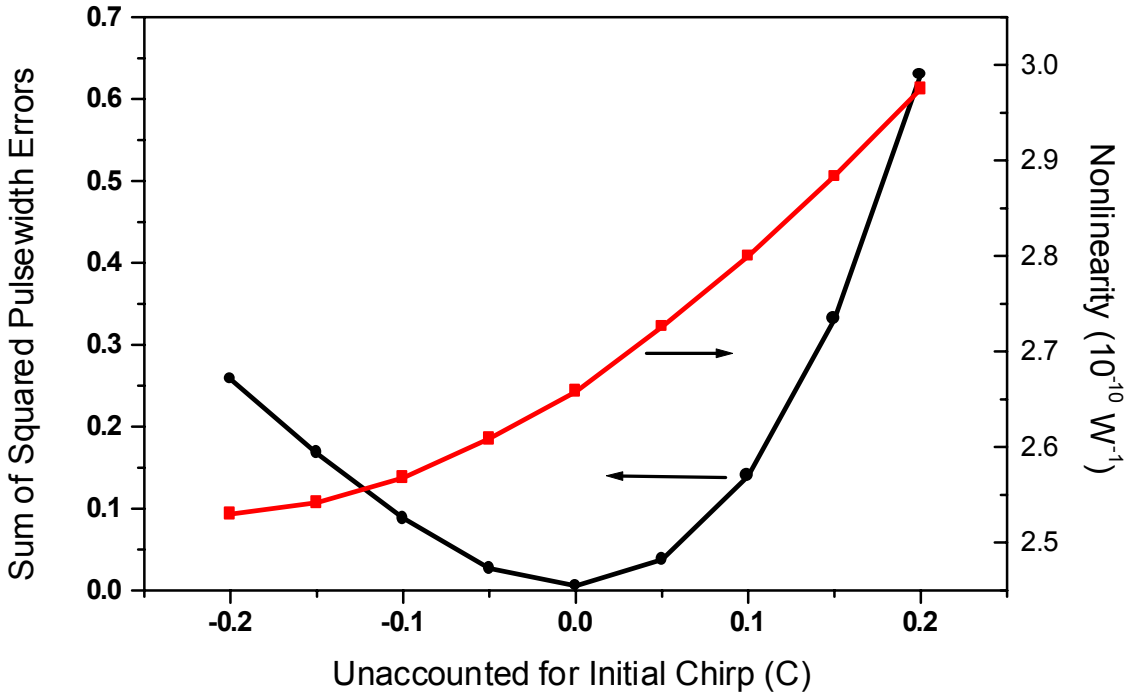

Figure 10

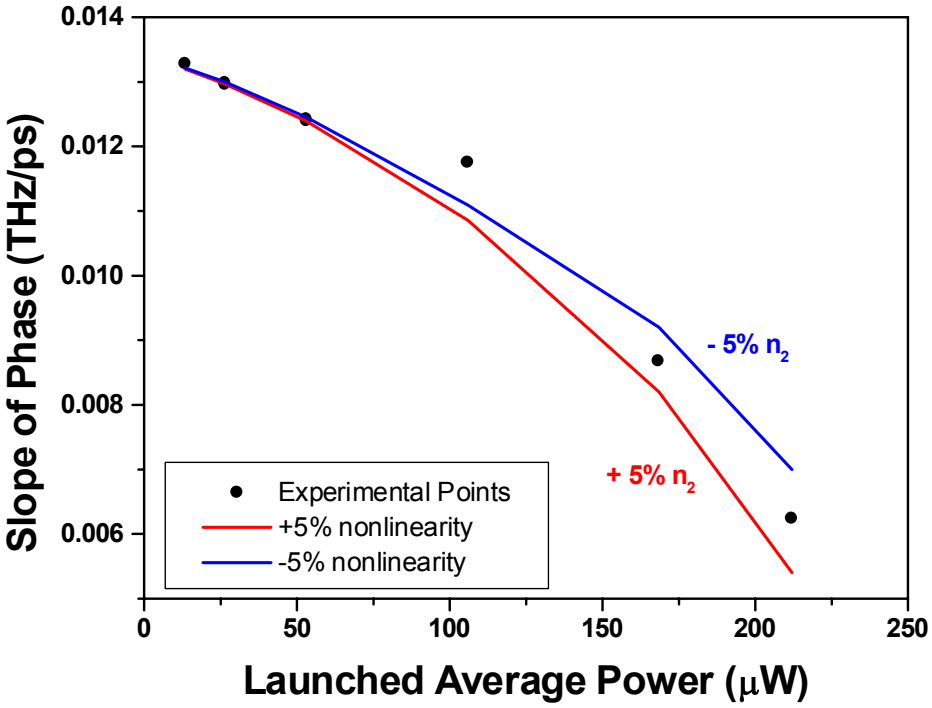

Figure 11

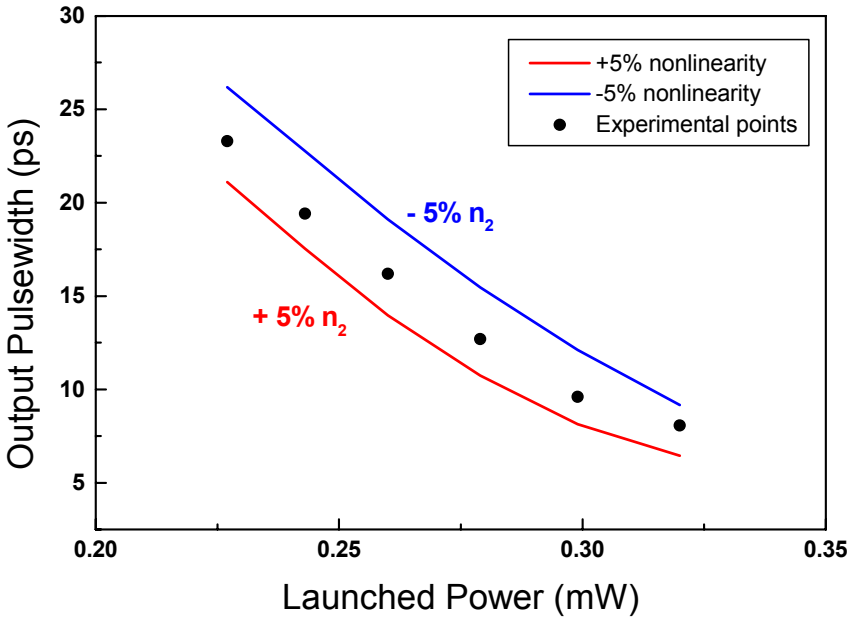

Figure 12

Appendix M

Demonstration and Performance Analysis for the Off-Ramp Portion of an All-Optical Access Node

O. Boyraz, J.W. Lou, K.H. Ahn, Y. Liang, T.J. Xia, Y.-H. Kao, and M.N. Islam
Department of Electrical Engineering and Computer Science, 1214 EECS Building,
University of Michigan, 1301 Beal Avenue, Ann Arbor, MI 48109

Abstract

Ultrafast processing of packets is demonstrated and the performance analyzed for the off-ramp portion of an all-optical access node. The off-ramp consists of synchronized fiber lasers driving an all-optical header processor that includes nonlinear optical loop mirrors (NOLM), electro-optic router, and demultiplexer in the form of a two-wavelength NOLM. We achieve switching contrasts of 10:1 for the header processor and demultiplexer with switching energies of 10 pJ and 1 pJ, respectively. Also, a proposed measurement technique to obtain eye diagrams is used to analyze the all-optical header processor using the synchronized lasers. Using this technique, we obtain an eye diagram with a Q value of 7.1±0.36, which corresponds to a worst case BER value of 8.8×10^{-12} for a 95% confidence level. Finally, simulation models are used to verify and compare the experimental results, and we find good agreement. We also use the model to study the various causes for the degradation of the Q value through our system.

I. Introduction

As single-channel speeds exceed electronic limitations for packet processing in time-division multiplexing (TDM) networks, all-optical packet processing becomes necessary to avoid speed bottlenecks. Toward this goal, we experimentally demonstrate the packet drop (off-ramp) functions for an all-optical access node for a 100 Gbit/s packet network, and we analyze this performance using an eye diagram measurement technique to look at the statistical bit-error-rate (BER). By integrating synchronized fiber lasers [1], all-optical header processor in the form of nonlinear optical loop mirrors (NOLM) [2], electro-optical packet router, and payload demultiplexer, we demonstrate an integrated system as opposed to individual components. This also allows us to study the system performance of the all-optical off-ramp.

The integration gives insight into some of the key challenges of 100 Gbit/s packet TDM networks, including multiple levels of all-optical logic gates operation, synchronization between the incoming data and the local source, and power budget for operation of the node. This demonstration shows the inter-compatibility of the various optical components as well as the network functionality of the all-optical header processor and demultiplexer. Using an 8-bit, 100 Gbit/s word, we achieve 10:1 contrast ratios from the header processor and the demultiplexer and 17 dB contrast ratio from the packet router.

Beyond demonstrating the functionalities, measurement techniques must be devised to test the error performance of these ultrafast devices. Currently, the method to measure the performance of a telecommunication device is to use a bit-error-rate (BER) tester, which sends a long bit pattern to the test device and counts the number of errors that occur through the device. However, these BER testers are currently limited to about 15 Gbit/s. Therefore, to overcome this limitation, we use a method based on a sampling technique [3], using a cross-correlator and reference pulse. This allows the measurement of eye diagrams with picosecond resolutions. However, the speed of the technique is limited to the sampling speed. We apply this technique to the all-optical header processor and obtain an eye diagram with a Q value of 7.1 at 12 pJ switching energy for the header processor. This Q value corresponds to a statistical BER value of 7.0×10^{-13}.

There have been previous sub-system demonstrations using semiconductor devices and simplified architectures. Cotter *et al*. route 100 Gbit/s, six bit packets using a single AND-gate as the header processor [4]. The use of a single AND-gate to process the header requires special bit patterns for the AND gate to be able to distinguish the headers. In addition, Glesk *et al.* demonstrate all-optical address recognition and self-routing in a 250 Gbit/s packet-switched network [5], in which a switch operating only one bit for each packet is used. Unlike these previous demonstrations, our node architecture enables more general optical serial processing capabilities because of increased flexibility through the possibility of using multiple levels of logic operations. The fiber based NOLMs, which are used as the optical logic gates in this paper, have been shown to have unique properties such as ultrafast speed, cascadability, and Boolean completeness [2]. Although only two levels of logic operation have been demonstrated in this paper, further levels of operation are possible because the logic gates are regenerative. Multiple levels of logic operation permit multiple processing on the header, for example, to check empty packets, bit errors, or special conditions.

This article focuses on two aspects of the packet processing capabilities for the off-ramp. The first aspect, described in sections II and III, is the functionality of the off-ramp with focus on switching contrasts and switching energies. Then in sections IV and V, the second aspect, system performance is discussed with the focus on potential statistical BER measurements of the off-ramp. To start with in section II, we describe the experimental setup for the off-ramp portion of the access node. Then, in section III, we present the experimental results for the packet processing. In section IV, we describe the system performance measurement technique and the experimental setup for that measurement, and in section V, the experimental results for the eye diagram are presented. Subsequently, in section VI, we compare the experimental results with simulation models for analysis of our results and for discussion about future designs. Finally, we conclude with a summary of our results and discuss future work for the all-optical access node.

II. Experimental Setup for Access-Node

Figure 1 shows a detailed experimental setup with a simplified block diagram for the off-ramp in the inset. The incoming packet from a distant transmitter enters the node. Upon entering the node, part of the packet energy is tapped to the header processor, and the rest is passed to the router through a delay line. In the node, a local laser, which is synchronized to the incoming packet rate, is used to generate the local clock pulses and the local address. The header processor, consisting of an inverter and an XOR gate, processes the incoming packets and controls the switch/router. A demultiplexer reads the payloads of the incoming packets using another synchronized local laser of a different wavelength.

The transmitter, which consists of a fiber laser (master laser) and an encoder, produces 8-bit packets (3 bit header '101', 5 bit payload '10010') that are sent to the node. The synchronized local laser (slave laser #1) with the same wavelength as the master laser passes through a clock encoder to generate clock bit patterns and a local address encoder to generate the local address pattern for the all-optical inverter and XOR gates. The inverter determines whether the incoming packet is empty or not. An empty packet would have header bits that are all '1'. If the packet is not empty, then the inverter sends an inverted header pattern to the XOR gate. A local address generator sends the inverted local address to the XOR gate. If the header and local address match at the XOR gate, then there is no output, and the packet will go to the demultiplexing unit. If the headers do not match, the XOR gate output has at least one bit that is '1', which will trigger the control of the packet router to shift the packet back to the network. The payload in the packet goes to the demultiplexer, which is a two-wavelength nonlinear optical loop mirror (2-λ NOLM) driven by the other synchronized local laser (slave laser #2) with the wavelength different from that of the transmitter [1, 2].

The master laser and the slave lasers are passively mode locked, Er/Yb co-doped fiber lasers [6]. The pulse widths are 2 ps at 1535 nm for the master laser and slave laser #1 and at 1543 nm for the slave laser #2. Synchronization of the master laser and the slave lasers is achieved by sending a separate clock pulse from the master laser to the slave lasers [7]. Although the laser repetition rate is 21 MHz, splitting each laser pulse and combining them with couplers and delay lines to have pulse-to-pulse separations of 10 ps creates 100 Gbit/s words. The local laser pulse is aligned to the first pulse of the packet.

Therefore, the clock and local header align to the header and payload automatically for fixed header and payload lengths.

This synchronization is designed to force the local lasers to follow the slow drifts of the remote clock pulse rate and to simulate an all-optical clock recovery in the network. The response bandwidth of the synchronization circuit is 10 kHz and it is limited by the acousto-optic modulator (AOM). In addition, the speed of the circuit is limited by the opto-electronic detectors and the RF components used in the phase locked loop circuit design. In this experiment, we use 1 GHz RF components and the synchronization is limited by the maximum frame rate of 1 GHz. However, in real network design, an access node should recover both timing of packet and bit separation. With this synchronization scheme this would be possible for low repetition rate applications because of the limitations of electronics at high frequencies.

The all-optical logic gates are constructed by using low birefringent nonlinear optical loop mirrors (low-bi NOLMs). The low birefringence ($\Delta n \sim 10^{-6}$) is obtained by wrapping fibers with very low background birefringence on aluminum mandrels. This technique allows for longer interaction lengths between co-propagating, orthogonally polarized pulses than in conventional polarization maintaining fiber while maintaining a high polarization extinction ratio (PER~40:1). An advantage of this kind of optical logic gate is its cascadability. Because the logic gate is also regenerative, this allows multiple levels of all-optical logic operation. Another advantage is the timing window, which makes the NOLMs tolerant to possible timing jitter between the bits. The logic gates have switching energies of 10 pJ/pulse, timing windows of 5ps, and nonlinear transmissions of 50% [2].

The demultiplexing and packet routing use guided-wave optical structures. The 2-λ NOLM with a timing window of 6 ps demultiplexes the payload into individual bits. This 2-λ NOLM uses a high nonlinearity, dispersion-shifted fiber (λ_0=1530nm), which has a smaller core size (effective area A_{eff} = 17 μm^2) to increase optical intensity and a higher germanium doping to increase the intrinsic nonlinear coefficient. The effective nonlinearity is 4.4 times that of a normal dispersion-shifted fiber. The switching energy of this device is less than 1 pJ/pulse. A commercial 2x2 $LiNbO_3$ modulator is used as the packet router.

III. Experimental Results for Access Node

The output of the various components of the all-optical off-ramp is measured by using a cross-correlator. Because the pulses are only 10 ps apart in our packets and because we are looking at energy contrasts of the individual pulses, the cross-correlator gives us the most relevant information. We use a fixed reference pulse as one of the inputs to the cross-correlator.

The output for the header processor is shown in Fig. 2. Figure 2a shows the incoming data packet, including the header bits, ‘101’. The inverted header output, ‘010’, from the inverter is shown in Fig. 2b with an intensity contrast of ≥10:1 between the ‘1’ and ‘0’. This output is used as the input to the XOR gate. Figures 2c and 2d show the XOR gate output when the header and the local address match and not match, respectively. In both cases, the intensity contrast between the ‘1’ and ‘0’ is at least 10:1. This contrast ratio is limited by the in-complete switching caused by pulse distortion due to non-soliton

pulse propagation and the induced chirp during the amplification of the pulses at the erbium-doped fiber amplifiers (EDFAs).

The output from the header processor containing the information of matched or unmatched header is used to drive the packet router with the results shown in Fig. 3. The packet router is a $LiNbO_3$ modulator. When the incoming header does not match the local address, the packet is routed back onto the network. The energy contrast ratio of the signal returning to the network over the leakage through the modulator is 17 dB. In this experiment, the performance of the demultiplexer is not affected by the packet router, however, to add a new packet into the network, on-off ratio of the router will be important. Theoretically, the on-off ratio of 17 dB might cause a maximum amplitude modulation of (+/-) 25% in packet addition due to the interference between the leakage and the new packet. A two-stage packet router can be used to prevent the interference problems.

When there is a match between the header and the local address, the packet is routed to the demultiplexer. The demultiplexed output for each channel is shown in Fig. 4. For channels (1-5), the pump pulse for the demultiplexer is delayed by 10 ps each time to select the appropriate bit. The contrast ratio is 10:1 between the '1' and '0' bits. Residual signals in the '0' bits indicate pump leakage and energy tails from the adjacent '1' bit of the payload. These residual signals are not visible in Fig. 4 because we use an auto-correlation to see each individual bit, and the 10:1 contrast ratio is too high to distinguish the relative difference between '1's and '0's in the auto-correlation.

These preliminary results show inter-compatibility of the all-optical components towards a packet TDM access node. The major challenges are multiple levels of all-optical logic operation, low jitter synchronization, and power budget. Our results prove that the fiber-based optical logic gates are cascadable and can be used to perform multiple levels of all-optical logic operation. The synchronization scheme used in this paper shows a very low timing jitter (< 1 ps). By using low birefringence to increase the walk-off distance in the header processor, we have been able to lower the switching energy to about 10 pJ/pulse. The range of switching energies for the header processor is 5 to 15 pJ/pulse, and that for the demultiplexer is 0.5 to 1.0 pJ/pulse. The output switching contrast is directly related to the switching energy. However, if the input switching energy is too high, pulse distortion occurs in the loop mirror and the switching contrast will degrade. Here, the header is fixed to specify the destination address within the ring network structure. In order to have broadcasting capabilities, a special address can be added to the header and one more level of optical logic operation may be needed. To avoid errors from possible node failure, the packet router switch will be set to direct the data back to network when there is no power to the node.

IV. Eye Diagram Measurement Technique and Experimental setup

A sampling method to measure the eye diagram is applied to the header processor portion of the off-ramp using the synchronized fiber lasers. Using a cross-correlator with a reference pulse, we can measure the eye diagram with picosecond resolution for 100 Gbit/s packets. The conventional bit-error-rate tester (BERT) does not have the required resolution to measure the eye diagram for such tightly spaced bits.

Figure 5 shows the detailed experimental setup, and the inset shows the general overview for the setup. As in the previous setup, the synchronized sources for the

header processor are the master laser, representing a transmitter and the slave laser, acting as the local laser. Both lasers produce 2 ps pulses at 1535 nm with a repetition rate of 21.6 MHz. Unlike the previous case, the encoder for the master laser now produces the packet pattern '0001011100' with 10 ps bit-to-bit separations. The reason for this particular pattern is that by taking some particular 3-consecutive bits of this pattern, we can form all of the possible 3-bit patterns that start with a '1' bit. This is important for looking at any pattern dependent effects on the performance of the header processor. The starting bit of the header packet must be a '1' for synchronization purposes and for feedback purposes in order to stabilize the system. Also, for this first bit, the first gate does not act as an inverter, which makes a '1' output at the first bit position for all of the four different patterns. The output from the slave laser passes through the clock encoder to produce the 3-bit pattern '111'. As before, the inverter determines if the incoming packet is empty, and the XOR gate determines if there is a match to the local address.

We also use a feedback loop within the experimental setup to control timing drifts between the two gates caused by thermal expansion of the fiber in the first logic gate. A schematic of this feedback scheme is shown in Fig. 6. By using the fact that in our architecture, all of the header packets will start with a '1' bit for clock recovery purposes, we use this first bit for timing corrections within the header processor. Since the thermal change is slow, the feedback circuit can also be slow with the feedback loop checking roughly every 5 sec. The feedback uses a cross-correlator (cross-correlator 2 in Fig. 5) and an optical delay stage to maintain the timing between the cascaded gates. We set the gates appropriately so that the first bit, which is always a '1' bit, of the incoming header packet will produce a '1' bit in both gates. Then, by looking at the peak of the first bit output of the header processor with the cross-correlator and maximizing this value, we control the delay stage to maintain the timing between the two gates. This method works because the first bit is a constant value and because the timing drift due to thermal effects is slow, requiring only a slow adjustment. Without this feedback control, the timing would cause a degradation of switching contrast, which would degrade the performance.

The output of the header processor, which can be any one of four possible 2-bit patterns, is split and sent to the diagnostics for performance analysis. Cross-correlator 1 is carefully set up to use the fast response (~10 ns rise and decay time, packet separation of ~47 ns) of the photomultiplier tube (PMT) to remove any of the averaging effects. By using a digital scope to take single-shot scans of the signal from the PMT, a single pulse response is taken per scan. We take a large number of scans while varying the timing between the reference pulse and the output of the header processor. Then, by overlaying the scans, we can map out the eye diagram with picosecond resolution for all the possible patterns. There are a few limitations in this sampling technique, which will be addressed in the discussion section.

V. Performance Measurement Results and Analysis

The eye diagram for the header processor is shown in Fig. 7. This is one of several measurements that we have taken for the eye diagram. The eye diagram is for return-to-zero, hyperbolic secant pulses, and it is an overlay of all possible outputs from the header processor. The input headers are four nonrandom, but different and equal numbers of 2-bit patterns, and the local address bit may be a '1' or '0'. Because there can be incomplete balancing for the NOLM when acting as an inverter or XOR gate, the '0'

level will not be a true '0'. This causes a finite switching contrast. Also, the NOLM has a finite polarization extinction ratio causing pump leakage to be present for both the '1' and '0' outputs. For the '1' output, the pump leakage is always present, which effectively adds a constant background. However, for the '0' output, there are two possible cases in the XOR ($\oplus$) gate. The '0' level can arise for the case without any pump pulses (i.e. $0 \oplus 0 = 0$ + no leakage) and for the case with two-pump pulses (i.e. $1 \oplus 1 = 0$ + leakage from two pump pulses + incomplete balancing). This leads to a spread of the '0' level in the eye diagram, where half of the '0's will be without any pump leakage and the other half with pump leakage and energy from incomplete balance within the NOLM. However, there is no such spread for the '1' level because the '1' output occurs when the NOLM is unbalanced and the leakage is always present. This leads to less distribution at the eye diagram as compare to the '0' output case.

By looking at the center points of the eye diagram as done by Matsumoto *et al.* [8], we can measure the Q parameter from which we can statistically calculate the potential BER. Unlike Matsumoto, who looks at the tail of the pulse, we look at the center of the eye for the '0' level because we must also consider the pump leakage, which will give the worst case. The Q parameter, which describes the quality of the received signal, is defined as:

$$Q = \frac{I_1 - I_0}{\sigma_1 + \sigma_0} \tag{1}$$

with I_1 and I_0 being the sampled means of the 'on' and 'off', respectively and with σ_1 and σ_0 being the sampled standard deviations of the 'on' and 'off', respectively [9]. The statistical BER is given by:

$$BER = \frac{1}{2} erfc(\frac{Q}{\sqrt{2}}) \tag{2}$$

where the *erfc* is the complementary error function based on the assumption of Gaussian distribution. For each 2-bit pattern, 300 data points are taken. Because there are 4 different possible 2-bit patterns, the total number of data points is 1200. In addition, because the local bit can be '0' or '1', there are 1200 data points for the '1' level and the '0' level. With these points, we find a Q value of 7.1 for the eye diagram of Fig. 7, which corresponds to a BER of 7.0×10^{-13}. We measured the Q value 5 times with the measured values all within 10 percent of each other, thus showing a repeatability of the measurement.

As a check, we look at the Q value versus the number of data points to make sure that the 300 data points per pattern is valid. Figure 8 shows the calculated Log(BER) versus the number of sampled points corresponding to the data of Fig. 7, and we can see that the performance result converges fairly rapidly and stays relatively constant after the first 100 overall points. Therefore, we can see that taking more points per pattern only reduces the error bar of the measurement without changing the end result.

Because this is a statistical method, we must look at the associated confidence interval to calculate possible errors in the measurement. The confidence interval is an interval of values that contains the true value of a parameter with a given confidence level. For a given system, the confidence interval for the mean [10] is given by:

$$P[I_n - t_{n-1,1-\alpha/2}\frac{\sigma_n}{\sqrt{n}} < \mu < I_n + t_{n-1,1-\alpha/2}\frac{\sigma_n}{\sqrt{n}}] = 1-\alpha\,, \quad (3)$$

and the confidence interval for the variance is given by:

$$P[\frac{(n-1)\sigma_n^2}{\chi^2_{n-1,1-\alpha/2}} < \sigma^2 < \frac{(n-1)\sigma_n^2}{\chi^2_{n-1,\alpha/2}}] = 1-\alpha \quad (4)$$

where I_n is the sampled mean, μ is the (unknown) true mean, σ_n is the sampled standard deviation, σ is the (unknown) true standard deviation, n is the number of sampled points, and (1 - α) x 100% is the confidence interval level. The $t_{v,p}$ and the $\chi_{v,p}$ are the standard t-distribution and the chi-square distribution, respectively, with subscripts being appropriately substituted with the subscripts defined by the confidence intervals. By looking at the confidence interval and setting the confidence level to 95%, we can calculate the error range of the Q value to be from 6.7 to 7.4 for the eye diagram of Fig. 7. This means a worst case BER of $8.8\text{x}10^{-12}$ and a best case BER of $4.8\text{x}10^{-14}$. Note that this error range is inversely related to the number of sample points for a given confidence level. While this method has a better resolution than the regular BERT, the BERT typically uses many more data points. Therefore, the confidence level for a BERT result can be much higher than this sampling technique.

To test the variation in parameters of this technique, we also look at the performance of the header processor as a function of input packet pulse energy. To study this, we measure the Q value of the header processor while varying the pulse energies of the incoming packet. We start with an input pulse energy of 12 pJ and decrease it at increments of 2 pJ for a total of 4 sets.

Figure 9 shows the variation of (a) the Q value and (b) the extrapolated BER value as the input packet pulse energy is varied. The error bars on the data points are calculated with a 95% confidence interval level, and the range of the error bars is defined by the confidence interval. Because the ratio of error range over the measured value is nearly constant for a given confidence level, the error bars are larger for the higher Q values (lower BER). We find that both the Q values and the corresponding BER values degrade linearly with the input power. This is primarily caused by the degradation of the switching contrast of the gates, which also degrades linearly with the switching energy.

VI. Modeling and Simulation Results

We also compare our experimental results with results of a simulation that we developed. In our simulation, we try to separate each parameter, which can degrade the Q value. For the header processor, there are several sources of noise that we must take into account. These include the laser sources, amplifiers, timing jitter, and intersymbol interference (ISI). In addition, the incomplete switching/balancing of the NOLMs along with the pump leakage can enhance these noise effects. Because it is not possible in the experiment to separate out each of these sources of noise, we look at a simulation model to understand the significance for each cause of noise.

Before we look at the full model, we look at the noise parameters for our system. The source is a passively modelocked fiber laser where the noise of concern is the amplitude fluctuation in the pulses. We measure the amplitude jitter by looking at the

fundamental harmonic of the repetition rate [11], and we find the variance of the amplitude fluctuation to be 6.67 for the master laser and 3.37 for the slave laser. With this measurement, the input SNR is 36.6 dB for the incoming packets and 43.4 dB for the locally generated clock signals. For the amplifiers, which are EDFAs, we base our model upon the work of Desurvire [12]. In the EDFA model, the gain is given by

$$\langle n(z)\rangle = G(z)\langle n(0)\rangle + N(z) \tag{5}$$

where n(z) is the output number of photons that is directly proportional to the output power, n(0) is the input number of photons, and G(z) is the overall gain of the amplifier. N(z) is given by

$$N(z) = \frac{\eta N_2}{\eta N_2 - N_1}(G-1) = n_{sp}(G-1) \tag{6}$$

where N_2 and N_1 are the populations of the upper and lower energy levels, respectively, η is the quantum efficiency of the amplifier, G is the gain, and n_{sp} is the spontaneous emission factor. The variance of this output signal is given by

$$\sigma^2(z) = \langle n^2(z)\rangle - \left[\langle n(z)\rangle\right]^2, \tag{7}$$

and substituting in Eq. 5, we obtain

$$\begin{aligned}\sigma^2(z) = {} & G^2(z)\left[\sigma^2(0) - \langle n(0)\rangle\right] + G(z)\langle n(0)\rangle + N(z) \\ & + 2G(z)N(z)\langle n(0)\rangle + N^2(z)\end{aligned} \tag{8}$$

where $\sigma(0)$ is the standard deviation of the input signal. We also look at the noise figure (NF) of the amplifiers, which is given by

$$NF = \log(SNR_i) - \log(SNR_o) \tag{9}$$

where SNR_i is the signal-to-noise ratio of the input signal to the amplifier and SNR_o is the signal-to-noise ratio of the output signal from the amplifier. The SNR is represented by

$$\begin{aligned} SNR_i &= \frac{\langle n(0)\rangle^2}{\sigma^2(0)} \\ SNR_o &= \frac{\langle n(z)\rangle^2}{\sigma^2(z)} \end{aligned}. \tag{10}$$

Substituting in the above equations, we find the general expression for the NF to be

$$NF = \frac{SNR_i}{\langle n(0)\rangle}\left\{\frac{\sigma^2(0)}{\langle n(0)\rangle} - 1 + \frac{1+2N(z)}{G(z)} + \frac{N(z)\left[N(z)+1\right]}{G^2(z)\langle n(0)\rangle}\right\} \tag{11}$$

where by using the experimentally measured values of n_{sp} and G(z), we can calculate N(z) and then solve for $\sigma^2(z)$ and NF. Because this is the general expression for NF, the NF depends upon the input mean and variance. We can experimentally measure the n_{sp} for the amplifiers using the standard method [13] with the formula

$$NF = \frac{2P_{ASE}}{h\nu B(G-1)} \tag{12}$$

where P_{ASE} is the power of the amplified spontaneous emission, h is Planck's constant, ν is frequency of the input signal, B is the bandwidth used for the measurement and G is the gain. By using equations 5, 6, and 8, we can use the measured n_{sp} values of each amplifier to calculate the output means and output variances. We find the n_{sp} values of the different amplifiers in our system to be 1.58, 2.01, 2.04, 2.45, and 2.56.

As a test of this model, we compare the numerical model of the EDFAs with the analytic equations for cascaded amplifiers and find good agreement as, shown in Fig. 10. For this test, we assume an ideal input source with Poisson distribution for the noise parameter and a n_{sp} value of 2 for each of the amplifiers and a lumped loss element between each amplifiers. The loss element introduces loss to balance the gain of the amplifier in each segment.

The other sources of noise are the timing jitter and ISI. The timing jitter is modeled as a uniform random variable with a 0.5 ps variance centered at the center of the eye diagram. This value is calculated using the cross-correlation and autocorrelations for the two synchronized lasers [1]. This timing jitter between the incoming packet and the locally generated clock pulses translates into an amplitude jitter out of the first gate for the header processor. The degree of this transfer of jitter is determined by the timing window of the first gate, where a flatter timing window can reduce most of the jitter. The timing window for our device is shown in Fig. 11, which shows for a 0.5 ps variance in timing jitter, there could have significant effects on the performance. The other factor, which is the ISI, is included in the propagation portion of the simulation model where any pulse interactions will be reflected within the code. We will look at any pulse-to-pulse interactions by looking at the tail of the pulse for the various patterns.

In addition, the PMT also generates noise because of the gain produced in the detection scheme. Assuming the input signal to the PMT is Gaussian, the SNR at the PMT becomes

$$SNR = \frac{i^2}{\sigma_g^2 + \sigma_r^2} \tag{13}$$

where the first term in the denominator is the gain noise and the second term is the circuit noise [14]. The numerator is the square of the mean current generated by the incoming signal. After calculation and substitution for the generated currents from the incoming photons and assuming the circuit noise is negligible compared to the gain noise, the SNR of the incoming signal degrades by the factor (1/F), where F is known as the excessive gain noise. This F factor is typically between 1 and 2 for PMTs [14], and we set it to be 2 for our model because we used a high drive voltage for the PMT.

The NOLM will also add some noise to the output signal because the output is an interaction of two or three input signals, which have noise on them. Because there is no real analytic solution for calculating the NF for a NOLM, we study it numerically, and find the approximate equation for the NF as a function of the ratio of the incoming input energies and the ratio of the incoming SNRs. Figure 12a shows the degradation of NF in

gate 1 as we change the ratio of incoming SNRs, and fig. 12b shows degradation of NF in gate 2.

We can look at the SNR degradation of the system based upon the NFs of the amplifiers, NOLMs, and PMT. By using the analytic calculations for each of the amplifiers, the calculated NFs for each of the NOLMs as shown in Fig. 12, and with the 3 dB degradation from the PMT, we calculate the overall degradation of the SNR to be 11.7 dB. However, this SNR cannot be directly related to the Q value for this system because it does not include several key effects. First, there is uneven switching found in the second gate of the header processor due to the fact the unequal pulse widths interact in the loop, which is too short to have a full walk-through. Consequently, when the energies are set to have the best balancing possible (i.e. $1 \oplus 1 = 0$), the individual '1' bits are not at the same level. Second, due to pump leakage from each gate, there is a spread of the '0' level. Third, as mentioned above, the timing jitter will also close the eye diagram due to amplitude jitter. Fourth, pulse quality can also affect the performance by degrading the switching contrasts for each of the gates.

To include all of these additional effects, we numerically model the low-bi-NOLM by the use of the coupled nonlinear Schrödinger equation (NLSE) for birefringent fibers [15] with the addition of noise sources, which were discussed above. These equations include the birefringent walk-off between two orthogonally polarized pulses, group velocity dispersion, self-phase modulation, cross-phase modulation, and the Raman effect. In addition, we include a chirp parameter that is represented in the pulse by

$$u(t) = u_0 \operatorname{sech}\left(\frac{t}{\tau}\right)\exp\left(-\frac{iC_p t^2}{2\tau^2}\right) \tag{14}$$

where C_p is the chirp parameter [16] and u_0 is the amplitude. The chirp on the pulse has a large effect on the pulse evolution within the loop, which could affect both the timing window and output pulse shape. We include the chirp parameter because the EDFL produces slightly chirped pulses.

In the simulation, we convert all the measured values to standard normalized soliton parameters [15]. These parameters are calculated by using the following equations. The soliton period is given by

$$u(t) = u_0 \operatorname{sech}\left(\frac{t}{\tau}\right)\exp\left(-\frac{iC_p t^2}{2\tau^2}\right) \tag{15}$$

where c is the speed of light in free space, τ is the pulse width, λ is the center wavelength, and D is the dispersion. The walk-off length, l_{wo}, defined to be the length required for the peaks of two pulses to separate by one pulse width, is

$$l_{wo} = \frac{c\tau}{\Delta n} \tag{16}$$

where Δn is the birefringence. The normalized birefringence is given by

$$\delta = \frac{\pi \Delta \mathrm{n}\, \tau}{1.763\lambda^2 |D|} \tag{17}$$

The fundamental soliton peak power is given by

$$P_c = \frac{\lambda A_{eff}}{2\pi n_2 Z_c} \tag{18}$$

where A_{eff} is the effective are of the fiber and n_2 is the Kerr coefficient for fiber. Also, Z_c is the characteristic length given by

$$Z_c = \frac{2Z_0}{\pi} \tag{19}$$

From these the control and signal amplitudes are calculated by

$$u = \sqrt{\frac{P_u}{P_c}}$$
$$v = \sqrt{\frac{P_v}{P_c}} \tag{20}$$

where P_u and P_v are the peak powers of the control and signal pulses, respectively. The normalized parameters that are used in the simulations are shown in Table 1.

Using the above simulation model with the addition of noise as outlined above, we find the eye diagram for the overall header processor. The eye diagram is shown in Fig. 14. The Q value for this eye is 7.7 and the corresponding calculated BER is 6.8×10^{-15}. The discrepancy from the experimentally measured Q value of 7.1 is probably due to thermal drifts during the time scale of the measurement process, which can change the power levels or polarization states. Also, the varying non-uniformity of the encoders also adds an additional variance that is not included in the model. This non-uniformity cannot be modeled with any steady random distribution because this non-uniformity changes from day to day as well as during the measurement process due to thermal drifts in the fiber and pulse interactions within the encoders. Consequently, the difference between the simulation and experiment is not unexpected.

We also look at the individual contributions of the various sources of noise. By changing the timing jitter value, local laser chirp and switching energies, we calculate the Q value. We find that the Q value matches the experimental results for jitter values less than 0.6 ps, which is approximately equal to the experimental value of 0.5 ps. Figure 13a shows the change in Q value for different timing jitter values. Since we are using many different types of fibers that may chirp pulses, we simulate the effect of the initial chirp in our local laser. We find that the Q value goes up to 8.2 for negative chirp and gradually decreases as we go to the positive chirp as shown in Fig. 13b. This indicates that better gate performance may be achieved by adding some chirp to the two input arms.

Using the simulations, we also try to look at pattern dependent effects. We cannot split out this effect from the code. However, by looking at the tails of the pulses for any pulse-to-pulse interaction, we find that there are insignificant differences from the various input patterns with a change of 4 percent on the performance. Considering the statistical nature of the experiment, this indicates that the ISI from bit-to-bit interaction is negligible. In addition, the energy at the tail is 1.4 percent of the pump leakage energy. Therefore, the pump leakage dominates any pattern dependent effects on the switching performance.

Because of the relatively short length of the header processor (less than 1 km), any ISI effects from pulse-to-pulse interactions should be negligible.

VII. Discussion

Although the simulation results agree with the experimental results, there are some limitations for the sampling technique that must be discussed. First, while the eye diagram is measured experimentally, because of the lack of long, random bit patterns, any long-pattern ISI information cannot be extracted with the technique. However, because the header processor only looks at the packet headers of incoming packets and not at long streams of bits, the long random pattern ISI is not significant. By looking at the different possible patterns as described above, the relevant ISI degradation should be represented. In addition, we find that the most significant cause of degradation is the pump leakage from the wrapped fibers. The second limitation is that the BER values are calculated statistically from the eye diagram assuming a Gaussian noise distribution. Depending on the actual noise distribution, this may give an inaccurate value for the BER. However, the Gaussian assumption generally underestimates the performance because the major contribution of noise is from the amplifiers, which have an exponential noise distribution [17]. Finally, because the BER measurement is a statistical measurement, there is an error bar (confidence interval) associated with the value. This error bar is related to the number of data points (or bits) taken in the sample. For example, for the 1200 points of Fig. 7, the error of the Q value is ±5%, and as shown in Fig. 8, the accuracy of the method can be improved by using more points (or bits) without changing the statistical value.

The other limitations are regarding the speed of the measurement technique since the PMT's 10 ns rise and decay time is slower than the bit-to-bit separation or even the packet-to-packet separation. Because we are using a cross-correlator, the signal only appears from the PMT when a reference pulse is present. Consequently, even though the packet repetition rate may be high, as long as the reference pulse used for the performance measurement has a slower repetition rate (larger than 10 ns pulse-to-pulse separation for this PMT), there is no averaging of more than one pulse per sample points. Therefore, the resolution can be set by the pulse width used for the reference pulse. However, the flip side is that because the reference pulse repetition rate can be much slower than the packet rate in a 100 Gbit/s system, not all of the packets are used for the eye diagram. The result is that even if we can run the process every 10 ns and assuming 1 ns long packets, we would get 1 out of every 10 packets to be processed in the test. Since the method is a statistical one, performing the statistics on every 10^{th} packet or every packet should be the same. Nevertheless, by using a faster detector (with 40GHz commercially available) and a faster digital scope (with 50 GHz bandwidth commercially available) to speed up the process, the method can potentially do the statistics using all of the packets. In our experiment, the communication rate between the scope and the computer could be another speed limitation and this limitation can be fixed by storing the eye data on the scope during experiment and downloading and the processing the data after the experiment. The accuracy of the statistical method could be increased by using a fast programmable encoding scheme to change the header of the packet.

VIII. Conclusion

In summary, we have demonstrated and analyzed all-optical serial packet processing for 100 Gbit/s words in the off-ramp part of a TDM network access node. The demonstration consists of integrating the various components and looking at the device performance of the off-ramp. The header processor, consisting of two cascaded low-bi NOLMs, has switching energies of 10 pJ/pulse and switching contrast of 10:1. The demultiplexer has a switching energy of less than 1 pJ/pulse and switching contrast of 10:1. The packet is routed with a contrast ratio of 17 dB.

We test the system performance of the all-optical header processor driven by two synchronized fiber lasers by measuring the eye diagram. We use a sampling technique to obtain an eye diagram and statistical methods to calculate the Q value and the corresponding BER. We measure an eye diagram with a Q value of 7.1 with a ±5% error for 100 Gbit/s word packets, which corresponds to a statistically calculated BER value of 8.8×10^{-12}. Finally, we compare the experimental results with simulation models and find good agreement. The simulations calculate a Q value of 7.7, which corresponds to a BER of 6.8×10^{-15}. We also test the degradation of the Q parameter as a result of timing jitter and chirp, and find that the system performance can be improved by adjusting the initial pulse quality and reducing the timing jitter between the two synchronized lasers. This demonstration is used to study the integration issues for combining several different optical components for all-optical packet processing. In addition, the system performance measurement shows that such integration is possible with acceptable performance.

This work is supported by DARPA.

Figure captions

Figure 1. Block diagram and detailed diagram for the off-ramp experiment. The transmitter consists of a master laser and a packet encoder. The off-ramp part consists of synchronized local lasers, a local header generator, a clock pulse train generator, a header processor, a packet router, and a demultiplexer. (INV = inverter, XOR = exclusive OR, 2λ NOLM = two-wavelength nonlinear optical loop mirror, and EDFL = Erbium Doped Fiber Laser)

Figure 2. Cross-correlation results for the header processor. (a) Input data packet. (b) Output of the inverter. (c) Output at the XOR gate when the headers match. (d) Output at the XOR gate when the headers do not match (the inverted incoming header is 010 and the local header is 100).

Figure 3. Cross-correlation results of the output of the packet router. (a) The incoming header does not match the local header (packet sent back to network). (b) The header matches the local header (packet sent to demultiplexer).

Figure 4. Autocorrelation results of the demultiplexer. (a) Input data packet. (b-f) Output of the 2λ NOLM by adjusting the delay of the local pulse by an additional 10 ps each time.

Figure 5. Experimental setup for eye diagram measurement. The Master laser passes through the encoder producing '0001011100', and the Slave laser passes through clock producing '111'. The output of the header processor, consisting of two NOLMs, is sent to cross-correlator 1 for measuring the eye diagram. Cross-correlator 2 is used for the feedback control. The solid lines are optical paths, and the dashed lines are electrical paths. (PLL = Phase Locked Loop, NOLM = Nonlinear Optical Loop Mirror, AOM = Acousto-Optic Modulator, EDFA = Erbium Doped Fiber Amplifier, PBS = Polarization Beam Splitter).

Figure 6. Schematic of feedback loop for timing drift control. The first output bit of header processor is sent to a cross-correlator. Using the signal as feedback signal, the computer receives the signal from the voltmeter and controls the optical delay stage between the two logic gates. The solid lines are optical paths, and the dashed lines are electrical paths. (NOLM = Nonlinear Optical Loop Mirror, EDFA = Erbium-Doped Fiber Amplifier, PBS = Polarization Beam Splitter).

Figure 7. Eye diagram of header processor (cross-correlation). This is the trace of the eye diagrams taken with the setup of Fig. 5 where the trace is taken by moving an optical delay stage in the cross-correlator. It is an overlay of all the different possible combinations of the 3-bit incoming header and the two possible values of '0' or '1' for the local bit.

Figure 8. Calculated Log(BER) vs. number of data points. This shows that the performance of the header processor converges to a stable value after roughly 100 data points. By using 300 data points, the performance does not change, but only the error bar of the measurement is decreased.

Figure 9. Results for various incoming packet pulse energies. Looking at the center of the eye diagram, we measure (a) Q value and (b) Calculated BER while changing the pulse energy of the incoming packet. Error bars are set for 95% confidence level.

Figure 10. Test of numerical EDFA model vs. analytical EDFA model for cascaded amplifiers. The NF is calculated for various numbers of cascaded amplifiers.

Figure 11. Timing window of Gate 1. The solid line shows the experimentally measured timing window for the first gate, and the dots represent the simulation timing window used in the model.

Figure 12. NF degradation calculated for each of the logic gates. (a) Gate 1. (b) Gate 2. The numerical data is fitted using a linear fit for each gate with the NF being a function of input energies and input SNRs.

Figure 13. Degradation of the Q value with (a) Increasing timing jitter (b) Chirp in local laser. By changing the timing jitter between two synchronous lasers and the chirp in the local laser, a Q value of 8.2 is achievable.

Figure 14. Simulation result for eye diagram of header processor (simulated pulse). It is an overlay of all the different possible combinations of the 2-bit incoming header and the two possible values of '0' or '1' for the local bit.

Table Captions

Table 1. The parameters for the two logic gates used in simulations. The λ_0 is 1518 nm for both logic gates. The input pulse width is 2 ps, and the wavelength is 1535 nm.

References

1. M. Jiang**,** K.H. Ahn, X.-D. Cao, P. Dasika, Y. Liang, M.N. Islam, A.F. Evans, R.M. Hawk, D.A. Nolan, and D.L. Weidman, "Synchronization of Passively Mode-Locked Erbium-Doped Fiber Lasers and Its Application to Optical Communication Networks," *J. Lightwave Technol.*, vol. 15, pp. 2020-2028, Nov. 1997.

2. K.H. Ahn, X.D. Cao, Y. Liang, B.C. Barnett, S. Chaikamnerd, and M.N. Islam, "Cascadability and functionality of all-optical low-birefringent nonlinear optical loop mirror: experimental demonstration," *J. Opt. Soc. Am. B*, vol. 14, pp. 1228-1236, May 1997.

3. T. Kanada, and D.L. Franzen, "Optical waveform measurement by optical sampling with a mode-locked laser diode," *Opt. Lett.*, vol. 11, pp. 4-6, Jan 1986. H. Takara, S. Kawanishi, and M. Saruwatari, "Optical signal eye diagram measurement with subpicosecond resolution using optical sampling," *Electron. Lett.*, vol. 32, pp. 1399-1400, Jul 1996.

4. D. Cotter, J. K. Lucek, M. Shabeer, K. Smith, D. C. Rogers, D. Nesset and P. Gunning, "Self-routing of 100Gbit/s packets using 6 bit 'keyword' address recognition," *Electron. Lett.*, vol. 31, pp. 1475-1476, Aug 1995.

5. I. Glesk, J. P. Solokoff and P. R. Prucnal, "All-optical address recognition and self-routing in a 250 Gbit/s packet-switched network," *Electron. Lett.*, vol. 30, pp. 1322-1323, Aug 1994.

6. B. C. Barnett, L. Rahman, M. N. Islam, Y. C. Chen, P. Bhattacharya, W. Rida, K.V. Reddy, A.T. Howe, K. A. Stair, H. Iwamura, S. R. Friberg and T. Mukai, "High-power erbium-doped fiber laser modelocked by a semiconductor saturable absorber," *Opt. Lett.*, vol. 20, pp. 471-473, Mar 1995.

7. M. Jiang, W. Sha, L. Rahman, B. C. Barnett, J. K. Andersen, M. N. Islam and K. V. Reddy, "Synchronization of two passively mode-locked erbium-doped fiber lasers by an acousto-optic modulator and grating scheme," *Opt. Lett.*, vol. 21, pp. 809-811, Jun 1996.

8. M. Matsumoto, and H.A. Haus, "Stretched-Pulse Optical Fiber Communications," *IEEE Phot. Tech. Lett.*, vol. 9, pp. 785-787, 1997.

9. G.P. Agrawal, *Fiber-Optic Communication Systems*. New York: Wiley, 1992.

10. R.M. Bethea, B.S. Duran, and T.L. Boullion, *Statistical Methods for Engineers and Scientists*. New York: Marcel Dekker, 1995.

11. U. Keller, K.D. Li, M. Rodwell, and D.M. Bloom, "Noise Characterization of Femtosecond Fiber Raman Soliton Lasers," *IEEE J. Quantum Electron.*, vol. 25, pp. 280-287, 1989.

12. Emmanuel Desurvire, *Erbium-Doped Fiber Amplifiers*. New York: John Wiley & Sons, Inc., 1994.

13. C.R. Giles, E. Desurvire, J.L. Zyskind, and J.R. Simpson, "Noise Performance of Erbium-Doped Fiber Amplifer Pumped at 1.49 μm, and Application to Signal Preamplification at 1.8 Gbits/s," *IEEE Phot. Tech. Lett.*, vol. 1, pp. 367-369, 1989.

14. B.E.A. Saleh, and M.C. Teich, *Fundamentals of Photonics*. New York: John Wiley & Sons, Inc., 1991.

15. Mohammed N. Islam, *Ultrafast Fiber Switching Devices and Systems*. Cambridge: University Press, 1992.

16. Govind P. Agrawal, *Nonlinear Fiber Optics*. San Diego: Academic Press, 1995.

17. D. Marcuse, "Derivation of analytical expressions for the bit-error probability in lightwave systems with optical amplifiers," *J. Lightwave Technol.* vol. 8, pp. 1816-1823 1990.

Appendix N